Doctoral theses at NTNU, 2018:73

Johan Kolstø Sønstabø

Behaviour and modelling of flow-drill screw connections

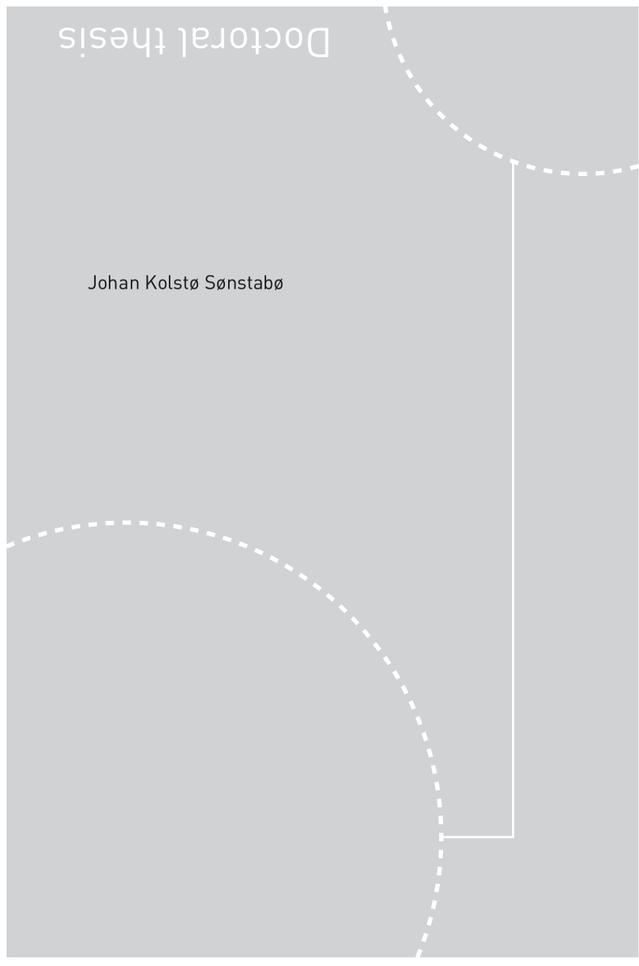

ISBN 978-82-326-2936-7 (printed ver.)
ISBN 978-82-326-2937-4 (electronic ver.)
ISSN 1503-8181

NTNU
Norwegian University of
Science and Technology

NTNU
Norwegian University of Science and Technology
Thesis for the Degree of
Philosophiae Doctor
Faculty of Engineering
Department of Structural Engineering

Doctoral theses at NTNU, 2018:73

NTNU
Norwegian University of
Science and Technology

Johan Kolstø Sønstabø

Behaviour and modelling of flow-drill screw connections

Thesis for the Degree of Philosophiae Doctor

Trondheim, March 2018

Norwegian University of Science and Technology
Faculty of Engineering
Department of Structural Engineering

NTNU
Norwegian University of
Science and Technology

NTNU
Norwegian University of Science and Technology

Thesis for the Degree of Philosophiae Doctor

Faculty of Engineering
Department of Structural Engineering

ISBN 978-82-326-2936-7 (printed ver.)
ISBN 978-82-326-2937-4 (electronic ver.)
ISSN 1503-8181

Doctoral theses at NTNU, 2018:73

Printed by NTNU Grafisk senter

Preface

This thesis is submitted in partial fulfilment of the requirements for the degree Philosophiae Doctor (PhD) at Norwegian University of Science and Technology (NTNU). The doctoral work has been funded by Department of Structural Engineering at NTNU, Centre for Advanced Structural Analysis (CASA), and Honda R&D Americas, Inc. Professor Magnus Langseth (NTNU) and Associate Professor David Morin (NTNU) have been supervisors of the work.

The thesis consists of four parts, which cover separate but related topics. Each part has resulted in an article, denoted Paper 1 to Paper 4. Papers 1 and 2 have been published in international peer-reviewed journals, while Papers 3 and 4 have been submitted for possible journal publication. A synopsis binds the different parts together.

Declaration of the author's contribution: The author has been responsible for the planning and execution of all experiments, extraction and interpretation of the experimental data, building all numerical models, running all numerical simulations, identifying the parameters used in the various material and connection models, interpreting the numerical results, producing all figures (where not otherwise stated), writing all journal and conference articles, and writing this thesis. One exception is that Mr Petter Henrik Holmstrøm, who co-authored Paper 1, was equally responsible for the planning and execution of the experiments in that paper. He also contributed with reviewing the manuscript for Paper 1. Another exception is that Dr Miguel Costas conducted the material tests and inverse modelling to obtain the material parameters used in Paper 4. The supervisors, who co-authored all articles, contributed with supervision of the work, discussions, and reviewing of the articles. The experiments were performed in collaboration with a technician, and in some cases with the assistance of master students.

Johan Kolstø Sønstabø
Trondheim, Norway
October 2017

Abstract

This PhD thesis consists of experimental and numerical studies of the behaviour and modelling of flow-drill screw connections. It is comprised of four parts, and each part has been published, or accepted for publication, in scientific peer-reviewed journals. As such, each paper may be read independently. The papers are preceded by a synopsis that brings each part into a broader perspective, states the motivation, objectives, scope and research methodology of the work, and provides a summary of the work. A brief case study is presented at the end of the synopsis.

Paper 1 is a purely experimental investigation of the behaviour of a flow-drill screw connection between sheets of aluminium alloy AA 6016 T4. Different quasi-static loadings were studied using cross, single lap-joint and peeling tests. This provided knowledge about the global force-displacement behaviour of the connections, as well as different deformation and failure modes. The paper also contains axial crushing tests of single-hat sections, joined with flow-drill screws. These tests were dominated by material deformation outside of the connections, which made it difficult to evaluate the connection behaviour.

Paper 2 addresses macroscopic modelling of flow-drill screw connections in large-scale finite element simulations. Five common models were studied, of which two were element-based and three were constraint-based. They were evaluated for two different connections. The two element-based models did not perform well, as they over-estimated the force in mixed-mode loadings. The constraint-based models yielded better results. One stood out as marginally better, appearing to be the most suited, of the five models, to represent flow-drill screw connections.

Paper 3 deals with a detailed numerical model of a flow-drill screw connection, where the geometry of the connection was discretised with a fine solid element mesh. Five different tests were simulated, and the results compared to equivalent experimental tests. A microstructure analysis and Vickers hardness tests indicated that there was a process-affected zone close to the screw. Despite that process effects were neglected in the numerical model, satisfactory results were achieved. The simulations provided a deeper understanding of the underlying deformation and failure mechanisms.

Paper 4 presents a component suited for quasi-static and dynamic testing of flow-drill screw connections, of which the design is such that the dominating deformation is taking place in the connections, and at the same time has relevant and sufficiently complex loadings in the connections. Large-scale simulations were carried out, where the preferred model in Paper 2 was employed at the connections. An improvement of the connection modelling technique was presented. The component was well-suited for validation of large-scale finite

element models.

Acknowledgements

I have gone through one of the best periods in my life during my PhD study. I am more than grateful to all the people who have accompanied me on this four year long dive into unknown space.

First I would like to thank my supervisors. Professor Magnus Langseth, the strategist and experimentalist, made sure that I had clear goals ahead and pushed me along. Associate Professor David Morin, the simulation guy, who always has his office door open, gave me invaluable guidance during the project. Their understanding, encouragement and continuous support throughout the course of this work are deeply acknowledged.

Thanks goes to Honda R&D Americas, Inc. and Mr Eric DeHoff for suggesting the topic, providing funds, and for preparing test samples. We have had many fruitful scientific discussions throughout the project, which has ensured industrial relevance. I had the opportunity to work with them for ten weeks in the Spring of 2016, for which I am grateful.

The contribution of EJOT GmbH & Co. KG, who joined test samples free of charge, is appreciated.

It is a pleasure to extend my gratitude to all who have participated in the preparation of this thesis. I am grateful to Mr Trond Auestad and Mr Tore Wisth for the help with preparing and performing the tests. Dr Torodd Berstad has provided me with invaluable guidance to the numerical work. Thanks to Professor Arild Holm Clausen for getting me interested in pursuing a PhD in the first place, back when I was a student. Mr Petter Henrik Holmstrøm co-authored Paper 1. His thorough reviewing elevated the quality of the manuscript. I had the opportunity to supervise Mr Dan Hugo Amundsen and my good friend Mr Jo Amund Utne Gustad during their master thesis, and I am thankful for their contribution to the project, as well as the positive experience I gained by supervising them. Dr. Miguel Costas is acknowledged for performing the material tests and material model calibration for Paper 4. I would further like to thank my colleagues at the department, and especially those at SIMLab, for providing a warm, encouraging and inspiring atmosphere, and for making this experience fun and enjoyable.

Last but not least, I would like to thank my family and friends for the encouragement and support, even though you find it funny that it is possible to get a doctoral degree by studying a screw. I express my deep gratitude to Katinka, for your patience and understanding. A special thank you goes to our daughter, Nora, for being so fun, kind and easy to put to bed.

Contents

Appended papers

Paper 1 Sønstabø, J. K., Holmstrøm, P. H., Morin, D., and Langseth, M. "Macroscopic strength and failure properties of flow-drill screw connections". *Journal of Materials Processing Technology* 222 (2015), pp. 1-12. https://doi.org/10.1016/j.jmatprotec.2015.02.031

Paper 2 Sønstabø, J. K., Morin, D., and Langseth, M. "Macroscopic modelling of flow-drill screw connections in thin-walled aluminium structures". *Thin-Walled Structures* 105 (2016), pp. 185-206. https://doi.org/10.1016/j.tws.2016.04.013

Paper 3 Sønstabø, J. K., Morin, D., and Langseth, M. "Testing and modelling of flow-drill screw connections under quasi-static loadings". Accepted for publication in *Journal of Materials Processing Technology*.

Paper 4 Sønstabø, J. K., Morin, D., and Langseth, M. "Static and dynamic testing and modelling of aluminium joints with flow-drill screw connections". *International Journal of Impact Engineering* 115 (2018), pp. 58-75. https://doi.org/10.1016/j.ijimpeng.2018.01.008

Other publications not included in thesis

Sønstabø, J. K., Holmstrøm, P. H., Morin, D., and Langseth, M. "Behaviour of flow-drilling screw connections". *Aluminium Alloys 2014 - ICAA14*. Vol. 794. Materials Science Forum. Trans Tech Publications, July 2014, pp. 413-415. https://doi.org/10.4028/www.scientific.net/MSF.794-796.413

Sønstabø, J. K., Morin, D., and Langseth, M. "Macroscopic modelling of flow-drill screw connections". *10th European LS-DYNA Conference, Würzburg, Germany*. 2015. http://www.dynalook.com/10th-european-ls-dyna-conference/2%20Crash%20III%20-%20Connection/03-Morin-NorwegianUniv-A.pdf

Sønstabø, J. K., Morin, D., and Langseth, M. "A cohesive element model for large-scale crash analyses in LS-DYNA". *14th International LS-DYNA Users Conference, Detroit, USA*. 2016. http://www.dynalook.com/14th-international-ls-dyna-conference/connections/a-cohesive-element-model-for-large-scale-crash-analyses-in-ls-dyna-r

Sønstabø, J. K., Morin, D., and Langseth, M. "Macroscopic modelling of flow-drill screw connections". *Aluminium Constructions: Sustainability, Durability and Structural Advantages*. Vol. 710. Key Engineering Materials. Trans Tech Publications, Oct. 2016, pp 143-148. https://doi.org/10.4028/www.scientific.net/KEM.710.143

Synopsis

1 Context and motivation

To meet customer requirements, the automotive industry is striving towards more and more lightweight, and therefore essentially energy efficient, car designs. One strategy has been to use lighter materials such as aluminium as an alternative to steel. Aluminium space frame bodies substantially reduce weight, compared to traditional steel bodies, while maintaining essential strength and stiffness. An example of a space frame mainly consisting of aluminium is shown in Fig. 1. With the introduction of many dissimilar materials, new challenges arise, for instance with respect to joining of the different parts.

The conventional technique to join steel frames in cars is spot welding, which is fast and easily can be automated. However, it is difficult to spot weld aluminium, partly because of the high melting temperature of the aluminium oxide layer, which naturally covers the surface of aluminium parts. Therefore the automotive industry has introduced alternative joining techniques to join their aluminium parts.

One alternative that has gotten attention is flow-drill screws. This joining technique combines flow drilling and thread forming in a single procedure, where the screw is both functioning as tool and as fastener. The process consists of the following six stages (see Fig. 2): *heating*, *penetration*, *extrusion forming*, *thread forming*, *screw driving* and *tightening*. In the heating stage the screw is forced against the plate material while rotating to heat up

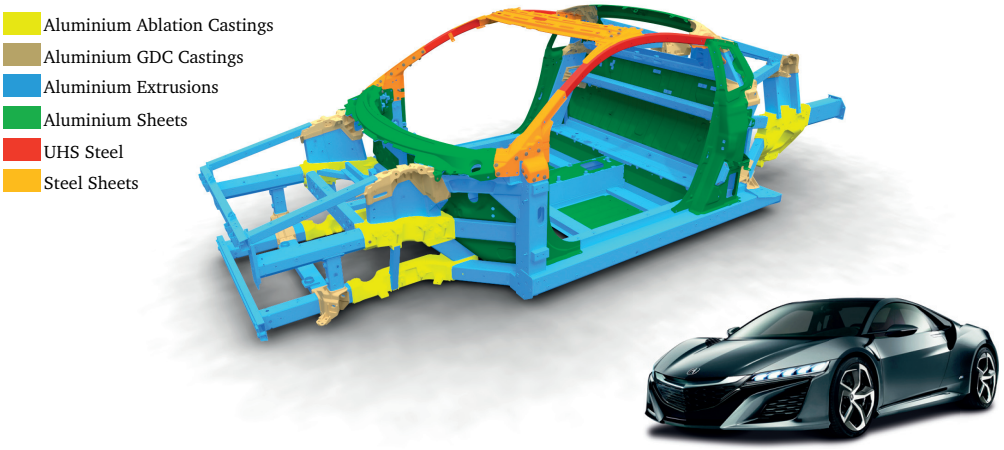

Fig. 1. Material usage in the space frame of the Honda NSX 2016. Image courtesy of Honda R&D Americas, Inc. Embedded photo from pngpix.com [1].

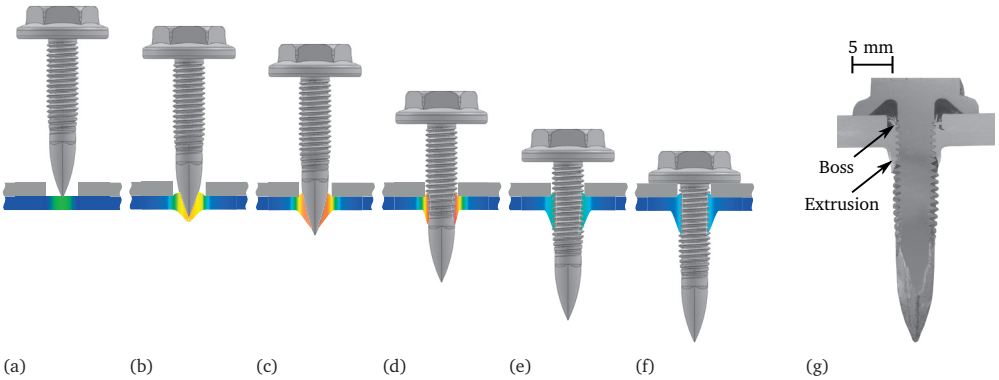

Fig. 2. The FDS process. (a) Heating. (b) Penetration. (c) Extrusion forming. (d) Thread forming. (e) Screw driving. (f) Tightening. A picture of an FDS connection is shown in (g), with the boss and extrusion indicated.

the material, facilitating the penetration. Subsequently an increasing downward force is applied and the screw penetrates the plate. Material flows up and down along the length of the screw and forms a boss (material that flows upwards between the plate and the screw head). When the tail of the screw pierces the bottom surface of the plate, a so-called extrusion is formed as material flows downwards along the screw shaft. Threads are created by a thread-forming zone on the fastener, and the screw is driven in until the head hits the top plate. The forming of the boss and extrusion extends the thread-forming zone further than the thickness of the plate, facilitating a stronger connection. A final torque is applied to a pre-set value in order to ensure a tight connection. The whole process usually takes between 1.5 and 4 seconds, depending on the material combination, plate thickness and type of screw. The process may be used with or without a pre-hole in the top plate.

An advantage of this process is that it requires tool access only from one side, as opposed to for instance self-pierce riveting, which require access to both sides of the connection. This makes the flow-drill screw process preferable in certain configurations, for instance when joining sheets to extrusions. It can join a variety of dissimilar materials, including for example steel to steel, steel to aluminium, aluminium to aluminium and even polymers to steel or aluminium. It may also be combined with adhesive bonding.

The performance of cars during crash loadings is to a great extent dependent on the performance of joints, and designers must therefore choose suitable joining methods. In order to make thorough design decisions they are reliant on knowledge about the physical behaviour of the connections. Physical insight is usually gained through extensive experimental testing, with experiments at different levels of complexity.

Moreover, due to high competition, the automotive industry is striving to reduce car development time, and therefore tries to lower the number of prototypes. Thus, they increasingly rely on numerical simulations for car design. Large-scale full-vehicle finite

element crash models are usually explicit, where the maximum stable time increment scales with the minimum element size of the model. Since the models are large and complex, limitations in computational power set requirements for the mesh size. The common approach today is to model the car frames using shell elements, with a mesh size between 3 and 7 mm. As an example, the crash model for the car in Fig. 1 contained 15 million elements, where half of them were fully integrated shells, with a mesh size of approximately 3 mm. It is not possible to discretise the detailed geometry of for example flow-drill screw connections with such a mesh size. Therefore, simplified macroscopic connection models are used instead. These models must be calibrated using experiments.

Although the behaviour of flow-drill screw connections is important for the response of car frames during crash loadings, and the designers rely on numerical models for large-scale crash simulations, limited knowledge on this topic is available in the open literature. The current PhD project was therefore initiated.

2 Objectives

The primary objective of the PhD project is to provide better understanding of the behaviour of flow-drill screw connections subjected to crash loadings, and provide knowledge about how to model them in large-scale simulations with macroscopic models. This is done through experimental testing and numerical simulations at several scales. Specific objectives are summarised as follows:

- Build up an experimental database, to study the behaviour of flow-drill screw connections under various loading conditions and material combinations. The experimental data are basis for calibration and validation of the numerical models throughout the thesis.
- Evaluate the ability of existing macroscopic modelling techniques developed for other connection types to represent flow-drill screw connections in large-scale finite element analyses.
- Develop a detailed mesoscopic finite element model where the geometry of the flow-drill screw connection is discretised with a fine solid element mesh, to study the physical phenomena occurring locally during testing.
- Develop a suitable component for quasi-static and dynamic testing of flow-drill screw connections, which can be used for validation of large-scale numerical models.

3 Scope

The current study focuses on the behaviour and modelling of two-layered flow-drill screw connections under crash loading conditions. Multi-layered connections and issues like fatigue, vibration resistance and corrosion are not covered. The research is limited to distinct plate materials and distinct screw geometries. Only connections between aluminium plates are considered, putting any other material combinations outside of scope. The chosen aluminium alloys are typical for the automotive industry. The connections studied had a pre-hole in the top plate.

The flow-drill screw process itself is highly complex, including significant plastic deformations and temperature increase as well as many process parameters. Even though Paper 3 contains a discussion about process effects, it is not the intention of this PhD project to study the process or any process effects.

The purpose has been to use existing material models in the numerical simulations, and thus not to develop novel models.

4 Research methodology

The work flow of the PhD project is illustrated in Fig. 3. It consists of three main parts. The central part of the figure represents the experiments carried out throughout the project. The right side represent the work done on macroscopic modelling of the connections in large-scale finite element simulations, which relies on the experiments for calibration and validation purposes. The left side of the figure illustrates the mesoscopic investigation, in which a flow-drill screw connection is modelled in detail with the finite element method.

The pyramid in Fig. 3 represents the validation strategy for numerical simulations. The various experiments have different levels of complexity, each represented with a floor in the pyramid. In the simplest experiments the loading on the connections is simple and relatively controlled. These tests are basis for calibration of macroscopic models in large-scale simulations. Benchmark tests, which are slightly more complex than the calibration tests, are used for a first validation. Furthermore, component tests are performed to validate the models under complex and arbitrary loadings. The arrows in Fig. 3 signify the flow of information. As seen, the calibration tests feed the macroscopic models, which are then compared with the experiments at several levels of complexity. The product level represent real structures. To keep the research on a generic level, emphasis has not been put on product-specific experiments in this project. However, a small case study at the product

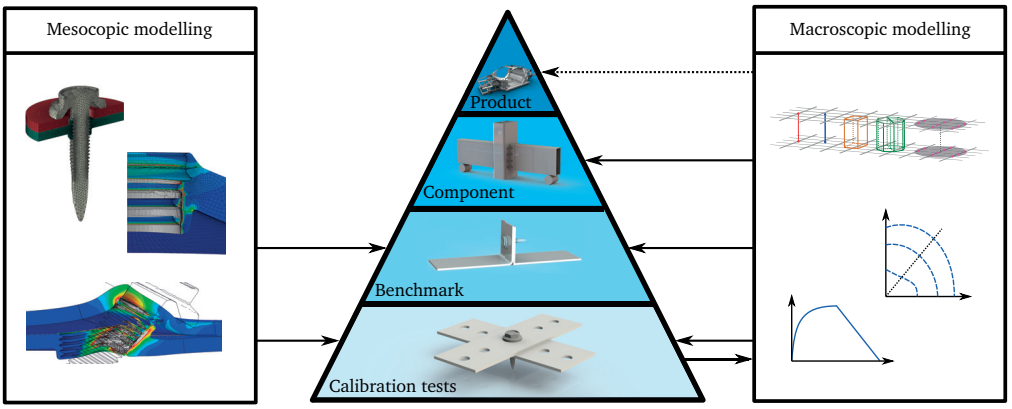

Fig. 3. Work flow of the PhD project. Arrows signify information flow.

level is included in Section 6 of this synopsis. This study has not been published in the scientific literature.

Experiments are useful to measure global force-displacement curves, but give limited information about the physical deformation and failure mechanisms of the connections. The mesoscopic model was therefore introduced to provide more insight to the behaviour of flow-drill screw connections than what is possible to gain only with experiments. The simulation was validated using the experiments at the calibration and benchmark level, as indicated with arrows in Fig. 3.

The experimental programmes were carried out using the facilities at SIMLab, Department of Structural Engineering, NTNU. Specimens were machined at NTNU and external workshops, and joined by Honda R&D Americas, Inc. in USA and EJOT GmbH & Co. KG in Germany.

The large-scale simulations were carried out using the explicit code LS-DYNA®. This software is often used for crash simulations in the automotive industry, and is used both at Honda R&D Americas and at SIMLab. The mesoscopic simulations were performed using the more flexible software Abaqus.

5 Summary of the work

5.1 Overview

The PhD work is divided into four distinct parts. A journal article has been published or submitted for each part. The first paper is a purely experimental investigation of the

behaviour of flow-drill screw connections. The second paper deals with modelling of flow-drill screw connections in large-scale finite element simulations. This is related to the right part of the work-flow illustration in Fig. 3. Paper 3 presents the mesoscopic model which was developed, which is related to the left part of Fig. 3. Lastly, the fourth paper presents an innovative component for quasi-static and dynamic testing of flow-drill screw connections, together with improvements in the macroscopic modelling technique.

In the following a short summary of each of the parts are given together with selected results.

5.2 Experimental investigation - Paper 1

The first objective of the PhD project was to build up an experimental database, to study the behaviour of the connections and to provide an experimental basis for calibration and validation of macroscopic connection models. In this study, a connection with a small screw joining two sheets of aluminium alloy AA 6016 in temper T4 was tested (see Fig. 4).

The test programme was chosen based on previous work on other mechanical fasteners, and consisted of two main parts. In the first part, different quasi-static loading conditions were investigated using cross, single lap-joint and peeling specimens with a single connector. In the cross tests the connection was tested for three different loadings: tensile, combined tensile and shear, and shear loading. The second part of the test programme consisted of quasi-static and dynamic axial crushing of single-hat sections. Due to the progressive buckling occurring in such tests the connections are subjected to complex and non-controlled load paths. An equivalent test programme was carried out with self-piercing riveted connections, for comparison.

Test results showed that the strength of the flow-drill screw connection increased with the amount of shear loading, while the ductility decreased (Fig. 5). Inspection of post-mortem specimens revealed that under tensile and mixed mode loadings failure occurred by thread

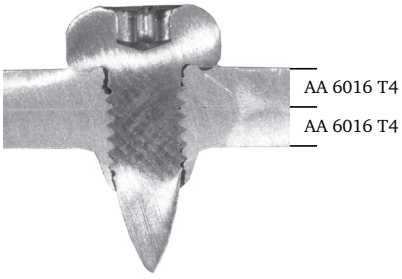

Fig. 4. Connection studied in Paper 1.

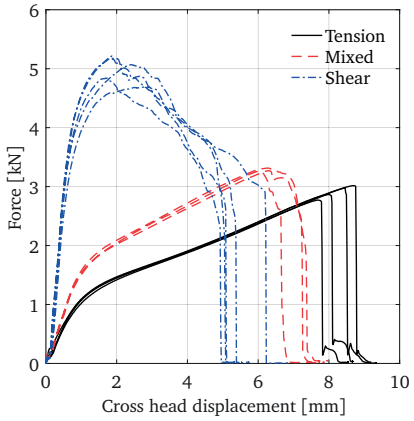

Fig. 5. Force-displacement curves from cross tests. Reprint from [2].

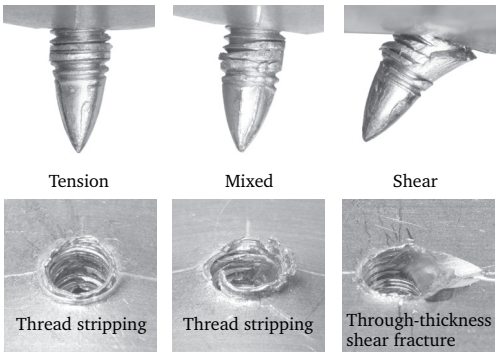

Fig. 6. Various deformed specimens from cross tests.

stripping from the bottom plate, while failure occurred by through-thickness shear fracture of the bottom plate material in the shear-dominated tests (Fig. 6).

Fig. 7 shows a representative deformed single-hat specimen from the dynamic axial crushing test, viewed from different sides. Because of the progressive buckling, the force response in the axial crushing tests was dominated by material deformation outside of the connections. It was therefore difficult to assess the behaviour of the connections from the force curves. However, four different deformation and failure modes of the screw connections were observed when inspecting the deformed specimens: screw rotation, screw pull-out, screw push-out and screw fracture, see Fig. 8. It was noted that the latter two failure modes were not observed in the single-connector tests, which can be of importance from a finite element modelling perspective. Macroscopic models of connections are usually calibrated using single-connector tests. Thus, deformation mechanisms which are only observed in component tests, and not in the tests used for calibration, will not be captured by the macroscopic model.

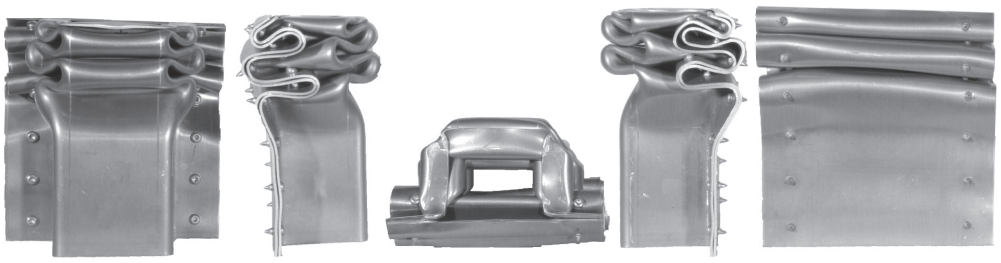

Fig. 7. Deformed single-hat section from dynamic axial crushing test, viewed from different directions. Reprint from [2].

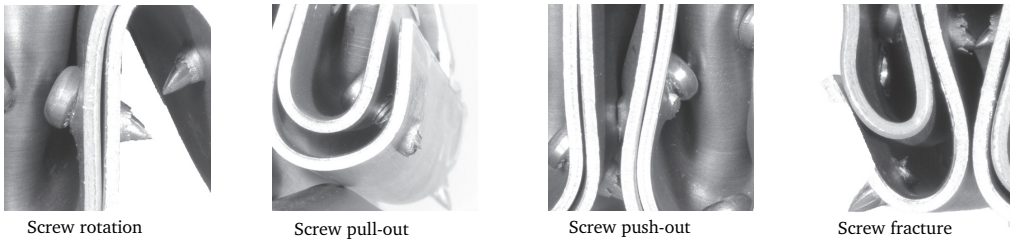

Fig. 8. Failure and deformation modes seen in axial crushing tests.

This part was published in Journal of Materials Processing Technology [2], and was summarised in a conference paper [3]. The experiments were carried out during the master thesis of Sønstabø and Holmstrøm [4].

5.3 Macroscopic modelling - Paper 2

This paper addressed the second objective of the PhD, which deals with macroscopic modelling of flow-drill screw connections in large-scale finite element simulations. In the paper, the ability of five common state-of-the-art connection models to represent flow-drill screw connections was studied, of which two models were element-based, and three were constraint-based. In an element-based model the connection is represented by solid or cohesive elements which are tied to the shell surfaces. In a constraint-based model the connection is represented by a constraint formulation. The two modelling techniques are illustrated in Fig. 9.

The macroscopic models were evaluated for two different flow-drill screw connections. First, the experiments from the single-connector tests in Paper 1 were used to assess the models. To expand the experimental database, an equivalent experimental programme was carried out for a connection with a larger screw and a different plate material combination, see Fig. 10. In addition, T-component tests where carried out for both connections. Thus, this paper also contributed to the first objective of the PhD.

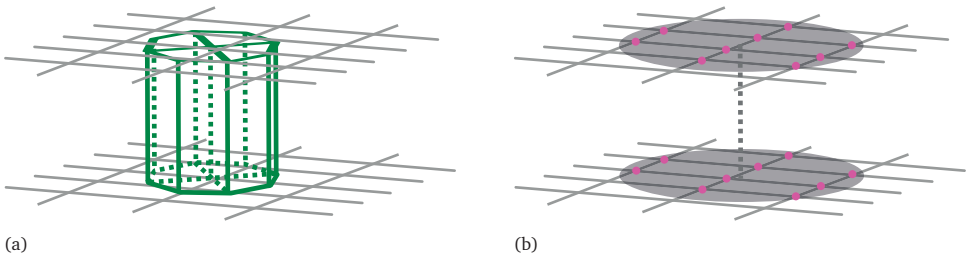

Fig. 9. Principle of (a) element-based and (b) constraint-based connection models for large-scale simulations.

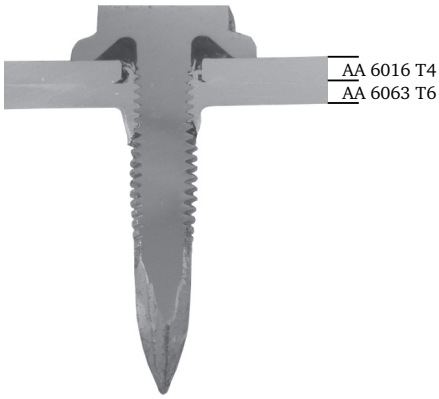

Fig. 10. New connection studied in Paper 2.

The connection models were calibrated using cross tests in tension, mixed mode and shear. A thorough two-step procedure for validation was presented and used. First, single lap-joint and peeling tests were used for validation at the benchmark level. A second level of validation (component level) was obtained using T-component tests, which represent more complex and uncontrolled macroscopic loadings on the connections. This calibration/validation procedure is basis for the pyramid in the centre of Fig. 3.

The performance of the models in the simulations of the cross tests of the large screw connection (Fig. 10) is shown in Fig. 11. Note that it was chosen not to include damage or failure in element model 1. The two investigated element-based models both performed poorly in the calibration simulations, as they over-estimated the force in mixed-mode loadings. Neither of the two models exhibit flexibility to control the mixed-mode behaviour, and it was therefore not possible to adjust any parameters to get better results. All three

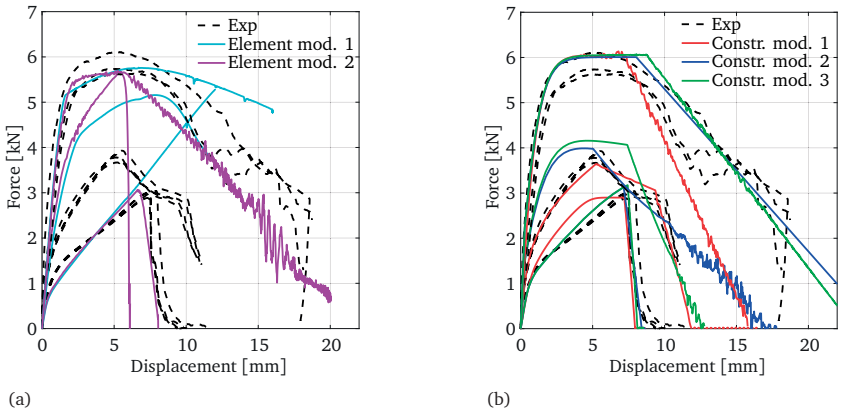

Fig. 11. Force-displacement curves from simulations of the cross tests of the large screw connection with (a) the two element-based models and (b) the three constraint-based models.

constraint-based models, on the other hand, possess flexibility for the mixed-mode, and therefore performed better. Of the three models, one stood out appearing to be most suited for flow-drill screw connections. It performed marginally better for both connections, and was the easiest to calibrate.

A modified version of element model 2, with added flexibility to control the mixed mode, was implemented as a user cohesive element. The modified model yielded better results in the simulations of the mixed-mode cross tests. This work was not included in Paper 2, but was presented in a conference paper [5].

This part of the project was published in Thin-Walled Structures [6], and contributed to three conference papers [5, 7, 8]. A master thesis [9] was also linked to this activity.

5.4 Mesoscopic model - Paper 3

In this part, a mesoscopic finite element model was built up of the screw connection in Fig. 10. The aim of the study was to provide a deeper understanding of the underlying deformation and failure mechanisms occurring during experimental testing. Such a model can in addition be used for virtual testing, for instance to calibrate macroscopic models without using experiments.

A generic connection was generated by discretising a simplified geometry with a fine solid element mesh. The connection was then inserted into different parts, resembling each of the

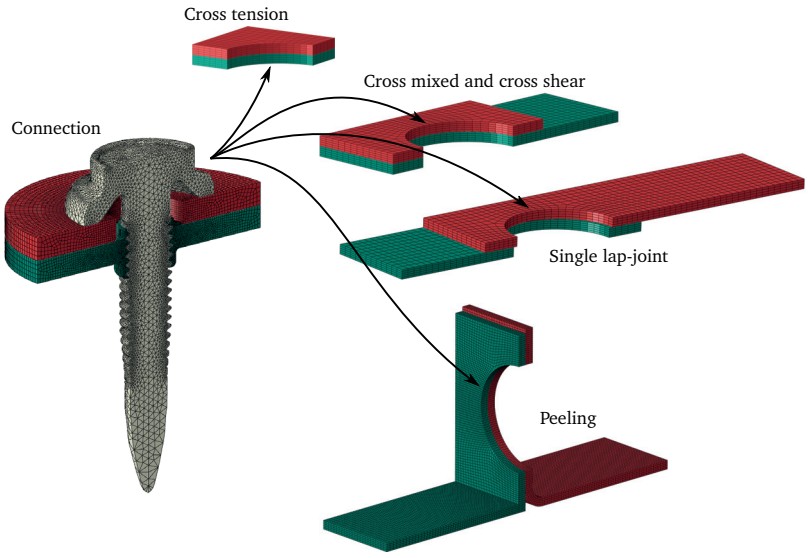

Fig. 12. Illustration of how the connection mesh was inserted into various specimens.

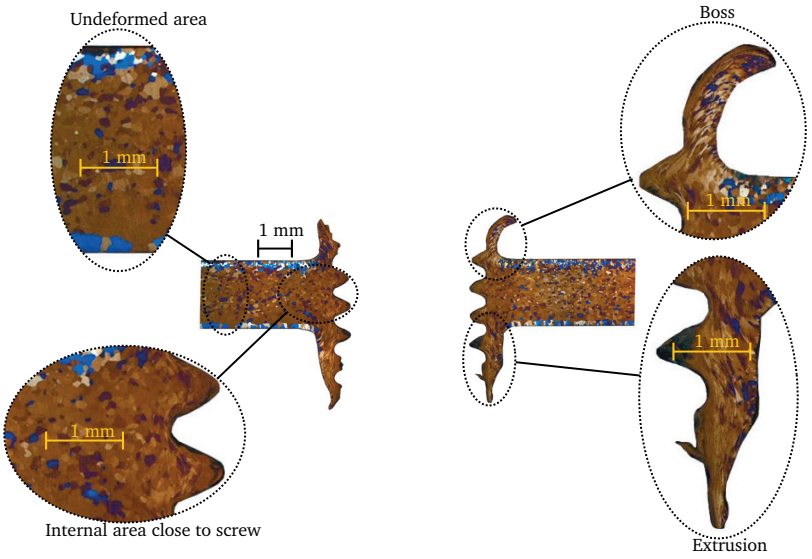

Fig. 13. Metallographic photograph of the cross-section of the bottom plate, with zoomed-in details.

single-connector tests, see Fig. 12. Symmetry was utilized where possible. The materials (plates and screw) were modelled using a rate-independent isotropic hypoelastic-plastic material model. Failure was included in the model by element erosion, using the Cockcroft-Latham failure criterion.

Process effects were not accounted for in the finite element model, and a study was conducted to assess this simplification. The study consisted of an analysis of the microstructure in the bottom plate, and Vickers hardness tests. Fig. 13 shows a metallographic photograph of the bottom plate from the microstructural analysis. The study indicated that there was a local process-affected zone extending approximately 0.5 mm from the screw into the bottom plate.

The finite element model was validated by comparing the five different simulations with the corresponding experiments. Satisfactory correlation was achieved, despite the simplifications made in the model. The results from the cross test simulations are shown in Fig. 14. Fig. 15 shows the equivalent plastic strain field in the cross shear simulation.

This part of the project has been accepted for journal publication [10].

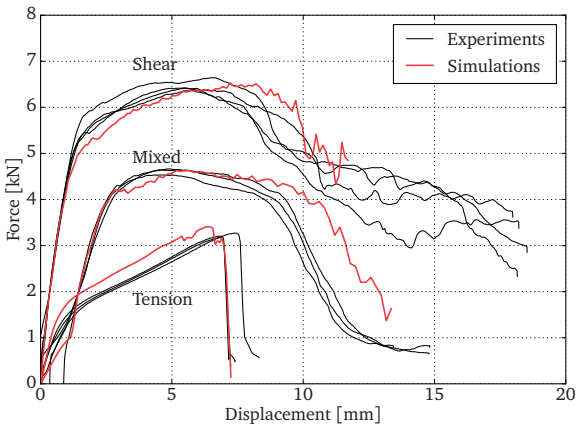

Fig. 14. Force-displacement curves from cross test simulations compared to experiments.

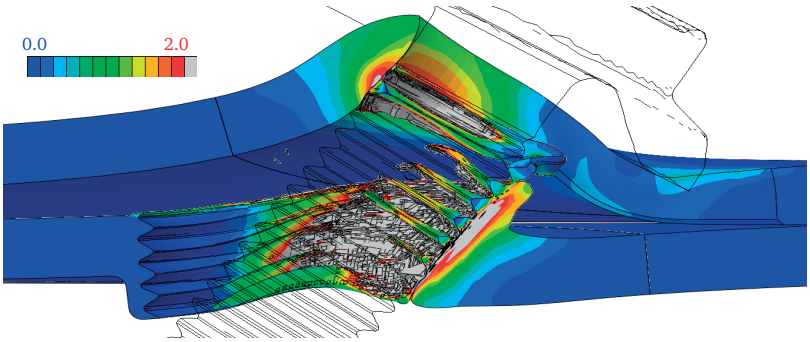

Fig. 15. Equivalent plastic strain field on deformed configuration in the cross shear test simulation.

5.5 Component testing - Paper 4

A literature survey revealed that the open literature contains limited information about component testing of flow-drill screw connections. The axial crushing tests in Paper 1 [2] was dominated by large material deformations outside of the connections (progressive buckling), which made it difficult to evaluate the behaviour of the connections. A limitation with the T-component tests in Paper 2 [6] is that it was difficult to transfer the test boundary conditions to numerical simulations, which makes it challenging to use the test for validation.

Therefore, a new component test for flow-drill screw connections was developed in this part of the PhD (Fig. 16). The test is suited for quasi-static and dynamic testing, and the design of the component is such that the dominating deformation is taking place in the connections, and at the same time has relevant and sufficiently complex loadings in the connections. Simple boundary conditions, that can easily be transferred to numerical simulations, make the test suitable for validation of large-scale numerical simulations. The specimen design was partly based on the constraints introduced by the available dynamic testing machine, the SIMLab Kicking Machine, which is a device designed for impact testing of structural components (Fig. 17). The quasi-static tests were performed in a regular tensile testing machine. In both cases the specimen was simply supported. The component included flow-drill screw connections with two material combinations, and each of them were characterised with single-connector tests.

The quasi-static and dynamic test results agreed well (Fig. 18), and did thus not suggest any significant rate effects on the global behaviour for the investigated velocity range, nor any inertia effects. Progressive connection failure was achieved, which means that the test is suited to evaluate progressive connection failure in numerical simulations.

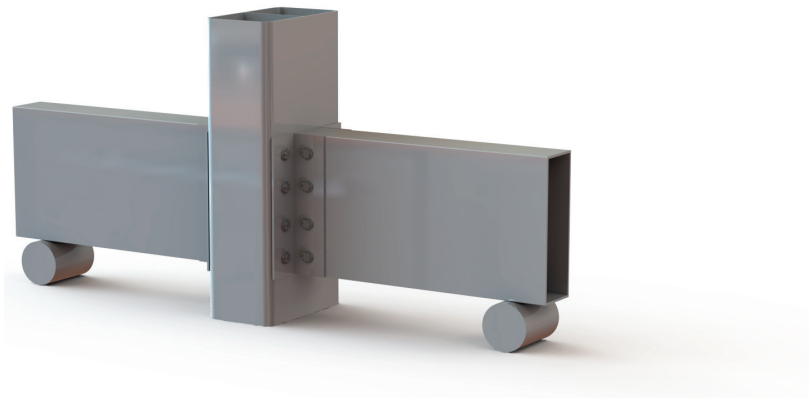

Fig. 16. The new component.

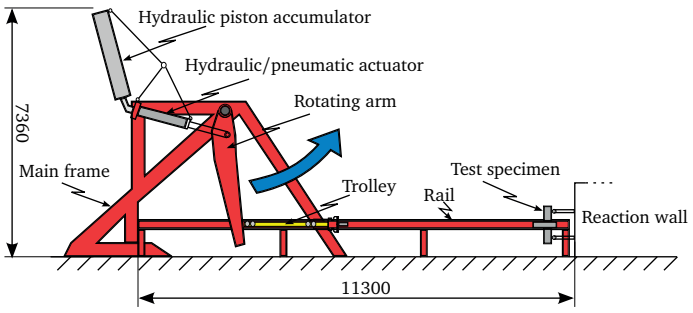

Fig. 17. The kicking machine, used for the dynamic component tests [11].

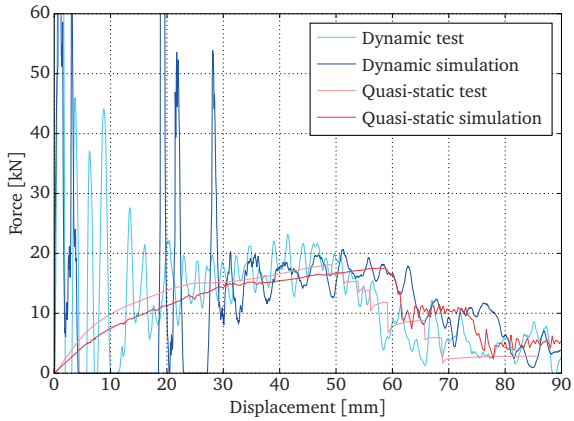

Fig. 18. Selected component test results together with corresponding simulation results.

Large-scale finite element simulations of the component tests, where the macroscopic connection model that was found to be most suitable for flow-drill screw connections in Paper 2 [6] was used to model the connections, were in good agreement with the experiments (Fig. 18). The initial stiffness was too low, causing a delay in maximum force and failure initiation in the quasi-static simulation compared to experiments. The failure of the first two connections was adequately captured, while it was delayed for the third connection, which indicates that prediction of progressive connection failure may be difficult with this modelling technique. The dynamic simulation gave similar results as the quasi-static.

An improvement of the connection modelling technique was employed, where the screw head geometry was modelled by a patch of linear elastic solid elements. This significantly improved the component simulation results, see Fig. 19.

This part of the project has been accepted for journal publication [12].

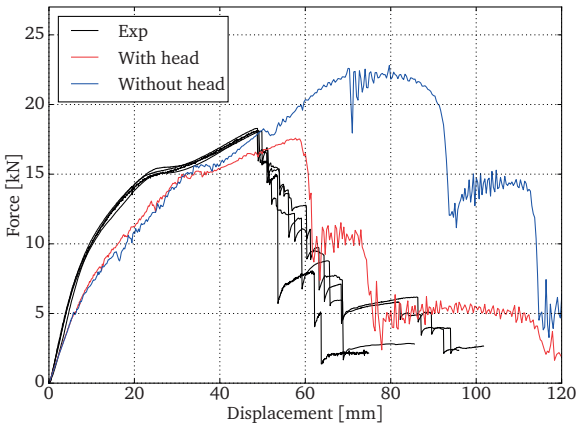

Fig. 19. Quasi-static component simulation with and without the screw head.

6 A case study at the product level

During my stay with Honda R&D Americas in the Spring of 2016, I had the opportunity to work with modelling of flow-drill screw connections in a full-vehicle crash simulation. Although these results have not been published, a short summary of the study with selected results is included here for the sake of completeness of the project.

The aim of the study was to assess two different strategies for modelling of flow-drill screw connections in a full-vehicle model, and to evaluate if they where practical to apply. The first model was constraint model 1 from Paper 2, which was found to be the most suited. The second model was an element-based version of the same model, i.e. constraint model 1 was re-implemented in a cohesive element framework as a user cohesive element model. Thus a one-to-one comparison between a constraint-based and an element-based model in a full-vehicle simulation could be obtained. The results of using the cohesive element version of the model at the calibration, benchmark and component level (see Fig. 3) was shown in a conference paper to be similar to the constraint-based version [8]. This study deals with the product level. For details of element-based models vs. constraint-based models, readers are referred to Paper 2.

The simulation chosen for the study was a 64 km/h frontal crash into an offset deformable barrier with 40 % overlap, of the Honda NSX 2016. The forces in the test are similar to those that would result from a frontal offset crash between two vehicles of the same weight, each going 64 km/h. The model consisted of 15 million elements, half of them fully integrated shells, with a mesh size of 3 mm. It contained 1560 different parts and 254 flow-drill screws. Pictures from the test and the corresponding simulation are shown in Fig. 20.

(a) (b)

(c) (d)

Fig. 20. Frontal offset deformable barrier crash of Honda NSX 2016, with 40 % overlap. (a) Test before impact. (b) Simulation before impact. (c) Test after impact. (d) Simulation after impact. Image courtesy of Honda R&D Americas, Inc.

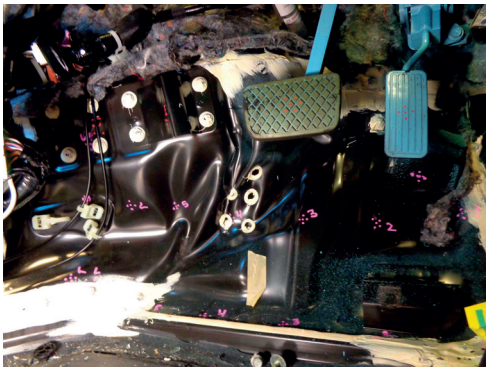

(a)

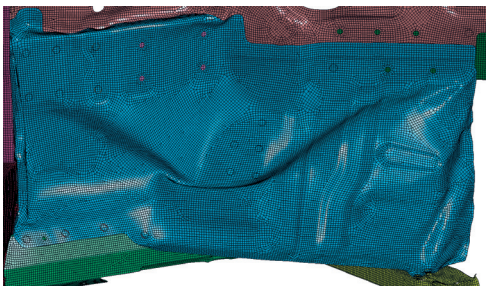

(b)

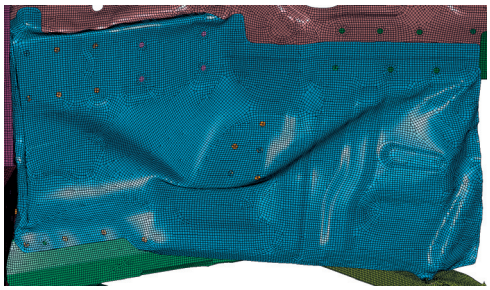

(c)

Fig. 21. Deformed lower dashboard in front of driver from (a) test, (b) simulation with constraint-based model, and (c) simulation with element-based model. Image courtesy of Honda R&D Americas, Inc.

Full-vehicle models are complex, and a large number of uncertainties makes direct comparisons between tests and simulations on part level difficult. An example is shown in Fig. 21, which depicts the deformed lower dashboard in front of the driver from test and simulations. As seen, the deformed shape of the part is different in the test and simulations.

To assess the structural performance of the car, engineers instead measure the amount of intrusion into the occupant compartment at key locations after the crash. The amount and pattern of intrusion show how well the front-end crush zone managed the crash energy and how well the safety cage held up [13]. These measurements are also used to compare simulations with tests. Fig. 22 shows the intrusion at various locations after the test and the simulations for the car at hand, where the coloured areas correspond to the ratings *poor*, *marginal*, *acceptable* and *good*, used by the Insurance Institute of Highway Safety [13]. As seen, small differences were observed in the results between the two approaches. The constraint-based approach yielded results marginally closer to the experiment.

Fig. 23 shows fringe plots of the equivalent plastic strain around some selected connections in the lower dashboard. While the plastic strain pattern was similar outside of the

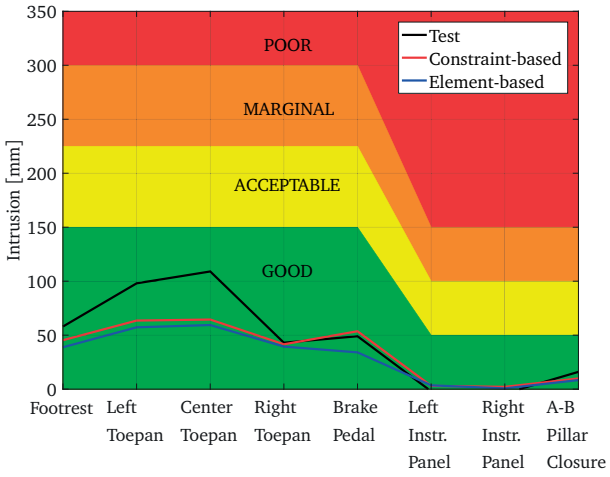

Fig. 22. Intrusions at various locations in test and simulations.

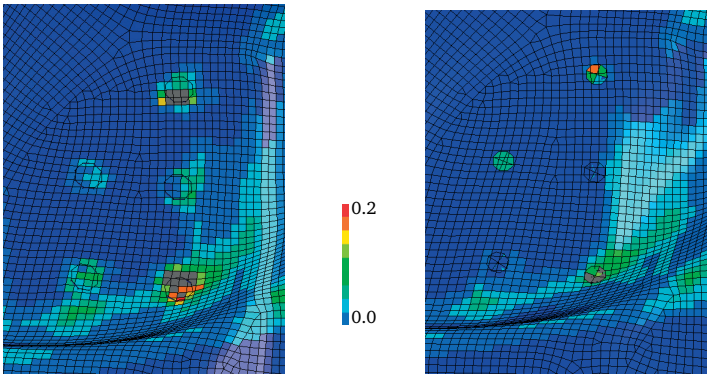

(a) (b)

Fig. 23. Equivalent plastic strain plots around some connections at the lower dashboard. (a) Simulation with constraint-based model. (b) Simulation with element-based model.

connections, one notable difference may be seen in the vicinity of the connections. In the simulation with the constraint-based model, significant plastic strains evolved in the shell elements surrounding the connections. With the cohesive element approach, however, these strains were less prominent. If the material model for the plate includes failure, plastic strains in the shells around the connection can cause element deletion and eventually premature failure of the connection. It is desired that the connection model takes care of the connection failure, and thus that excessive strains in the surrounding shells are limited.

As has been shown, the two modelling approaches gave similar simulation results. When it comes to the practical side, it took approximately a day to set up each model for all connections in the car. Moreover, the modelling techniques did not influence the

overall computational time. Thus, both the constraint-based and element-based approaches seem to be good choices for modelling of flow-drill screw connections in full-vehicle simulations.

7 Concluding remarks

Knowledge about the behaviour of flow-drill screw connections, and how to model them in large-scale finite element simulations, is important for the automotive industry in order to facilitate safe and cost-effective design of cars. At the time when this PhD project was initiated, limited information about the topic was available in the open scientific literature. The main objective of the project was to remedy this lack of knowledge. This was done through experimental testing and numerical simulations at several scales. Through the four parts of this thesis, each of the specific objectives listed in Section 2 has been addressed and fulfilled.

The experimental database built up during the project consists of tests on in total four different flow-drill screw connections, i.e. four combinations of screw geometry and aluminium plate materials. The global behaviour of single connections was established by means of cross, single lap-joint and peeling tests, which challenged the connections under various quasi-static loading conditions. For each test, the global force-displacement behaviour and observed failure modes were reported in detail.

Existing state-of-the-art connection modelling techniques for large scale finite element simulations were evaluated for flow-drill screw connections. The two element-based models that were tried did not have sufficient flexibility, and were therefore abandoned. Of the three constraint-based models, one stood marginally out as the most accurate, robust and the easiest to calibrate. This model was therefore used in the remaining of the PhD.

A detailed mesoscopic finite element model of a flow-drill screw connection was built, where the geometry was discretised with a fine solid element mesh. The connection was inserted into five different specimens, resembling each of the single-connector tests. A study of the microstructure and Vickers hardness tests indicated that there was a process-affected zone close to the screw, that was not accounted for in the mesoscopic model. The finite element model was validated by comparing the five different simulations with the corresponding experiments. Satisfactory correlation was achieved, despite the simplifications made in the model.

In the last part of the project, a new component test was developed, for quasi-static and dynamic testing of flow-drill screw connections. The component design was such that the

dominating deformation mode took place in the connections, had relevant and sufficiently complex loadings, and had boundary conditions that could easily be transferred to numerical simulations. The test proved to be suitable for validation of numerical models. With a suggested improvement of the connection modelling technique, large-scale finite element simulations agreed well with the experiments.

8 Suggestions for further work

The focus of this thesis has been experimental testing and numerical modelling of two-layered aluminium-aluminium flow-drill screw connections. This has left many topics outside of the scope, and several extensions of the treated subjects can be considered. Some possible topics for further research are briefly presented below.

- Expand the experimental database by introducing more material combinations, not only aluminium-aluminium. Szlosarek et al. [14] performed tests on a connection between a carbon fibre reinforced polymer and aluminium. Other possible material combinations could for example be polymer-aluminium, steel-steel, steel-aluminium or aluminium-steel.
- Although this thesis contains dynamic component tests, the single-connector tests were only performed under quasi-static conditions. A natural extension of the work would be to develop a method for dynamic testing of single connections. Even though the component tests do not suggest that the investigated connections are significantly rate-dependent, this is still an open question for other material combinations.
- It is common in the automotive industry to combine different joining methods, to so-called hybrid joints. It could for instance be of interest to study a combination of flow-drill screw connections and adhesive bonding.
- This thesis was limited to connections between two plates. It is, however, common to include three, or even four, plates in a single flow-drill screw connection. Experimental testing of multi-layered connections is challenging, since more loading configurations are possible. Furthermore, the scientific literature does not provide information about how to model multi-layered connections in large-scale simulations. The master thesis of Amundsen and Gustad [9] touched upon this topic. They performed tests on a connection consisting of three plates, and did a preliminary study of how to model them in large-scale analyses. An obvious possibility for further work is to pick up where they left off.
- The mesoscopic model of Paper 3 has been shown to predict the behaviour of flow-

drill screw connections within acceptable accuracy. The model can therefore be used to study all of the topics above, as supplement to, or instead of, experimental tests. If validated material models are obtained of the plate and screw materials, and the geometry of the connection is discretised in a proper way, new material combinations can be studied, including multi-layered combinations. Virtual dynamic tests can be carried out by including strain-rate dependence in the material models, to investigate possible rate effects on the global behaviour. It may be possible to study hybrid joints, by including the adhesive layer in an appropriate way.

– The flow-drill screw process was not studied in detail during this project. A possibility to better understand the process is to carry out process simulations. This could for instance follow the lines of the work by Grujicic et al. [15], who made an attempt by employing a fully coupled thermo-mechanical combined Eulerian-Lagrangian finite element simulation.

References

[1] pngpix.com. http : / / www. pngpix . com / download / acura - nsx - car - png - image. [Online; accessed 2017-10-24]. 2017.

[2] Sønstabø, J. K., Holmstrøm, P. H., Morin, D., and Langseth, M. "Macroscopic strength and failure properties of flow-drill screw connections". *Journal of Materials Processing Technology* 222 (2015), pp. 1–12. https://doi.org/10.1016/j.jmatprotec.2015.02.031.

[3] Sønstabø, J. K., Holmstrøm, P. H., Morin, D., and Langseth, M. "Behaviour of Flow-Drilling Screw Connections". *Aluminium Alloys 2014 - ICAA14*. Vol. 794. Materials Science Forum. Trans Tech Publications, July 2014, pp. 413–415. https://doi.org/10.4028/www.scientific.net/MSF.794-796.413.

[4] Sønstabø, J. K. and Holmstrøm, P. H. "Behaviour and modelling of self-piercing screw and self-piercing rivet connections". Master thesis. Norwegian University of Science and Technology, 2013. https://brage.bibsys.no/xmlui/handle/11250/237314.

[5] Sønstabø, J. K., Morin, D., and Langseth, M. "A cohesive element model for large-scale crash analyses in LS-DYNA". *14th International LS-DYNA Users Conference, Detroit, USA*. 2016. http : / / www. dynalook . com / 14th - international - ls - dyna - conference/connections/a-cohesive-element-model-for-large-scale-crash-analyses-in-ls-dyna-r.

[6] Sønstabø, J. K., Morin, D., and Langseth, M. "Macroscopic modelling of flow-drill screw connections in thin-walled aluminium structures". *Thin-Walled Structures* 105 (2016), pp. 185–206. https://doi.org/10.1016/j.tws.2016.04.013.

[7] Sønstabø, J. K., Morin, D., and Langseth, M. “Macroscopic modeling of flow-drill screw connections”. *10th European LS-DYNA Conference, Würzburg, Germany*. 2015. http://www.dynalook.com/10th-european-ls-dyna-conference/2%20Crash%20III%20-%20Connection/03-Morin-NorwegianUniv-A.pdf.

[8] Sønstabø, J. K., Morin, D., and Langseth, M. “Macroscopic Modelling of Flow-Drill Screw Connections”. *Aluminium Constructions: Sustainability, Durability and Structural Advantages*. Vol. 710. Key Engineering Materials. Trans Tech Publications, Oct. 2016, pp. 143–148. https://doi.org/10.4028/www.scientific.net/KEM.710.143.

[9] Amundsen, D. H. and Gustad, J. A. U. “Behaviour and modelling of flow-drilling screw connections”. Master thesis. Norwegian University of Science and Technology, 2014. https://brage.bibsys.no/xmlui/handle/11250/233128.

[10] Sønstabø, J. K., Morin, D., and Langseth, M. “A numerical study of the behaviour of flow-drill screw connections under quasi-static loadings” (2018). Accepted for publication in Journal of Materials Processing Technology.

[11] Grimsmo, E. L., Clausen, A. H., Langseth, M., and Aalberg, A. “An experimental study of static and dynamic behaviour of bolted end-plate joints of steel”. *International Journal of Impact Engineering* 85 (2015), pp. 132–145. https://doi.org/10.1016/j.ijimpeng.2015.07.001.

[12] Sønstabø, J. K., Morin, D., and Langseth, M. “Static and dynamic testing and modelling of aluminium joints with flow-drill screw connections”. *International Journal of Impact Engineering* 115 (2018), pp. 58–75. https://doi.org/10.1016/j.ijimpeng.2018.01.008.

[13] Insurance Institute for Highway Safety. http://www.iihs.org. [Online; accessed 2017-11-08]. 2017.

[14] Szlosarek, R., Karall, T., Enzinger, N., Hahne, C., and Meyer, N. “Mechanical testing of flow drill screw joints between fibre-reinforced plastics and metals”. *Materials Testing* 55.10 (2013), pp. 737–742. https://doi.org/10.3139/120.110495.

[15] Grujicic, M., Snipes, J., and Ramaswami, S. “Process and product-performance modeling for mechanical fastening by flow drilling screws”. *International Journal of Structural Integrity* 7.3 (2016), pp. 370–396. https://doi.org/10.1108/IJSI-03-2015-0011.

Paper 1

This paper was published in:

Sønstabø, J. K., Holmstrøm, P. H., Morin, D., and Langseth, M. “Macroscopic strength and failure properties of flow-drill screw connections”. *Journal of Materials Processing Technology* 222 (2015), pp. 1-12. https://doi.org/10.1016/j.jmatprotec.2015.02.031

Abstract

Force–displacement responses and failure behaviour of connections using flow-drill screws to join aluminium sheets were investigated under various quasi-static loading conditions. This included single connector tests under tensile, shear and combined tensile and shear loadings, using cross test coupons in a new test set-up, and peeling and single lap-joint tests. The strength of the connection increased with the amount of shear loading, while the ductility decreased. No effect of the anisotropy of the sheets on the behaviour in the single connector tests was found. Axial crushing tests of aluminium single-hat sections joined with flow-drill screws were also performed. Two connection failure modes not observed during the single connector test were found in these tests. For comparison, equivalent single connector and component tests were carried out for self-piercing rivet connections. Similar trends with respect to the ductility, maximum force and shape of force–displacement curves were observed for the two connections, but the local failure modes were different.

Macroscopic strength and failure properties of flow-drill screw connections

1 Introduction

Joining with Flow-Drill Screws (FDS) is a technology which may be used to join a variety of dissimilar materials, and is increasingly used to join aluminium parts in the load bearing structure of cars. By this technique sheets, extrusions, castings or combinations of these may be joined with a high strength steel screw. The joining process is a one-step procedure consisting of six stages, as shown in Fig. 1: (a) warming up due to friction between the screw and the sheet, (b) penetration of the sheet material, (c) forming of the draught, (d) thread forming, (e) full thread engagement and (f) tightening [1]. A pilot hole is usually drilled in the top sheet prior to joining. One of the main advantages with this technology is that tool access only is required from one side of the assembly. This may enable the process to be used in configurations where other joining techniques fail.

The FDS process is based on the technology of flow drilling (also called form drilling, thermal drilling or friction drilling), which is a method for making holes in metals; see e.g. Head et al. [2]. A synthesis of several studies on the flow-drilling process was given by Miller and Shih [3], including measurement of thrust force and torque, study of microstructural alterations, flow drilling of cast metals, tool wear and analytical and finite element modelling. A literature survey revealed no publications concerning the FDS process.

No publications have been found on connecting two aluminium sheets with flow-drill

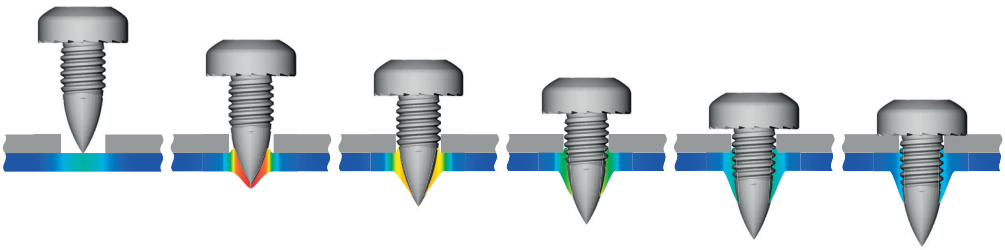

Fig. 1. Different stages of the flow-drill screw process. (a) Warming up. (b) Penetration of the material. (c) Forming of the draught. (d) Thread forming. (e) Full thread engagement. (f) Tightening.

screws. However, an experimental study of FDS connections was published by Szlosarek et al. [4], who investigated the behaviour of a carbon-fibre-reinforced polymer plate joined to an aluminium plate. They performed tests by loading the connection in shear, tension and different combinations of shear and tension, and found that the failure load was similar for all load combinations, but observed two different failure modes.

Even though little information about FDS connections is found in the open literature, other related joining technologies used in the automotive industry, e.g. resistance spot welding and self-piercing riveting, have been widely covered and can be used as guidelines for experimental studies of FDS connections. Examples of experimental strategies for characterization of connections are presented in the following.

The common approach to study the behaviour of connections is to subject test coupons, consisting of a single connector joining two metal plates, to different controlled macroscopic load paths. Typical paths are tensile, shear, different combinations of tensile and shear and peeling loads.

Pedreschi and Sinha [5] investigated the potential of press-joining in cold-formed steel structures by means of a series of lap-shear and bending tests. Lennon et al. [6] did a comparative investigation of the mechanical behaviour of clinching, self-piercing rivet, pop rivet and self-tapping screw connections in thin gauge steel using the shear dominated lap-joint test. Similarly, Lorenzo and Landolfo [7] carried out a comparative study of the shear response of blind rivets, circular press-joints and self-piercing rivets joining two and three steel sheets. The lap-joint specimen was used in the tests, with two connections in each sample. Briskham et al. [8] performed lap-shear and peeling tests to assess the functional suitability of self-piercing rivet, resistance spot weld and spot friction joint connections for use in aluminium automotive structures.

Langrand et al. [9] carried out experimental studies on the behaviour of blind rivets, which are commonly used in modern fighters and commercial aircraft frameworks. They did quasi-static and dynamic single connector tests on aluminium tension and lap-joint specimens instrumented with strain gauges.

The spot welded connection is probably the most investigated connection type used in the automotive industry. Lee et al. [10] utilized a special designed test fixture similar to the Arcan type set-up [11] to investigate the quasi-static behaviour of spot welded steel coupons under tensile, shear and various combined loadings. Wung [12] carried out lap-shear, in-plane rotation, peeling, normal separation as well as different combined loading mode tests. In addition, a more sophisticated test with a more complex combined load path was performed [13]. Langrand and Combescure [14] used an Arcan type test to characterize the spot weld behaviour under tensile, shear and combined loading modes, and performed

tensile pull-out, single lap-shear and peeling tests. This work was extended by Langrand and Markiewicz [15] to include dynamic testing.

Self-piercing riveting (SPR) is a joining technology similar to FDS. The shear, tensile and combined shear and tensile quasi-static load responses of SPR connections between aluminium extrusions were investigated by Porcaro et al. [16]. They also studied the influence of the plate thickness, rivet geometry, material properties and loading conditions [17], and conducted dynamic tests to assess the rate effect on the behaviour of SPR connections [18]. Sun and Khaleel [19] investigated the quasi-static behaviour of SPR connections using cross-shaped tension specimens. This work was extended to also include dynamic testing [20]. Similar and dissimilar materials were joined, and tests were carried out using cross tension, lap-shear and peeling specimens.

As there is a lack of knowledge about the behaviour of FDS connections in the peer-review literature, thorough experimental studies are required on this topic to provide a better understanding of the connections in order to allow for reliable designs of future vehicle structures.

Based on previous work on mechanical fasteners an experimental programme was carried out to investigate the behaviour of single connector FDS connections under various quasi-static loading conditions. In addition, quasi-static and dynamic component tests were carried out in order to investigate the structural behaviour of the connections under complex, non-controlled load paths. To assess the behaviour of FDS connections compared to other mechanical fasteners, an equivalent experimental programme was carried out for SPR connections.

2 Connector and sheet material

In this work it is distinguished between the terms *connector* and *connection*. The term *connection* is here defined as *the system which mechanically fastens two or more parts together*. This definition is based on the definition of a connection in Eurocode 9 [21]. The connector is in this work the steel screw that is used to form the connection. Thus, the connection is the system comprised of the connector and the surrounding aluminium sheet material (see Fig. 2a).

The connector used herein was an M4 screw with a nominal length of 10 mm, made of case hardened mild steel, with standard tip and produced by EJOT. A cross-sectional view of the connection and the geometry of the connector are shown in Figs. 2a and 2b, respectively.

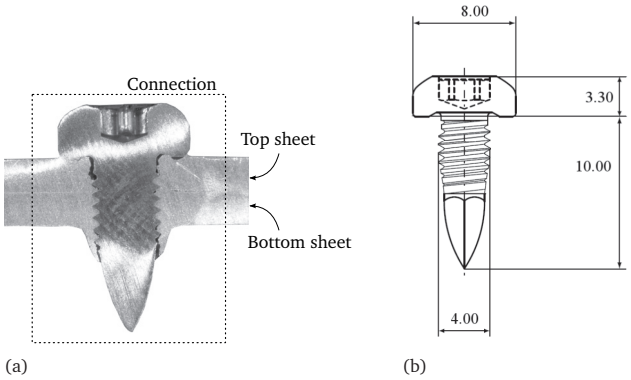

Fig. 2. Connection and connector. (a) Cross-section of connection. (b) Geometry of connector.

The plates used in the single connector and component tests were rolled sheets of AA 6016 in temper T4 with a nominal thickness of 2 mm. Due to the rolling procedure such sheets usually exhibit orthotropic plastic anisotropy [22].

In order to assess the strength and anisotropy of the sheet material, uniaxial tensile tests were carried out in seven different directions with respect to the rolling direction. Fig. 3 shows the results in terms of (a) engineering stress and strain curves to the onset of diffuse necking and (b) plastic strain ratios. The plastic strain ratio in the direction with respect to the rolling direction is defined as $R_\alpha = \dot{\epsilon}_w^p / \dot{\epsilon}_t^p$, where $\dot{\epsilon}_w^p$ and $\dot{\epsilon}_t^p$ are the true plastic strain increments in the width and thickness directions, respectively. It is seen from Fig. 3a that the sheets exhibited significant ductility and work hardening, but no significant anisotropy

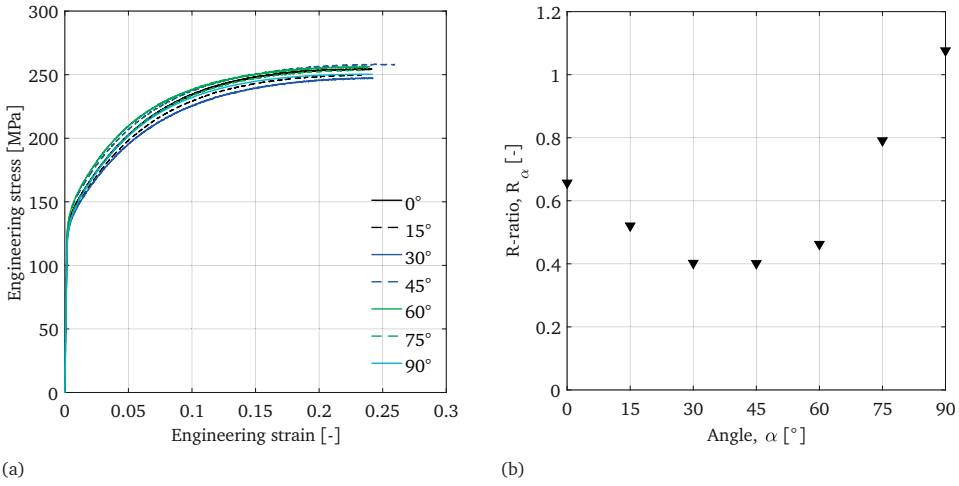

Fig. 3. Results from uniaxial tensile tests in seven different directions with respect to the rolling direction of the sheets. (a) Engineering stress and strain curves. (b) Plastic strain ratios.

with respect to the strength. From Fig. 3b it is evident that they exhibited significant plastic anisotropy.

3 Experimental programme and test set-up

An extensive experimental programme consisting of two parts was defined (Table 1); one part with single connector tests and one with component tests. In the first part, different quasi-static loading conditions were investigated using cross, single lap-joint and peeling specimens with a single connector. In the cross tests the connection was tested for three different loadings: tensile, combined tensile and shear and shear loading. Based on the work of Porcaro et al. [18] on SPR connections, it was assumed that there were no significant rate effects on the behaviour of the single FDS connections. Thus, the single connector tests were limited to quasi-static tests.

The second part of the test programme consisted of quasi-static and dynamic axial crushing of single-hat sections. Due to the progressive buckling occurring in such tests the connections are subjected to complex and non-controlled load paths. Furthermore, as the folding and thus the behaviour of the connections depends on the impact velocity, this component test provides conditions similar to a real case scenario. Emphasis was put on the dynamic component tests, while the quasi-static tests served as reference to estimate the dynamic effects on energy absorption of the components and failure modes of the connections.

In the following, the experimental test set-up is explained, first for each single connector test and subsequently for the component tests.

Table 1
Test matrix for experimental programme.

	Test type	Orientation of sheet rolling direction		Loading angle	Repetitions
		Top sheet	Bottom sheet		
Single connector tests	Cross (tensile)	Transversal	Longitudinal	90	4
	Cross (mixed)	Transversal	Longitudinal	45	3
	Cross (shear)	Transversal	Longitudinal	0	5
	Single lap-joint	Longitudinal	Longitudinal		4
	Single lap-joint	Transversal	Transversal		3
	Peeling	Transversal	Transversal		3
Component tests	Quasi-static crushing	Longitudinal	Longitudinal		2
	Dynamic crushing	Longitudinal	Longitudinal		3

3.1 Single connector tests

It is important to understand that the loading conditions discussed herein, i.e. tensile loading, mixed tensile and shear loading and shear loading, are from a global, macroscopic perspective. The local loading conditions within the connection and on the connector itself are complex and unknown and changes continuously throughout the tests. For instance, in the cross shear tests - which arguably may be considered as pure shear from a macroscopic perspective - the screw is loaded in shear in the start, but after a while the connection deforms and the screw starts to rotate, introducing a more complex loading situation within the connection.

The geometry of the cross specimens is shown in Fig. 4a. The specimens consisted of two rectangular sheets connected with a single connector in the centre. A specially designed testing rig based on the set-up of Porcaro et al. [23] was adapted (illustrated in Figs. 4b and 4c). With this testing rig the combination of macroscopic tensile and shear loads was controlled. The ratio of macroscopic tensile and shear load was exactly defined by the loading angle θ; see Fig. 4b. The load application line was defined by two pull-bars, and the test set-up was designed such that this line intersected the specimen plane at the centre of the connection (see Fig. 4a). The pull-bars were clamped to the crosshead of the testing machine. In this work, three different loading angles were considered: 90°, 45° and 0°. The holes in the cross specimens (see Fig. 4a) were used for clamping the specimen to the testing rig using massive steel blocks and bolts. The rolling directions of the sheets are indicated with arrows in Fig. 4a. The shear loads were applied normal to the rolling direction.

The single lap-joint specimen is shown in Figs. 5a and 5b. It consisted of two rectangular plates joined with a single connector in the centre of an overlap area. To evaluate the effect of sheet anisotropy on the behaviour of the connection, single lap-joint tests were carried out on specimens with the sheet rolling direction oriented in both the longitudinal (Fig. 5a) and transversal (Fig. 5b) direction of the specimen. The peeling specimen (Fig. 5c) consisted of two identical bent plates joined with a single connector at the short flange. Each end of the single lap-joint and peeling specimen was clamped using mechanical grips. The grips were aligned along the load application line of the test machine without any offset. Hence, the single lap-joint specimens were slightly deformed when tightening the grips. The deformation was purely elastic, and is shown schematically in Fig. 5d.

All single connector tests were carried out under displacement control at a displacement velocity of 10 mm/min. Force and displacement histories were recorded. Additionally, the single lap-joint and peeling specimens were instrumented with an extensometer (50 mm gauge length). The tests were terminated when the force level reached zero.

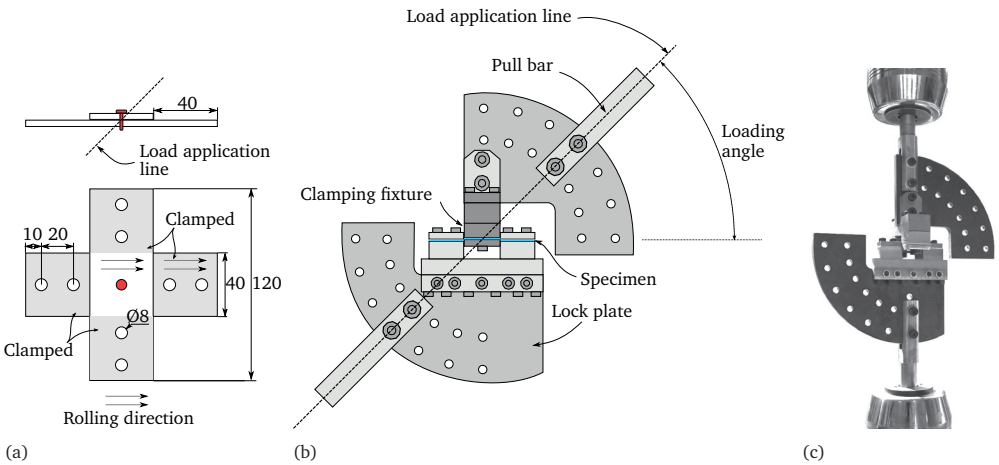

Fig. 4. Cross test set-up. (a) Geometry of specimen. (b) Schematic illustration of testing rig. (c) Picture of testing rig.

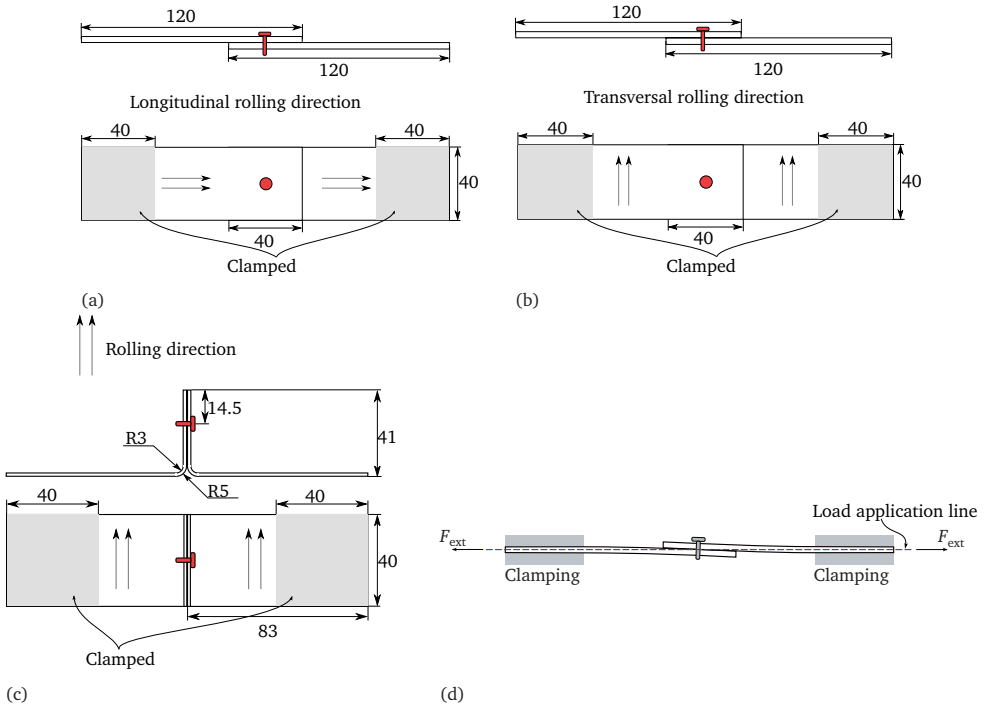

Fig. 5. Single lap-joint and peeling test set-up. (a) Longitudinal material orientation. (b) Transversal material orientation. (c) Peeling specimen. (d) Clamping deformation in single lap-joint test.

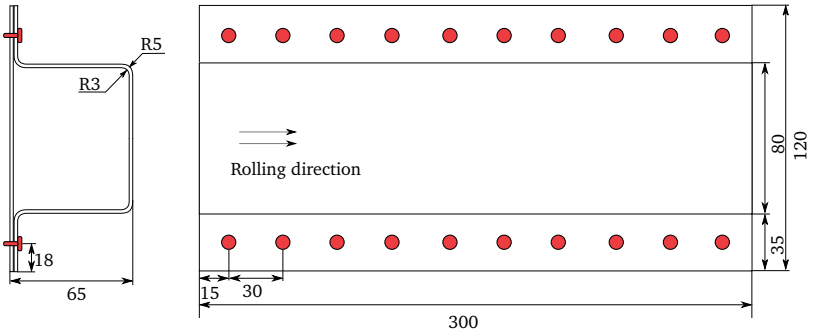

Fig. 6. Geometry of single-hat specimen.

3.2 Component tests

Fig. 6 shows the geometry of the single-hat specimen, which consisted of a flat and a hat-shaped sheet. The hat shape was obtained by four bending operations, and connected to the flat sheet with ten equally spaced screws on each flange. The rolling direction of the sheets was oriented in the longitudinal direction of the component.

A pendulum accelerator was employed to conduct the dynamic axial crushing tests. Cf. Hanssen et al. [24] for a detailed description of the test set-up. The impacting mass was 395.5 kg and the velocity was approximately 10 m/s.

The specimen was positioned in the test machines such that the centre line of the impactor was aligned with the centre line of the specimen, using a custom made clamping fixture (Fig. 7).

In order to ensure the same progressive buckling mode in all crushing tests and to minimize the scatter in the results, the specimens were manually triggered prior to the tests with a geometrical imperfection at the end facing the impactor (see Fig. 7c).

The quasi-static component tests were carried out under displacement control with a velocity of 10 mm/min, using the same clamping device as for the dynamic tests. Total crushing distance was 150 mm.

4 Experimental results

In this section the results from the FDS single connector and component tests are presented and discussed.

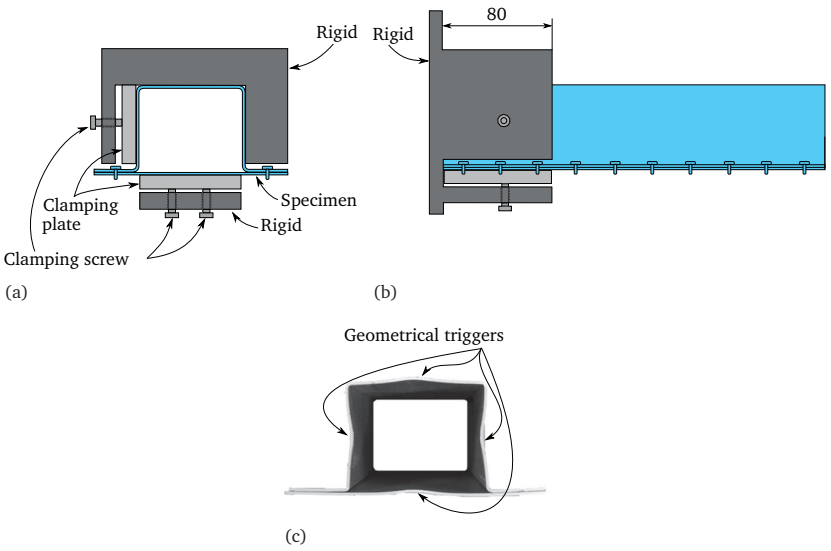

Fig. 7. Schematic illustration of clamping device used in crushing tests. (a) Top view. (b) Side view. (c) Geometrical triggers.

4.1 Single connector tests

The force-displacement curves from the cross tests are shown in Fig. 8. The tensile mode exhibits lowest force and highest ductility, while the shear mode exhibits highest force and lowest ductility. The mixed mode results show intermediate force level and ductility. The repeatability of the test results was acceptable.

No visible plastic deformations were observed in the screws (which was the case for all single connector tests). Details of the separated cross specimens are shown in Fig. 9.

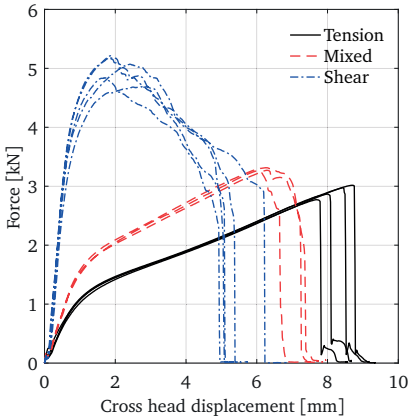

Fig. 8. Force-displacement curves from cross tests.

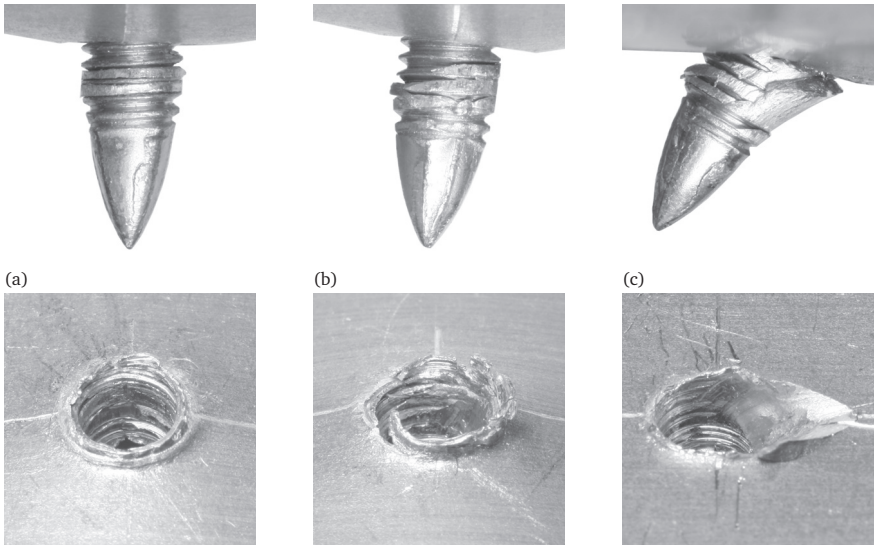

Fig. 9. Details of separated cross specimens. (a), (b) and (c): residue material on screws after separation for tensile, mixed and shear loading cases, respectively. (d), (e) and (f): screw hole in bottom sheet (viewed from the top side) after separation for tensile, mixed and shear loading cases, respectively.

Under pure tensile loading the sheets deformed until a critical force was reached. The knee in the force-displacement curves corresponds to yielding of the sheets. A rapid failure occurred quickly after the force peak. By inspecting Figs. 9a and 9d it is evident that the connection failed due to thread stripping of the bottom sheet material. As seen, some residue material was visible on the screw after failure, indicating that the threads in the bottom sheets were broken off due to shear fracture.

A similar force-displacement relationship was observed in the tests with combined tensile and shear loadings. Yielding of the sheet material caused also for these tests a knee in the force-displacement curve, and after the maximum force was reached, softening occurred before a rapid failure terminated the test. During deformation a slight rotation of the screw was observed, resulting in thread engagement mostly on one side of the screw hole. Thread stripping therefore occurred on this side of the screw hole, again of the bottom sheet. This is clearly seen in Figs. 9b and 9e. On one side the threads remained relatively intact; on the other side they were stripped.

Under pure shear loading a stiffer response was observed until maximum force was reached. As the connection was further loaded, the screw gradually rotated up to 30-40 degrees. During this rotation the threads on one side of the screw hole were gradually disengaged in a similar manner as observed for the combined loading case, leading to a gradual decrease of force to about 60 percent of maximum force after the peak (see Fig. 8). The rotation and

thread disengagement on one side led to failure of the bottom sheet material at the loaded side of the screw hole, such that the screw was pulled out. This corresponds to the abrupt decrease of force at the end of the test. The failure differed from what was found for tensile and mixed loadings. As seen in Figs. 9c and 9f, a more significant amount of residue material remained attached to the screw after failure, indicating that failure occurred by through thickness shear fracture of the bottom sheet material, rather than thread stripping.

A similar force response as in the cross shear tests was observed for the single lap-joint tests, see Fig. 10. This was expected, since the loading conditions on the connection in the two tests were similar. After approximately 80 percent of maximum force was reached, the force level flattened out and increased slowly until maximum force. After maximum force was reached the force decreased almost linearly to approximately 60 percent of maximum force, where the connection failed.

From Fig. 10 it is evident that the effect of the sheet anisotropy on the force-displacement response is negligible from a design point of view. Furthermore, no effect of the sheet anisotropy was observed on the deformation and failure of the connection.

The specimen deformation is shown in Fig. 11. Also here rotation of the screw due to the shear force led to a one-sided thread engagement and a through thickness shear fracture of the bottom sheet material, see Figs. 11b and 11c. The screw rotation caused bending deformations of the top sheet near the screw, as seen in Fig. 11a. This was not observed in the shear cross tests, due to the more restrictive clamping in the cross tests.

The force-displacement curves from the peeling tests are given in Fig. 12. The force increased rapidly at first, until the sheets yielded. A rapid fracture occurred immediately

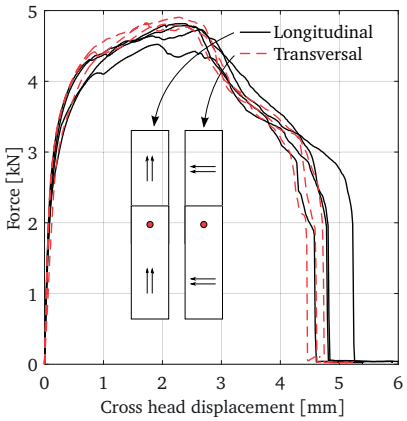

Fig. 10. Force-displacement curves from single lap-joint tests. Results from both material orientations are shown.

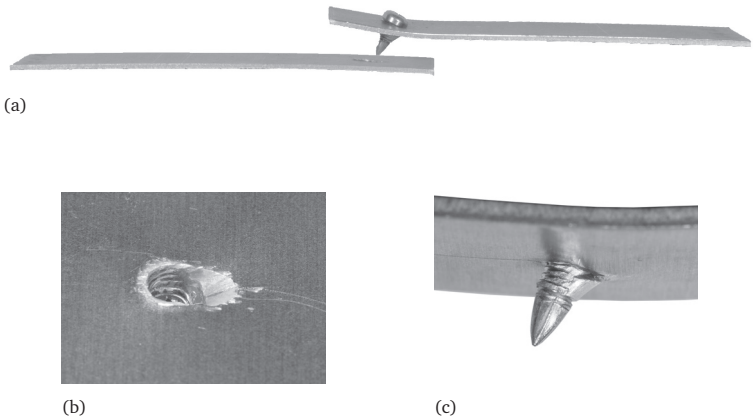

Fig. 11. Deformed single lap-joint specimen. (a) Whole specimen. (b) Top side of bottom sheet. (c) Underside of top sheet.

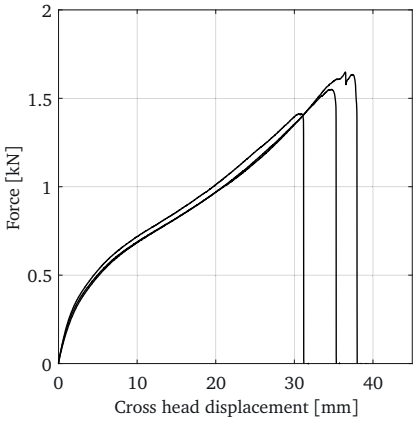

Fig. 12. Force-displacement curves from peeling tests.

after maximum force was reached.

A representative deformed peeling specimen is shown in Fig. 13. As the load increased, the bends in the L-shaped plates were stretched out, resulting in new bends in the sheets around the screw. The screw head stiffened the top sheet, resulting in rotation of the screw and asymmetry in the bending deformations, as may be seen in Fig. 13a (the bottom sheet is bent more). Failure occurred by stripped threads in the bottom sheet, as may be seen in Figs. 13b and 13c, where the screw and screw hole are depicted after failure.

The load on the connection in the peeling tests was tensile dominated. However, compared to the cross tension tests it is evident that the global strength of the connection was reduced under peeling loading. This may partially be explained by the presence of a lever force.

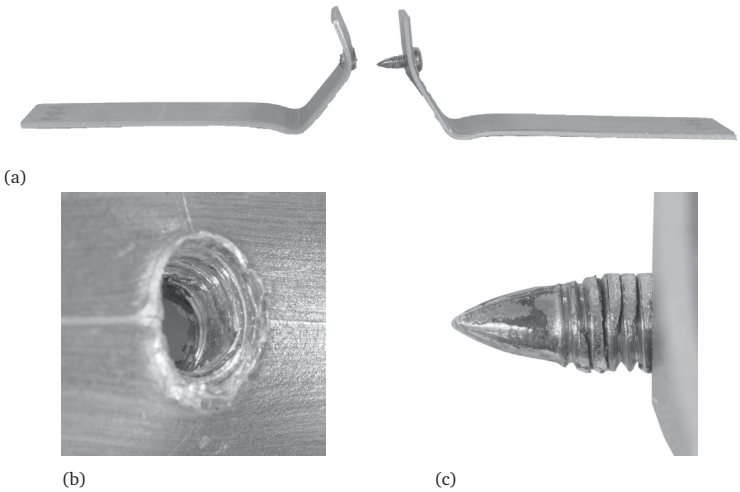

Fig. 13. Deformed peeling specimen. (a) Whole specimen. (b) Top side of bottom sheet. (c) Screw.

Fig. 14 illustrates the forces acting on one part of the specimen in the start of the test, where the lever force is idealized as a concentrated force for simplicity. By force equilibrium it is obvious that the force transferred through the screw connection in this test is higher than the external force. Thus, as expected the connection failed for a smaller external load than under pure tensile loading.

4.2 Component tests

The force-displacement and mean force-displacement histories for the component tests are shown in Figs. 15a and 15b, respectively. Little scatter was observed. The mean force was approximately 15-20 % higher for the dynamic compared to the quasi-static tests. Since strain rate effects are small for this material [25], the main reason for the increased energy absorption in the dynamic test is lateral inertia forces set up in the profile during progressive folding.

A deformed sample from the dynamic test is pictured in Fig. 16. After the tests, four lobes

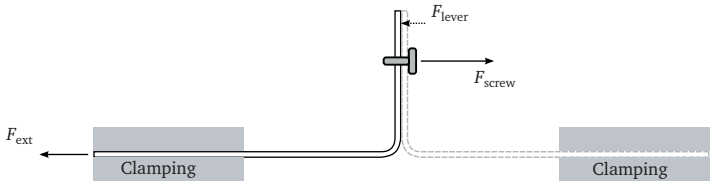

Fig. 14. Illustration of lever effect in peeling test.

were clearly visible in each specimen. The creation of a fifth lobe was interrupted by the clamping and the termination of the tests. The same progressive buckling mode was observed in the dynamic and quasi-static tests; only minor differences were observed in the pattern. Differences in the force-displacement responses between quasi-static and dynamic tests may be explained by the differences in initial geometrical imperfections and thus the buckling pattern.

Some cracks were observed in the sheets, located in tensile dominated zones in the lobes at the corner of the specimens, where large plastic strains occurred both during forming of the single-hat and during crushing. The global response is not believed to be affected by the crack formations.

The deformation of each screw connection was investigated closely after the tests, and four deformation and fracture modes were found: screw rotation, screw pull-out, screw push-out and shear fracture of screws, depicted in Fig. 17a. The figure includes a graphical illustration where lines indicate for which screws the different modes were observed in the dynamic tests. The screw positions are numbered from 1 to 7, and the corresponding positions are shown for a representative deformed specimen in Fig. 17b. The same modes were observed in the quasi-static tests, except for the shear fracture.

Deformation took place in the sheet material. Other than the shear fracture observed in the dynamic tests, no visible deformation occurred to any of the screws.

Rotation of screws was caused by relative movement between the sheets, and was the most frequent mode; over half of the screws experienced this mode. It was observed in all screw

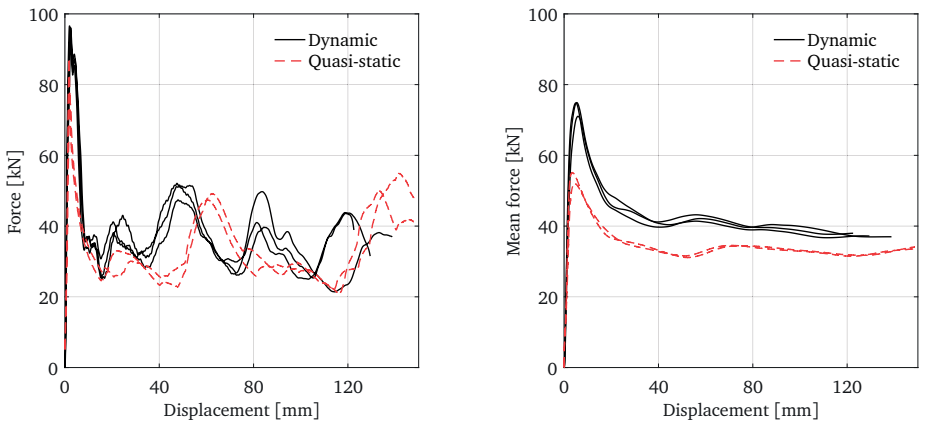

(a) (b)

Fig. 15. Force-displacement (a) and mean force-displacement (b) curves from dynamic and quasi-static axial crushing tests.

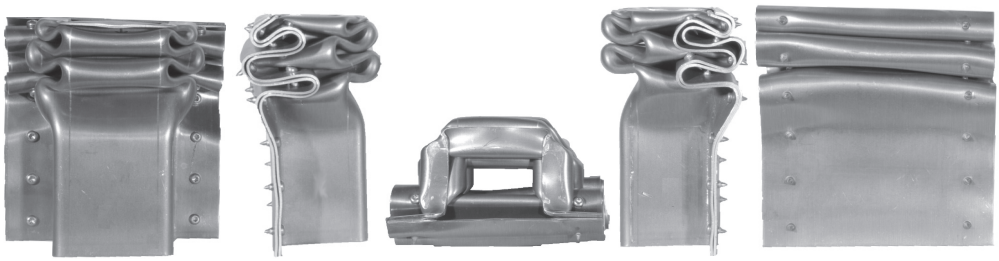

Fig. 16. Deformed single-hat section from dynamic axial crushing test, viewed from different directions.

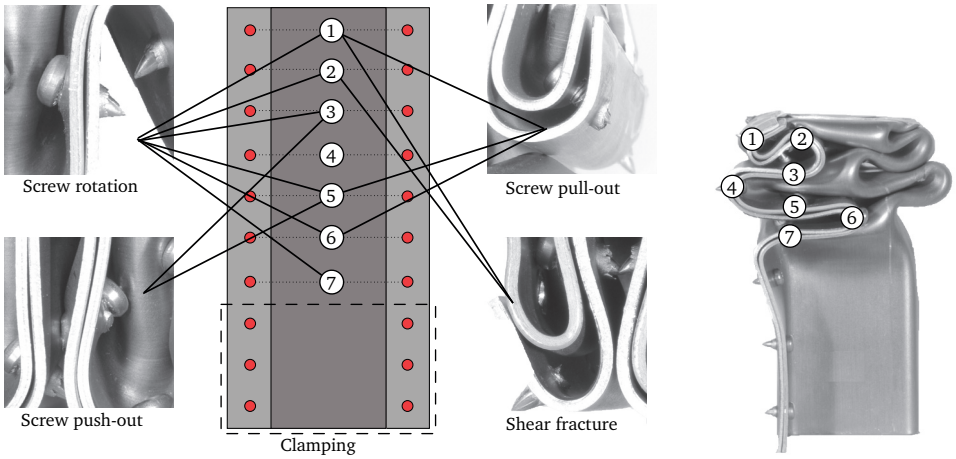

Fig. 17. Graphical illustration of the observations of screw deformation and failure modes in the dynamic tests. Screw positions are indicated with numbers, both positions on the deformed specimens (a) and initial positions (b). The different lines (b) indicate where the screw deformation modes were observed.

positions except for position 4. This mode is closely related to the deformation observed in the cross shear and single lap-joint tests.

The screw pull-out mode is related to the deformation observed in the cross tension tests. It was observed for screws in positions 1, 5 and 6, and was often seen together with screw rotation.

Screw push-out occurred when the tail of the screw had contact with other parts of the specimen during buckling, and was observed in straight parts between lobes (position 3 and 5). The push-out mode was not observed in the single connector tests.

Two screws fractured near the screw head in the dynamic tests. These screws were located near the impacted end of the specimen (positions 1 and 2). The reason for this fracture mode is not well understood, but could be a result of over-torqueing during the screwing process, dynamic effects in the tests, or both.

As seen in Fig. 17, no connections in position 4 had visible deformation in the dynamic tests. These screws were located at the middle of the second outward lobe where little relative movement between the sheets occurred.

While both the screw rotation and pull-out modes also were observed in the single connector tests, the push-out and shear fracture modes only occurred in the component tests. This could be important from a finite element modelling perspective. In large-scale shell simulations (for instance full-scale car crash simulations) connections are typically represented by simple constraint-based macroscopic models representing the physical behaviour of the connections. Such models are usually calibrated using single connector tests (e.g. cross tests) and validated with component tests. Thus, physical behaviour only observed in the component tests (such as the push-out and shear fracture modes in this case) will not be represented by the macroscopic models.

5 Comparison with self-piercing rivet connections

The rivets used were of the Böllhof standard, type C-SKR, made of high strength steel with a nominal diameter of 5 mm, which is a typical rivet used in the automotive industry. The geometry of the rivet and the cross-section of the rivet connection are shown in Fig. 18. A flat die was used in the riveting process.

5.1 Single connector tests

High repeatability was obtained in the tests with SPR. To highlight the differences between FDS and SPR connections, representative curves are presented herein.

The results from the single connector tests are shown in Fig. 19. Generally, the SPR connection was stronger than the FDS connection. It should be emphasized that the nominal diameter of the screws was 4 mm while it was 5 mm for the rivets. Additionally, the legs of the rivets expand during the riveting process (see Fig. 18), resulting in an effectively larger connection diameter than for the FDS connection. Accordingly, a higher strength was expected. The observed deformation and failure modes of the SPR connections were in accordance with the observations of Porcaro et al. [16]

Cross test results are compared in Fig. 19a. For tensile and mixed mode loading the ductility was highest for SPR compared to for FDS, while it was slightly lower than for FDS in shear. The largest differences in the force-displacement results were observed after the peak force.

Under tensile loading a less abrupt failure was seen for SPR than for FDS, softening occurred before failure of the SPR connection. The rivet failed due to pull-out of the legs from the bottom sheet.

During loading in mixed mode a rotation of the rivet was observed. Failure occurred from both the top and bottom of the rivet. As the rivet rotated, the head was pulled through the top sheet when the surrounding material slowly failed, at the same time as the legs were pulled out of the bottom sheet. This occurred during the near linear decrease of force occurring after maximum force (Fig. 19a).

The deformation and failure of the riveted connections under shear loading were similar to what was observed under mixed mode loading. A rotation of the rivet occurred until the top sheet material failed, and the rivet legs were pulled out of the bottom sheet. After maximum force was reached, a steep force reduction was observed before the force flattened out to a plateau close to zero. In Fig. 19b the single lap-joint test results are compared. While no effect of the material orientation was observed for FDS, there is clearly an effect on the ductility of the SPR connection. Highest ductility was observed when the connection

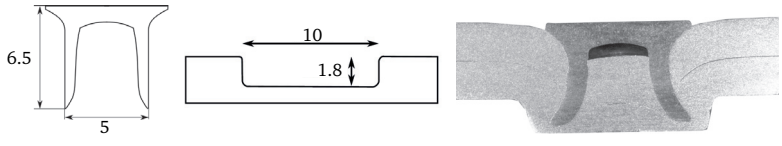

Fig. 18. Rivet connection. (a) Geometry. (b) Cross-section.

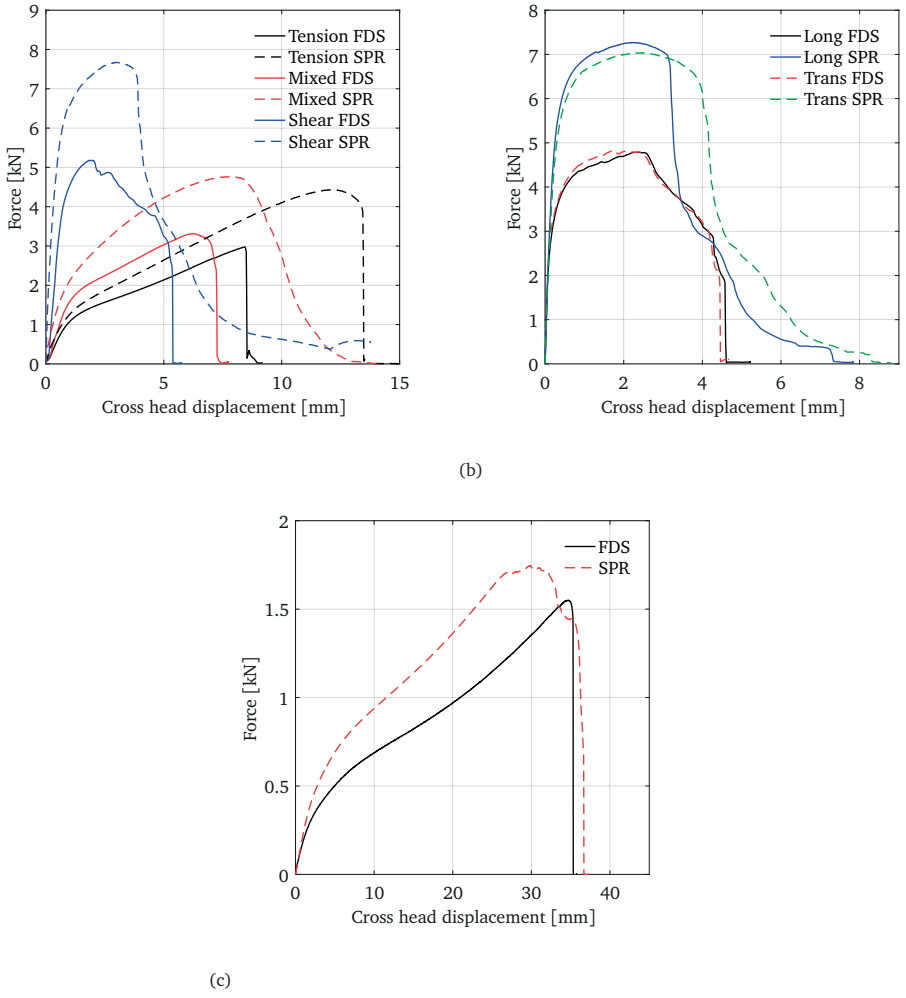

Fig. 19. Representative force-displacement curves from single connector tests with FDS and SPR. (a) Cross tests. (b) Single lap-joint tests. (c) Peeling tests.

was loaded in the transversal material direction. A small effect was also observed on the maximum force, as slightly higher force was achieved when the connection was loaded in the longitudinal material direction.

As was the case for the FDS connection, the behaviour of the SPR connection in the single lap-joint test was similar to the behaviour in the shear cross test. The rivet rotated until the head was pulled through the top sheet, and the legs were pulled out of the bottom sheet.

The difference in strength between SPR and FDS was significantly lower in the peeling test compared to the other single connector tests (see Fig. 19c). This indicates that the resistance to peeling loading is relatively high for FDS connections, compared to SPR connections.

The deformation of the SPR peeling specimen was similar to the deformation observed for the FDS specimens. However, since the stiffest side of an SPR connection is the bottom side, the top sheet was bent more than the bottom sheet (opposite than for the FDS connection). Failure occurred when the head was pulled through the top sheet.

From the single connector tests it is evident that the macroscopic behaviour of FDS connections is similar to that of SPR connections under tensile, combined tensile and shear and shear loading, as well as in single lap-joint and peeling tests. The force level was higher for the SPR connections, but similar trends with respect to ductility, maximum force and shape of force-displacement curves were observed for both connections. However, the deformation and failure modes of the two connections were different.

5.2 Component tests

The dynamic force-displacement and mean force-displacement responses for SPR and FDS connections are compared in Fig. 20. As seen, the trends are similar in terms of shape and force levels up to approximately 60 mm displacement, after which more scatter was evident. The riveted components sustained a slightly higher force level throughout the tests, apart from the initial peak. Consequently, more energy was absorbed by the riveted components.

The increased energy absorption may be explained by the effective diameter of the SPR connection. Due to the die shape of the bottom sheet the effective diameter of the SPR connection was significantly larger than of the FDS connection. Thus, the rivet connection better prevented sheet separation during buckling (which was observed when examining the crushed specimens), leading to increased plastic deformations in the lobes of the flanges and therefore increased energy absorption.

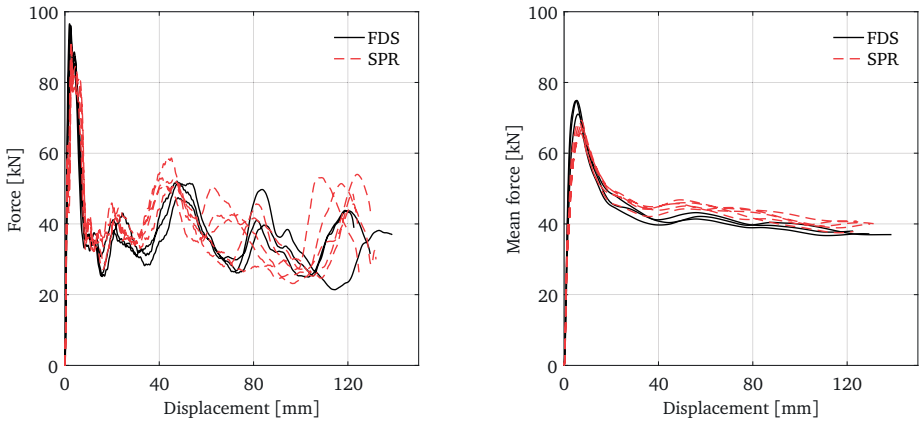

(a) (b)

Fig. 20. Force-displacement (a) and mean force-displacement (b) curves from dynamic axial crushing tests with FDS and SPR connections.

The same observations were made for the quasi-static component tests. For this reason the force-displacement curves are not plotted herein. Each specimen was closely investigated after the tests. Similar differences in the buckling pattern between the dynamic and quasi-static tests were observed for SPR as was observed for FDS.

The deformation and fracture of the SPR connections in the component tests were investigated and compared to the observations for the FDS connections. In general, failure of the FDS connection was more often observed than failure of the SPR connection, and the physical deformation and failure modes of the two connection types were different.

6 Conclusions

The following main conclusions can be drawn from the single connector tests of flow-drill screw connections:

- The strength of the connections increased with the amount of shear loading, while the ductility decreased.
- Under tensile and combined tensile and shear loadings failure occurred by thread stripping from the bottom sheet material, while in the shear tests failure occurred by through thickness shear fracture of the bottom sheet material.
- No effect of anisotropy of the sheet material was observed on the behaviour of the connections.

For the component tests with flow-drill screws the following was found:

– Four deformation and failure modes of the screw connections were observed: screw rotation, screw pull-out, screw push-out and screw fracture. Screw push-out and screw fracture was not observed in the single connector tests.

The comparison with self-piercing rivet connections revealed the following main conclusion:

– Similar trends with respect to ductility, maximum force and shape of force-displacement curves were observed for the two connections. Largest differences were observed under shear dominated loadings. However, the underlying physical deformation and failure phenomena were different.

References

[1] EJOT. 2014. http://www.ejot.com.

[2] Head, G., Master, W., Bredesky, L., and Winter, D. "For Forming a Hole and a Brushing in a Metal Workpiece". *Google Patents* (1984).

[3] Miller, S. F. and Shih, A. J. "Friction Drilling - A Chipless Hole-Making Process". *Proceedings of the ASME International Conference on Manufacturing Science and Engineering, Ypsilanti*. Vol. 8. 11. 2006.

[4] Szlosarek, R., Karall, T., Enzinger, N., Hahne, C., and Meyer, N. "Mechanical testing of flow drill screw joints between fibre-reinforced plastics and metals". *Materials Testing* 55.10 (2013), pp. 737–742. https://doi.org/10.3139/120.110495.

[5] Pedreschi, R. and Sinha, B. "The potential of press-joining in cold-formed steel structures". *Construction and Building Materials* 10.4 (1996), pp. 243–250. https://doi.org/10.1016/0950-0618(96)00006-2.

[6] Lennon, R., Pedreschi, R., and Sinha, B. "Comparative study of some mechanical connections in cold formed steel". *Construction and Building Materials* 13.3 (1999), pp. 109–116. https://doi.org/10.1016/S0950-0618(99)00018-5.

[7] Lorenzo, G. D. and Landolfo, R. "Shear experimental response of new connecting systems for cold-formed structures". *Journal of Constructional Steel Research* 60.3 (2004). Eurosteel 2002 Third European Conference on Steel Structures, pp. 561–579. https://doi.org/10.1016/S0143-974X(03)00130-5.

[8] Briskham, P., Blundell, N., Han, L., Hewitt, R., Young, K., and Boomer, D. "Comparison of Self-Pierce Riveting, Resistance Spot Welding and Spot Friction Joining for Aluminium Automotive Sheet". *SAE 2006 World Congress & Exhibition*. SAE International, Apr. 2006. https://doi.org/10.4271/2006-01-0774.

[9] Langrand, B., Patronelli, L., Deletombe, E., Markiewicz, E., and Drazétic, P. "Full scale experimental characterisation for riveted joint design". *Aerospace Science and Technology* 6.5 (2002), pp. 333–342. https://doi.org/10.1016/S1270-9638(02)01175-6.

[10] Lee, Y.-L., Wehner, T. J., Lu, M.-W., Morrissett, T. W., and Pakalnins, E. "Ultimate strength of resistance spot welds subjected to combined tension and shear". *Journal of Testing and Evaluation* 26.3 (1998), pp. 213–219. https://doi.org/10.1520/JTE11994J.

[11] Arcan, L., Arcan, M., and Daniel, I. M. "SEM fractography of pure and mixed-mode interlaminar fractures in graphite/epoxy composites". *Fractography of Modern Engineering Materials: Composites and Metals*. ASTM International, 1987. https://doi.org/10.1520/STP25614S.

[12] Wung, P. "A force-based failure criterion for spot weld design". *Experimental Mechanics* 41.1 (Mar. 2001), pp. 107–113. https://doi.org/10.1007/BF02323112.

[13] Wung, P., Walsh, T., Ourchane, A., Stewart, W., and Jie, M. "Failure of spot welds under in-plane static loading". *Experimental Mechanics* 41.1 (Mar. 2001), pp. 100–106. https://doi.org/10.1007/BF02323111.

[14] Langrand, B. and Combescure, A. "Non-linear and failure behaviour of spotwelds: a global finite element and experiments in pure and mixed modes I/II". *International Journal of Solids and Structures* 41.24 (2004), pp. 6631–6646. https://doi.org/10.1016/j.ijsolstr.2004.06.009.

[15] Langrand, B. and Markiewicz, E. "Strain-rate dependence in spot welds: Non-linear behaviour and failure in pure and combined modes I/II". *International Journal of Impact Engineering* 37.7 (2010), pp. 792–805. https://doi.org/10.1016/j.ijimpeng.2010.01.004.

[16] Porcaro, R., Hanssen, A., Langseth, M., and Aalberg, A. "The behaviour of a self-piercing riveted connection under quasi-static loading conditions". *International Journal of Solids and Structures* 43.17 (2006), pp. 5110–5131. https://doi.org/10.1016/j.ijsolstr.2005.10.006.

[17] Porcaro, R., Hanssen, A., Langseth, M., and Aalberg, A. "An experimental investigation on the behaviour of self-piercing riveted connections in aluminium alloy AA6060". *International Journal of Crashworthiness* 11.5 (2006), pp. 397–417. https://doi.org/10.1533/ijcr.2005.0108.

[18] Porcaro, R., Langseth, M., Hanssen, A., Zhao, H., Weyer, S., and Hooputra, H. "Crashworthiness of self-piercing riveted connections". *International Journal of Impact Engineering* 35.11 (2008), pp. 1251–1266. https://doi.org/10.1016/j.ijimpeng.2007.07.008.

[19] Sun, X. and Khaleel, M. A. “Performance Optimization of Self-Piercing Rivets Through Analytical Rivet Strength Estimation”. *Journal of Manufacturing Processes* 7.1 (2005), pp. 83–93. https://doi.org/10.1016/S1526-6125(05)70085-2.

[20] Sun, X. and Khaleel, M. A. “Dynamic strength evaluations for self-piercing rivets and resistance spot welds joining similar and dissimilar metals”. *International Journal of Impact Engineering* 34.10 (2007), pp. 1668–1682. https://doi.org/10.1016/j.ijimpeng.2006.09.092.

[21] CEN. *Eurocode 9: Design of Aluminium Structures Part 1-1: General Structural Rules*. 2007.

[22] Lademo, O.-G., Engler, O., Keller, S., Berstad, T., Pedersen, K., and Hopperstad, O. “Identification and validation of constitutive model and fracture criterion for AlMgSi alloy with application to sheet forming”. *Materials & Design* 30.8 (2009), pp. 3005–3019. https://doi.org/10.1016/j.matdes.2008.12.020.

[23] Porcaro, R., Hanssen, A., Aalberg, A., and Langseth, M. “Joining of aluminium using self-piercing riveting: testing, modelling and analysis”. *International journal of crashworthiness* 9.2 (2004), pp. 141–154. https://doi.org/10.1533/ijcr.2004.0279.

[24] Hanssen, A., Auestad, T., Tryland, T., and Langseth, M. “The kicking machine: A device for impact testing of structural components”. *International journal of crashworthiness* 8.4 (2003), pp. 385–392. https://doi.org/10.1533/ijcr.2003.0246.

[25] Moore, M. and Bate, P. “Microstructural inhomogeneity and biaxial stretching limits in aluminium alloy AA6016”. *Journal of Materials Processing Technology* 125-126.Supplement C (2002), pp. 258–266. https://doi.org/10.1016/S0924-0136(02)00304-7.

Paper 2

This paper was published in:

Sønstabø, J. K., Morin, D., and Langseth, M. “Macroscopic modelling of flow-drill screw connections in thin-walled aluminium structures”. *Thin-Walled Structures* 105 (2016), pp. 185-206. https://doi.org/10.1016/j.tws.2016.04.013

Abstract

This paper presents an investigation on the modelling of flow-drill screw connections in thin-walled aluminium plates in large-scale finite element analyses using different macroscopic modelling techniques. Five models that were originally developed for adhesive bonds, spot welds and self-piercing rivet connections were examined. Two sets of experimental data were used, each with a different screw and material combination. Different trends were observed for the two sets, which challenged the flexibility of the models. The results indicated that a constraint-based model originally developed for self-piercing rivet connections was the best suited model. A two-step validation strategy was proposed and used for the present models.

Macroscopic modelling of flow-drill screw connections in thin-walled aluminium structures

1 Introduction

Joining with flow-drill screws (FDS) is a common technique for joining dissimilar materials in the load-bearing structure of cars. Under impact loadings, the behaviour and fracture of connections are important for the response of the thin-walled structure. In the automotive industry, large-scale finite element (FE) simulations with shell elements (for instance, crash simulations) are extensively used in the vehicle design process, and accurate modelling of connections plays an important role in obtaining reliable predictive results. Due to time step limitations, the physical geometry of connections and potential process effects cannot be modelled; rather, simplified models are necessary to represent the connections. These models should be capable of describing the macroscopic response while being computationally efficient.

Several different approaches have been used for different connection types, and various models have been designed for, e.g., spot welds, adhesives and self-piercing rivet connections. However, no models have been specifically developed for modelling FDS connections. Furthermore, no reports regarding the modelling of FDS connections have been found in the available literature. The aim of this study was to assess the ability of existing macroscopic connection models to represent FDS connections. Different strategies for connection modelling are presented in the following.

One of the simplest approaches is to assign a rigid link between two nodes on opposing shell surfaces (Fig. 1a). However, this approach requires the nodes to be aligned, which is an exhausting restriction for large-scale analyses, and with this approach, the local deformation behaviour of the connection cannot be taken into account. An easier approach is to use a beam element for the connection attached to the surfaces with tie constraints (Fig. 1b). Then, deformation behaviour may be accounted for, but this approach has been shown to be mesh dependent, as noted by Malcolm and Nutwell [1], who used a material model designed for spot welds in the beams. A drawback of this method is that the time step may be limited by the beam length. Another method is to use one or several hexahedral elements in an assembly to represent a connection (Figs. 1c and 1d), and this method has been shown to be mesh independent if eight or more elements are included in the assembly [1]. However,

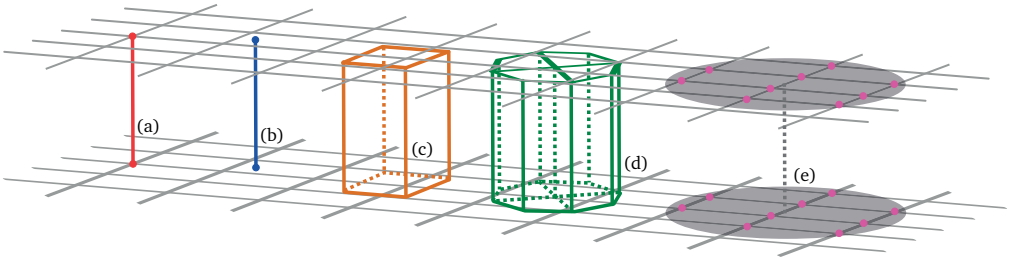

Fig. 1. Illustration of different connection modelling techniques. (a) Rigid link. (b) Beam element. (c) Hexahedral element. (d) Cluster of hexahedral elements. (e) Constraint.

refining the connection mesh might decrease the time step. To predict accurate responses, different material models can be assigned to these clusters of elements. Such models are herein referred to as *element-based* models.

Element-based models are commonly used for modelling of structural bonds (e.g. [2]). In some part configurations structural bonding and discrete connections (such as FDS connections) are commonly combined. A way to model such hybrid joints is to use an element-based model for the adhesive bond, in combination with a discrete model for the discrete connections (e.g. [3]).

A material model designed to predict spot weld failure was presented by Hallquist et al. [4], under the name *mat spotweld*. This model is an elastic-plastic model with isotropic linear hardening coupled with different failure models. Seeger et al. [5] showed that this model could realistically describe spot welds using either a single beam element, a single hexahedron element or four hexahedron elements to represent the connection (see Figs. 1b, 1c and 1d). These authors argued that using four hexahedron elements was too expensive because it limited the simulation time step. Bier et al. [6] evaluated the ability of the cohesive element model presented by Marzi et al. [7] to represent spot welds (this model is available in the FE software LS-DYNA under the name *mat cohesive mixed mode elastoplastic rate* [4]). It was compared to *mat spotweld*, and they found that the model of Marzi et al. [7] was beneficial for some load cases. They obtained better results with a cluster of four or eight elements rather than with a single element.

A model tailored for self-piercing rivet connections was reported by Hanssen et al. [8] (available in LS-DYNA as the model *constrained spr2* [4]). This is a *constraint-based* model, which means that the connection is represented by a constraint formulation rather than by an assembly of elements (Fig. 1e). Tensile and shear behaviours are uncoupled, and damage is taken into account. They defined a strong coupling between mode mixity and damage evolution based on experimental observations. It was shown that mesh dependency was limited and that the model was well suited for self-piercing rivet connections.

Another constraint-based model (named *constrained interpolation spotweld* (model 1 in LS-DYNA®) by Hallquist et al. [4]) was developed for spot welds. In this model, tensile and shear behaviours are coupled through a plasticity-like formulation.

Sommer and Maier [9] investigated the abilities of *mat spotweld*, the model *mat arup adhesive* [4], the element-based model of Marzi et al. [7], the constraint-based model of Hanssen et al. [8], and *constrained interpolation spotweld* to represent self-piercing rivet connections. They found that the model of Marzi et al. [7] was the most promising and that *mat spotweld* was the least promising. However, they noted that the model proposed by Marzi et al. [7] was insufficient under peeling loadings and that it had no flexibility to control the mixed-mode behaviour. The model *mat arup adhesive* is a cohesive zone model with linear elasticity and damage (no plasticity), which is too simple for FDS connections, and therefore, this model is not included in the present study.

Further modifications to *constrained interpolation spotweld* were presented by Bier and Sommer [10], and they showed that the ability to model self-piercing rivet connections was enhanced (this model is availbale in LS-DYNA® as *constrained interpolation spotweld* (model 2)).

When calibrating macroscopic models, it is important to have a proper strategy for validation. The model should be calibrated to tests under controlled loading paths and validated to tests with different and more complex loadings. Hoang et al. [11] used U-shaped specimens under controlled tensile, combined tensile and shear, and shear loadings for calibration and validated the model using a complex component test (T-component). Similarly, Bier and Sommer [10] used KSII tests for calibration and a complex component (T-joint) test for validation.

In this work, the ability of five common state-of-the-art connection models to represent FDS connections was studied. The examined models were the element-based *mat spotweld*, the element-based model by Marzi et al. [7], the constraint-based model by Hanssen et al. [8] and the two versions of the constraint-based model *constrained interpolation spotweld*. These models were calibrated to experimental data from two different connections with different screw and material combinations. A thorough two-step procedure for validation is presented and used.

2 Experiments

Here, the term *connection* is based on the definition of Sønstabø et al. [12], i.e., *a system that mechanically fastens two or more parts together*. Thus, a connection consists of a screw

and surrounding plate material (see Fig. 2). In the first set of experiments, a short screw with a nominal length of 10 mm, a nominal shaft diameter of 4 mm and a nominal head diameter of 8 mm joined two aluminium sheets (alloy 6016 T4), while in the second set of experiments, a long screw with a nominal length of 30 mm, a nominal shaft diameter of 5 mm and a nominal head diameter of 14 mm joined an aluminium sheet (alloy 6016 T4) to an aluminium extrusion (alloy 6063 T6). The nominal thicknesses of the sheet and extrusion were 2 mm. A pre-hole was used in the top plate for both connections. The two connections are hereafter denoted as the *small screw connection* and the *large screw connection*, respectively. Each set of experiments consisted of cross tests in three loading directions (tension, shear and combined tension and shear), single lap joint and peeling tests, and T-component tests.

An extensive study of the behaviour of the small screw connection has previously been reported by Sønstabø et al. [12], which included cross, single lap joint and peeling tests. Using the same experimental set-up, corresponding tests were conducted in this work for the large screw connection. Drawings of the specimens with their nominal dimensions are presented in Fig. 3. The cross specimens (Fig. 3a) were identical for the two connections, whereas there were some differences for the single lap joint (Figs. 3b and 3d) and peeling specimens (Figs. 3c and 3e). The cross-head force and displacement were measured during the tests.

In addition to the single-connector tests, T-component tests were performed. The T-component specimens consisted of a hat-shaped sheet joined to a U-shaped sheet/extrusion. Drawings of the specimens with their nominal dimensions are presented in Figs. 4a and 4b. The test set-up was adopted from Hoang et al. [11]. Pictures of the test rig are presented in Figs. 4c and 4d. As shown, the U-shaped part was clamped at both ends, and the load was applied in the longitudinal direction of the hat-shaped part. Three-dimensional digital image correlation was used as a virtual extensometer, measuring the relative displacement between the sheets by tracking one point on each part, as illustrated with yellow dots in Fig. 4e.

Force-displacement curves from the single lap joint tests are presented along with the

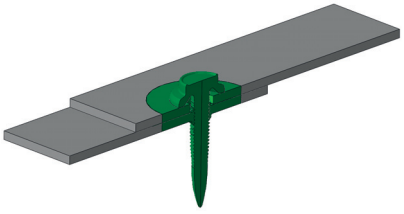

Fig. 2. Illustration of the definition of a *connection* (green).

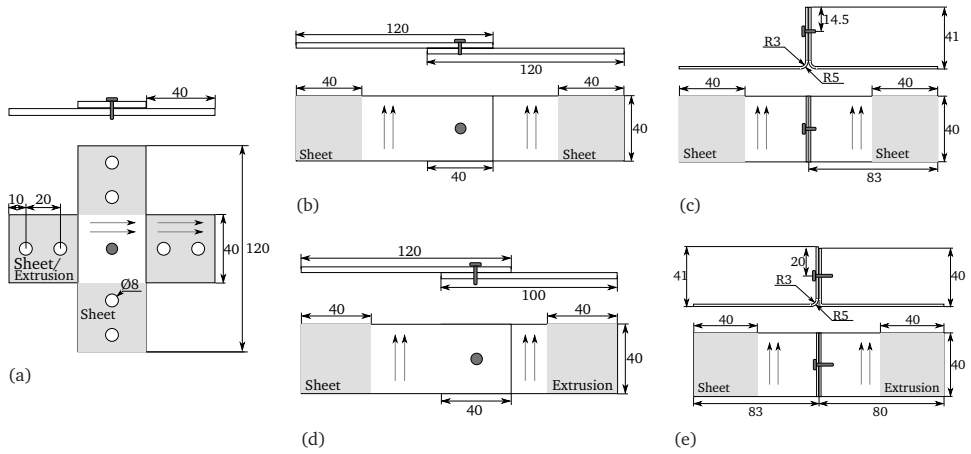

Fig. 3. Single-connector test specimens. Arrows indicate the rolling/extrusion direction. (a) Cross specimen. (b) Single lap-joint specimen for the small screw connection. (c) Peeling specimen for the small screw connection. (d) Single lap-joint for the large screw connection. (e) Peeling specimen for the large screw connection.

simulation results in Section 5. However, selected results from the cross, peeling and T-component tests are included here to highlight the differences observed between the two connections, which were significant for the present study.

Representative curves from the cross tests are presented in Fig. 5. As shown, when going from shear to mixed and tensile loading, the maximum load decreased and the displacement at maximum load increased for both connections. However, for the displacement at failure, the trend differed for the two connections. For the small screw connection, the displacement at failure increased when going from shear to mixed and tensile loading, whereas it decreased for the large screw connection. It was also observed that the macroscopic behaviour in mixed mode appears to be very different for the two connections.

Fig. 6 presents representative curves from the peeling tests. The difference between the two connections is the increased slope observed for the large screw connection just before the maximum load (at approximately 23 mm). This was an effect of contact between the tail of the screw and the plate material. Tail contact did not occur for the small screw connection due to the shorter length of the screw.

Force-displacement curves from the T-component tests are presented in Fig. 7. All repetitions are included because some scatter was evident. As shown in this figure, the behaviour after the maximum force differed for the two connections. For the small screw connection, failure occurred almost immediately after the maximum force was reached, without any softening. For the large screw connection, however, significant softening was observed before failure occurred. Moreover, the sudden failure that occurred for both connections differed from the failure observed in the cross shear tests, which might indicate that the failure mechanisms

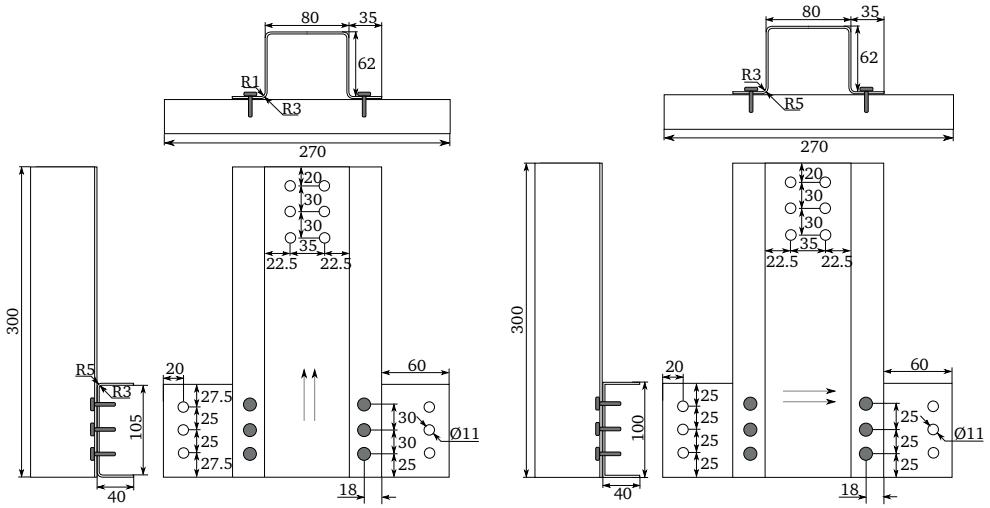

(c)

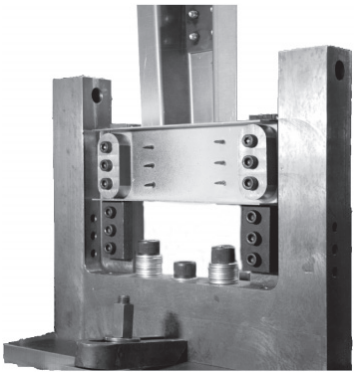

(d)

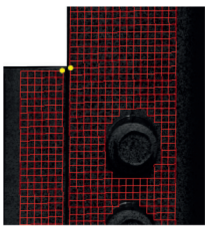

(e)

Fig. 4. Test set-up in T-component tests. Arrows indicate the rolling/extrusion direction. The nominal thickness is 2 mm. (a) T-component specimen for the small screw connection. (b) T-component specimen for the large screw connection. (c) Front of the test rig. Red rectangle shows the location of the DIC mesh (see Fig. 4e). (d) Back of test rig. (e) DIC displacement measure (see Fig. 4c).

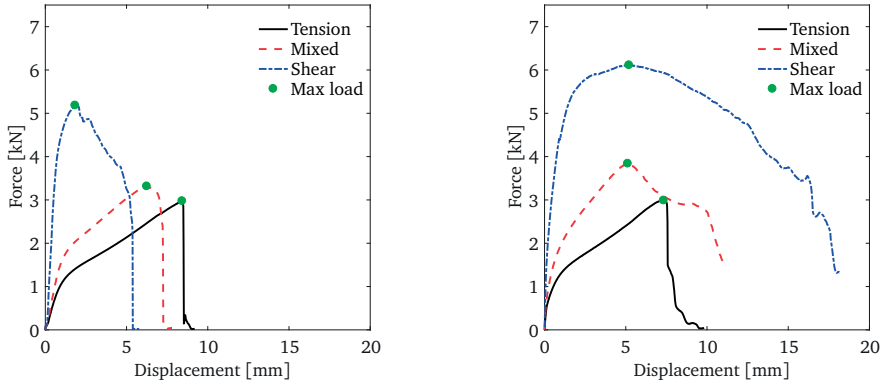

(a) (b)

Fig. 5. Representative curves from cross tests. (a) Small screw connection (after Sønstabø et al. [12]). (b) Large screw connection.

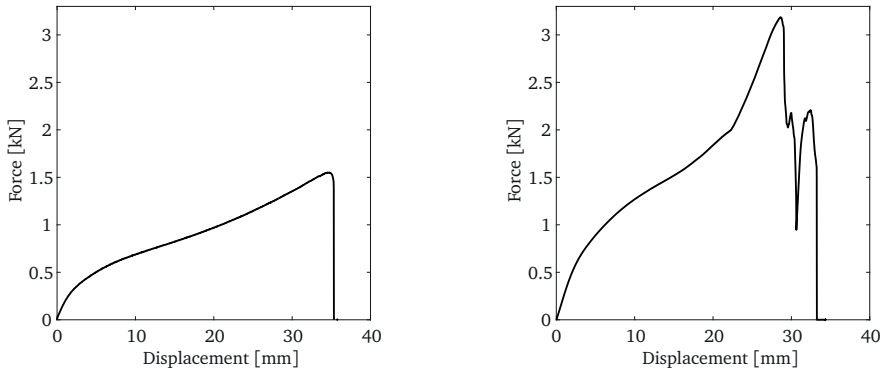

(a) (b)

Fig. 6. Representative curves from peeling tests. (a) Small screw connection (after Sønstabø et al. [12]). (b) Large screw connection.

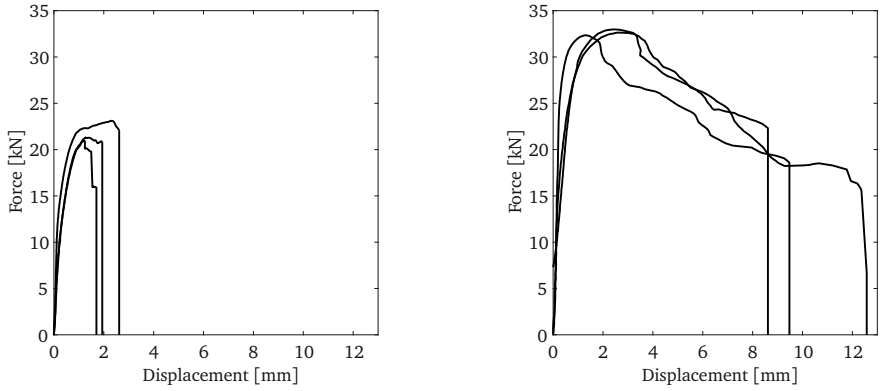

(a) (b)

Fig. 7. Curves from T-component tests. (a) Small screw connection. (b) Large screw connection.

at the component level differ from those observed in the single-connector tests. This result was observed in the study of Sønstabø et al. [12] when comparing axial crushing tests to cross tests for the small screw connection.

The differences discussed herein indicate that a high level of model flexibility is required for a macroscopic connection model to represent the behaviours of both connections.

3 Modelling of plate materials

To minimise the uncertainty linked to the plate material when modelling connections, an advanced rate-independent hypoelastic-plastic material model was applied for the rolled sheet in alloy 6016 temper T4 and the extrusion in alloy 6063 temper T6. An anisotropic yield surface was used, the associated flow rule was assumed, and isotropic work hardening was applied. Kinematic hardening was not considered because the loadings were assumed to be monotonic.

Material tests were performed to characterise the materials. One set of material tests (uniaxial tensile tests and disk compression tests) was used to calibrate the yield surface and hardening parameters. Plane strain tension and in-plane single shear tests were used to validate the material models because they challenge other parts of the yield surface.

In the following section, the material model and the calibration/validation procedure are presented.

3.1 Material model

Because rolled and extruded alloys typically exhibit significant plastic anisotropy [13], the 18-parameter anisotropic yield function Yld2004-18p [14] was selected to describe the yielding and the plastic flow of the aluminium plates. This yield surface was chosen for its flexibility to cover a wide range of aluminium textures. It is constructed by two linear transformations of the deviatoric stress tensor, where the two transformation tensors include a total of 18 independent coefficients that weight the components of the deviatoric stress tensor to account for plastic anisotropy. In addition, the function includes an exponent m that determines the curvature. With the yield function

$$f = \phi - (\sigma_0 + R) \leq 0,$$

where σ_0 is the yield stress and R is an isotropic hardening variable, Barlat et al. [14] proposed the function ϕ, as follows,

$$\begin{aligned}4\phi^m = &\left|\tilde{S}'_1-\tilde{S}''_1\right|^m+\left|\tilde{S}'_1-\tilde{S}''_2\right|^m+\left|\tilde{S}'_1-\tilde{S}''_3\right|^m\\&+\left|\tilde{S}'_2-\tilde{S}''_1\right|^m+\left|\tilde{S}'_2-\tilde{S}''_2\right|^m+\left|\tilde{S}'_2-\tilde{S}''_3\right|^m\\&+\left|\tilde{S}'_3-\tilde{S}''_1\right|^m+\left|\tilde{S}'_3-\tilde{S}''_2\right|^m+\left|\tilde{S}'_3-\tilde{S}''_3\right|^m.\end{aligned}$$

Here, $\tilde{S}'_1$, $\tilde{S}'_2$, $\tilde{S}'_3$ and $\tilde{S}''_1$, $\tilde{S}''_2$, $\tilde{S}''_3$ are the principal values of the tensors $\tilde{\mathbf{s}}'$ and $\tilde{\mathbf{s}}''$, respectively, which are defined through the transformations

$$\begin{aligned}\tilde{\mathbf{s}}' &= \mathbf{C}'\cdot\mathbf{s}\\ \tilde{\mathbf{s}}'' &= \mathbf{C}''\cdot\mathbf{s},\end{aligned}$$

where $\mathbf{s}$ is the deviatoric part of the Cauchy stress tensor. The transformation tensors $\mathbf{C}'$ and $\mathbf{C}''$ each contain nine independent coefficients. If $\mathbf{s}$ is expressed in matrix form using Voigt notation, the transformation tensors may be expressed in matrix form as

$$\boldsymbol{C}' = \begin{bmatrix} 0 & -c'_{12} & -c'_{13} & 0 & 0 & 0\\ -c'_{21} & 0 & -c'_{23} & 0 & 0 & 0\\ -c'_{31} & -c'_{32} & 0 & 0 & 0 & 0\\ 0 & 0 & 0 & -c'_{44} & 0 & 0\\ 0 & 0 & 0 & 0 & -c'_{55} & 0\\ 0 & 0 & 0 & 0 & 0 & -c'_{66}\end{bmatrix}$$

$$\boldsymbol{C}'' = \begin{bmatrix} 0 & -c''_{12} & -c''_{13} & 0 & 0 & 0\\ -c''_{21} & 0 & -c''_{23} & 0 & 0 & 0\\ -c''_{31} & -c''_{32} & 0 & 0 & 0 & 0\\ 0 & 0 & 0 & -c''_{44} & 0 & 0\\ 0 & 0 & 0 & 0 & -c''_{55} & 0\\ 0 & 0 & 0 & 0 & 0 & -c''_{66}\end{bmatrix}.$$

The 18 coefficients have no physical meaning and must be determined by using optimisation methods.

To represent isotropic work hardening, the Voce hardening law was used. With the Voce law, the isotropic hardening variable R is

$$R = \sum_{i=1}^{N_R} Q_{Ri}\left(1-\exp\left(-\frac{\theta_{Ri}}{Q_{Ri}}p\right)\right), \tag{1}$$

where p is the equivalent plastic strain, N_R is the number of terms, and Q_{Ri} and θ_{Ri} are the

saturation value and initial hardening moduli for term i, respectively. Three terms were required for the sheet, whereas two terms were sufficient for the extrusion material.

3.2 Calibration of material model

To determine the shape of the yield surface, uniaxial tensile tests were performed in seven material directions (0°, 15°, 30°, 45°, 60°, 75° and 90° to the rolling/extrusion direction), and disk compression tests (coin tests) were performed.

For each tensile test, the flow stress ratio (r-ratio), which is defined as

$$r_\alpha(W^\mathrm{p}) = \left.\frac{\sigma_\alpha}{\sigma_\mathrm{ref}}\right|_{W^\mathrm{p}}, \tag{2}$$

was calculated. In Eq. (2), σ_α and σ_ref are the flow stresses in the α and reference directions, respectively, and W^p is the amount of plastic work. The rolling/extrusion direction was chosen as the reference direction. An average r-ratio was calculated for each test as follows,

$$r_\alpha^\mathrm{avg} = \frac{1}{W^\mathrm{p}_\mathrm{max}} \int_0^{W^\mathrm{p}_\mathrm{max}} r_\alpha(W^\mathrm{p}) \mathrm{d}W^\mathrm{p},$$

where $W^\mathrm{p}_\mathrm{max}$ is the amount of plastic work at the onset of diffuse necking.

The plastic strain ratio (R-ratio), which is defined as

$$R_\alpha = \left.\frac{\dot{\varepsilon}^\mathrm{p}_\mathrm{w}}{\dot{\varepsilon}^\mathrm{p}_\mathrm{t}}\right|_\alpha \approx \left.\frac{\varepsilon^\mathrm{p}_\mathrm{w}}{\varepsilon^\mathrm{p}_\mathrm{t}}\right|_\alpha, \tag{3}$$

was calculated from measurements of the specimen cross-sections before and after the uniaxial tensile tests. In Eq. (3), $\dot{\varepsilon}^\mathrm{p}_\mathrm{w}$ and $\dot{\varepsilon}^\mathrm{p}_\mathrm{t}$ are the plastic strain rates in the width and thickness directions, respectively, and $\varepsilon^\mathrm{p}_\mathrm{w}$ and $\varepsilon^\mathrm{p}_\mathrm{t}$ are the corresponding plastic strains during the uniaxial tensile tests, obtained from thickness and width measurements of the tensile specimens before and after the tests.

The gradient of the yield surface in equi-biaxial tension was determined using coin tests, in which a circular disk is compressed uniaxially. Under the assumption that only deviatoric stresses influence plasticity, one can argue that the plastic flow in the compressed disk is equivalent to the plastic flow under equi-biaxial tension [15, 16]. Thus, plastic strain measurements of the disk provide information that determines the gradient of the yield surface at the point of equi-biaxial tension through the equi-biaxial plastic strain ratio, which

is defined as

$$R_{\mathrm{EqB}} = \frac{\varepsilon^{\mathrm{p}}_{yy}}{\varepsilon^{\mathrm{p}}_{xx}}.$$

Here, $\varepsilon^{\mathrm{p}}_{yy}$ and $\varepsilon^{\mathrm{p}}_{xx}$ are the plastic strains in the transversal and longitudinal material directions, respectively. The coin tests were conducted using the test set-up of Vysochinskiy [17].

For the sheet material (6016 T4), crystallographic texture data were available in addition to the data from the uniaxial tensile and coin tests. From the texture data, a yield surface was calculated with the crystal plasticity finite element method (CP-FEM) using the method of Dumoulin et al. [18]. The parameters of the yield function were optimised to fit both the CP-FEM data and the uniaxial tensile test and coin test data (r-ratio, R-ratio and R_{EqB}), with a weight ratio of 1 to 100, respectively. For the extrusion material (6063 T6), texture data were not available and the parameters were solely optimised to the uniaxial tensile and coin test data. The resulting yield surface was instead correlated to previous work on the same alloy [18], and satisfactory agreement was found.

The yield function parameters for both materials were found by minimising the sum of squares of error. The value of the exponent m was set to 8 in both cases, as this value has been shown to describe the behaviour of FCC materials [14].

The hardening parameters were found through reverse engineering by simulating the uniaxial tensile test in the reference direction with the FE method using the explicit solver LS-DYNA® (version R7.1). The Levenberg-Marquardt algorithm was employed in the optimisation using the software LS-OPT® (version 5.0).

The resulting material model parameters are presented in Table 1. Graphical representations are presented in Figs. 8 and 9 for the two materials, respectively. The yield surfaces are represented as contours of the shear stress σ_{xy} projected onto the σ_x-σ_y-plane normalised to the yield stress σ_0 in Figs. 8a and 9a, while the experimental and computed r-values and R-values are presented in Figs. 8b, 8c, 9b and 9c. As shown, acceptable fits were achieved. The sheet and extrusion both exhibited significant plastic anisotropy, whereas only slight anisotropy was observed for the flow stresses.

The FE model of the uniaxial tensile test in the reference direction is shown in Fig. 10a. The specimen was modelled with two symmetry planes: one in the thickness direction and one along the length of the specimen (dashed line). The model consisted of constant stress solid elements with reduced integration, with six elements through half the thickness in the central part. A tie constraint was applied between the coarse and fine mesh regions (red and blue parts in Fig. 10a), located such that they did not affect the results. In the

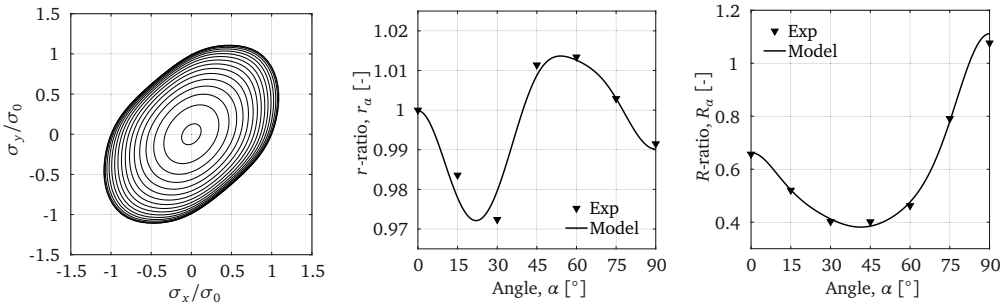

Fig. 8. Calibrated yield function compared to experimental data in the reference direction for AA 6016 T4. (a) Yield surface. (b) Experimental and computed r-values. (c) Experimental and computed R-values.

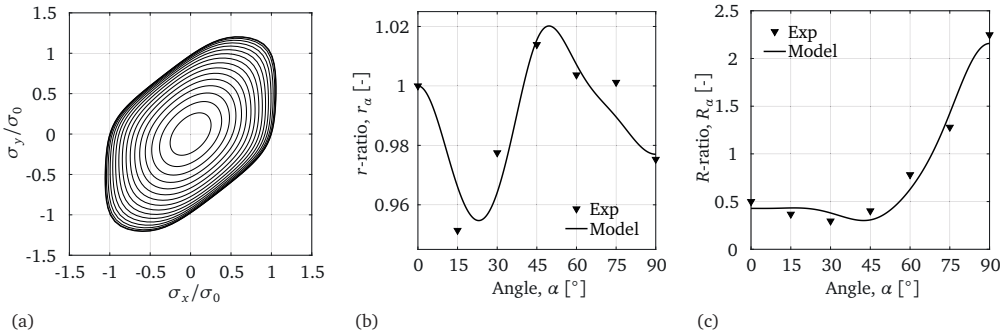

Fig. 9. Calibrated yield function compared to experimental data in the reference direction for AA 6063 T6. (a) Yield surface. (b) Experimental and computed r-values. (c) Experimental and computed R-values.

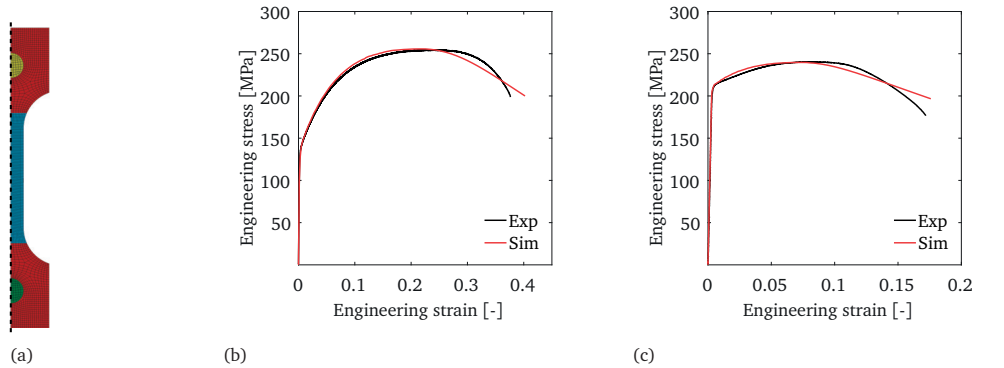

Fig. 10. FE model and results for uniaxial tensile test simulations in the reference direction after calibration of material model parameters. (a) FE model. (b) Results for AA 6016 T4. (c)Results for AA 6063 T6.

Table 1
Material model parameters for the base materials.

		6016 T4	6063 T6
σ_0	[MPa]	107.6	204.6
m	[-]	8.0	8.0
c'_{12}	[-]	-16.70	-1.51
c'_{13}	[-]	-6.69	-1.32
c'_{21}	[-]	18.56	0.82
c'_{23}	[-]	12.34	-0.19
c'_{31}	[-]	9.23	2.29
c'_{32}	[-]	-9.68	2.18
c'_{44}	[-]	0.70	0.55
c'_{55}	[-]	1.00	1.00
c'_{66}	[-]	1.00	1.00
c''_{12}	[-]	-17.46	0.93
c''_{13}	[-]	-7.22	-0.47
c''_{21}	[-]	11.26	-0.71
c''_{23}	[-]	12.34	-0.92
c''_{31}	[-]	7.49	0.39
c''_{32}	[-]	-11.15	1.62
c''_{44}	[-]	0.99	1.06
c''_{55}	[-]	1.00	1.00
c''_{66}	[-]	1.00	1.00
Q_{R1}	[MPa]	29.2	8.0
θ_{R1}	[MPa]	25000	12300
Q_{R2}	[MPa]	149.5	55.0
θ_{R2}	[MPa]	2011	1472.6
Q_{R3}	[MPa]	100	
θ_{R3}	[MPa]	230.8	

physical tests, the specimens were simply supported with a pin through a hole in each end. The pins (yellow and green in Fig. 10a) were modelled as rigid bodies, and a node-to-surface algorithm was used for the contact between the pins and the specimen. A prescribed displacement along the longitudinal direction was enforced on one of the pins, whereas the other was fully clamped. Although the tests were conducted using a quasi-static strain rate, time scaling was applied in the simulations to reduce the computational time. Inertia effects were ensured to be negligible. The material model was implemented as a user material. The resulting engineering stress-strain curves are shown in Figs. 10b and 10c, which also include representative curves for the experiments. As shown in these figures, the results from the experiments were reproduced in the simulations.

3.3 Validation of material model

The material models were validated by challenging the yield surface outside the calibration domain using plane strain tension and in-plane single shear tests and corresponding simulations. Both the plane strain tension and the in-plane single shear specimens were cut out in the reference (rolling/extrusion) directions. The FE models are shown in Figs. 11a and 12a. These models were constructed in a manner similar to that of the uniaxial tension model (i.e., constant stress solid elements, reduced integration, symmetry planes where

applicable, prescribed displacement, tie constraints, and time scaling), and the explicit solver LS-DYNA® (version R7.1) was again used. Six and ten elements were used through half the thickness, respectively. In the plane strain tension tests, mechanical grips were used for clamping, which was represented by modelling the outer parts as rigid bodies (green and yellow in Fig. 11a). The in-plane single shear test specimens were simply supported as in the uniaxial tensile tests with rigid body pins and a contact algorithm.

In the FE models of the material tests it was necessary to use solid elements, in order to accurately describe the specimen deformations at large strains (beyond diffuse necking). Shell elements are not sufficient to describe phenomena such as strain localization accurately. The obtained material model parameters were considered transferable to the large-scale simulations with shell elements in this work, as the plastic deformations of the shells were moderate, and no strain localization occurred in these simulations. For the same reason it was not necessary to include a fracture criterion.

The results of the validation simulations are shown in Figs. Figs. 11b, 11c, 12b and 12c in terms of force-displacement curves with representative curves for the experiments. As shown in these figures, the initial stiffness and the initiation of yielding were correctly captured in all simulations. The work hardening in the plane strain tension tests was well captured for both materials. For the in-plane single shear test, the work hardening was well captured for the sheet, whereas it was somewhat over-estimated for the extrusion. This result is not believed to have a significant impact in the large-scale simulations in this work because the level of in-plane shear strains was limited.

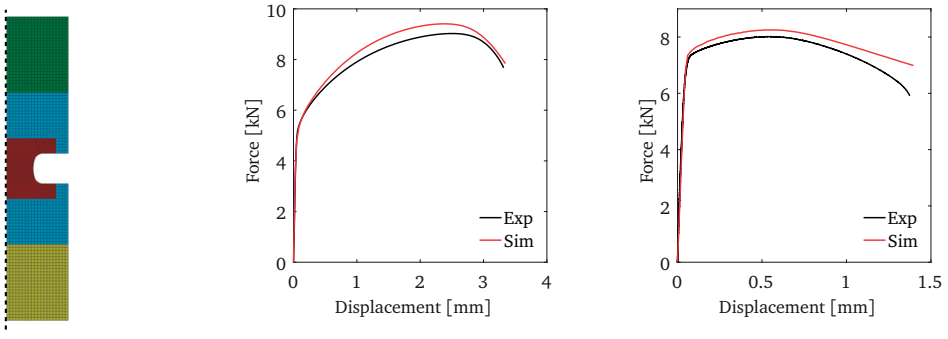

(a) (b) (c)

Fig. 11. FE model and results of simulations of plane strain tension tests. (a) FE model. (b) Results for AA 6016 T4. (c)Results for AA 6063 T6.

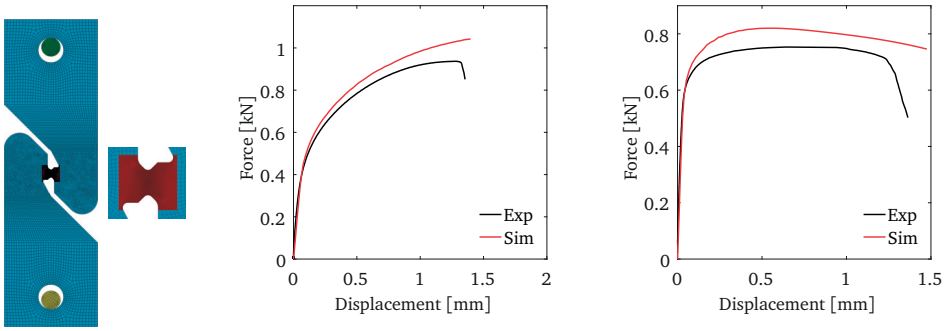

(a) (b) (c)

Fig. 12. FE model and results of simulations of in-plane single shear tests. (a) FE model (central part enlarged). (b) Results for AA 6016 T4. (c)Results for AA 6063 T6.

4 Modelling of flow-drill screw connections

In this section, the investigated connection models are briefly presented. The element-based models are described first, followed by the constraint-based models and a summary highlighting the important differences between the models. The details of the models are presented in Appendix A. Readers are encouraged to read the appendix because the discussion in Section 5 involves details of the models. All the investigated models are available in the explicit FE solver LS-DYNA® version R7.1 (for *constrained interpolation spotweld* model 2 version R8.0 was used). The calibration/validation procedure is explained at the end of this section.

4.1 Element model 1

The first investigated model is *mat spotweld*, which was presented by Hallquist et al. [4]. For readability, this model is henceforth denoted as *element model 1*. This is a material model intended for beams and solid elements tied between two opposing shell surfaces (recall Fig. 1). It incorporates an isotropic elasto-plastic material model (J2 flow theory) with isotropic linear hardening coupled to different damage and failure models. This model was originally developed to model spot welds. The elasto-plastic behaviour is governed with four user parameters, i.e., Young's modulus E, Poisson's ratio ν, yield stress σ_y and plastic hardening modulus H. In addition, several other parameters linked to the different damage and failure models may be specified.

4.2 Element model 2

The second investigated element-based model is the tri-linear cohesive element model presented by Marzi et al. [7] (henceforth denoted as *element model 2*). This model calculates the stresses on the mid-surface of the cohesive element as a function of the differences of the displacements of its upper and lower surfaces. This model is tri-linear in the sense that it incorporates linear elasticity, perfect plasticity and linear softening. Fig. 13a presents the tri-linear stress-separation curves for pure tensile and pure shear separation. Eight parameters define the tri-linear shape under pure tensile and pure shear loading, which also completely define the behaviour in mixed mode (Fig. 13b). This model is presented in detail in Section A.1.

4.3 Constraint model 1

This model (denoted as *constraint model 1*) was developed by Hanssen et al. [8], and it was originally intended for self-piercing rivet connections. It includes a force-deformation model for uncoupled tensile and shear behaviour. As deformation occurs, the model calculates the force and moment resultants, which are lumped to the nodes within a user-specified radius according to an interpolation function.

It it assumed that the rivet follows the motion of the master sheet, and the normal and tangential stretches δ_n and δ_t are calculated based on the relative displacement between the tail of the rivet and the slave sheet. A deformation history variable $\eta_{\max}$ is calculated using an interaction formula between δ_n and δ_t. This formula is scaled with a term that accounts for damage-dependent mode mixity dependency (Eq. (A.9)), where the mixed-mode response is governed by user parameters. The normal and tangential forces f_n and

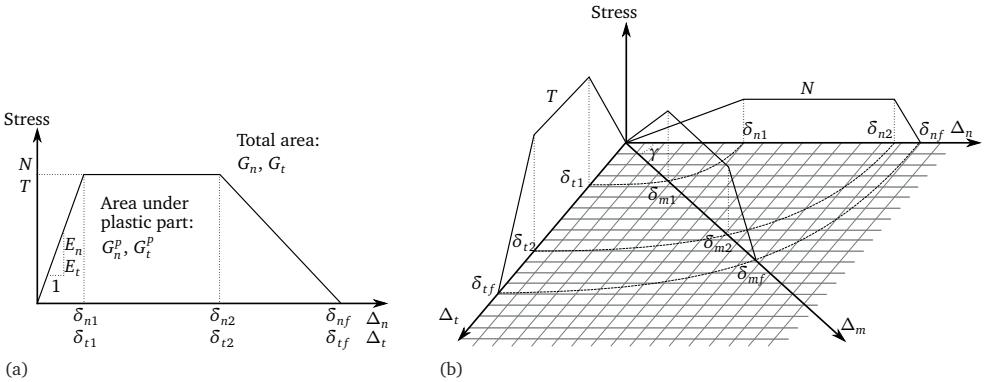

Fig. 13. Tri-linear stress-separation curves for *element model 2*. (a) Pure tensile and pure shear loading. (b) Mixed mode. See Section A.1 for descriptions of the parameters. After Marzi et al. [7].

f_t are then directly calculated as functions of $\eta_{\max}$. The normal and tangential forces are applied to the nodes in the directions normal and tangential to the master sheet, respectively. Softening is obtained by damage coupling. The model is given in detail in Section A.2.

4.4 Constraint model 2

The second constraint-based model investigated is the first version of the model *constrained interpolation spotweld* [4] (henceforth denoted as *constraint model 2*). This model was originally intended for modelling spot-welded connections. Its numerical implementation is similar to that of *constraint model 1*. In *constraint model 2*, the connection is treated in a symmetrical manner. The stretches are defined from the relative displacement between the sheets, and the direction of the normal load is defined by the average vector between the unit normal of both sheets (see Eq. (A.11)). To capture sheet rotation, a third kinematical quantity, the relative rotation angle ω_b, is used.

The normal and tangential forces f_n and f_t and the moment m_b are calculated in an elasto-plastic manner, with a stiffness, a yield function, a flow rule, and a hardening rule. Softening is included by damage coupling. See Section A.3 for further details.

4.5 Constraint model 3

Bier and Sommer [10] presented some modifications to *constrained interpolation spotweld* (the modified version is henceforth denoted as *constraint model 3*). The differences are manifested in the utilisation of ω_b and in the calculation of damage initiation and failure. See Section A.4 for details.

4.6 Summary of connection models

An overview of the models (except for *element model 1*) is given in Table 2 to highlight their similarities and differences. This table presents the definitions of kinematics, mode mixity angle, force computation and damage evolution.

A key difference between the models is the definition of the mode mixity angle. In *element model 2* and *constraint model 1*, the mode mixity angle is defined as a function of the stretches, whereas for *constraint model 2* and *constraint model 3*, it is defined from resultant forces. This difference was found to be important for the calibration and validation, as discussed in Section 5.

Table 2
Overview of element model 1 and constraint models 1, 2 and 3, showing the important differences. All models and their parameters are presented in detail in Appendix A.

	Element model 2	Constraint model 1	Constraint model 2	Constraint model 3
Kinematics	Separations calculated from element's relative displacements: $\Delta_n = \max(u_n, 0)$ $\Delta_t = \sqrt{u_{t1}^2 + u_{t2}^2}$ $\Delta_m = \sqrt{\Delta_n^2 + \Delta_t^2}$	Total stretch $\boldsymbol{\Delta}$ defined as the vector between the slave end and its original location on the deformed slave sheet. Normal and tangential stretch: $\Delta_n = \lvert\boldsymbol{\Delta}\cdot\mathbf{n}_m\rvert, \quad \Delta_t = \lvert\boldsymbol{\Delta}\cdot\mathbf{n}_t\rvert$ $\mathbf{n}_t = \mathbf{n}_0 \times \mathbf{n}_m$	Total stretch defined as the relative displacement between the two sheets: $\boldsymbol{\Delta} = \mathbf{u}_2 - \mathbf{u}_1$ Normal and tangential stretch: $\Delta_n = \lvert\boldsymbol{\Delta}\cdot\mathbf{n}_n\rvert, \quad \Delta_t = \lvert\boldsymbol{\Delta}\cdot\mathbf{n}_t\rvert$ $\mathbf{n}_n = \frac{\mathbf{n}_m + \mathbf{n}_s}{\lvert\mathbf{n}_m + \mathbf{n}_s\rvert}, \quad \mathbf{n}_t = \mathbf{n}_0 \times \mathbf{n}_n$ Relative rotation between sheets: $\omega_b = \arccos \frac{\mathbf{n}_s \cdot \mathbf{n}_m}{\lvert\mathbf{n}_s\rvert\lvert\mathbf{n}_m\rvert}$	
Mode mixity	$\theta = \arccos \frac{\langle u_n \rangle}{\Delta_m}$	$\theta = \arctan\left(\frac{\Delta_n}{\Delta_t}\right)$	$\theta = \arctan\left(\frac{F_n}{F_t}\right)$ $F_n = f_n + \alpha m_b$ $F_t = f_t$	$F_n = f_n$ $F_t = f_t$
Elasticity	$\tilde{\boldsymbol{\sigma}} = \boldsymbol{E}\boldsymbol{u}^e$ $\tilde{\boldsymbol{\sigma}} = [\tilde{\sigma}_n, \tilde{\sigma}_{t1}, \tilde{\sigma}_{t2}]^\intercal$ $\boldsymbol{u}^e = [u_n^e, u_{t1}^e, u_{t2}^e]^\intercal$ $\boldsymbol{E} = \begin{bmatrix} E_n & 0 & 0 \\ 0 & E_t & 0 \\ 0 & 0 & E_t \end{bmatrix}$	Forces are calculated directly from mathematical expressions: $f_n = \frac{f_n^{\max}\Delta_n}{\eta_{\max}\Delta_n^{\text{fail}}}\hat{f}_n$ $f_t = \frac{f_t^{\max}\Delta_t}{\eta_{\max}\Delta_t^{\text{fail}}}\hat{f}_t,$ where $\hat{f}_n = 1 - \left(\frac{\xi_n - \eta_{\max}}{\xi_n}\right)^8$ $\hat{f}_t = 1 - \left(\frac{\xi_t - \eta_{\max}}{\xi_t}\right)^8$	$\tilde{\boldsymbol{f}} = E\boldsymbol{u}$ $\tilde{\boldsymbol{f}} = [f_n, f_t, m_b]$ $\boldsymbol{u} = [\Delta_n, \Delta_t, \omega_b]$	$\tilde{\boldsymbol{f}} = [f_n, f_t]$ $\boldsymbol{u} = [\Delta_n, \Delta_t]$
Plasticity	Uncoupled perfect plasticity in normal and tangential directions.		Yield surface: $\left[\left(\frac{F_n}{F_n^c}\right)^{\beta_1} + \left(\frac{F_t}{F_t^c}\right)^{\beta_1}\right]^{\frac{1}{\beta_1}} - F_0 = 0$ $F_n = f_n + \alpha_1 m_b$ $F_t = f_t$ $F_n^c = R_n$ $F_t^c = R_t$	$F_n = f_n$ $F_t = f_t$ $F_n^c = R_n(1 - \alpha_1\omega_b)$ $F_t^c = R_t$
Damage	Damage variable: $d = \frac{\Delta_m - \delta_{m2}}{\delta_{mf} - \delta_{m2}}$ Stresses scaled by damage variable: $\boldsymbol{\sigma} = (1-d)\tilde{\boldsymbol{\sigma}}$	Damage variables: $d_n = \frac{\eta_{\max} - \xi_n}{1 - \xi_n}, \; d_t = \frac{\eta_{\max} - \xi_t}{1 - \xi_t}$ When $\eta_{\max} \geq \xi_n$ and/or $\eta_{\max} \geq \xi_t$, forces are scaled by damage variables: $f_n = \frac{f_n^{\max}\Delta_n}{\eta_{\max}\Delta_n^{\text{fail}}}(1-d_n)$ $f_t = \frac{f_t^{\max}\Delta_t}{\eta_{\max}\Delta_t^{\text{fail}}}(1-d_t)$	Damage variable: $d = \frac{\tilde{u}^{\text{pl}} - \tilde{u}_0^{\text{pl}}(\theta)}{\tilde{u}_f^{\text{pl}}(\theta)}$ $\tilde{u}_0^{\text{pl}}(\theta)$ and $\tilde{u}_f^{\text{pl}}(\theta)$ are functions tabulated by the user.	$\tilde{u}_0^{\text{pl}}(\theta)$ and $\tilde{u}_f^{\text{pl}}(\theta)$ are defined by mathematical expressions (Eqs. (A.18) and (A.19)).
			Forces scaled by damage variable: $\boldsymbol{f} = (1-d)\tilde{\boldsymbol{f}}$	

Another difference between the models is the calculation of stresses and forces. *Element model 2* is elasto-perfect plastic, but because the plasticity is ideal, it is not necessary to solve any non-linear equations linked to plasticity. In *constraint model 1*, the forces are calculated directly from mathematical expressions. In *constraint model 2* and *constraint model 3*, however, an elasto-plastic formulation is used. To calculate the forces, a set of non-linear equations has to be solved.

Note that *element model 1* and *element model 2* have no flexibility for controlling the mixed-mode behaviour. In contrast, the constraint-based models do have parameters for controlling the mixed-mode behaviour. Due to this limitation, it was expected that better mixed-mode results would be obtained with the constraint-based models than with the element-based models.

4.7 Calibration/validation procedure

A robust validation procedure is important when modelling connections. The models should be calibrated to experiments with controlled macroscopic loading conditions. These tests should be easy to perform, and the number of tests needed should be limited to reduce the costs associated with the experiments, which is important from an industrial perspective.

Recall that a connection consists of the screw plus surrounding plate material (Fig. 2), and thus, the *macroscopic deformation* of a connection is *not* the same as the local deformations within the connection. Within the connection, the stress and deformation fields are complex and unknown, involving rotation of the screw and large plastic deformations and fracture of the plate materials. These deformations occur on a lower scale and can therefore not be captured by the macroscopic models. For this reason, the tests are discussed here on a macroscopic level.

Data from cross tests were used for calibration. The mechanical clamping of the plates in these tests constrained the deformation of the specimens such that the macroscopic deformation of the connections was approximately equal to the global displacement of the specimens. Thus, the macroscopic displacement path was simple and to some extent known. These tests were therefore well suited for calibration. Fig. 14a shows the calibration tests on a general fracture locus. The blue dots indicate the macroscopic connection displacement assumed in the tests.

The macroscopic models should subsequently be validated through another set of experiments. These experiments should challenge the connection under different loadings than the calibration tests and have varying degrees of complexity. A two-step validation

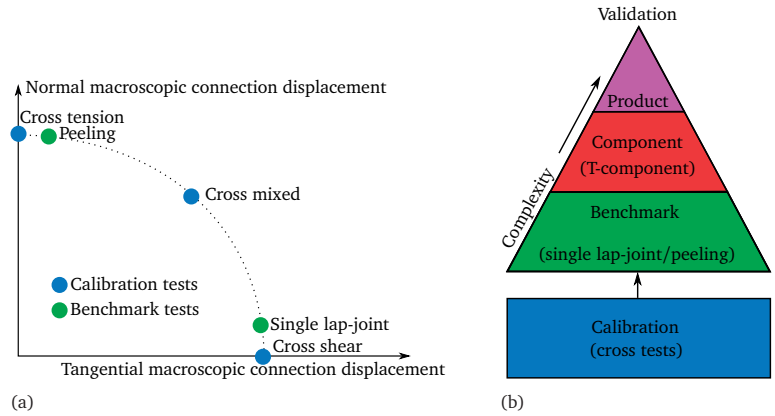

Fig. 14. Illustrations explaining the calibration/validation procedure. (a) General connection failure locus. The calibration tests are illustrated with blue dots, and the approximate assumed locations of the benchmark tests are indicated with green dots. (b) Illustration of validation strategy.

strategy is proposed, as illustrated in Fig. 14b.

First, single lap joint and peeling tests were used for validation at the benchmark level. In these tests, the macroscopic deformation of the connections was non-proportional and less controlled than in the calibration tests. The single lap joint test was shear dominated, but due to less clamping close to the connection, the plates were less constrained and more free to rotate than in the cross shear test. This rotation introduced a varying tensile component of the macroscopic displacement of the connection. Similarly, in the peeling test, the macroscopic connection displacement was tensile dominated. During the test, the plates deformed, thereby introducing a shear component in the macroscopic connection displacement. Using these two tests for validation therefore provided useful information regarding the ability of the large-scale models to represent more challenging loadings. The benchmark tests are included in Fig. 14a, in which their approximate location on the fracture locus is indicated with green dots.

A second level of validation (component level) was obtained using T-component tests, which represent more complex and uncontrolled macroscopic loadings on the connections. Due to the unknown nature of the loading on the connections, it is possible that failure mechanisms different than those observed in the calibration tests occurred in the component tests. For instance, in axial crushing tests with the small screw connection, Sønstabø et al. [12] observed failure due to shear fracture of the screw head and push-out of the screw due to contact between the tail and other parts of the specimen. These mechanisms were not observed in any other tests. Mechanisms that do not occur in calibration tests cannot be captured by macroscopic models. Additionally, the T-component specimens contained several connections next to each other (see Figs. 4a and 4b), which might induce interaction effects between them.

Tests on the product level (see Fig. 14b) are highly complex and expensive, and therefore, such test were not considered in this study.

Large-scale FE models of the calibration and validation tests were constructed. The connection model parameters were identified through reverse engineering of the cross tests. Force-displacement curves from the simulations were compared to the cross-head force and displacement in the experiments. The tension and shear parameters were optimised first, and then the mixed-mode parameters were optimised. Some parameters were taken directly from the experiments or manually tuned to fit the results. The Levenberg-Marquardt algorithm was used to optimise the remaining parameters, using the optimisation software LS-OPT® (version 5.0). After the model parameters were identified, they were validated with the benchmark and component simulations. The FE models used are presented in the following section.

4.8 FE models

The plates were modelled using Belytschko-Tsay shell elements with reduced integration with a mesh size of 2×2 mm. To limit the present study, the effect of mesh size in the plates was not investigated. Five integration points were used through the thickness. For contact between the different parts, a surface-to-surface algorithm with a penalty formulation was applied with a static friction coefficient of 0.2. The material models presented in Section 3 were applied to the sheet and extrusion materials. One plane of symmetry was utilised in the T-component simulation. The clamped parts were modelled as rigid bodies, and clamping was represented by constraining displacements. Loads were applied by enforcing displacements in the loading directions while constraining the other directions. The FE models are shown in Fig. 15a.

To obtain the hat- and U-shape of the sheets in the T-components and the bends of the sheets in the peeling specimens, the sheets were bent by pressing them into a die with a punch. The work hardening that occurred during the bending operation was investigated by simulating the bending process. The punch and die were modelled as rigid bodies, and the sheet was modelled using Belytschko-Tsay shell elements. To obtain a better description of the bend, a finer mesh size of 1×1 mm was used. The resulting fields of equivalent plastic strain and hardening variables for each through-thickness integration point were then mapped to the integration points in the bends of the peeling and T-component models. The process is illustrated in Fig. 15b, in which the fields of equivalent plastic strains are shown as contour plots on the specimens. To account for the different mesh sizes in the mapping, the values inserted in the 2×2 mm elements were the average value of the corresponding two elements in the 1×1 mm mesh. To determine the effect of the work hardening, the large-scale

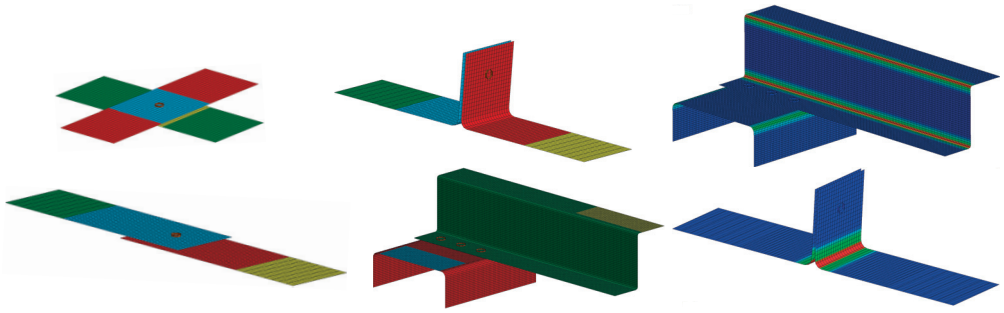

(a) (b)

Fig. 15. FE models. (a) FE models used for calibration and validation of the connection models: cross (top left), single lap joint (bottom left), peeling (top right) and T-component (bottom right). (b) Fields of initial equivalent plastic strains in peeling and T-component models.

simulations were run with and without the mapped fields. The results indicated that the work hardening had a limited effect on the simulation results.

5 Results and discussion

In the following, the results from the calibration and validation of the connection models are presented as force-displacement curves from simulations compared with experimental curves. The calibration is addressed first, followed by the validation. The discussion in Section 5.3 demonstrates the importance of having a proper validation procedure.

The element-based models are presented first, and then the constraint-based models are presented. The obtained parameters are summarised in Tables 3 and 4.

5.1 Calibration of element-based models

The results from the calibration of the element-based models are shown in Figs. 16 and 17, where the simulation and experimental curves are compared for both connections, respectively. As shown, the simulations and experiments match well in tension and shear (no damage/failure model was utilised in *element model 1*), but the force is severely over-predicted in mixed mode loading (Figs. 16b and 17b). As noted in Section 4.6, neither of the element-based models have flexibility for controlling the mixed mode behaviour; it is completely defined from the tension and shear parameters. It was therefore not possible to obtain more accurate results with these models, and they were determined to not be suitable for modelling flow-drill screw connections. Validation simulations were therefore not performed for the element-based models, and no damage/failure model was utilised in

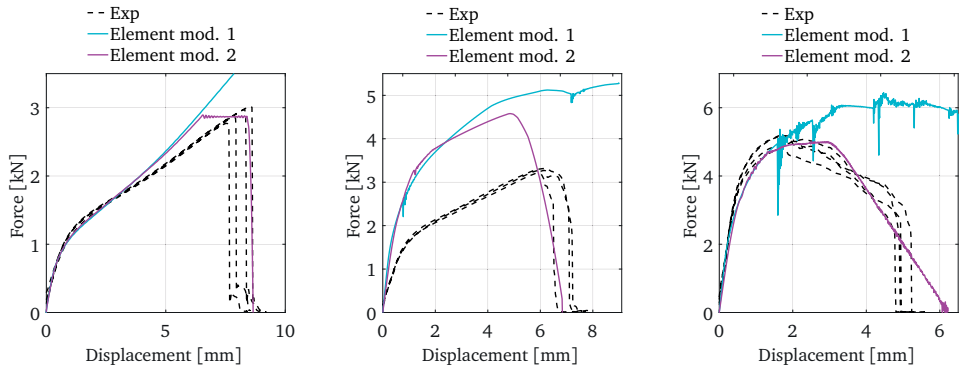

Fig. 16. Results from the calibration of the element-based models to cross tests for the small screw connection. (a) Cross tension. (b) Cross mixed. (c) Cross shear.

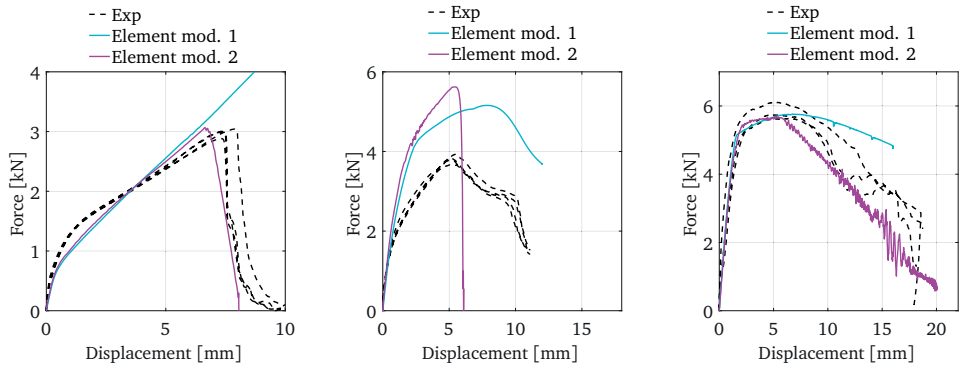

Fig. 17. Results from the calibration of the element-based models to cross tests for the large screw connection. (a) Cross tension. (b) Cross mixed. (c) Cross shear.

element model 1.

As stated in Table 3 the element cluster used with *element model 1* was comprised of 16 elements. This resulted in small elements, which decreased the time step and thus increased the computational time significantly, compared to the constraint-based models. This may be avoided by using fewer and larger elements in the cluster. With *element model 2* the time step was not affected. However, it was observed that the computational time was longer than for the constraint-based models by approximately a factor of 4.

5.2 Calibration of constraint-based models

The calibration results for the constraint-based models are shown for the two connections in Figs. 18 and 19, respectively. As shown in these figures, an acceptable fit was achieved in

Table 3
Parameters of the element-based models obtained for the two connections, including descriptions.

	Parameter	Description	The small screw connection	The large screw connection
Element model 1		Number of elements in connection	16	16
	D	Diameter of cluster of elements	1.5 mm	3.0 mm
	E	Young's modulus	4000 MPa	2000 MPa
	ν	Poisson's ratio	0.3	0.3
	σ_y	Yield stress	700 MPa	725 MPa
	H	Hardening modulus	0 MPa	300 MPa
Element model 2		Number of elements in connection	4	4
	D	Diameter of cluster of elements	3.0 mm	3.5 mm
	E	Elastic stiffness in tension	5000 N/mm	5000 N/mm
	N	Yield stress in tension	345.9 MPa	265 MPa
	G_n	Total area under traction-separation curve in tension	888.3 N/mm	400 N/mm
	f_{Gn}	Fraction of total area that is plastic in tension	0.834	0.325
	G	Elastic stiffness in shear	2703.9 N/mm	1000 N/mm
	T	Yield stress in shear	809.2 MPa	681.8 MPa
	G_t	Total area under traction-separation curve in shear	2856 N/mm	23800 N/mm
	f_{Gn}	Fraction of total area that is plastic in shear	0.496	0.19

Table 4
Parameters of the constraint-based models obtained for the two connections, including descriptions.

	Parameter	Description	The small screw connection	The large screw connection
Constraint model 1	r	Radius of influence	3.0 mm	6.0 mm
	$f_n^{\max}$	Maximum pure normal force	3000 N	2900 N
	$f_t^{\max}$	Maximum pure shear force	5000 N	6000 N
	Δ_n^{fail}	Deformation at failure for pure normal deformation	2.0 mm	5.2 mm
	Δ_t^{fail}	Deformation at failure for pure shear deformation	4.8 mm	16.0 mm
	ξ_n	Fraction of Δ_n where softening starts in pure normal deformation	0.9	0.72
	ξ_t	Fraction of Δ_t where softening starts in pure shear deformation	0.5	0.45
	α_1	Parameter to control influence of mode mixity on η	0.05	0.34
	α_2	Parameter to control influence of mode mixity on η	0.65	0.89
	α_3	Parameter to control influence of mode mixity on η	1.4	1.25
Constraint model 2	E	Elastic stiffness	9800 N/mm	9000 N/mm
	r	Radius of influence	4.3 mm	5.0 mm
	R_n	Load capacity in normal direction	2504 N	2509 N
	R_t	Load capacity in shear direction	4467 N	4360 N
	β_1	Exponent controlling shape of force interaction curve	1.3	1.25
	R_0	User parameter in hardening term (defined by authors)	0.692765	0.50829
	Q_1	User parameter in hardening term (defined by authors)	0.45	0.87
	θ_1	User parameter in hardening term (defined by authors)	0.000358 $\text{N}^{-1}\text{mm}^{-1}$	0.000325 $\text{N}^{-1}\text{mm}^{-1}$
	$\bar{u}_0^{\text{pl}}(90°)$	Plastic relative damage initiation displacement in tension	6656 Nmm	5078 Nmm
	$\bar{u}_0^{\text{pl}}(10°)$	Plastic relative damage initiation displacement in mixed loading	16182 Nmm	10485 Nmm
	$\bar{u}_0^{\text{pl}}(0°)$	Plastic relative damage initiation displacement in shear	9857 Nmm	31472 Nmm
	$\bar{u}_f^{\text{pl}}(90°)$	Plastic relative failure displacement in tension	2144 Nmm	4845 Nmm
	$\bar{u}_f^{\text{pl}}(10°)$	Plastic relative failure displacement in mixed loading	1228 Nmm	25889 Nmm
	$\bar{u}_f^{\text{pl}}(0°)$	Plastic relative failure displacement in shear	11506 Nmm	73277 Nmm
Constraint model 3	E	Elastic stiffness	9000 N/mm	9000 N/mm
	r	Radius of influence	3.2 mm	5.0 mm
	R_n	Load capacity in normal direction	2504 N	2509 N
	R_t	Load capacity in shear direction	4467 N	4360 N
	β_1	Exponent controlling shape of force interaction curve	1.3	1.4
	R_0	User parameter in hardening term (defined by authors)	0.692765	0.50829
	Q_1	User parameter in hardening term (defined by authors)	0.45	0.87
	θ_1	User parameter in hardening term (defined by authors)	0.000358 $\text{N}^{-1}\text{mm}^{-1}$	0.000325 $\text{N}^{-1}\text{mm}^{-1}$
	$\bar{u}_{0,t}^{\text{pl}}$	Plastic relative damage initiation displacement in tension	5808 Nmm	5520 Nmm
	$\bar{u}_{0,s}^{\text{pl}}$	Plastic relative damage initiation displacement in shear	8711 Nmm	34640 Nmm
	β_2	Exponent controlling shape of damage initiation interaction curve	2.0	2.0
	$\bar{u}_{f,t}^{\text{pl}}$	Plastic relative failure displacement in tension	6000 Nmm	8921 Nmm
	$\bar{u}_{f,s}^{\text{pl}}$	Plastic relative failure displacement in shear	21251 Nmm	98076 Nmm
	β_3	Exponent controlling shape of failure interaction curve	10.1	1.546

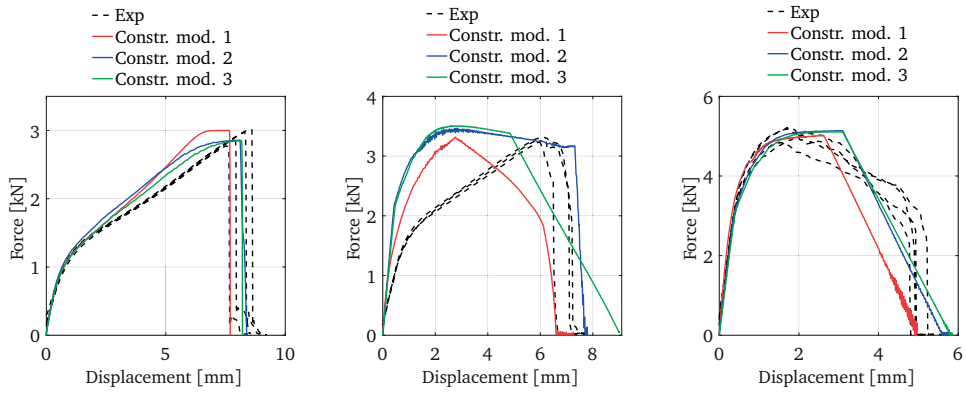

Fig. 18. Results from the calibration of the constraint-based models to cross tests for the small screw connection. (a) Cross tension. (b) Cross mixed. (c) Cross shear.

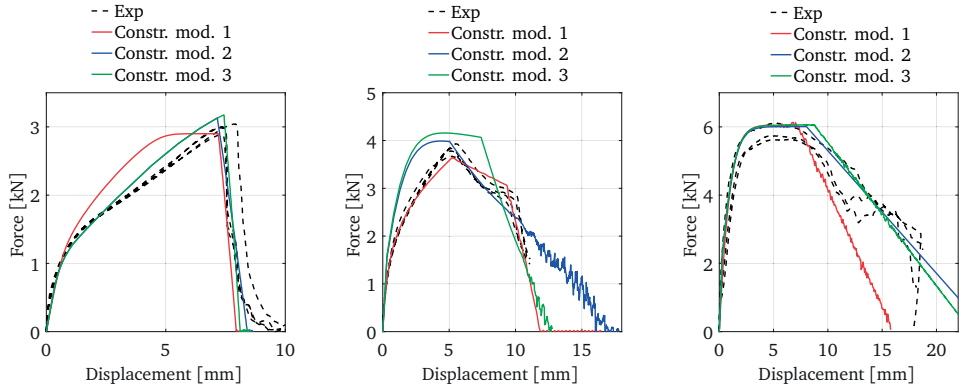

Fig. 19. Results from the calibration of the constraint-based models to cross tests for the large screw connection. (a) Cross tension. (b) Cross mixed. (c) Cross shear.

tension and shear for both connections for all three models. The initial stiffness, maximum force, ductility and overall shape of the curves were well captured. Some discrepancies are observed in the damage part in shear because all of the models predict linear softening in pure shear.

Under mixed mode loading, larger differences were observed. Consider the small screw connection (Fig. 18b). *Constraint model 1* over-estimated the initial stiffness and force level before maximum force. Softening was initiated too early, but the model was flexible enough to correctly capture the displacement at failure. The initial stiffness and force level before maximum force were also over-estimated by *constraint model 2* and *constraint model 3*. For *constraint model 2*, good agreement was achieved for the damage part, whereas damage was initiated too early and failure occurred too late for *constraint model 3*. The level of maximum force was also relatively well captured by all of the models in mixed mode.

For the large screw connection under mixed mode loading (Fig. 19b), a relatively good fit was achieved by all of the models. Excellent agreement was obtained with *constraint model 1*. The force prior to maximum force was over-estimated by *constraint model 2* and *constraint model 3*.

No significant difference was observed between the computational times for the three constraint-based models. These simulations were, however, faster than the simulations with the element-based models. The presence of the connection models did not alter the critical time step.

5.2.1 Definition of mode mixity angle

At this point, it is worthwhile to discuss some points associated with the mode mixity angle definition in *constraint model 2* and *constraint model 3*. Recall that for these models, the mode mixity angle θ is defined as a function of the ratio of forces (see Eqs. (A.16) and (A.20)). This way of defining θ resulted in some challenges associated with calibration. When simulating the cross tension and cross shear tests, θ was, as expected, close to 90° and 0°, respectively. During the cross mixed simulations, however, θ varied between 5° and 20° due to varying forces for both connections. This had different implications on the calibration of the damage part for *constraint model 2* and *constraint model 3*, as explained in the following.

Recall that for *constraint model 2*, the relative plastic motions at damage initiation and failure, $\bar{u}_0^{\text{pl}}(\theta)$ and $\bar{u}_f^{\text{pl}}(\theta)$, must be tabulated by the user. Each of the three calibration tests provides one point in each tabulated function. Values were obtained for $\theta = 90°$ and $\theta = 0°$ by reverse engineering the cross tension and cross shear tests, respectively. However,

because θ varied between 5° and 20° during the cross mixed simulations, a compromise had to be made, and data points associated with the cross mixed tests were tabulated for $\theta = 10°$. Furthermore, to capture the damage behaviours observed in the tests, the relative plastic motions at damage initiation and failure in shear ($\theta = 0°$) had to be different from mixed mode ($\theta = 10°$). Consequently, the relative plastic motions at damage initiation and failure were very sensitive to variations in θ for low values of θ (close to pure shear). This is illustrated in Fig. 20a, which shows two possible interaction curves for relative plastic motions at damage initiation and failure. The axes are labelled with both $\bar{u}_0^{\text{pl}}$ and $\bar{u}_f^{\text{pl}}$ to indicate that this challenge occurs for both the damage initiation and failure curves. In the dashed curve, the values in shear are larger than the values in mixed mode, and in the solid curve, the values in mixed mode are larger. For both cases, a small variation in θ close to $\theta = 0°$ leads to a large variation in the values of $\bar{u}_0^{\text{pl}}(\theta)$ and $\bar{u}_f^{\text{pl}}(\theta)$. Consequently, if the mode mixity angle in a simulation varies from 0° to 10°, the response quickly changes from that of cross shear to that of cross mixed. This was indeed the case for the single lap joint simulations, as will be discussed in Section 5.3.

For *constraint model 3*, damage initiation and failure displacements are given by the interaction formulas in Eqs. (A.18) and (A.19). These formulas include parameters for relative displacement at damage initiation and failure in pure tension and pure shear, which were found by reverse engineering the cross tension and cross shear tests, respectively. The

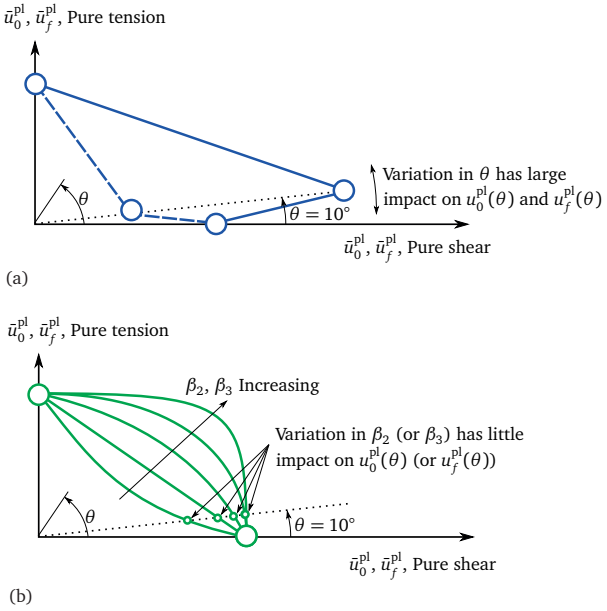

Fig. 20. Conceptual illustrations of normal-tangential interaction curves for $\bar{u}_0^{\text{pl}}(\theta)$ and $\bar{u}_f^{\text{pl}}(\theta)$ to illustrate challenges with mode mixity angle θ defined by forces. (a) *Constraint model 2*. Blue circles indicate the tabulated points, and the two lines indicate two possible interaction curves. (b) *Constraint model 3*. Green circles represent the values in pure tension and pure shear.

interaction curves are super-ellipses, whose shapes are determined by the exponents β_2 and β_3, which were calibrated by reverse engineering the cross mixed tests. However, because the mode mixity angle in the cross mixed simulation was so close to pure shear, different values of the exponents had little impact on the response in this simulation, as illustrated in Fig. 20b. As shown, the values of $\bar{u}_0^{\text{pl}}$ and $\bar{u}_f^{\text{pl}}$ in the cross mixed simulation were more or less locked to the value in pure shear. The mixed mode flexibility of this model could therefore not be fully utilised. This is believed to be the reason why softening was poorly represented by this model in the cross mixed simulations (Figs. 18b and 19b).

A remedy to these challenges could be to introduce additional calibration tests with mode mixities further away from pure shear. However, from an industry perspective, it is desirable to keep the number of tests as low as possible to minimise the costs. Additionally, several validation tests are needed for robustness of the validation procedure. Therefore, the number of calibration tests was limited to three in this work. As an example, Bier and Sommer [10] used five different tests for calibration and one for validation.

In *constraint model 1*, the mode mixity angle is defined as a function of the stretches (Eq. (A.10)). With this definition, the mode mixity angles in the simulations were close to the global loading angle in the tests (90°, 45° and 0° for cross tension, mixed and shear, respectively). Thus, the challenges associated with the calibration of *constraint model 2* and *constraint model 3* did not arise for this model. Higher flexibility was obtained in the cross mixed simulations, and the model was easier to calibrate.

5.2.2 Influence of relative rotation angle ω_b

To account for the relative rotation between the sheets, *constraint model 2* and *constraint model 3* utilise the relative rotation angle ω_b (Eq. (A.12)). The influence of the relative rotation is adjusted by user parameters (see Eqs. (A.14) and (A.17) to (A.19)). However, the influence of the relative rotation was set to zero in this work. The reason for this choice is two-fold.

First, to calibrate the influence parameters, experimental tests with significant relative sheet rotations are needed. Thus, additional calibration tests are required, which is undesirable from a cost perspective. Bier and Sommer [10] proposed calibrating the influence parameters using peeling tests. However, this approach is also undesirable because it will remove a validation test and thus weaken the validation strategy.

Second, the only simulation that would be affected by including the influence of relative rotation in this work is the peeling simulation. In all other simulations, the relative rotation between the sheets is negligible. As will be shown in Section 5.3, the results of the peeling

simulations are already satisfactory without the influence of relative rotation.

5.3 Validation of constraint-based models

For the calibration simulations, the choice of constraint-based model had no significant influence on the computational time of the validation simulations. The numerical and experimental results from the validation tests (single lap joint, peeling and T-component) for the two connections are presented in Figs. 21 and 22, respectively.

For the single lap joint tests (Figs. 21a and 22a), *constraint model 1* provided good predictions for both connections. The force level and the softening were well captured. For the small screw connection, the initial stiffness was somewhat under-estimated by all models. The force level and softening were poorly described by *constraint model 2* and *constraint model 3* for both connections. This result may be explained by the challenges associated with the mode mixity definition (see Section 5.2.1). Recall that the mode mixity angle in the cross mixed simulations ranged between 5° and 20° and that the models were therefore calibrated to the cross mixed results for this angle. However, in the single lap joint simulations the mode mixity angle also varied between 5° and 20°. Consequently, the damage evolution of *constraint model 2* and *constraint model 3* could not discern between cross mixed and single lap joint simulations, even though the physical behaviours in the tests were different. This becomes clear when comparing Figs. 21a and 22a with Figs. 18b and 19b. As shown in these figures, the responses are similar. This clearly demonstrates the challenge with the mode mixity angle defined by resultant forces.

Acceptable fits were obtained in the peeling simulations (Figs. 21b and 22b). For the small screw connection, the force levels before maximum force were in good agreement with the experiments. The maximum force was over-predicted by all models, which was caused by over-predicting the ductility. For the large screw connection, the maximum force was under-predicted by all models. As explained in Section 2, rotation of the screw caused the screw tail to come into contact with the extruded plate, thereby causing the higher force slope occurring at approximately 2 kN (see Fig. 22b). This physical effect cannot be captured by the investigated models; thus, the under-prediction of the maximum force was expected. The displacement at failure was over-predicted by *constraint model 1*, whereas *constraint model 2* and *constraint model 3* were in good agreement with the experiments for this part.

Generally good predictions of the maximum force level were achieved for all models in the T-component simulations. For the small screw connection, *constraint model 2* over-estimated the maximum force, and all models over-estimated the ductility (Fig. 21c). A

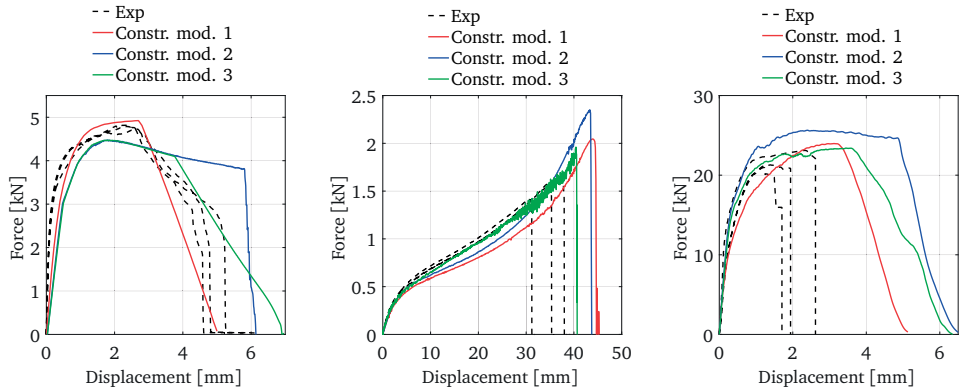

Fig. 21. Validation results for the small screw connection. (a) Single lap joint. (b) Peeling. (c) T-component.

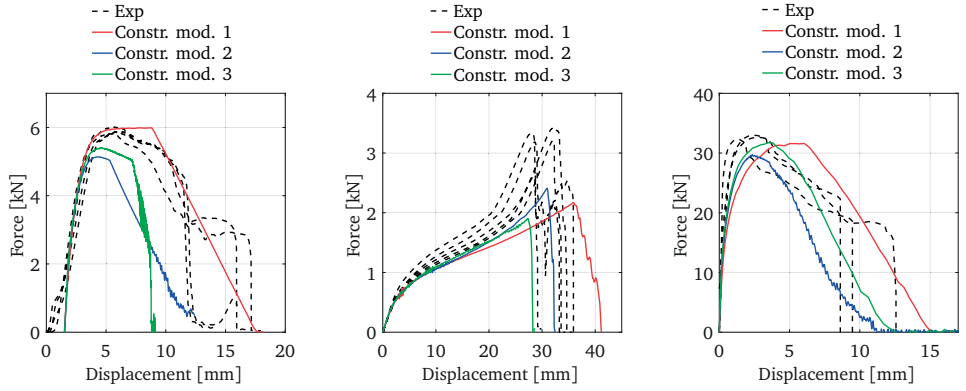

Fig. 22. Validation results for the large screw connection. (a) Single lap joint. (b) Peeling. (c) T-component.

possible explanation for the latter is the abrupt fracture behaviour that was observed in the T-component tests but not in the cross shear tests. For the large screw connection (Fig. 22c), good agreement between the simulations and experiments was obtained. *Constraint model 2* under-estimated the maximum force level by a small fraction, and *constraint model 1* slightly over-estimated the ductility.

By comparing the T-component simulations (Figs. 21c and 22c) with the cross mixed (Figs. 18b and 19b) and the single lap joint simulations (Figs. 21a and 22a), similarities are observed in the shapes of the curves, particularly in the softening parts. This result may indicate that the T-component simulations were also affected by the problem of the mode mixity definition. This is supported by the fact that the mode mixity angle for the connections varied between 0° and 25° in the simulations.

In summary, of the five connection models investigated, *constraint model 1* appears to be the most suited for modelling flow-drill screw connections. This model appears to be the most robust, providing the most accurate reproduction of the calibration and validation tests for both connections. Furthermore, this model was the easiest to calibrate. The challenges discussed in this section demonstrate that it is indeed important to have a proper validation strategy in which the models are challenged in different ways than in the calibration tests.

5.4 Static vs. dynamic problems

As all tests in this work were quasi-static, the discussed modelling techniques have been assessed for static problems. Currently there is a lack of published experimental data from dynamic testing of FDS connections. Whether or not the modelling techniques presented here are applicable to dynamic problems is therefore an open question. However, Porcaro et al. [19] performed dynamic tests of a self-piercing rivet connection under tension and shear, and observed no significant rate-effect on the resulting force-displacement curves or failure modes. Furthermore, Sønstabø et al. [12] showed that self-piercing rivet connections and FDS connections behave in a similar way. Considering the observed similarities, and the fact that the aluminium alloys used in this work exhibit insignificant strain-rate dependence, it is believed that the obtained model parameters are usable for the dynamic regime as well as the static.

6 Conclusions

Five different macroscopic models were evaluated for modelling flow-drill screw connections in thin-walled aluminium structures. These models were calibrated to cross tests and validated first with single lap joint and peeling tests and then with T-component tests. The following main conclusions may be drawn from the present investigation:

- A two-step validation strategy for modelling flow-drill screw connections was presented and used. The validation consisted of benchmark and peeling tests. The validation results demonstrated the need to have a proper validation strategy.
- Of the investigated models, *constraint model 1* was the most suitable for describing flow-drill screw connections. This model provided the best results and was the easiest to calibrate.
- The two element-based models were not sufficiently flexible to represent the cross mixed tests and were thus not validated.
- The definition of the mode mixity angle as a function of forces in *constraint model 2* and *constraint model 3* was a challenge for modelling flow-drill screw connections.

Appendix A Details of macroscopic models

A.1 Element model 2

This is the cohesive element model presented by Marzi et al. [7].

The tri-linear stress-separation curves for pure normal and pure shear loadings are presented in Fig. 13a. The shapes of the curves are defined by user parameters as follows. The total area (energy) under the curves is defined by G_n and G_t. Henceforth, the subscripts n and t denote pure normal and pure tangential loadings, respectively. The elastic stiffnesses E_n and E_t are calculated by

$$E_n = \frac{E}{t}$$
$$E_t = \frac{G}{t},$$

where E and G are the Young's and shear moduli provided by the user and t is the thickness of the cohesive element. The yield stresses N and T are defined by the user. The last parameters needed for defining the shape of the stress-separation curves are the areas under

the plastic parts, given as fractions f_{Gn} and f_{Gt} of the total areas. That is,

$$0 \leq f_{Gn} = \frac{G_n^p}{G_n} < 1 - \frac{N^2}{2G_nE_n}$$
$$0 \leq f_{Gt} = \frac{G_t^p}{G_t} < 1 - \frac{T^2}{2G_tE_t}.$$

The plastic areas G_n^p and G_t^p cannot include the elastic areas (hence the right inequalities).

The yield initiation displacements δ_{n1} and δ_{t1} may now be calculated as

$$\delta_{n1} = \frac{N}{E_n}$$
$$\delta_{t1} = \frac{T}{E_t}.$$

The yield initiation displacement in mixed mode, δ_{m1}, is calculated using a quadratic interaction formula as follows,

$$\delta_{m1} = \delta_{n1}\delta_{t1}\sqrt{\frac{1+\beta^2}{\delta_{t1}^2 + (\beta\delta_{n1})^2}},$$

where

$$\beta = \frac{\Delta_t}{\Delta_n}.$$

Note that there is a mistake in the definition of β in the references [4, 7]. The above definition is correct.

Similarly, the mixed-mode damage initiation displacement is defined as

$$\delta_{m2} = \delta_{n2}\delta_{t2}\sqrt{\frac{1+\beta^2}{\delta_{t2}^2 + (\beta\delta_{n2})^2}},$$

where

$$\delta_{n2} = \delta_{n1} + \frac{f_{Gn}G_n}{N}$$
$$\delta_{t2} = \delta_{t1} + \frac{f_{Gt}G_t}{T}.$$

The failure displacement in mixed mode, δ_{mf}, is defined as (see the paper of Marzi et al.

[7] for explanation)

$$\delta_{mf} = \frac{\delta_{m1}\left(\delta_{m1}-\delta_{m2}\right)E_n G_t \cos^2\theta + G_n\left(2G_t + \delta_{m1}(\delta_{m1}-\delta_{m2})E_t \sin^2\theta\right)}{\delta_{m1}\left(E_n G_t \cos^2\theta + E_t G_n \sin^2\theta\right)},$$

where

$$\theta = \arccos\frac{\langle u_n\rangle}{\Delta_m}.$$

With this, the shape of the mixed-mode stress-separation curve is determined (see Fig. 13b), and the stresses may be calculated, as shown in the following. Let u_n, u_{t1} and u_{t2} denote the element's relative displacements in the normal and in both tangential directions of the element coordinate system in the mid-plane. Then, the two separations Δ_n in the normal direction and Δ_t in the shear direction are defined as follows,

$$\Delta_n = \max(u_n, 0)$$
$$\Delta_t = \sqrt{u_{t1}^2 + u_{t2}^2}.$$

The total separation (mixed mode) Δ_m is further defined as

$$\Delta_m = \sqrt{\Delta_n^2 + \Delta_t^2}.$$

The plastic separations in each element direction, u_n^p, u_{t1}^p and u_{t2}^p, may now be calculated. In the normal direction, the plastic separation is given by

$$u_n^p = \max\left(u_{n,\Delta t-1}^p, u_n - \delta_{m1}\cos\theta, 0\right),$$

where the subscript $\Delta t-1$ denotes the variable at the previous time step. Thus, if plasticity occurs, the plastic normal separation is equal to the total normal separation minus the elastic part. If loading is purely elastic, then the plastic normal separation remains zero or equal to the value at the previous time step.

For the shear direction, a shear yield separation δ_{ty} is defined as

$$\delta_{ty} = \sqrt{\left(u_{t1} - u_{t1,\Delta t-1}^p\right)^2 + \left(u_{t2} - u_{t2,\Delta t-1}^p\right)^2}.$$

If $\delta_{ty} > \delta_{m1}\sin\theta$, then plasticity occurs, and u^p_{t1} and u^p_{t2} are updated according to

$$u^p_{t1} = u^p_{t1,\Delta t-1} + \left(u_{t1} - u_{t1,\Delta t-1}\right)$$
$$u^p_{t2} = u^p_{t2,\Delta t-1} + \left(u_{t2} - u_{t2,\Delta t-1}\right).$$

If $\Delta m > \delta_{m2}$, then a damage variable d increases linearly,

$$d = \max\left(\frac{\Delta_m - \delta_{m2}}{\delta_{mf} - \delta_{m2}}, d_{\Delta t-1}, 0\right).$$

When d reaches unity, damage is complete and the integration point fails.

The stresses in the element coordinate system may now be calculated. In the normal direction, damage is only considered under tensile loading. That is, if $u_n - u^p_n < 0$,

$$\sigma_n = E_n\left(u_n - u^p_n\right);$$

otherwise,

$$\sigma_n = E_n(1-d)\left(u_n - u^p_n\right).$$

The shear stresses are

$$\sigma_{t1} = E_t(1-d)\left(u_{t1} - u^p_{t1}\right)$$
$$\sigma_{t2} = E_t(1-d)\left(u_{t2} - u^p_{t2}\right).$$

Rate dependency may be included, but it was not considered in this work.

A.2 Constraint model 1

This model was originally developed by Hanssen et al. [8] for self-piercing rivet connections.

The kinematics of the model are shown in Fig. A.1a. All considerations of the model are performed in the so-called plane of maximum opening, which is defined by the normal vector

$$\mathbf{n}_0 = \mathbf{n}_s \times \mathbf{n}_m, \tag{A.4}$$

where $\mathbf{n}_s$ and $\mathbf{n}_m$ are the unit normal vectors of the slave and master sheets, respectively.

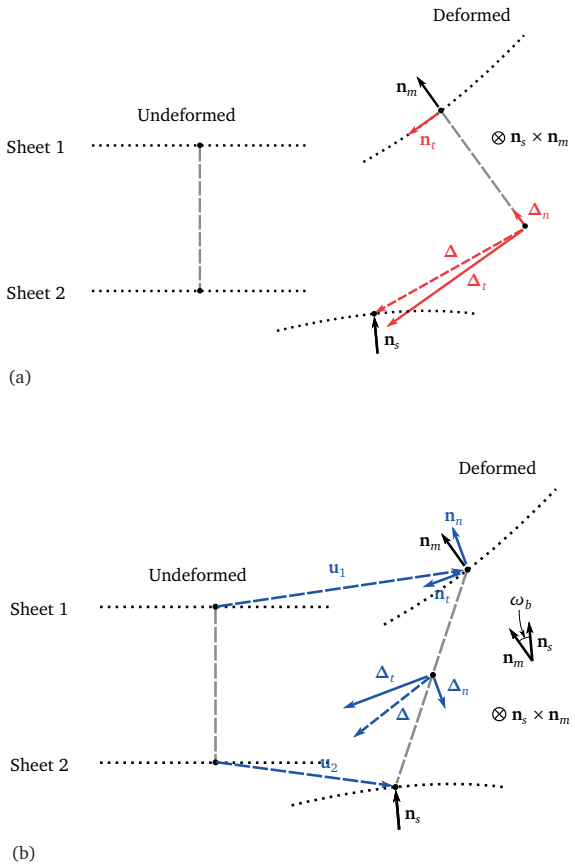

Fig. A.1. Illustration of kinematics of (a) *constraint model 1* and (b) *constraint model 2* and *constraint model 3*.

The tangential unit vector of the rivet is defined by

$$\mathbf{n}_t = \mathbf{n}_0 \times \mathbf{n}_m. \tag{A.5}$$

It is assumed that the rivet is following the motion of the master sheet (see Fig. A.1a). The local deformation of the rivet is given by the normal stretch vector $\boldsymbol{\Delta}_n$ and the tangential stretch vector $\boldsymbol{\Delta}_t$. Total stretch $\boldsymbol{\Delta} = \boldsymbol{\Delta}_n + \boldsymbol{\Delta}_t$ is defined as the vector between the slave end and its original location on the deformed slave sheet (see Fig. A.1a), from which the scalar normal and tangential stretches may be computed as

$$\begin{aligned} \Delta_n &= |\boldsymbol{\Delta} \cdot \mathbf{n}_m| \\ \Delta_t &= |\boldsymbol{\Delta} \cdot \mathbf{n}_t|\,. \end{aligned} \tag{A.6}$$

The model calculates the normal and tangential forces, f_n and f_t, based on the deformation and deformation history of the rivet, as explained in the following.

The normal and tangential forces are calculated according to

$$f_n = \frac{f_n^{\max}\Delta_n}{\eta_{\max}\Delta_n^{\text{fail}}}\hat{f}_n(\eta_{\max}) \tag{A.7}$$

$$f_t = \frac{f_t^{\max}\Delta_t}{\eta_{\max}\Delta_t^{\text{fail}}}\hat{f}_t(\eta_{\max}), \tag{A.8}$$

where

$$\hat{f}_n(\eta_{\max}) = \begin{cases} 1-\left(\dfrac{\xi_n-\eta_{\max}}{\xi_n}\right)^8 & \eta_{\max} \le \xi_n \\ 1-\dfrac{\eta_{\max}-\xi_n}{1-\xi_n} & \eta_{\max} > \xi_n \end{cases}$$

$$\hat{f}_t(\eta_{\max}) = \begin{cases} 1-\left(\dfrac{\xi_t-\eta_{\max}}{\xi_t}\right)^8 & \eta_{\max} \le \xi_t \\ 1-\dfrac{\eta_{\max}-\xi_t}{1-\xi_t} & \eta_{\max} > \xi_t \end{cases}.$$

The parameters $f_n^{\max}$, $f_t^{\max}$, Δ_n^{fail}, Δ_t^{fail}, ξ_n and ξ_t are determined by the user, and $\eta_{\max}$ is defined as

$$\eta_{\max} = \max(\eta(t)).$$

The effective displacement measure $\eta(t)$ is defined by a scaled interaction formula as follows,

$$\eta(\theta, \eta_{\max}, t) = \left[\xi(\theta) + \frac{1-\xi(\theta)}{\alpha(\eta_{\max})}\right]\sqrt{\left(\frac{\Delta_n(t)}{\Delta_n^{\text{fail}}}\right)^2 + \left(\frac{\Delta_t(t)}{\Delta_t^{\text{fail}}}\right)^2}, \tag{A.9}$$

where θ is the mode mixity angle defined by the kinematical motion (stretches) as

$$\theta = \arctan\left(\frac{\Delta_n}{\Delta_t}\right). \tag{A.10}$$

The scaling factor in Eq. (A.9) contains the parameter $\xi(\theta)$, which scales the effective displacement as a function of the mode mixity angle according to the polynomial

$$\xi(\theta) = 1 - \frac{27}{4}\left(\frac{2\theta}{\pi}\right)^2 + \frac{27}{4}\left(\frac{2\theta}{\pi}\right)^3.$$

The parameter $\alpha(\eta_{\max})$ is included in Eq. (A.9) to allow the directional scaling of the

effective displacement to be damage dependent, and it is defined as follows,

$$\alpha(\eta_{\max}) = \begin{cases} \dfrac{\xi_t - \eta_{\max}}{\xi_t}\alpha_1 + \dfrac{\eta_{\max}}{\xi_t}\alpha_2 & \eta_{\max} < \xi_t \\ \dfrac{1-\eta_{\max}}{1-\xi_t}\alpha_2 + \dfrac{\eta_{\max}-\xi_t}{1-\xi_t}\alpha_3 & \eta_{\max} \geq \xi_t \end{cases},$$

where α_1, α_2 and α_3 are user parameters.

After the forces have been determined using Eqs. (A.7) and (A.8), the moments at the master and slave ends, M_m and M_s, respectively, are calculated using the relations

$$M_m = \begin{cases} \dfrac{h_m + h_s}{4} f_t & \eta_{\max} < \xi_t \\ \dfrac{h_m + h_s}{4}\left(1 + \dfrac{\eta_{\max}-\xi_t}{1-\xi_t}\right) f_t & \eta_{\max} \geq \xi_t \end{cases}$$

$$M_s = \begin{cases} \dfrac{h_m + h_s}{4} f_t & \eta_{\max} < \xi_t \\ \dfrac{h_m + h_s}{4}\left(1 - \dfrac{\eta_{\max}-\xi_t}{1-\xi_t}\right) f_t & \eta_{\max} \geq \xi_t \end{cases},$$

where h_m and h_s are the thicknesses of the master and slave sheet, respectively. Moment balance is thus satisfied.

To summarise, six parameters are required to define the behaviour in pure tension ($f_n^{\max}$, Δ_n^{fail}, and ξ_n) and pure shear ($f_t^{\max}$, Δ_t^{fail}, and ξ_t). Flexibility in mixed mode is obtained with the three parameters α_1, α_2 and α_3. In addition, the radius of influence r, within which the forces and moments are lumped to the nodes on each shell surface, must be specified (see Fig. 1e).

A.3 Constraint model 2

This is the model *constrained interpolation spotweld* available in LS-DYNA® [4].

The kinematics of this model are different than *constraint model 1*, as shown in Fig. A.1b. As for *constraint model 1*, all considerations are performed in the plane of maximum opening (Eq. (A.4)). The connection is, however, treated symmetrically, which means that the rivet is not following the master sheet. Rather, a unit vector defines the direction of normal loads as the average of the unit normals of the sheets (see Fig. A.1b),

$$\mathbf{n}_n = \frac{\mathbf{n}_m + \mathbf{n}_s}{|\mathbf{n}_m + \mathbf{n}_s|}. \tag{A.11}$$

The corresponding tangential direction is given by

$$\mathbf{n}_t = \mathbf{n}_0 \times \mathbf{n}_n.$$

The total stretch $\boldsymbol{\Delta}$ is defined here as the relative displacement between the two sheets (see Fig. A.1b),

$$\boldsymbol{\Delta} = \mathbf{u}_2 - \mathbf{u}_1,$$

where $\mathbf{u}_1$ and $\mathbf{u}_2$ are the displacement vectors of the two sheets. The scalar normal and tangential stretches may then be calculated as

$$\begin{aligned} \Delta_n &= |\boldsymbol{\Delta} \cdot \mathbf{n}_n| \\ \Delta_t &= |\boldsymbol{\Delta} \cdot \mathbf{n}_t| \,. \end{aligned}$$

To capture the relative rotation between the sheets, a third kinematical quantity ω_b is defined as the angle between the shell normals in the plane of maximum opening (see Fig. A.1b),

$$\omega_b = \arccos \frac{\mathbf{n}_s \cdot \mathbf{n}_m}{|\mathbf{n}_s|\,|\mathbf{n}_m|}. \tag{A.12}$$

The corresponding forces f_n and f_t and the moment m_b are calculated in an elastic-plastic manner, with a stiffness E, a yield function, a flow rule and a hardening rule. Linear mode mixity-dependent damage is incorporated. An effective elastic force vector is defined as

$$\tilde{\mathbf{f}} = [f_n, f_t, m_b] = E\,[\Delta_n, \Delta_t, \omega_b] = E\mathbf{u}.$$

The yield function is defined as

$$\phi\left(\tilde{\mathbf{f}}, \bar{u}^{\mathrm{pl}}\right) = P\left(\tilde{\mathbf{f}}\right) - F^0\left(\bar{u}^{\mathrm{pl}}\right) \leq 0, \tag{A.13}$$

where the potential $P\left(\tilde{\mathbf{f}}\right)$ is defined as

$$P\left(\tilde{\mathbf{f}}\right) = \left[\left(\frac{f_n + \alpha_1 m_b}{R_n}\right)^{\beta_1} + \left(\frac{f_t}{R_t}\right)^{\beta_1}\right]^{\frac{1}{\beta_1}}. \tag{A.14}$$

The parameters R_n, R_t, β_1 and α_1 are determined by the user. Furthermore, associated flow

is assumed such that the rate of plastic relative motion $\dot{\mathbf{u}}^{\text{pl}}$ is defined as

$$\dot{\mathbf{u}}^{\text{pl}} = \dot{\bar{u}}^{\text{pl}} \frac{\partial \phi}{\partial \tilde{\mathbf{f}}}.$$

Here, $\dot{\bar{u}}^{\text{pl}}$ is the plastic multiplier, which must be non-negative to ensure non-negative plastic dissipation. The equivalent plastic relative motion $\bar{u}_{\text{pl}}$ is then defined as

$$\bar{u}^{\text{pl}} = \int_0^t \dot{\bar{u}}^{\text{pl}} \mathrm{d}t,$$

and is thus positive and always increasing with plasticity (it serves the same function as the equivalent plastic strain in regular plasticity theory). Note that $\bar{u}^{\text{pl}}$ has units of force times length.

Analogous to regular plasticity theory, loading/unloading conditions may be summarised as

$$\begin{aligned} \phi &\leq 0 \\ \dot{\bar{u}}^{\text{pl}} &\geq 0 \\ \dot{\bar{u}}^{\text{pl}} \phi &= 0, \end{aligned}$$

and the consistency condition states that

$$\dot{\bar{u}}^{\text{pl}} \dot{\phi} = 0.$$

The term $F^0\left(\bar{u}^{\text{pl}}\right)$ in Eq. (A.13) is an isotropic hardening function defined by the user, and in this work, it was defined as a Voce-like function as follows,

$$F^0\left(\bar{u}^{\text{pl}}\right) = R_0 + Q_1 \left(1 - \exp\left(-\frac{\theta_1}{Q_1} \bar{u}^{\text{pl}}\right)\right).$$

where R_0, Q_1 and θ_1 are user parameters.

The nominal force vector $\mathbf{f}$ is scaled by a damage variable as follows,

$$\mathbf{f} = (1 - d)\,\tilde{\mathbf{f}},$$

where

$$d = \begin{cases} 0 & \bar{u}^{\mathrm{pl}} < \bar{u}_0^{\mathrm{pl}}(\theta) \\ \dfrac{\bar{u}^{\mathrm{pl}} - \bar{u}_0^{\mathrm{pl}}(\theta)}{\bar{u}_f^{\mathrm{pl}}(\theta)} & \bar{u}^{\mathrm{pl}} \geq \bar{u}_0^{\mathrm{pl}}(\theta) \end{cases}. \tag{A.15}$$

Here, $\bar{u}_0^{\mathrm{pl}}(\theta)$ is the plastic relative motion at damage initiation and $\bar{u}_0^{\mathrm{pl}}(\theta) + \bar{u}_f^{\mathrm{pl}}(\theta)$ is the plastic relative motion at failure. They are defined by the user as tabulated functions of the mode mixity angle θ, which is defined in terms of resultant forces as follows,

$$\theta = \arctan\left(\frac{f_n + \alpha_1 m_b}{f_t}\right). \tag{A.16}$$

Thus, the parameters that must be determined by the user are E, R_n, R_t, β_1 and α_1; the functions $\bar{u}_0^{\mathrm{pl}}(\theta)$ and $\bar{u}_f^{\mathrm{pl}}(\theta)$; the radius of influence r; and the hardening parameters R_0, Q_1 and θ_1. In this work, α_1 was set to zero.

A.4 Constraint model 3

Bier and Sommer [10] presented some modifications to constraint model 2. The differences are addressed in the following.

First, the relative rotation angle ω_b is omitted from the vector of relative motion $\mathbf{u}$,

$$\mathbf{u} = [\Delta_n, \Delta_t],$$

and the corresponding force vector is given by

$$\mathbf{f} = [f_n, f_t].$$

The relative rotation angle is instead included in the potential in Eq. (A.13) as follows,

$$P\left(\tilde{\mathbf{f}}\right) = \left[\left(\frac{f_n}{R_n(1-\alpha_1\omega_b)}\right)^{\beta_1} + \left(\frac{f_t}{R_t}\right)^{\beta_1}\right]^{\frac{1}{\beta_1}}. \tag{A.17}$$

Second, the calculation of damage initiation and failure is performed differently. The damage variable is defined by Eq. (A.15), but $\bar{u}_0^{\mathrm{pl}}(\theta)$ and $\bar{u}_f^{\mathrm{pl}}(\theta)$ are determined by solving

the following system of six equations

$$\left[\left(\frac{\bar{u}_0^{\mathrm{pl},n}}{\bar{u}_{0,\mathrm{ref}}^{\mathrm{pl},n}(1-\alpha_2\omega_b)}\right)^{\beta_2}+\left(\frac{\bar{u}_0^{\mathrm{pl},t}}{\bar{u}_{0,\mathrm{ref}}^{\mathrm{pl},t}}\right)^{\beta_2}\right]^{\frac{1}{\beta_2}}=1 \tag{A.18}$$

$$\bar{u}_0^{\mathrm{pl},n}=\sin(\theta)\,\bar{u}_0^{\mathrm{pl}}$$
$$\bar{u}_0^{\mathrm{pl},t}=\cos(\theta)\,\bar{u}_0^{\mathrm{pl}}$$

$$\left[\left(\frac{\bar{u}_f^{\mathrm{pl},n}}{\bar{u}_{f,\mathrm{ref}}^{\mathrm{pl},n}(1-\alpha_3\omega_b)}\right)^{\beta_3}+\left(\frac{\bar{u}_f^{\mathrm{pl},t}}{\bar{u}_{f,\mathrm{ref}}^{\mathrm{pl},t}}\right)^{\beta_3}\right]^{\frac{1}{\beta_3}}=1 \tag{A.19}$$

$$\bar{u}_f^{\mathrm{pl},n}=\sin(\theta)\,\bar{u}_f^{\mathrm{pl}}$$
$$\bar{u}_f^{\mathrm{pl},t}=\cos(\theta)\,\bar{u}_f^{\mathrm{pl}}.$$

Here, $\bar{u}_{0,\mathrm{ref}}^{\mathrm{pl},n}$, $\bar{u}_{0,\mathrm{ref}}^{\mathrm{pl},t}$, $\bar{u}_{f,\mathrm{ref}}^{\mathrm{pl},n}$, $\bar{u}_{f,\mathrm{ref}}^{\mathrm{pl},t}$, α_2 and α_3 are parameters determined by the user, and the mode mixity angle θ is defined as

$$\theta=\arctan\left(\frac{f_n}{f_t}\right). \tag{A.20}$$

Eqs. (A.18) and (A.19) are super-ellipses that provide the normal-tangential interaction between $\bar{u}_0^{\mathrm{pl},n}$ and $\bar{u}_0^{\mathrm{pl},t}$ and between $\bar{u}_f^{\mathrm{pl},n}$ and $\bar{u}_f^{\mathrm{pl},t}$ in the plastic relative displacement plane.

The parameters that must be determined from experiments are thus E, R_n, R_t, β_1, α_1, $\bar{u}_{0,\mathrm{ref}}^{\mathrm{pl},n}$, $\bar{u}_{0,\mathrm{ref}}^{\mathrm{pl},t}$, $\bar{u}_{f,\mathrm{ref}}^{\mathrm{pl},n}$, $\bar{u}_{f,\mathrm{ref}}^{\mathrm{pl},t}$, β_2, β_3, α_2, α_3 and the radius of influence r, in addition to the hardening parameters R_0, Q_1 and θ_1. The parameters α_1, α_2 and α_3 were set to zero in this work.

References

[1] Malcolm, S. and Nutwell, E. "Spotweld failure prediction using solid element assemblies". *6th European LS-Dyna users conference. Gothenburg, Sweden*. 2007. http://www.dynalook.com/european-conf-2007/spotweld-failure-prediction-using-solid-element.pdf.

[2] Yamashita, M., Kenmotsu, H., and Hattori, T. "Dynamic crush behavior of adhesive-bonded aluminum tubular structureExperiment and numerical simulation". *Thin-Walled Structures* 69 (2013), pp. 45–53. https://doi.org/10.1016/j.tws.2013.04.005.

[3] Carlberger, T. and Stigh, U. “Dynamic testing and simulation of hybrid joined bi-material beam”. *Thin-Walled Structures* 48.8 (2010), pp. 609–619. https://doi.org/10.1016/j.tws.2010.03.003.

[4] Hallquist, J. O. et al. “LS-DYNA keyword users manual”. *Livermore Software Technology Corporation* 970 (2007).

[5] Seeger, F., Feucht, M., Frank, T., Keding, B., and Haufe, A. “An investigation on spot weld modelling for crash simulation with LS-DYNA”. *4th LS-DYNA User Forum, Bamberg*. 2005. ftp://ftp.lstc.com/outgoing/support/FAQ_kw/spotwelds/application_of_spotwelds.pdf.

[6] Bier, M., Liebold, C., Haufe, A., and Klamser, H. “Evaluation of a rate-dependent, elasto-plastic cohesive zone mixed-mode constitutive model for spot weld modeling”. *LS-DYNA Forum, Bamberg*. 2010. https://www.dynamore.se/en/resources/papers/10-forum/papers/B-II-03.pdf.

[7] Marzi, S., Hesebeck, O., Brede, M., and Kleiner, F. “A rate-dependent, elasto-plastic cohesive zone mixed-mode model for crash analysis of adhesively bonded joints”. *7th European LS-DYNA conference*. 2009. https://www.dynamore.de/en/downloads/papers/09-conference/papers/B-VI-02.pdf.

[8] Hanssen, A., Olovsson, L., Porcaro, R., and Langseth, M. “A large-scale finite element point-connector model for self-piercing rivet connections”. *European Journal of Mechanics - A/Solids* 29.4 (2010), pp. 484–495. https://doi.org/10.1016/j.euromechsol.2010.02.010.

[9] Sommer, S. and Maier, J. “Failure modeling of a self piercing riveted joint using ls-dyna”. *8th LS-DYNA European Conference, May*. 2008, pp. 23–24. http://www.dynalook.com/8th-european-ls-dyna-conference/session-2/Session2_Paper2.pdf.

[10] Bier, M. and Sommer, S. “Simplified modeling of self-piercing riveted joints for crash simulations with a modified version of constrained_interpolation_spotweld”. *9th European LS-DYNA Conference, Manchester*. 2013. http://www.dynalook.com/9th-european-ls-dyna-conference/simplified-modeling-of-self-piercing-riveted-joints-for-crash-simulation-with-a-modified-version-of-constrained_interpolation_spotweld.

[11] Hoang, N.-H., Hanssen, A.-G., Langseth, M., and Porcaro, R. “Structural behaviour of aluminium self-piercing riveted joints: An experimental and numerical investigation”. *International Journal of Solids and Structures* 49.23 (2012), pp. 3211–3223. https://doi.org/10.1016/j.ijsolstr.2012.05.039.

[12] Sønstabø, J. K., Holmstrøm, P. H., Morin, D., and Langseth, M. “Macroscopic strength and failure properties of flow-drill screw connections”. *Journal of Materials Processing Technology* 222.0 (2015), pp. 1–12. https://doi.org/10.1016/j.jmatprotec.2015.02.031.

[13] Lademo, O.-G., Hopperstad, O., and Langseth, M. “An evaluation of yield criteria and flow rules for aluminium alloys”. *International Journal of Plasticity* 15.2 (1999), pp. 191–208. https://doi.org/10.1016/S0749-6419(98)00064-3.

[14] Barlat, F., Aretz, H., Yoon, J., Karabin, M., Brem, J., and Dick, R. “Linear transfomation-based anisotropic yield functions”. *International Journal of Plasticity* 21.5 (2005), pp. 1009–1039. https://doi.org/10.1016/j.ijplas.2004.06.004.

[15] Barlat, F., Brem, J., Yoon, J., Chung, K., Dick, R., Lege, D., Pourboghrat, F., Choi, S.-H., and Chu, E. “Plane stress yield function for aluminum alloy sheetspart 1: theory”. *International Journal of Plasticity* 19.9 (2003), pp. 1297–1319. https://doi.org/10.1016/S0749-6419(02)00019-0.

[16] Reyes, A., Hopperstad, O., Lademo, O.-G., and Langseth, M. “Modeling of textured aluminum alloys used in a bumper system: Material tests and characterization”. *Computational Materials Science* 37.3 (2006), pp. 246–268. https://doi.org/10.1016/j.commatsci.2005.07.001.

[17] Vysochinskiy, D. “Formability of aluminium alloy subjected to prestrain by rolling”. PhD thesis. Norwegian University of Science and Technology, 2014.

[18] Dumoulin, S., Engler, O., Hopperstad, O., and Lademo, O. “Description of plastic anisotropy in AA6063-T6 using the crystal plasticity finite element method”. *Modelling and Simulation in Materials Science and Engineering* 20.5 (2012), p. 055008. https://doi.org/10.1088/0965-0393/20/5/055008.

[19] Porcaro, R., Langseth, M., Hanssen, A., Zhao, H., Weyer, S., and Hooputra, H. “Crashworthiness of self-piercing riveted connections”. *International Journal of Impact Engineering* 35.11 (2008), pp. 1251–1266. https://doi.org/10.1016/j.ijimpeng.2007.07.008.

Paper 3

This paper has been accepted for journal publication:

Sønstabø, J. K., Morin, D., and Langseth, M. "Testing and modelling of flow-drill screw connections under quasi-static loadings". *Accepted for publication in Journal of Materials Processing Technology*.

Abstract

The behaviour of a flow-drill screw connection under different quasi-static loadings was simulated using finite element models with detailed solid element meshes. The numerical models were developed with a rate-independent isotropic hypoelastic-plastic material model. A process-effect analysis was conducted, including investigation of the microstructure as well as hardness tests. Based on the investigation, the process effects were considered negligible. A simple approach for building up the geometry of the connection was presented. An experimental programme consisting of five different single-connector tests was carried out to characterise the connection, and was presented in detail. Each test was simulated, allowing for one-to-one comparisons between tests and simulations. Satisfactory results were achieved.

Testing and modelling of flow-drill screw connections under quasi-static loadings

1 Introduction

Flow-drill screws (FDS) are commonly used to join parts of dissimilar materials in the load-bearing structure of cars. Since connections play important roles for the crashworthiness of vehicles, knowledge about their physical behaviour under impact loadings is important for design decisions. Necessary knowledge and physical insight is usually gained through extensive experimental programmes, which typically involve loading specimens consisting of two or more plates joined with one or more connectors until failure [1]. Various loadings are achieved by changing the specimen design and loading directions.

A limited number of experimental studies on FDS connections can be found in the open literature. Szlosarek et al. [2] presented a novel testing and analysis method. It was demonstrated for an FDS connection between plates of a carbon fibre reinforced polymer and aluminium. Skovron et al. [3] studied the FDS process for a connection between sheets of aluminium alloy AA 5052-O. They explored feasible design space regions to determine how process parameters affect the geometry of the assembled connection. Mechanical tests were performed to validate the findings. Sønstabø et al. [1] carried out a large experimental programme to characterize an FDS connection between sheets of AA 6016 T4. The results were compared to equivalent tests on self-piercing rivet connections. Skovron et al. [4] studied the effect of thermally assisting the FDS process (i.e. pre-heating the plates with an external heat source), and performed mechanical tests on a connection between sheets of AA 6063 T5A. Sønstabø et al. [5] presented experiments on connections between an AA 6016 T4 sheet and an AA 6063 T6 extrusion, which they used to evaluate state-of-the-art macroscopic large-scale finite element modelling techniques. A *macroscopic model* here means a simplified model used to represent connections in large-scale analyses where time step restrictions prohibit detailed modelling of the connections. On the other hand, a *mesoscopic model* is a detailed three-dimensional finite element model with a fine solid mesh, where the actual geometry of the connection is taken into account.

To the best of the authors' knowledge limited scientific literature exist on mesoscopic modelling of FDS connections. A literature survey revealed one paper by Grujicic et al. [6], who made an attempt to simulate the FDS process. The results from the process

simulation were mapped to finite element models of different coupon tests. The global force-displacement curves from the coupon simulation results were qualitatively compared to corresponding curves from the experiments of Sønstabø and Holmstrøm [7] which have been presented in the journal article of Sønstabø et al. [1]. These experiments were with a different screw and different plate materials.

In addition to complement experiments with additional information not otherwise achievable, a validated mesoscopic model of the connection may be used to explore the design space as function of e.g. thicknesses, materials and screw geometries in an efficient way, or for example to investigate particular deformation or failure modes. Another incentive for building a validated mesoscopic model is to use it for virtual testing of the connections. Experiments are costly and time consuming, and from an industrial perspective it would be beneficial to replace experiments with validated simulations. The results can for instance be used to calibrate macroscopic connection models for large-scale simulations.

Although little information is available for FDS connections, detailed numerical studies using mesoscopic models have been carried out on other connection types, some examples of which are presented in the following. Bouchard et al. [8] used three-dimensional numerical models to study the behaviour of self-piercing rivet (SPR) connections under quasi-static loading conditions. They included mechanical properties obtained with two-dimensional axisymmetric riveting process simulations, and were in most cases able to reproduce the correct behaviour of the connection with reasonable accuracy in terms of force-displacement response and deformation mode. Chen et al. [9] conducted a numerical and experimental study of a riveted joint, including the riveting process and tension tests, to investigate the failure modes under tensile loads. Kong et al. [10] predicted the plastic and failure behaviour of a single lap-joint test of a resistance spot-weld between two steel sheets. Constitutive models were calibrated for different weld zones and coupled with a failure model. The finite element model was used to study the effect of nugget size and sheet thickness. A similar study was carried out by Nielsen [11], who used a modified Gurson material model to successively model plug failure for sufficiently large spot-weld diameter. Interface failure typically seen for smaller weld diameters was not well described. This was achieved later by Nielsen and Tvergaard [12] by modifying an extension to the Gurson model. Sabuwala et al. [13] used finite element analysis to study the behaviour of fully restrained steel connections subjected to blast loads. The results revealed that design criteria for steel connections subjected to blast loads were inadequate, and recommendations for modifications were presented. Liu et al. [14] performed experimental tests to investigate the dynamic response of top-and-seat with web angle steel beam-column connections subjected to a sudden column removal. They employed three-dimensional finite element

simulations to understand the deformation and failure mechanisms that were observed in the experimental tests.

Numerical simulations of the FDS process are difficult to set up. The process physics are complex, involving for instance friction, large plastic deformations and thermal softening. A coupled thermo-mechanical finite element model would be required, and accurate description of the different phenomena would be difficult. Moreover, the large deformations would cause numerical challenges, introducing the need for e.g. remeshing. In addition, one would need data of the process input parameters, e.g. rotational speed, torque and driving force. Besides, such a process simulation would be difficult to validate.

The present article explores the possibilities of modelling FDS connections between aluminium plates with a mesoscopic model, without taking the process into account. The developed numerical model was validated using experiments, both with respect to deformation modes and force-deformation characteristics. A simple approach for building up a sufficiently accurate model is presented. Five different finite element models were built up, each one resembling an experimental test, allowing for direct comparisons between simulations and experiments. The experimental programme consisted of cross tension, cross mixed, cross shear, single lap-joint and peeling tests. The novelty of this paper is related to the mesoscopic modelling of FDS connections, as well as the validation carried out using a new cross test set-up.

The experiments are explained and presented first, followed by a discussion about process effects. The finite element model is subsequently presented, and finally the simulation results are discussed.

2 Experiments

The term *connection* is in the present article defined as *a system that mechanically fastens two or more parts together* [1, 5], implying that it consists of the screw itself plus some surrounding plate materials. The connection investigated in this work consisted of an M5 through-hardened steel screw connecting a 2 mm thick rolled sheet of AA 6016 in temper T4 to a 2 mm thick extrusion of AA 6063 in temper T6. A schematic drawing with nominal dimensions and a cross-section picture of the connection are presented in Fig. 1. This material combination was chosen since it is representative of a typical FDS connection in cars, with the top sheet having a yield stress of approximately 120 MPa and the bottom extrusion a yield stress of approximately 210 MPa. A pre-hole of 7 mm diameter was used in the top plate. Engineering stress-strain curves for the plate and screw materials are presented in Fig. 2. As seen, the extrusion (6063) had a higher yield stress, but the

rolled sheet (6016) had stronger work-hardening and was significantly more ductile.

The connection was studied by means of cross tests in three loading directions (tension, shear, and combined tension and shear), and single lap-joint and peeling tests. Schematic drawings of the test specimens are presented in Fig. 3, where clamped areas are indicated with grey colour. The dark grey colour in Fig. 3a indicates where a smaller clamp was used in the cross mixed and shear tests. All tests were quasi-static. Three to five repetitions were carried out for each test. The global responses (force-displacement curves) are reported, together with detailed descriptions of the tests and post-mortem pictures of specimens. The global response in the single lap-joint and peeling tests has been briefly reported before [5].

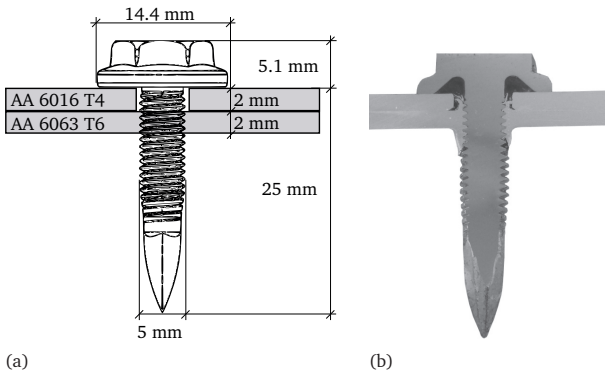

Fig. 1. FDS connection. (a) Schematic drawing. (b) Picture of the cross-section.

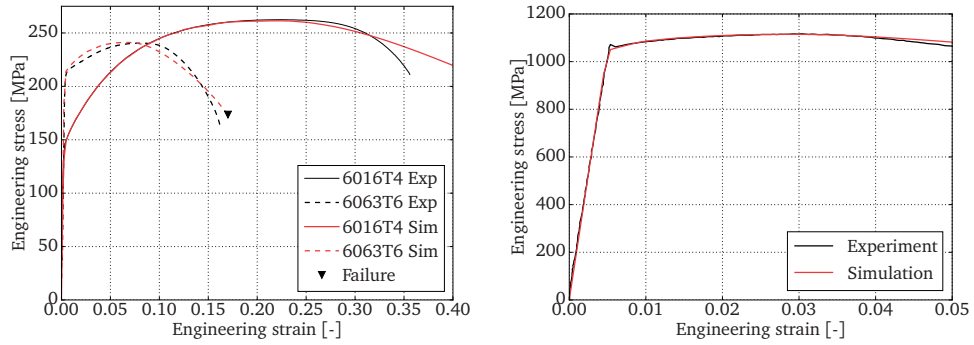

Fig. 2. Engineering stress-strain curves for the (a) plate materials and (b) screw material. Curves from simulations of the material tests are included (see Section 4.2).

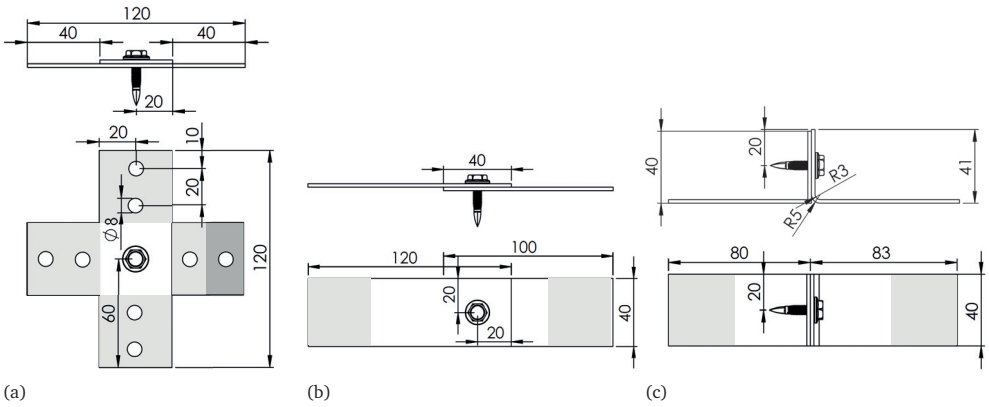

Fig. 3. Drawings of test specimens. (a) Cross test. (b) Single lap-joint test. (c) Peeling test. Clamped areas are coloured grey. The dark grey colour in (a) indicates the area where a smaller clamp was used in the cross mixed and cross shear tests.

2.1 Cross tests

Fig. 4a illustrates the principle of the cross tests. The coloured areas in the figure were clamped in the tests. The red parts were fixed, while the blue parts were pulled in the directions of the arrows corresponding to tension-, mixed- and shear loading. To allow for relative sliding of the plates, only half of the area on one side of the bottom plate was clamped in the cross mixed and shear tests. This is indicated with a lighter red colour where the clamping was omitted. The bottom plate was fixed, while the top plate was pulled in the direction of the arrows in the figure.

Fig. 4b shows a principle drawing of the cross tension test set-up. The specimen was mounted on two steel fixtures, using screws and clamping blocks. A picture of the set-up is shown in Fig. 4c. The steel fixtures were placed in a regular Instron tensile testing machine, where they were pulled apart in the vertical direction. Pure tensile loading was ensured by hinging the fixture in each end. The pulling force was measured with a load cell mounted in series between the top fixture and the cross beam of the testing machine. A camera was used to take photographs during the tests to record the relative displacement of the steel fixtures with a digital image correlation (DIC) method (readers are referred to Fagerholt [15] for details on DIC). Black and white checkerboard markers were glued on the steel fixtures, for the DIC analysis.

The shear and mixed mode cross tests were carried out using the rig shown in Figs. 4d to 4f. The test rig was designed so that it was easy to control the support conditions, such that a one-to-one relationship with numerical boundary conditions could be obtained. Principle drawings of the set-up are shown in Figs. 4d and 4e, and Fig. 4f shows a picture of the mixed-mode set-up. The cross specimen was clamped to two main steel parts (denoted as part 1 and part 2 in Fig. 4) with screws and clamping blocks. The main steel parts were placed

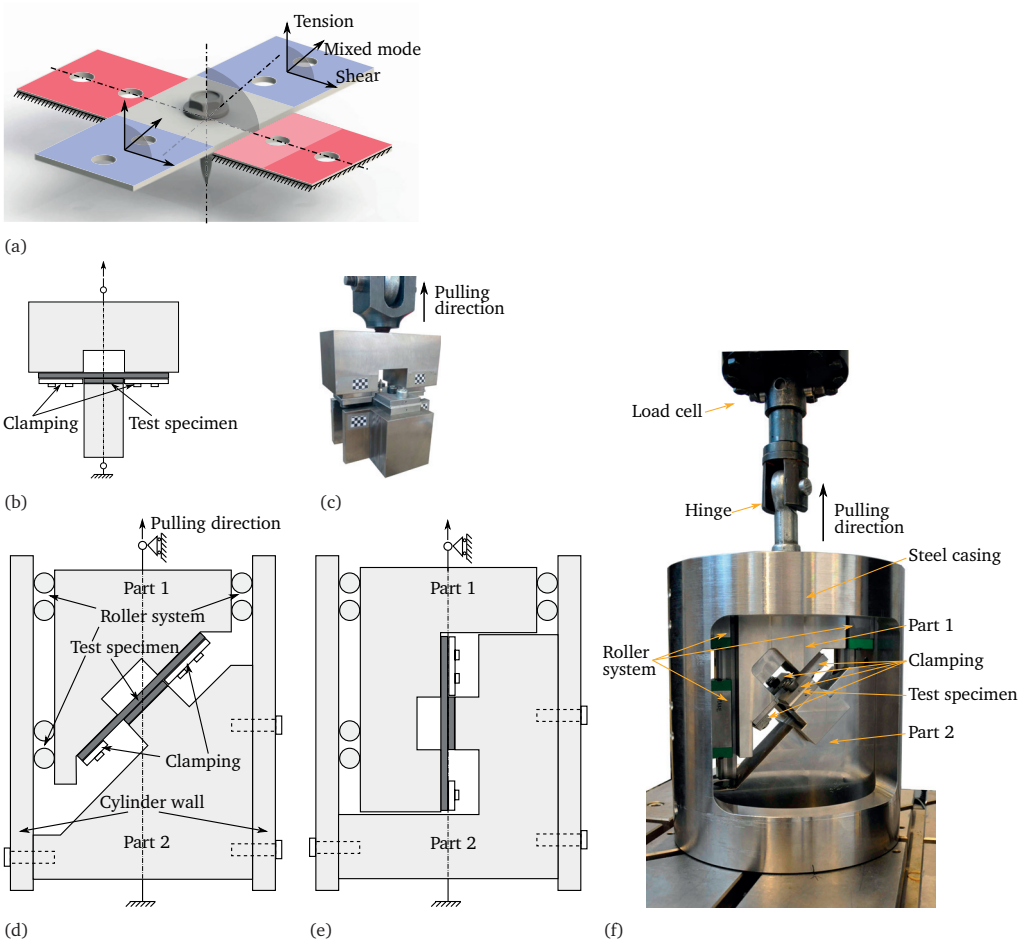

Fig. 4. Illustrations of the set-ups in the cross tests. (a) Principle of the cross tests. (b) Principle drawing of the tension set-up. (c) Picture of the tension set-up. (d) Principle drawing of the mixed-mode set-up. (e) Principle drawing of the shear set-up. (f) Picture of the mixed mode set-up.

inside a cylindrical steel casing, to control their motion, thus ensuring controlled boundary conditions in the test. Part 1 was attached to the cylinder with a roller system, allowing for smooth motion in the loading direction, whereas part 2 was bolted to the casing.

The rig was placed in a regular Instron tensile testing machine. The rig was hinged in the top, and attached to the testing machine with a single bolt between the centre of the bottom of part 2 and the testing machine. A load cell was mounted between the top hinge and the cross-beam of the testing machine. It was confirmed by in-house testing that the friction forces in the rollers were negligible compared to the pulling force, and thus that the force measured was equal to the force transmitted through the specimen. The clamping was carefully monitored to verify that no slipping occurred. A camera was used to take photographs during the tests. The pictures were used to monitor the rigid-body motion of

parts 1 and 2 using DIC. Black and white checkerboard markers were glued on parts 1 and 2, for the DIC analysis. It was verified that the rotation and translation in other directions than the pulling direction were negligible. The cross-head velocity in all cross tests was set to 5 mm/min, which was assumed to render quasi-static conditions.

All three cross test set-ups were designed such that the load application line passed exactly through the centre of the specimen (as indicated with stippled-dotted lines in Figs. 4a, 4b, 4d and 4e).

Force-displacement curves from the cross tests are shown in Fig. 5 and deformed specimens are depicted in Figs. 6a to 6d. The displacement plotted here is the relative displacement between parts 1 and 2 which was measured with DIC. As seen, the connection was strongest in shear and weakest in tension. The shear mode exhibited highest ductility while the tensile mode exhibited lowest. The mixed mode response showed intermediate force level and ductility. Large variation in initial stiffness was seen for the mixed mode and shear tests. This was due to the pre-hole which allowed for relative sliding between the top and bottom plate under shear loading. The force required to give sliding varied from specimen to specimen, which might be due to variations in the screw-driving process (e.g. pre-stressing, surface finish, cleanliness). Apart from this variation the repeatability of the test results was acceptable.

In tension significant plate yielding caused a distinct knee in the force-displacement curve after approximately 1 mm displacement. The force increased until approximately 3.2 kN where the threads were stripped from the bottom plate. This is clearly seen in Figs. 6a and 6b, where residue material from the stripped threads is seen on the screw. There were

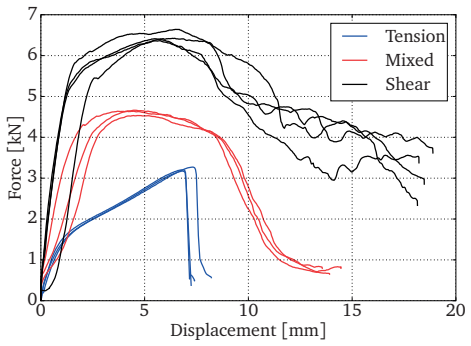

Fig. 5. Force-displacement curves from cross tests.

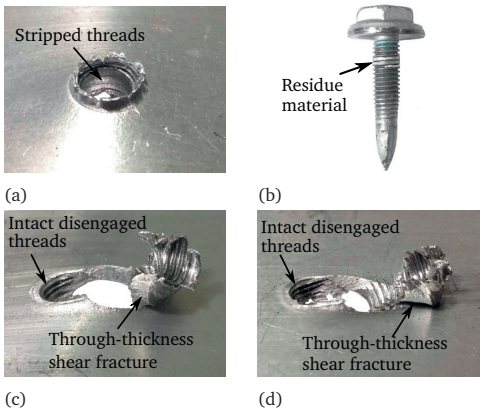

Fig. 6. Photographs of representative post mortem specimens from cross tests. (a) Cross tension, top side of bottom plate. (b) Cross tension, screw. (c) Cross mixed mode, top side of bottom plate. (d) Cross shear, top side of bottom plate.

limited deformation of the top plates, therefore they are left out from Fig. 6.

A stiffer response was observed for the mixed mode tests. The force reached a maximum of approximately 4.6 kN. Fig. 6c indicates that the main failure mechanism was through-thickness shear fracture of the bottom plate material. The tangential component of the displacement of the top plate pushed the screw sideways such that the threads were engaged only on one side of the hole. Fig. 6c clearly shows intact disengaged threads on the left side of the hole and through-thickness shear fracture on the right.

The connection gave stiffest response under pure shear loading. The maximum force was approximately 6.5 kN. As for the mixed mode tests the tangential displacement pushed the screw sideways and disengaged the threads on one side. Fig. 6d indicates that failure occurred by through-thickness shear fracture of the bottom plate. Slight plastic bending of the screw shaft was observed for some of the cross shear tests.

There was no clear end of the pure shear tests. In pure tension and mixed mode, the end of test was clearly seen as the force dropped to nearly zero and the plates were completely separated. This was not the case under pure shear loading (see Fig. 5). As the cross shear specimen was deformed the screw rotated and tried to push the plates apart. However, the steel casing of the testing rig prevented any motion other than the pulling direction, with the consequence that the screw was squeezed between the plates. Thus the force level did not drop to zero even after fracture took place, probably due to high frictional and contact forces between the screw and plates.

The top plate did not experience failure in any of the tests, only plastic deformations. They are therefore not depicted.

2.2 Single lap-joint and peeling tests

The single lap-joint and peeling tests were done using the set-up described by Sønstabø et al. [1], who carried out similar tests for a different connection. The specimens (illustrated in Figs. 3b and 3c) were clamped in a standard Instron tensile test machine using mechanical grips with a clamping length of 40 mm. The clamps were centred along the load application line, such that the single lap-joint specimen was slightly deformed during clamping (this is illustrated in Fig. 7). The deformation was purely elastic. The force was measured using an Instron load cell and the displacement was recorded from the cross-head displacement of the test machine. The cross-head velocity was set to 10 mm/min.

The force-displacement response in the single lap-joint tests (Fig. 8a) was similar to the cross shear test. The maximum force was slightly lower (approximately 5.9 kN) and the ductility was comparable. A clear failure was seen in the force curves, probably due to less

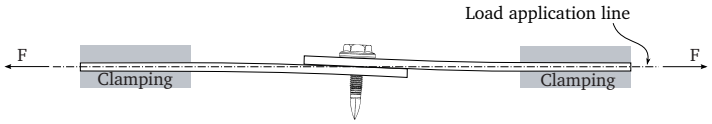

Fig. 7. Illustration of clamping in the single lap-joint test.

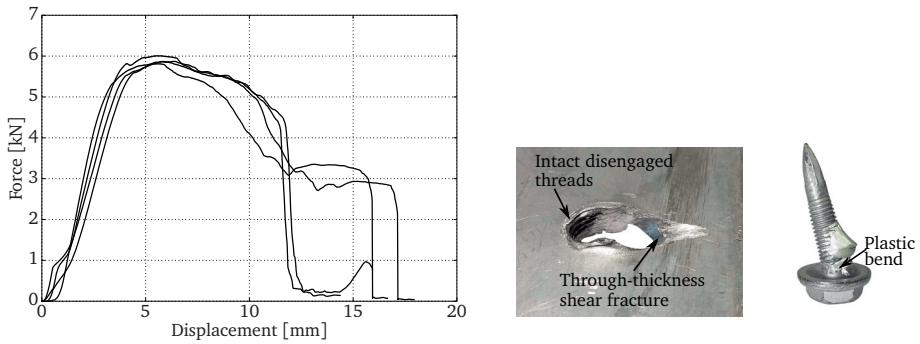

(a) (b) (c)

Fig. 8. Results from single lap-joint tests as (a) force-displacement curves, and representative post-mortem pictures of (b) top side of bottom plate and (c) screw.

restrictive clamping than in the cross shear tests. The simpler clamping conditions allowed the plates to bend more, possibly rotating the entire connection. This probably introduced tensile loading on the connection. Significant scatter is seen for the displacement at failure, which is not uncommon for tests on connections such as FDS. As for the cross mixed and shear tests the presence of the pre-hole caused large variation in initial stiffness. Parts of post-mortem specimens are depicted in Figs. 8b and 8c. As seen, the failure mechanism was similar to the cross shear tests, with through-thickness shear fracture of the bottom plate. Significant plastic bending of the screw shaft occurred in the single lap-joint tests.

Fig. 9a shows the force-displacement curve from the peeling tests. A knee was observed after ca. 2.5 mm displacement, caused by yielding of the plate materials. The force gradually increased up to 2 kN where the slope abruptly increased due to contact between the shaft of the screw and the bottom plate (traces of the contact is visible in Fig. 9b). Some variation was evident in the force level as well as in the displacement at the time of shaft contact. These variations were probably caused by discrepancies in the position of the screw. The maximum force was approximately 3.2 kN and failure occurred by thread stripping in the bottom plate (see Fig. 9c).

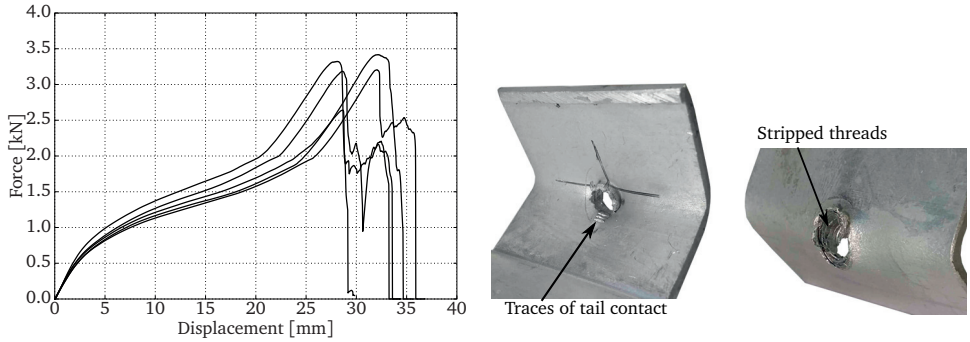

(a) (b) (c)

Fig. 9. Results from peeling tests as (a) force-displacement curves, and representative post-mortem pictures of (b) top side of bottom plate and (c) underside of bottom plate.

3 Process effects

In the FDS process flow-drilling and thread forming is combined into a single procedure where the screw is both used as tool to generate the hole and as fastener. The process (illustrated in Fig. 10) consists of the following six stages [1, 3]: *heating*, *penetration*, *extrusion forming*, *thread forming*, *screw driving* and *tightening*. In the heating stage the screw is forced against the plate material while rotating (usually 2000-6000 rpm) to heat up the material. Subsequently an increasing downward force is applied and the screw penetrates the plate. Material flows up and down along the length of the screw and forms a boss (material that flows upwards between the plate and the screw head). When the tail of the screw pierces the bottom surface of the plate a so-called extrusion is formed as material flows downwards along the screw shaft. Threads are created by a thread-forming zone on the fastener, and the screw is driven in until the head hits the top plate. A final torque is

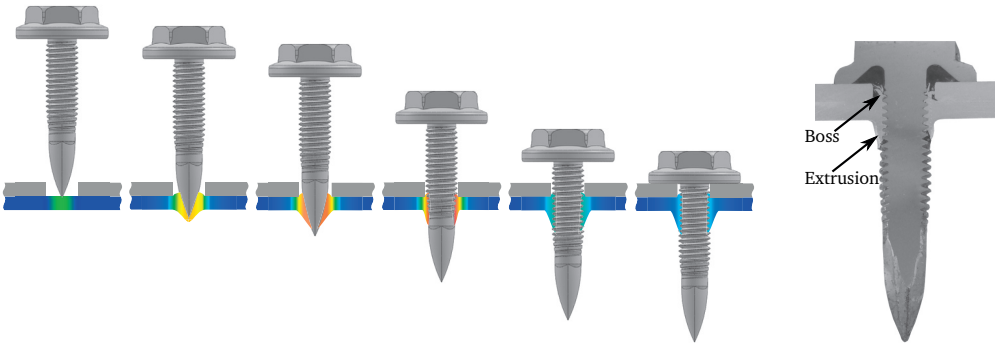

(a) (b) (c) (d) (e) (f) (g)

Fig. 10. The FDS process. (a) Heating. (b) Penetration. (c) Extrusion forming. (d) Thread forming. (e) Screw driving. (f) Tightening. A picture of an FDS connection is shown in (g), with the boss and extrusion indicated.

applied to a pre-set value in order to ensure a tight connection. The whole process usually takes between 1.5 and 4 seconds, depending on the material combination, plate thickness and type of screw.

During the process the plate material close to the screw simultaneously undergoes a temperature increase and significant plastic straining. The plastic straining leads to a work-hardened zone of unknown size. Skovron et al. [3] measured the surface temperature during the process for different fastener forces (which is inversely related to the temperature), and reported temperatures between 150 °C and 330 °C. The increased temperature may have two consequences. First, it leads to thermal softening which reduces the resistance against the plastic deformations during the process, which would facilitate penetration of the screw into the bottom plate. Second, the higher temperature might lead to permanent changes in mechanical properties of the aluminium alloy. This would imply that there is a process-affected zone of unknown size due to the process.

As explained in Section 4, potential process effects were neglected in the simulations. To assess this assumption, a study consisting of a microstructural analysis and Vickers hardness tests was carried out and is presented in the following.

3.1 Microstructural Analysis

Fig. 11 presents a metallographic photograph of the bottom plate cross-section (excluding the screw), where different colours indicate particular grain orientations. Various details are highlighted by zoomed-in pictures. When examining the pictures it is seen that the grains are markedly deformed close to the screw, implying that large plastic strains have occurred during the process. The deformation appears to be most severe near the surface of the threads (closest to the screw). Inside the boss and extrusion all grains seem deformed. This was expected, since these areas were formed by plastic material flow during the process. In the internal area close to the screw the deformations seem less severe, except for very close to the screw. At a distance of approximately 0.5 mm (one thread-width) away from the screw the grains are seemingly undeformed (see lower left part of Fig. 11). This observation indicates that the plastic deformations are localised and that the width of the plastically deformed zone is small.

3.2 Vickers Hardness Tests

Vickers hardness tests were carried out on the cross-section surface of the bottom plate to further study the effect of the process. The measurements were done with HV0.5 with 0.5

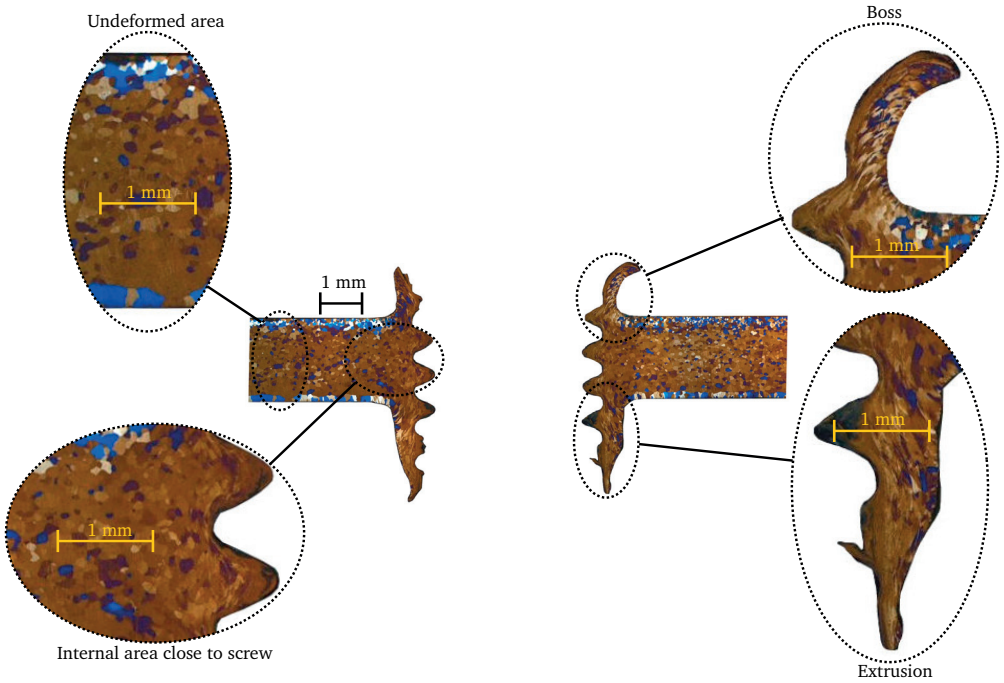

Fig. 11. Metallographic photograph of a cut FDS cross-section excluding the screw. Zoomed-in details are included.

mm distance between dents. This produced dents with a diameter of approximately 115 µm. A smaller weight and denser indenting pattern (micro hardness) were not desirable as individual grains would be indented. The results would then be more affected by the different grain orientations and produce more scatter. The grain size for this alloy typically ranges from 60 to 80 µm (Fig. 11). The measurements were done along two horizontal and one vertical line on both sides of the screw. Fig. 12a shows the measurement locations and illustrates the naming convention used to identify the individual dents. Each row was assigned a label (e.g. A2), and a location number. As an example, point A2-14 corresponds to the leftmost dent in the upper horizontal line on the left side.

The results show no significant variation in hardness in the horizontal direction away from the screw (Fig. 12b), except points A1-1 and B1-1 where a somewhat lower hardness was measured. These points were closest to the screw, located in the area between two threads. The measurements in the vertical direction along the boss and extrusion are given in Fig. 12c. Insignificant variation was observed for the three uppermost points (location 1, 2 and 3), compared to measurements far away from the screw in Fig. 12b, while somewhat lower hardness was measured for the three lowermost points (location 6, 7 and 8). It is noted that points A1-1, B1-1, A3-1, A3-8, B3-1 and B3-8 were close to the free edge which might affect the measured hardness for these points. The results from the Vickers hardness tests conform to findings by Skovron et al. [3] and support the hypothesis that the process-

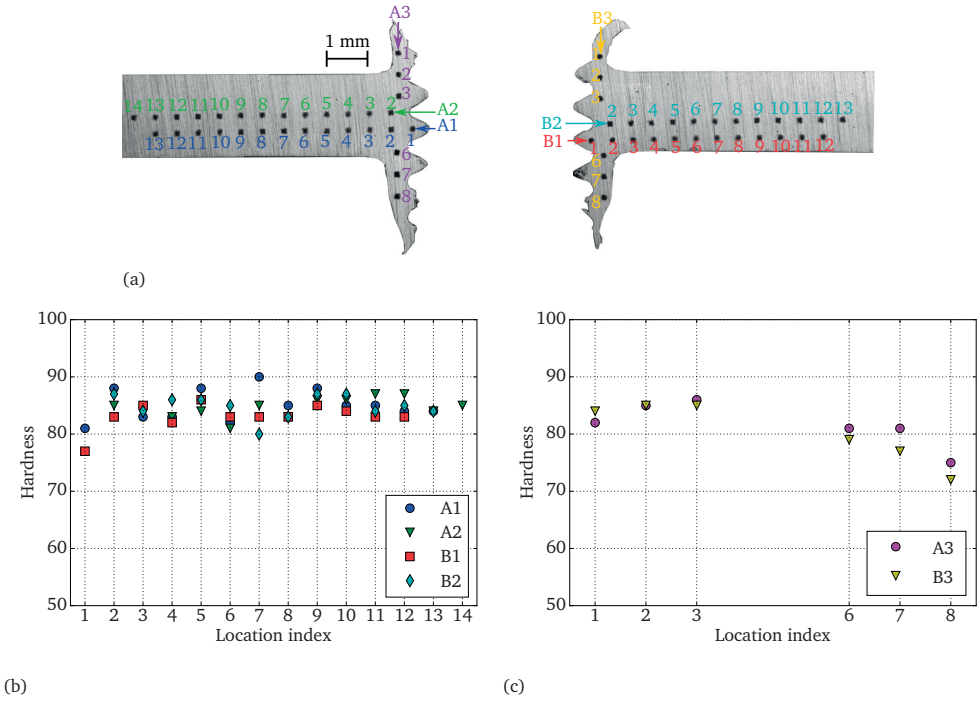

Fig. 12. Vickers hardness tests. (a) Dent locations. (b) Hardness values along horizontal lines. (c) Hardness values along vertical lines.

affected zone is small.

4 Numerical model set-up

4.1 Finite element models

In this section the finite element models and the material models used are presented and discussed.

A circular finely meshed model of the connection was generated and tied to five more coarsely meshed models corresponding to the five experimental tests (see Fig. 13). The connection model was generated as follows. Three parts were defined: the screw, the bottom plate and the top plate. Because the precise geometry of the screw was unknown an approximate geometry was measured using a simple camera technique, illustrated in Fig. 14. A screw was cut in half and a computer programme used to measure the outline of the screw cross-section from a picture, which was subsequently utilised to revolve a 3D part. This operation implies that the helix shape of the threads was neglected. This simplification

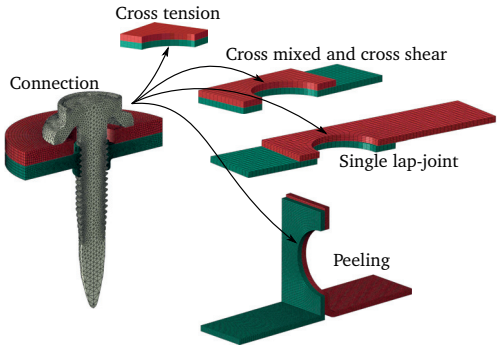

Fig. 13. Illustration of how the connection mesh was inserted into coarser specimens with tie constraints.

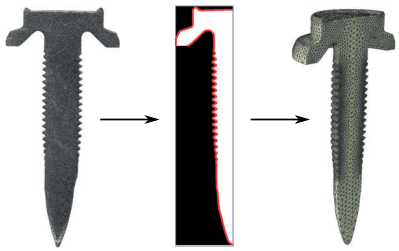

Fig. 14. Illustration of how the geometry of the screw part was generated.

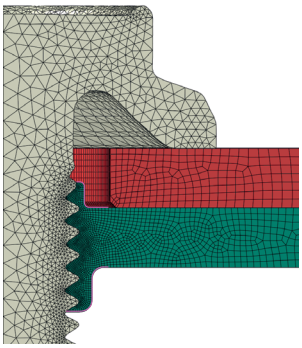

Fig. 15. Half cross-section of the finite element model.

was studied by Chen and Shih [16], who observed small changes in the load distribution compared with including the helix shape, but otherwise similar results. The outer edge of the boss and extrusion of the hole in the bottom plate was modelled in a general way by straight lines and circular arcs (see magenta lines in Fig. 15), and their dimensions were chosen based on the picture in Fig. 1b. The internal threads in the bottom plate were defined with a boolean operation. The bottom plate was generated without a hole, and the screw was positioned in place such that the two parts overlapped. The overlapping volume was then removed from the bottom plate. With this technique the internal threads of the bottom plate coincided with the external threads of the screw, which facilitates the meshing operation. Hence possible gaps between the screw and bottom plate were not accounted for. The top plate was modelled with a pre-hole of 7 mm diameter.

The screw was discretised using 10-node modified quadratic tet elements, while the plates were comprised of 8-node hex elements with reduced integration. As seen in Fig. 15, a fine mesh was required to resolve the geometry of the threads. The smallest element size of the bottom plate was approximately 0.03 mm, while the coarse parts were modelled with five elements through the plate thickness.

Fig. 16 illustrates the finite element models corresponding to the five tests. Figs. 16a and 16b show which parts of the cross specimens that were modelled. As seen, only the deformed part of the specimens were included (clamped areas were omitted), and displacements were prescribed on the surfaces corresponding to the clamped parts. For the bottom plate prescribed displacements were zero (fixed surfaces), while for the top plate they were zero in all directions except in the loading direction where a displacement was applied (indicated with arrows in Figs. 16c to 16g). The deformation during clamping in the single lap-joint tests was accounted for by applying a 2 mm displacement perpendicular to the loading direction before the main loading was applied (see Fig. 7).

The simulations were carried out using the Abaqus v6.11 explicit solver with double precision. Symmetry was utilised where possible, mass scaling was applied (inertia effects were ensured negligible), and a general surface-to-surface contact algorithm was used

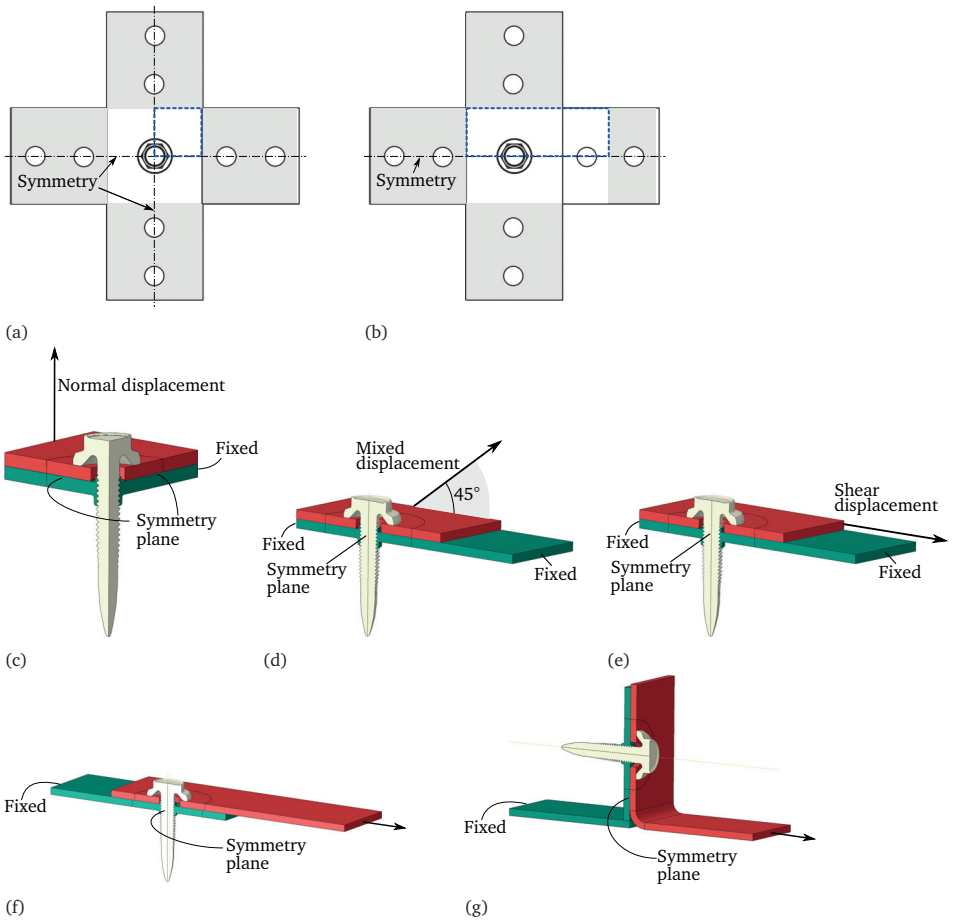

Fig. 16. Illustration of how each test was modelled. (a) and (b) shows which parts of the cross specimens that were modelled. (c) Cross tension model. (d) Cross mixed model. (e) Cross shear model. (f) Single lap-joint model. (g) Peeling model.

between the different parts. A friction coefficient of 0.1 was chosen. For reference, Porcaro et al. [17] chose a friction coefficient of 0.15. Prescribed displacements were applied with a smooth amplitude. Fracture was modelled with element erosion.

4.2 Material model

The aluminium plates and steel screw materials were modelled using a rate-independent isotropic hypoelastic-plastic material model. It is, however, well known that the herein used aluminium alloys exhibit orthotropic plastic anisotropy, for instance as shown by Lademo et al. [18], Lademo et al. [19] and Sønstabø et al. [5]. To obtain a more accurate description of local deformations one could use anisotropic phenomenological plasticity or even crystal plasticity together with the finite element method. The crystallographic texture varied through the thickness of the 6063-extrusion (Fig. 11). Khadyko et al. [20] showed that a very similar 6063-extrusion had a central layer with approximately cube orientation, an intermediate layer with random texture, and a small outer layer with Goss orientation. In spite of this an isotropic phenomenological plasticity material model was chosen in this work. A more advanced anisotropic phenomenological yield function or a crystal plasticity material model would greatly increase the computational time, due to the large number of elements in the mesh. It would require three different yield surfaces through the thickness. In addition, the mesh size was some places smaller than and some places larger than the grain size. Moreover, the global results of the simulations in this work were satisfactory, which indicates that the anisotropy of the material does not affect the global behaviour in a significant way. Therefore the marginal improvements crystal plasticity or a more advanced phenomenological yield surface could bring, do not justify the increase in computational time.

To model plasticity the von Mises yield surface was used, associated flow assumed, and isotropic hardening applied. The yield function may be written as

$$f = \sigma_{\text{eq}} - (\sigma_0 + R) \leq 0,$$

where σ_{eq} is the von Mises equivalent stress, σ_0 is the initial yield stress, and R is an isotropic hardening variable. The Voce hardening law was selected,

$$R = \sum_{i=1}^{N} Q_{\text{R}i} \left(1 - \exp\left(-\frac{\theta_{\text{R}i}}{Q_{\text{R}i}} p \right) \right), \tag{1}$$

where N is the number of terms used, and $Q_{\text{R}i}$ and $\theta_{\text{R}i}$ are the saturation stress and initial hardening modulus for term i, respectively. Two terms were sufficient for the bottom plate

while three terms were needed for the top plate and screw material.

In the experiments material fracture took place only in the bottom plate, the top plate and screw material did not fail. To model fracture in the bottom plate, element erosion with the Cockcroft-Latham criterion [21] was included for this part. The criterion states that failure occurs when the integral

$$W = \int_0^p \langle \sigma_1 \rangle \, \mathrm{d}p \tag{2}$$

attains a critical value W_C. Here σ_1 is the maximum principal stress and $\langle \cdot \rangle$ denotes the Macauley brackets. Hence damage grows for a positive principal stress only. The criterion is easy to calibrate from a single uniaxial tensile test and was chosen for its simplicity.

The procedure to calibrate the initial yield stress and hardening parameters for the plate materials has been reported by Sønstabø et al. [5]. The parameters were obtained by reverse engineering uniaxial tensile tests with finite element simulations. Fig. 2a shows adequate correlation between tests and simulations.

The critical failure value W_C was obtained from the uniaxial tensile test simulation of the bottom plate material, by calculating the integral in Eq. (2) in the most critical element when the nominal strain in the simulation matched the experimental nominal strain at time of fracture (see Fig. 2a). The mesh size in the neck area of the tensile simulation was approximately 0.06 mm. It is known that W_C is a mesh size dependent parameter, due to increased strain gradients for denser meshes [22]. The mesh size dependency was, however, not accounted for here, one value for W_C was used for all elements, which was considered representative for the mesh size where fracture took place in the FDS simulations. Fig. 17 shows the resulting failure loci for generalised tension ($L = -1$),

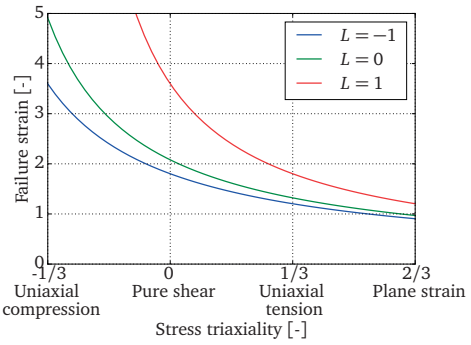

Fig. 17. Cockcroft-Latham failure loci for generalised tension ($L = -1$), generalised shear ($L = 0$) and generalised compression ($L = 1$).

Table 1
Material model parameters for the screw and plate materials.

	E [MPa]	ν [-]	σ_0 [MPa]	Q_{R1} [MPa]	θ_{R1} [MPa]	Q_{R2} [MPa]	θ_{R2} [MPa]	Q_{R3} [MPa]	θ_{R3} [MPa]	W_C [MPa]
Screw (steel)	210000	0.3	1051.1	16.8	12507	89.6	5726	1885	267	-
Top plate (AA 6016 T4)	70000	0.35	117.6	29.2	25000	149.5	2011	100	230	320
Bottom plate (AA 6063 T6)	70000	0.35	204.6	8.0	12300	55	1472	-	-	-

generalised shear ($L = 0$) and generalised compression ($L = 1$), where L is the Lode parameter defined as $L = -\cos 3\theta_L$ and θ_L is the Lode angle.

The screws were subjected to limited plastic deformations, and a simpler approach could be used to calibrate the hardening parameters. Uniaxial tensile tests of the screw material were carried out, using axisymmetric specimens which were cut out from the screw shaft (resulting engineering stress-strain curve is shown in Fig. 2b). The nominal strain was measured using an extensometer, and a digital camera was employed to track the diameter of the specimen. The post-necking plastic strain was calculated from the diameter measurements assuming plastic incompressibility. The post-necking equivalent stress was approximated using Bridgman correction [23], where the radius of the neck was measured from the digital images. Eq. (1) was then fitted to the obtained equivalent stress-plastic strain curve. Fig. 2b shows the result from a simulation of the material test using the obtained hardening parameters. As seen, the correlation was excellent for the relevant strain level.

Typical steel and aluminium values were used for the Young's modulus E and the Poisson ration ν. The material model parameters are summarised in Table 1.

4.3 Process effects

Possible process effects were discussed in Section 3. Metallographic photographs and Vickers hardness tests indicated that there was a local process-affected zone extending approximately 0.5 mm from the screw into the bottom plate. In the present finite element models, process effects were not taken into account. Satisfactory results were nevertheless obtained, which indicates that the process effects do not significantly affect the global behaviour.

5 Simulation results

In this section the results from the finite element simulations of the experimental tests are presented and discussed. Global force-displacement curves are graphed, the simulated deformation modes and failure mechanisms are explained, and various field variables are

plotted when needed for discussion. The cross test simulations are presented first, followed by the single lap-joint and peeling test simulations.

Overall good agreement was obtained between the simulations and experiments, both in terms of force-displacement responses and deformation modes, despite the simplifications made in the model (see Section 4).

5.1 Cross test simulations

As discussed in Section 2.1, variations in initial stiffness in the cross mixed and cross shear experiments occurred due to the pre-hole in the top plate, which allowed for relative sliding between the top and bottom plates (recall Fig. 5). The force required for sliding to occur was different from specimen to specimen, and was a function of unknown process parameters and the amount of prestress in the screw. Therefore this sliding could not be captured accurately by the finite element models. Acknowledging that the simulations did not capture the sliding accurately, it was chosen to shift the cross mixed and shear experimental curves to match the displacement of the simulations at 2 kN force. By doing this, the effect of the relative sliding in the experiments, and the poor representation of it in the simulations, was eliminated. It was assumed that all sliding occurred before 2 kN force was reached, and thus that the results afterwards could be compared. The shifting is illustrated in Fig. 18, which shows the start of the curves without and with shifting of the experimental curves. As seen, all shifted curves coincide at 2 kN force.

The force-displacement response from the cross test simulations are compared to the experimental results in Fig. 19, with the mixed and shear experimental curves shifted as

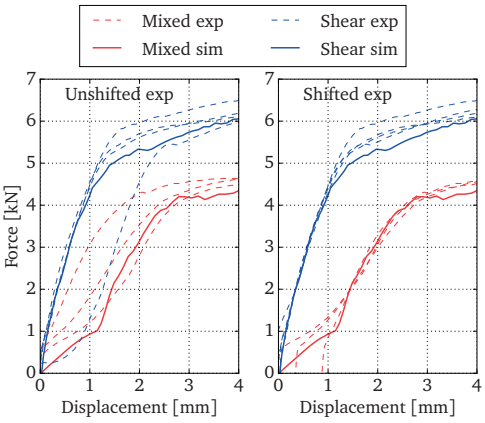

Fig. 18. Illustration of shifting of cross mixed and cross shear experimental curves.

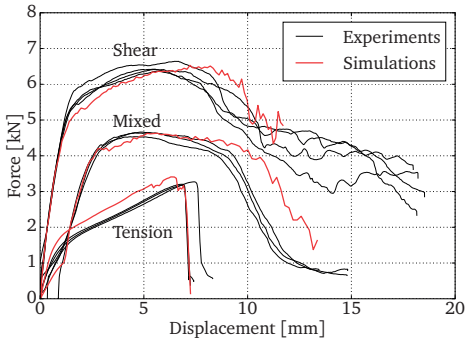

Fig. 19. Force-displacement curves from cross test simulations compared to experiments.

explained above. As shown, overall satisfactory results were obtained. The force levels and shape of the curves match well with the experiments.

Throughout the cross tension test simulation the initial stiffness and force level were somewhat higher than in the experiments. Good agreement was obtained for the displacement at global failure. The overall deformation mode and failure mechanism of the specimen agreed with the experiment. As the bottom plate was bent upward the topmost threads were disengaged such that the three bottommost carried all the load. This is seen in Figs. 20a and 20b where the equivalent plastic strain field is plotted on the initial and deformed configurations a short instance before failure, which occurred by fracture in the threads. Agreement in deformation and failure mode with the experiment may be seen when comparing Fig. 20b with Fig. 6a.

The over-estimated stiffness in the cross tension simulation may indicate inaccuracies in the boundary conditions. In the experiment the plates were subjected to membrane forces

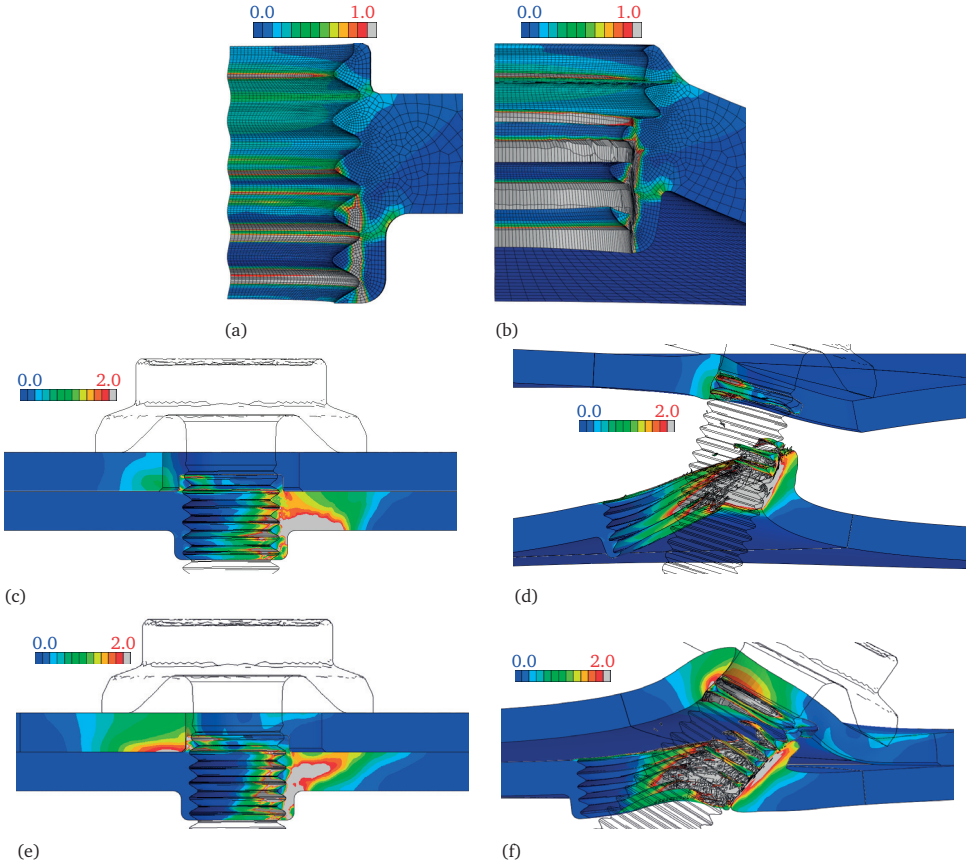

Fig. 20. Equivalent plastic strain field on undeformed and deformed configuration in (a and b) tension (right before failure), (c and d) mixed mode (last frame) and (e and f) shear (last frame).

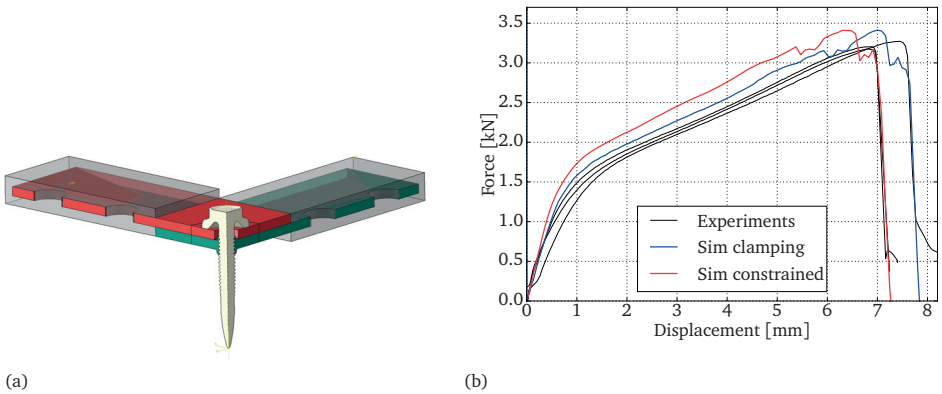

(a) (b)

Fig. 21. Finite element model to check the effect of the clamping. (a) Finite element model. (b) Force-displacement results compared to the original constrained simulation and experiments.

and bending, which could lead to some deformation of the material in the edge of the clamping, which was not accounted for in the finite element model. In an effort to evaluate this effect, a finite element model with a simple model of the clamping was made, see Fig. 21a. The clamps were modelled as rigid, and the clamping was handled by increasing the friction coefficient to 0.6 between the clamps and plates, which ensured little slipping. The result is graphed in Fig. 21b and shows better agreement for the initial stiffness and force level, suggesting that the overestimated stiffness and force by the constrained model was indeed caused by inaccurate boundary conditions. The maximum force was, as expected, unchanged.

In cross shear and mixed mode excellent agreement in stiffness and maximum force level was achieved when accounting for the pre-hole sliding. Deformed specimens with equivalent plastic strain fields on initial and deformed configurations are shown in Figs. 20c to 20f. As seen, the deformation modes in cross mixed and shear were somewhat similar. In mixed mode the screw was pushed sideways and pulled upwards by the top plate, causing the screw to rotate slightly and stressing the threads on the right side of the hole. In shear the screw was pushed sideways by the top plate, causing the screw to rotate significantly. However, in both simulations failure occurred later and the failure took place closer to the screw than in the experiments, which can be seen by comparing Figs. 20d and 20f with Figs. 6c and 6d, respectively. This is possibly explained by the Cockcroft-Latham failure model. As seen in Fig. 17, the model predicts a higher failure strain for pure shear and compressive stress states than under uniaxial tension (for which it was calibrated), and goes to infinity for pure compressive stress states. It has, however, been shown that for some ductile metals in the low stress triaxiality regime the failure strain does not increase monotonically with decreased hydrostatic stress (stress triaxiality) [24, 25]. In the cross mixed and cross shear test simulations the stress triaxiality in the area where failure took

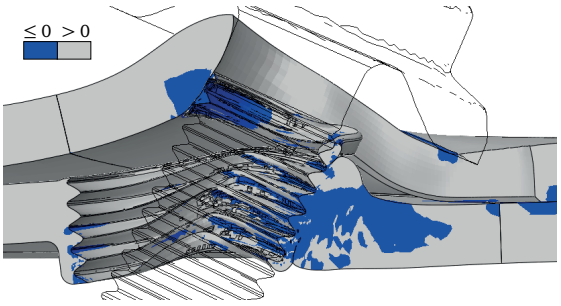

Fig. 22. Sign of main principal stress σ_1 at 8.9 mm displacement (time of maximum force) in the cross shear simulation. Blue colour indicates $\sigma_1 \leq 0$.

place in the experiments was low (≤ 0), suggesting that an over-estimation of the failure strain by the Cockcroft-Latham model was expected. Furthermore, as seen in Fig. 22 the stress state in the area where fracture took place in the cross shear experiment was purely compressive (negative main principal stress), which implies that damage does not grow (Eq. (2)). Hence the failure model was not able to predict the failure mode of the experiments correctly, and fracture was forced to occur elsewhere (closer to the screw). However, the global results were nevertheless satisfactory. Thus such a model can still provide valuable information, and be used for e.g. calibration of macroscopic connection models.

5.2 Single lap-joint and peeling test simulations

Fig. 23a shows that the single lap-joint simulation agreed acceptably with the experiments. The maximum force was slightly over-estimated. In the experiments the maximum force occurred early (approximately 4 mm displacement) and the force decreased gradually until onset of failure, while in the simulation the force increased gradually from onset of plasticity to maximum force at approximately 8 mm displacement after which failure occurred abruptly. A good match was attained for the displacement at failure. The initial stiffness was reasonably predicted. This may possibly be attributed to the fact that the cross-head displacement was used as displacement measure in the experimental tests, probably affected by compliance in the test set-up. Note that the experimental curves were shifted to coincide with the simulation at 2 kN force, as for the cross shear test simulations (see discussion above).

Figs. 23b and 23c depict the equivalent plastic strain field close to the screw at the end of the simulation on initial and deformed configurations, respectively. As seen when comparing with Figs. 20e and 20f the deformation was similar to the cross shear simulation. The less

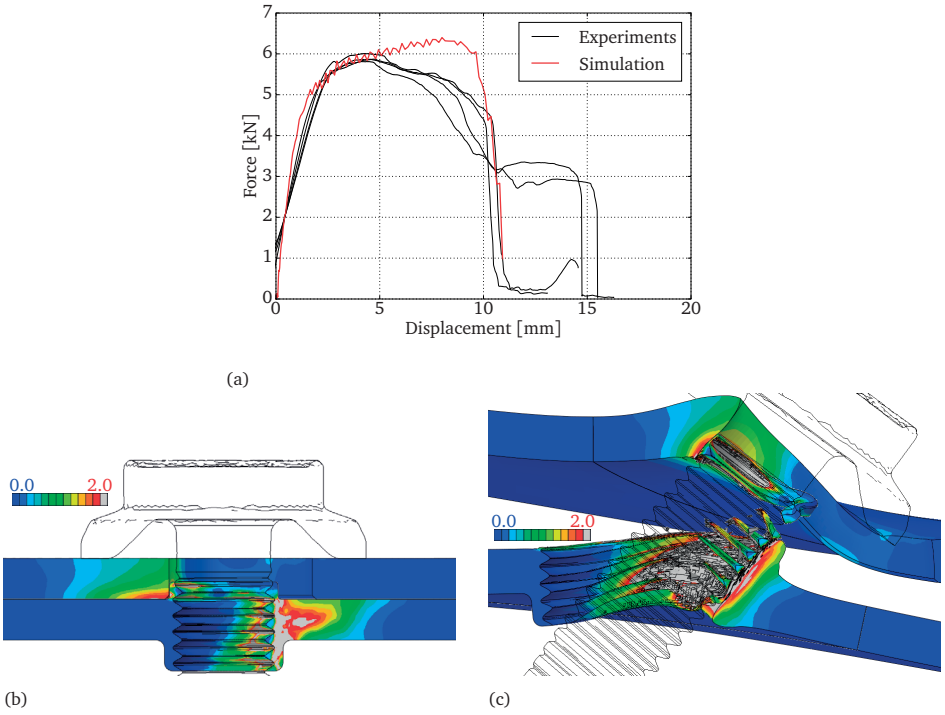

Fig. 23. Results from single lap-joint simulation. (a) Force-displacement curve. (b-c) Equivalent plastic strain field on undeformed and deformed configuration (last frame).

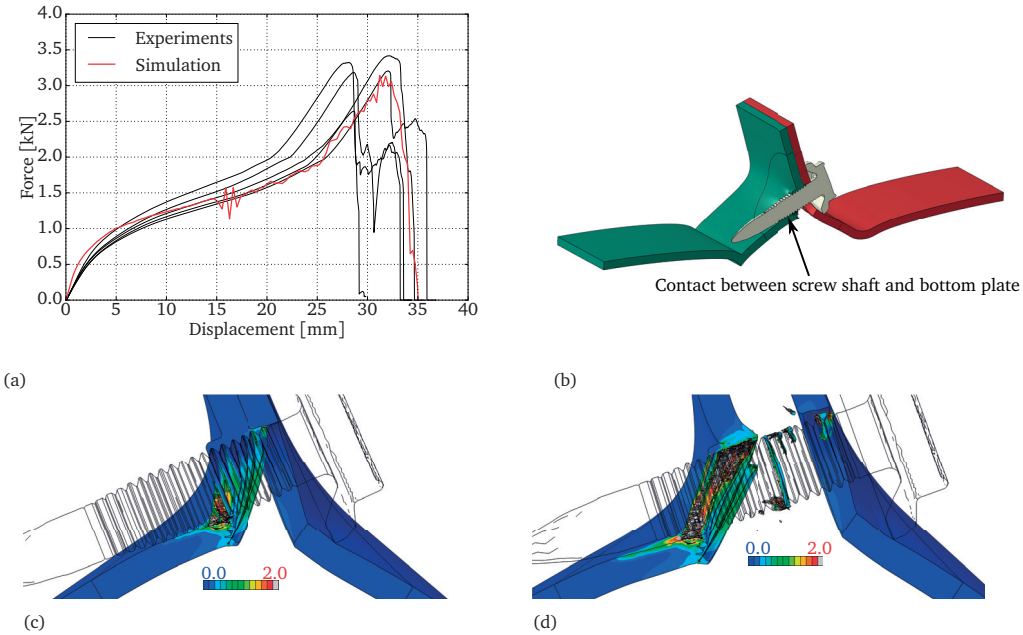

Fig. 24. Results from peeling simulation. (a) Force-displacement curve. (b) Deformed configuration at time of maximum force. (c) Equivalent plastic strain field at time of maximum force. (d) Equivalent plastic strain field after failure.

restrictive clamping in the single lap-joint test is clearly seen as the plates were further apart than in the cross shear simulation.

Favourable agreement was also obtained for the peeling simulation (Fig. 24a). The force level was generally satisfactory and the maximum force and displacement at failure were correctly predicted. The initial stiffness was slightly over-estimated, which, as for the single lap-joint tests, might be because the cross-head displacement was used as displacement measure in the experiments. It is also seen that the abrupt slope increase at 2 kN force caused by contact between the shaft of the screw and the bottom plate was well captured. Fig. 24b shows the deformed configuration at the time of maximum force, where the contact between the shaft of the screw and the bottom plate is indicated. Figs. 24c and 24d show the equivalent plastic strain field at the time of maximum force and after failure, respectively. Failure occurred by stripping the still-engaged threads. The deformation mode and failure mechanism conformed to experimental observations.

5.3 Effect of friction coefficient

To evaluate the effect of the friction coefficient on the numerical results, the simulations were also carried out with friction coefficients of 0.0, 0.2 and 0.3, in addition to the original chosen value of 0.1. The coefficient was varied for three different contact interfaces independently, namely between the screw and the top plate, between the screw and the bottom plate, and between the two plates. It turned out that for tension loading the friction coefficient had a negligible effect, while it was most prominent for shear loadings. Only the curves from the cross shear simulations are therefore shown. The results are summarised in Fig. 25. As seen, there was an effect on the maximum force level, while limited effect was seen on the ductility of the connections. Moreover, the variation due to friction coefficient was in the same order as the variation on the experimental curves. This is natural, due to uncertainties in the process parameters, such as surface cleanliness, pre-stressing and so on, causing diversity in friction in the connections. Changes in the friction coefficient did not alter the deformation modes significantly. Thus, changing the friction coefficients did not change the physics, the overall behaviour remained the same. Except for a slightly different maximum force, no conclusions would have changed if a friction coefficient of 0.3 had been chosen instead of 0.1.

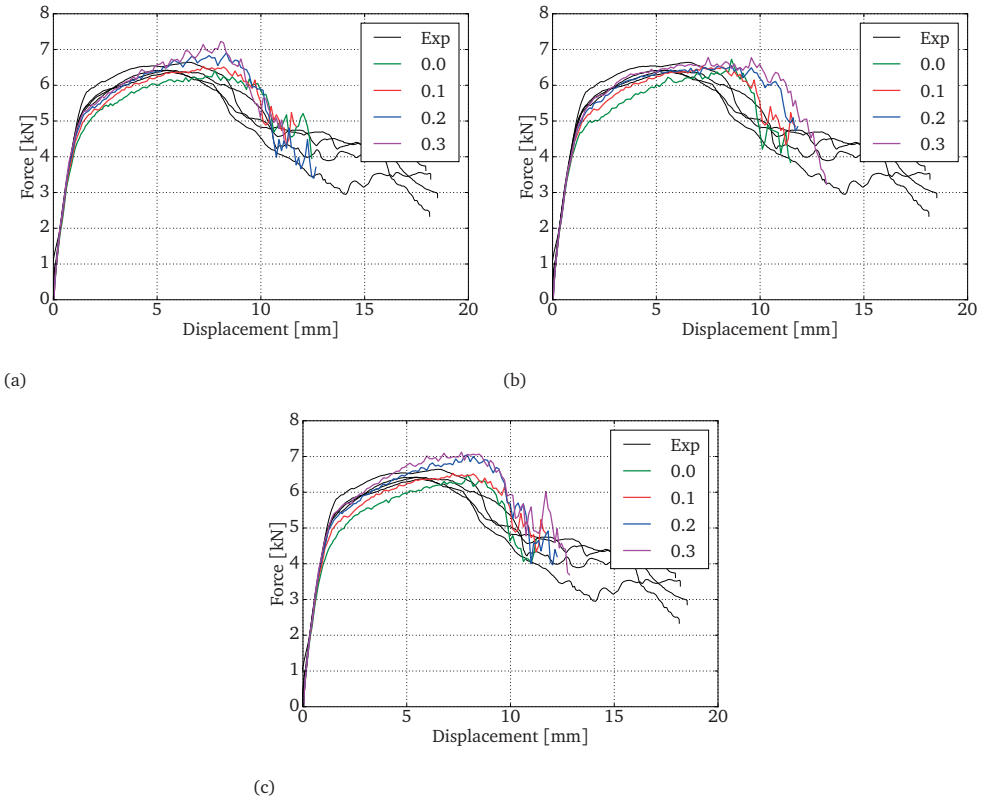

Fig. 25. The effect of friction coefficient on the global force-displacement curves in the cross shear simulation. The coefficient was varied at the contact interfaces between (a) the screw and top plate, (b) the screw and the bottom plate, and (c) between the plates.

6 Conclusions

In the present study the behaviour of flow-drill screw connections in quasi-static tests were simulated using finite element models with detailed solid element meshes. The experiments were described and presented in detail, including a new test set-up for cross tests. The numerical models were developed with a rate-independent isotropic hypoelastic-plastic material model. A simple approach for building up the geometry of the connection was presented. The following main conclusions may be drawn from the present investigation:

- A microstructural analysis indicated that the width of the plastically deformed zone due to the process is small. This was supported by Vickers hardness tests that showed no significant variation in the horizontal direction away from the screw.
- The finite element models gave satisfying results despite simplifications such as isotropic materials, simplified connection geometry, a simple failure criterion, and neglected process effects.
- Good matches between experimental and numerical global force-displacement curves were obtained for all tests.
- Overall deformation and failure modes agreed well with experiments. For shear-dominated loadings fracture tended to occur closer to the screw than in the experiments. This was attributed to the Cockcroft-Latham failure criterion's inability to account for damage at low stress triaxialities.
- Overall, the demonstrated modelling strategy was well-suited to investigate the behaviour of FDS connections under quasi-static loadings. This suggests that the approach may be used for virtual testing, for instance to calibrate macroscopic connection models for large-scale analyses.

References

[1] Sønstabø, J. K., Holmstrøm, P. H., Morin, D. and Langseth, M. "Macroscopic strength and failure properties of flow-drill screw connections". *Journal of Materials Processing Technology* 222 (2015), pp. 1–12. https://doi.org/10.1016/j.jmatprotec.2015.02.031.

[2] Szlosarek, R., Karall, T., Enzinger, N., Hahne, C. and Meyer, N. "Mechanical testing of flow drill screw joints between fibre-reinforced plastics and metals". *Materials Testing* 55.10 (2013), pp. 737–742. https://doi.org/10.3139/120.110495.

[3] Skovron, J., Mears, L., Ulutan, D., Detwiler, D., Paolini, D., Baeumler, B. and Claus, L. "Characterization of Flow Drill Screwdriving Process Parameters on Joint Quality". *SAE Int. J. Mater. Manf.* 8 (Sept. 2014), pp. 35–44. https://doi.org/10.4271/2014-01-2241.

[4] Skovron, J. D., Prasad, R. R., Ulutan, D., Mears, L., Detwiler, D., Paolini, D., Baeumler, B. and Claus, L. "Effect of Thermal Assistance on the Joint Quality of Al6063-T5A During Flow Drill Screwdriving". *Journal of Manufacturing Science and Engineering* 137.5 (2015), p. 051019. https://doi.org/10.1115/1.4031242.

[5] Sønstabø, J. K., Morin, D. and Langseth, M. "Macroscopic modelling of flow-drill screw connections in thin-walled aluminium structures". *Thin-Walled Structures* 105 (2016), pp. 185–206. https://doi.org/10.1016/j.tws.2016.04.013.

[6] Grujicic, M., Snipes, J. and Ramaswami, S. "Process and product-performance modeling for mechanical fastening by flow drilling screws". *International Journal of Structural Integrity* 7.3 (2016), pp. 370–396. https://doi.org/10.1108/IJSI-03-2015-0011.

[7] Sønstabø, J. K. and Holmstrøm, P. H. "Behaviour and Modelling of Self-piercing Screw and Self-piercing Rivet Connections: An Experimental and Numerical Investigation". MA thesis. Institutt for konstruksjonsteknikk, Norwegian University of Science and Technology (NTNU), 2013.

[8] Bouchard, P., Laurent, T. and Tollier, L. "Numerical modeling of self-pierce rivetingFrom riveting process modeling down to structural analysis". *Journal of Materials Processing Technology* 202.1 (2008), pp. 290–300. https://doi.org/10.1016/j.jmatprotec.2007.08.077.

[9] Chen, N., Luo, H., Wan, M. and Chenot, J.-l. "Experimental and numerical studies on failure modes of riveted joints under tensile load". *Journal of Materials Processing Technology* 214.10 (2014), pp. 2049–2058. https://doi.org/10.1016/j.jmatprotec.2013.12.023.

[10] Kong, X., Yang, Q., Li, B., Rothwell, G., English, R. and Ren, X. "Numerical study of strengths of spot-welded joints of steel". *Materials & Design* 29.8 (2008), pp. 1554–1561. https://doi.org/10.1016/j.matdes.2007.12.001.

[11] Nielsen, K. L. "3D modelling of plug failure in resistance spot welded shear-lab specimens (DP600-steel)". *International Journal of Fracture* 153.2 (Oct. 2008), pp. 125–139. https://doi.org/10.1007/s10704-008-9305-4.

[12] Nielsen, K. L. and Tvergaard, V. "Ductile shear failure or plug failure of spot welds modelled by modified Gurson model". *Engineering Fracture Mechanics* 77.7 (2010), pp. 1031–1047. https://doi.org/10.1016/j.engfracmech.2010.02.031.

[13] Sabuwala, T., Linzell, D. and Krauthammer, T. "Finite element analysis of steel beam to column connections subjected to blast loads". *International Journal of Impact*

Engineering 31.7 (2005), pp. 861–876. https://doi.org/10.1016/j.ijimpeng.2004.04.013.

[14] Liu, C., Tan, K. H. and Fung, T. C. “Investigations of nonlinear dynamic performance of top-and-seat with web angle connections subjected to sudden column removal”. *Engineering Structures* 99.Supplement C (2015), pp. 449–461. https://doi.org/10.1016/j.engstruct.2015.05.010.

[15] Fagerholt, E. “Field measurements in mechanical testing using close-range photogrammetry and digital image analysis”. PhD thesis. Norges teknisk-naturvitenskapelige universitet (NTNU), 2012.

[16] Chen, J.-J. and Shih, Y.-S. “A study of the helical effect on the thread connection by three dimensional finite element analysis”. *Nuclear Engineering and Design* 191.2 (1999), pp. 109–116. https://doi.org/10.1016/S0029-5493(99)00134-X.

[17] Porcaro, R., Hanssen, A., Langseth, M. and Aalberg, A. “The behaviour of a self-piercing riveted connection under quasi-static loading conditions”. *International Journal of Solids and Structures* 43.17 (2006), pp. 5110–5131. https://doi.org/10.1016/j.ijsolstr.2005.10.006.

[18] Lademo, O.-G., Hopperstad, O. and Langseth, M. “An evaluation of yield criteria and flow rules for aluminium alloys”. *International Journal of Plasticity* 15.2 (1999), pp. 191–208. https://doi.org/10.1016/S0749-6419(98)00064-3.

[19] Lademo, O.-G., Engler, O., Keller, S., Berstad, T., Pedersen, K. and Hopperstad, O. “Identification and validation of constitutive model and fracture criterion for AlMgSi alloy with application to sheet forming”. *Materials & Design* 30.8 (2009), pp. 3005–3019. https://doi.org/10.1016/j.matdes.2008.12.020.

[20] Khadyko, M., Dumoulin, S. and Hopperstad, O. “Texture gradients and strain localisation in extruded aluminium profile”. *International Journal of Solids and Structures* 97 (2016), pp. 239–255. https://doi.org/10.1016/j.ijsolstr.2016.07.024.

[21] Cockcroft, M. and Latham, D. “Ductility and the workability of metals”. *J Inst Metals* 96.1 (1968), pp. 33–39.

[22] Björklund, O., Larsson, R. and Nilsson, L. “Failure of high strength steel sheets: Experiments and modelling”. *Journal of Materials Processing Technology* 213.7 (2013), pp. 1103–1117. https://doi.org/10.1016/j.jmatprotec.2013.01.027.

[23] Bridgman, P. “The stress distribution at the neck of a tension specimen”. *Trans. ASM* 32 (1944), pp. 553–574.

[24] Bao, Y. and Wierzbicki, T. “On fracture locus in the equivalent strain and stress triaxiality space”. *International Journal of Mechanical Sciences* 46.1 (2004), pp. 81–98. https://doi.org/10.1016/j.ijmecsci.2004.02.006.

[25] Barsoum, I. and Faleskog, J. “Rupture mechanisms in combined tension and shear-Experiments”. *International Journal of Solids and Structures* 44.6 (2007). Physics and

Mechanics of Advanced Materials, pp. 1768–1786. https://doi.org/10.1016/j.ijsolstr.2006.09.031.

Paper 4

This paper was published in:

Sønstabø, J. K., Morin, D., and Langseth, M. “Static and dynamic testing and modelling of aluminium joints with flow-drill screw connections.” *International Journal of Impact Engineering* 115 (2018), pp. 58-75.
https://doi.org/10.1016/j.ijimpeng.2018.01.008

Abstract

A new component test suited for quasi-static and dynamic testing of flow-drill screw connections is presented. The component specimen was made of two different aluminium alloys, and included connections with two material combinations. Large-scale finite element simulations were carried out of each test, in which the connections were modelled with a constraint-based macroscopic model. An improvement of the connection modelling technique is presented. The model was calibrated to cross tension, cross mixed and single lap-joint tests, and validated with peeling and the component tests.

Static and dynamic testing and modelling of aluminium joints with flow-drill screw connections

1 Introduction

An increasing amount of different aluminium alloys is used in the production of cars, to meet requirements of vehicle weight reduction. This gives rise to challenges in the joining of parts, because traditional techniques such as for instance spot welding becomes problematic. Among other techniques, flow-drill screws (FDS) are therefore commonly used to join dissimilar materials in the load-carrying structure of cars. This joining technique combines flow drilling and thread forming in a single procedure, where the screw is both functioning as tool and as fastener, which makes the process suited for automation. An advantage with this technique is that it requires tool access to one side only, as opposed to for instance spot welding or self-pierce riveting, where access to both sides is required. More than two plates may be joined, and the process can be used with and without a pre-hole in the top plate.

Connections such as FDS play an important role for the structural integrity and energy dissipation during car crashes, and knowledge of their mechanical behaviour under crash loadings is therefore of importance to designers in order to make safe cars. Thus, they rely on experimental testing, which typically involve loading specimens consisting of plates joined with one or more screws until failure. Different levels of complexity are achieved by varying the specimen design and loading conditions, ranging from simple tests with two plates and one screw (single-connector tests) to component tests with several screws and complex loadings.

There exist several studies with single-connector testing of FDS connections. Szlosarek et al. [1] presented a new testing and analysis method, and used it for FDS connections between a carbon fibre reinforced polymer and aluminium. Skovron et al. [2] presented an experimental study on a connection between sheets of aluminium alloy AA 5052-O. They studied how process parameters affect the geometry of the assembled connection, and performed mechanical tests of the connections to support the findings. Sønstabø et al. [3] carried out an experimental programme to characterise an FDS connection between rolled sheets of AA 6016 in temper T4. The results were compared to equivalent tests on self-piercing rivet connections. Furthermore, Skovron et al. [4] evaluated the effect of

thermally assisting the FDS process by pre-heating the plates with an external heat source. They performed mechanical tests on connections between sheets of AA 6063 T5A. A study on an FDS connection between AA 6016 T4 and AA 6063 T6 was briefly presented by Sønstabø et al. [5], who used the results to evaluate large-scale finite element modelling techniques for connections.

However, information regarding component tests with FDS connections is limited in the scientific literature. Sønstabø et al. [3] carried out quasi-static and dynamic axial crushing tests of a single-hat crash box joined with FDS. A limitation with this test is that the global force-displacement behaviour was dominated by large material deformations outside of the connections (progressive buckling), which makes it difficult to evaluate the behaviour of the connections. A quasi-static T-component test was carried out by Sønstabø et al. [5]. In this test the material deformation outside of the connections was limited, and the loading on the connections was shear dominated. A limitation with this test is that it is difficult to transfer the test boundary conditions to numerical simulations, which makes it unsuitable for validation purposes.

Although limited information about component testing of FDS connections is available, several studies on component tests with other connection types exist. Some of them are referenced in the following. Porcaro et al. [6] carried out quasi-static and dynamic axial crushing tests on double-hat sections made of aluminium sheets joined with self-piercing rivets. The results were used to evaluate the accuracy and robustness of a numerical model. Belingardi et al. [7] performed similar crushing tests on four different steel sections joined by adhesive bonding, to assess the applicability of structural bonding in the crash-absorbing parts of the car structure. Xiang et al. [8] carried out quasi-static axial crushing tests of a top-hat section consisting of steel sheets joined with spot welds. The results were used to validate a numerical model, which was utilised to optimise the design of the top-hat section with respect to crashworthiness. Zhou et al. [9] executed axial crushing tests on an S-shaped frontal frame structure of a car body. The component was made of steel and aluminium sheets that were spot welded together. The aim of this study was to evaluate the influence of different design parameters on the crashworthiness of the structure. A three-point bending-like test was carried out by Chen [10], using components consisting of different closed top-hat sections of aluminium sheets. The sections were joined using spot welding and filled with an aluminium foam core. Carlberger and Stigh [11] performed similar bending tests on an aluminium-steel component. The aim of this study was to evaluate how different joining techniques affect the impact properties of the structure. They tested with adhesive bonding, screws and nuts, and hybrid joints consisting of both. A similar set-up was used by Qi et al. [12] to test a double-hat beam composed of an aluminium upper hat and a high strength steel lower hat, riveted together. Hoang et al. [13] performed quasi-static T-component

tests with two load configurations on a component consisting of two aluminium extrusions. They were joined using self-piercing rivets made of aluminium. The aim of the study was to assess the applicability of rivets made of aluminium under crash loadings.

Since limited information on the topic exists, a new component test for FDS connections is presented, where the dominating deformation mode is taking place in the connections, and at the same time has relevant and sufficiently complex loadings. A test where the failure of connections can be discerned in the global response of the specimens is desired. Moreover, except for the study of Sønstabø et al. [3], no scientific publications have been found on dynamic testing of FDS connections. Thus, there is also a lack of knowledge about their dynamic behaviour. An aim of this paper is to remedy both.

In addition to experimental testing, car designers rely heavily upon large-scale finite element crash simulations. Due to time step requirements, connections such as FDS cannot be modelled in detail. Instead, macroscopic models are used, in which the connections are excluded, but their global behaviour is modelled as a constraint or with simple elements. Such models must be calibrated and validated with experimental tests, for which component tests are important to assess the models' ability to represent complex loadings [5].

This paper presents an innovative component test suited for quasi-static and dynamic testing of FDS connections between aluminium extrusions, for validation of large-scale numerical simulations. The component specimen was made of two different aluminium alloys, and included connections with two material combinations. An improved modelling technique for large-scale finite element simulations was presented, and calibrated using cross tension, cross mixed and single lap-joint tests, and validated with peeling tests and the component tests. The component tests are presented first. Then follows a section about the finite element modelling. The component simulations are then presented and discussed, before a summary and conclusions. The single-connector tests are briefly presented in the appendix.

2 Component tests

In this section the component tests are presented. The component design is discussed first. The quasi-static test is then introduced, with a discussion of the test set-up, followed by the results. Thereafter follows the set-up of the dynamic component test and an analysis of the results.

2.1 Component design

For validation purposes, the following desirable properties were basis for the design of the component test specimen:

- Relevant and sufficiently complex loadings on the connections were desired. During a car crash, loadings are highly complex and difficult to evaluate. The component tests should represent relatively controlled deformation modes.
- The component specimen was designed such that material deformation outside the connections was limited. A test where the dominating deformation mode takes place in the connections, and where the failure of connections can be discerned in the global response of the specimens, was desired.
- Manageable boundary conditions was essential for test repeatability as well as for reproducibility in finite element models.

The resulting component design is shown in Fig. 1a. It consisted of a vertical two-chamber extrusion profile made of alloy AA 6005 T6 produced by SAPA, joined to two rectangular profiles of alloy AA 6060 T6 produced by Hydal Aluminium Profiler. Angle plates cut out of the rectangular profile were used to join the parts. Thus, the joint consisted of two different FDS connections, one between two plates of the 6060-extrusion and one between the 6060 and the 6005-extrusion (hereafter denoted the *HH-connection* and *HS-connection*, respectively). In both connections a case hardened carbon steel flow-drill screw from EJOT was used, and a pre-hole of 7 mm diameter was present in the top plate. Schematic drawings of the two connections are shown in Figs. 1b and 1c, where nominal dimensions of the screw are included. Nominal dimensions of the component specimen and screw locations are given in Fig. 1d, and schematic drawings of the extrusion profiles are presented in Figs. 1e and 1f. As seen in the figures, the specimen was simply supported. The supports were made of solid steel, round with a diameter of 50 mm, and placed 600 mm apart. The specimens were joined by EJOT GmbH & Co. KG.

Engineering stress-strain curves of the extrusions were obtained with uniaxial tensile tests in the extrusion direction. Representative curves are presented in Fig. 2. As seen, the 6005-alloy was strongest with approx. 50 % higher yield stress, while the 6060-alloy was approx. 20 % more ductile. It has previously been shown that the 6005-alloy exhibits some strain-rate sensitivity [14], while the 6060-alloy is only slightly strain-rate sensitive [15].

The component design and test set-ups were inspired by the work of Grimsmo et al. [16], who conducted quasi-static and dynamic tests on a double-sided beam-to-column joint configuration to study the behaviour of structural joints subjected to impact loading.

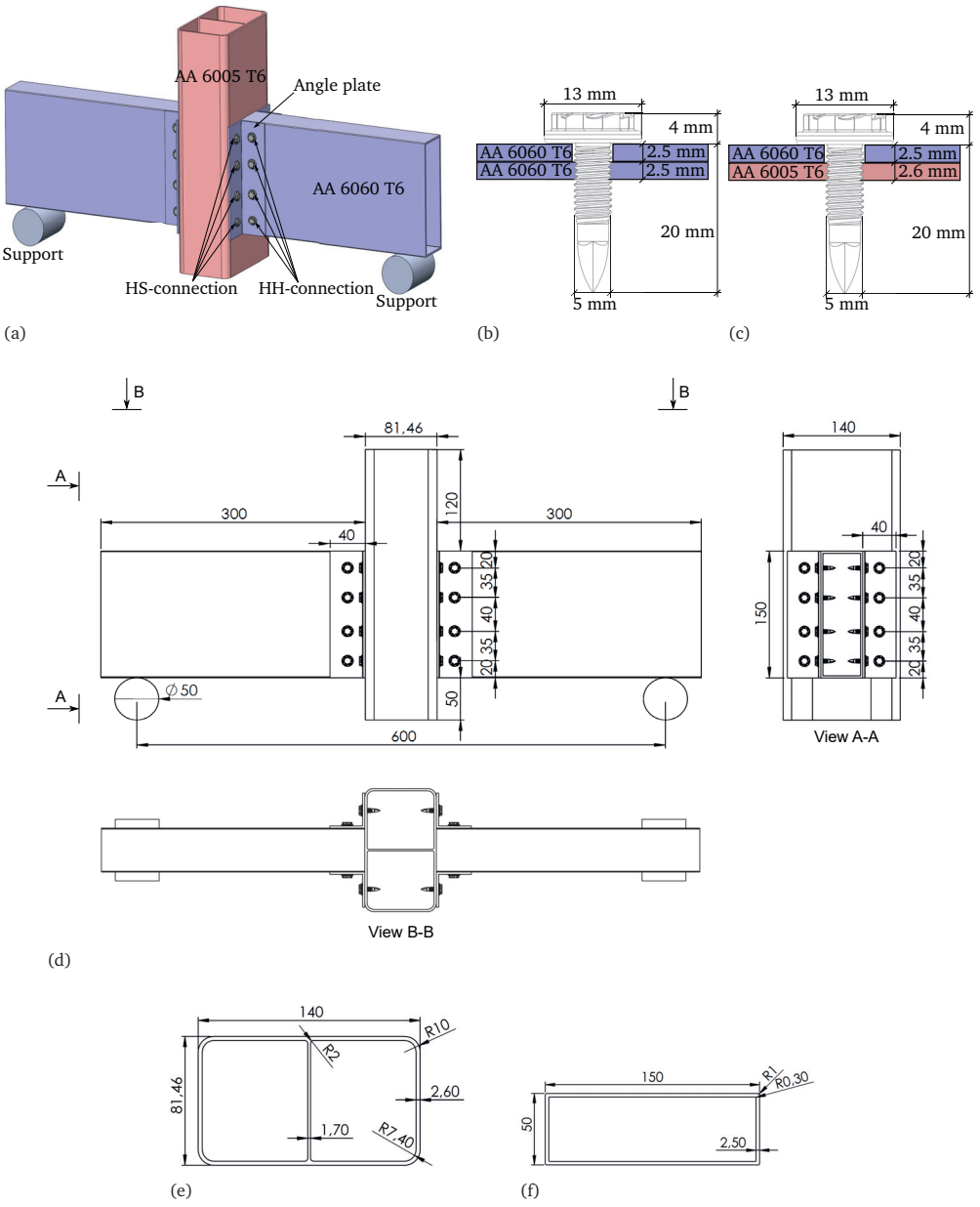

Fig. 1. Component design. (a) CAD model of component. (b) HH-connection. (c) HS-connection. (d) Schematic drawing of component (front, end and top view) (e) The 6005 extrusion profile. (f) The 6060 extrusion profile. All dimensions are nominal values.

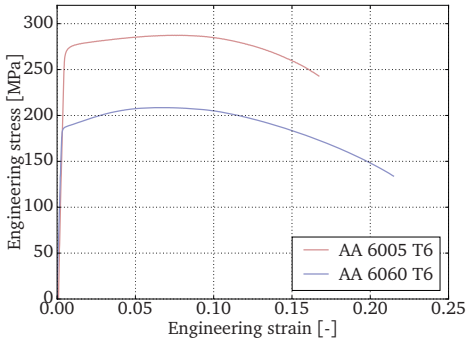

Fig. 2. Representative engineering stress-strain curves from uniaxial tensile tests in the extruded direction of the extrusion materials.

2.2 Quasi-static set-up

Fig. 3 depicts the quasi-static test set-up. The supports were firmly mounted to a regular tensile test machine. Care was taken to ensure that the supports and specimen were placed symmetrically about the centre of the test rig. The specimen was held in place with rubber bands. L-shaped steel bars were welded to the sides of each support, to hold the specimen in place in case of out-of-plane rotations. Such rotations did not occur in any of the tests, including the dynamic ones.

A downward-directed force was applied to the top of the vertical profile of the specimen, by pushing down a circular solid steel plate at a constant velocity of 10 mm/min. The force history was recorded with a load cell connected in series between the steel plate and the cross beam of the test machine. The vertical displacement of the steel plate and the deformation of the specimen were recorded with cameras taking one picture per second during the test. Five replicates were performed.

2.3 Quasi-static results

The resulting force-displacement curves are plotted in Fig. 4. As seen, excellent repeatability was obtained. The force increased gradually as the specimen was loaded until flattening out to a plateau at approximately 15 kN, caused by buckling of the inner wall in the vertical profile. After the plateau the force further increased until reaching the maximum capacity of the specimen at approximately 18 kN. Global failure then initiated by a rapid failure in one of the lowest HS-connections. Soon after, the corresponding connection on the other sides failed in the same manner. Failure of the lowest connections redistributed the load to the next screws, and so on, resulting in propagating connection failure along the rows of

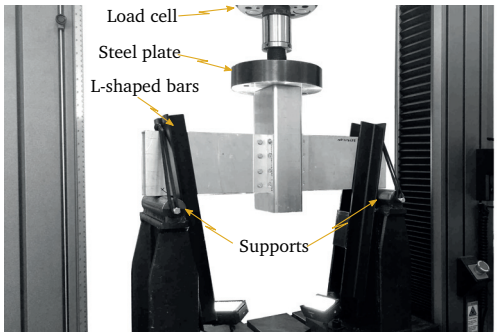

Fig. 3. Quasi-static test set-up.

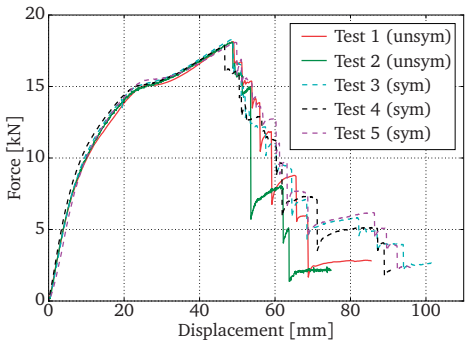

Fig. 4. Force-displacement curves from quasi-static component tests.

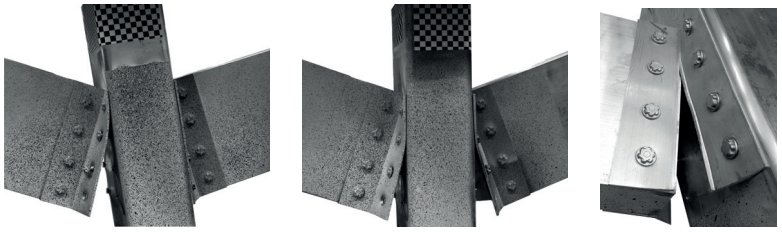

(a) (b) (c)

Fig. 5. Pictures of components during quasi-static testing showing (a) unsymmetrical and (b) symmetrical specimen deformation, and (c) material failure in test 4.

screws.

In the first two tests failure took place on one side of the vertical profile, resulting in an unsymmetrical specimen deformation mode. For the remaining three tests failure occurred symmetrically about the vertical profile. This is shown with pictures taken during testing in Figs. 5a and 5b. A possible cause for triggering different failure modes is variations in structural capacity and ductility of the connections. This could result in one side of the vertical profile being weaker than the other, possibly resulting in an unsymmetrical deformation mode.

In test 4, one of the four angles fractured in the corner, rather than failing in the connections. This is shown in Fig. 5c. In the three remaining angles connection failure occurred. The specimen deformed nevertheless symmetrically. Despite the fractured angle, the force-displacement curve was similar to the other tests. Test 4 was left out from the plots in the remaining of the paper.

2.4 Dynamic set-up

The dynamic component tests were carried out with a pendulum accelerator, which is a device designed for impact testing of structural components, see Fig. 6a. Details on the rig and its functions have previously been reported by Hanssen et al. [17], hence only the main aspects are explained herein. The specimen was mounted on the supports with rubber bands as in the quasi-static test, and the supports were fastened to a reaction wall, which weighs 150 000 kg and rests on neoprene supports. The specimen was impacted by a trolley with mass 399.9 kg travelling on rails, accelerated by a rotating arm. The arm was controlled by a hydraulic/pneumatic actuator. With this set-up the contact between the trolley and the arm ceases after a certain rotation, and the trolley subsequently travels down the rails at a near constant velocity. The velocity is controlled by varying the pressure in a hydraulic piston accumulator. More details of the test set-up are provided by Fig. 6b.

When the trolley impacts the specimen, the double-chamber profile is accelerated towards the reaction wall, leading to dynamic loading of the connections. After approximately 100 mm displacement after impact, buffer plates on the trolley hit a set of secondary crash absorbers. This is necessary since the specimen does not absorb enough energy to stop the

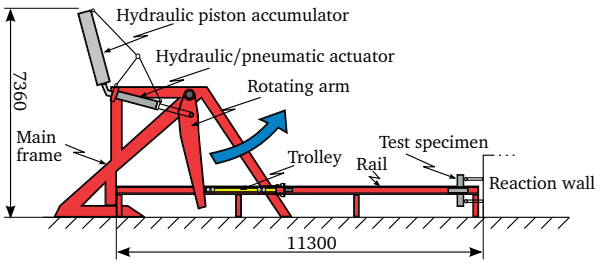

(a)

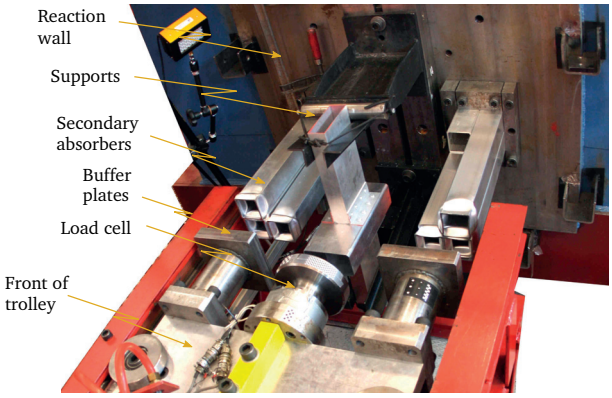

(b)

Fig. 6. Dynamic test set-up. (a) Illustration of the dynamic test rig [16]. (b) Picture showing details of the dynamic test set-up.

trolley.

Four high-speed cameras were utilized to capture the test. Two were aimed towards the top of the specimen where the impact occurred, and the remaining two at the connections in one of the four angles. The cameras took pictures at rates ranging between 20 000 and 30 000 frames per second. The impact velocity was measured with a photocell system, mounted on top of one of the rails. A laser mounted on the floor measured the displacement of the reaction wall (it was verified that the reaction wall displacement was negligible).

A load cell was mounted between the trolley and the specimen. It consisted of two circular solid steel plates and a thin-walled steel cylinder. Two strain gauges were mounted on the cylinder. Assuming that the load cell behaved elastically, the force was calculated from the average strain from the gauges. Adequate accuracy of the load cell was verified beforehand. The sampling rate of the load cell and laser was 250 kHz.

The trolley displacement was calculated from the force signal, by dividing with the mass of the trolley (Newton's second law) and integrate the acceleration twice in time. The obtained displacement was verified with digital image correlation (DIC), using the pictures from the high-speed cameras (readers are referred to Fagerholt [18] for details on DIC).

Five repetitions were carried out, all with an impact velocity of 7 m/s. In each test care was taken to place the specimen symmetrically on the supports.

2.5 Dynamic results

Fig. 7 shows the force-time curves measured by the load cell for all five repetitions. As seen, adequate test repeatability was achieved. Immediately after the first impact a peak force developed and then rapidly decreased and oscillated around zero for some time. Approximately 1 ms into the test the force somewhat increased again, still oscillating significantly. At 2 ms the oscillations stabilised noticeably, and the force steadily increased to a maximum between 15 and 20 kN, before decreasing again.

The oscillations in the force recordings were expected and is a result of the dynamic nature of the test. Throughout the test the specimen exerted many impulses on the front of the load cell. These impulses generated stress waves travelling through the load cell, into the trolley, and to the end of the trolley where they were reflected. As a consequence, throughout the test a myriad of stress waves travelled back and forth in the load cell, causing the strain signal (and thus the force signal) to oscillate.

From the high-speed camera recordings it was evident that after the initial impact the specimen gained a higher velocity than the trolley, and therefore departed from the trolley

and the contact between the load cell and specimen ceased. The time period without contact was measured to last approximately 0.8 ms, and is indicated with a shade of grey in Fig. 7. Within this time period the trolley-load cell system vibrated "freely", such that the force signal at this time only contained information from the trolley-load cell system. By measuring the period of the first oscillation following the initial peak, the frequency of the vibration may be calculated as approximately 2700 Hz. This is supported by Fig. 8, which shows the fast Fourier transform of the force signal from each test. It is seen that there were significant frequency components in the vicinity of 2700 Hz.

Hanssen et al. [17] argued for filtering of the load cell signal. When examining Figs. 7 and 8 it may be tempting to filter out frequencies higher than, for instance, 2000 Hz with a low-pass filter. However, Fig. 9 disfavours such a decision. The figure shows a contour plot of a short time Fourier transform of the force signal from test 1. The force signal was divided into smaller segments, and for each segment the fast Fourier transform was computed and the frequency spectrum plotted. Thus Fig. 9 shows how the frequency spectrum of the force signal varied throughout the test. From the figure it is evident that during the time without contact between the load cell and the specimen the significant frequency components ranged approximately between 1500 and 4000 Hz. After 2 ms, when firm contact between the specimen and trolley was achieved, the significant frequency components ranged from 0 to approximately 2000 Hz. Thus, filtering out the frequencies higher than 2000 Hz would not reveal any new information, but lead to a degradation of the quality of the results. Therefore it was decided to not filter the results, except for some high-frequency noise in the force signals which were filtered out with a zero-phase Butterworth filter with a cut-off frequency of 20 000 Hz.

A representative force curve is plotted against the trolley displacement in Fig. 10, where a corresponding representative quasi-static force-displacement curve is included for comparison. As seen, the two curves overlay each other, which indicate that no global inertia effects in the specimen influenced the impact. This is due to the fact that the impacting mass was large compared to the mass of the specimen. The results did not suggest any significant rate effects on the global force-displacement behaviour of the FDS connections between these materials, for this velocity range.

Pictures from test 1 taken by one of the high-speed cameras are displayed in Fig. 11a, and an overview highlighting the section depicted is shown in Fig. 11b. The corresponding time and trolley displacement are given for each frame. In the first frame the specimen is undeformed. The second frame was taken at the time corresponding to the displacement where the inner wall of the double-chamber profile buckled in the quasi-static test. Frame three is from just before the force started to drop due to failure of the first connection. In the fourth frame the second connection is about to fail. The fifth was taken shortly before

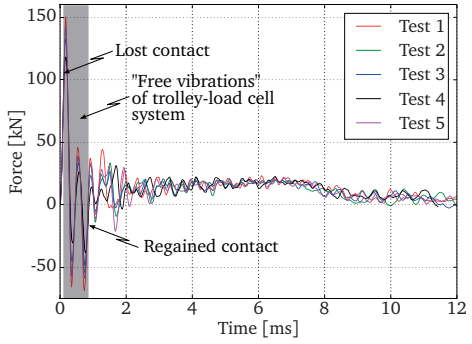

Fig. 7. Force-time curves from dynamic component tests.

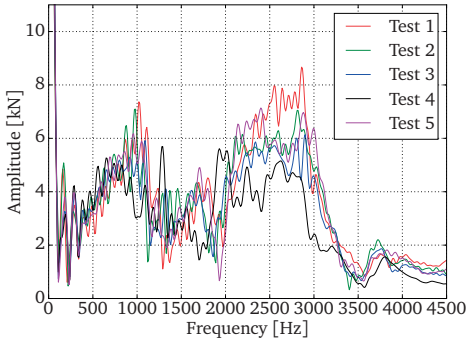

Fig. 8. Fast Fourier transform of the force signals.

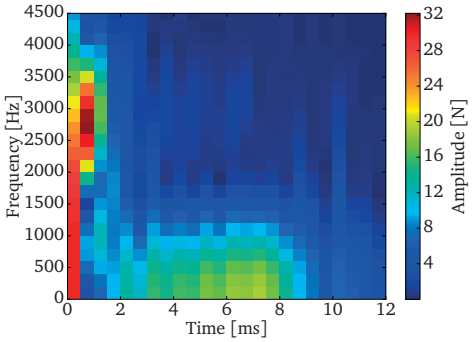

Fig. 9. Short time Fourier transform of the force signal from test 1.

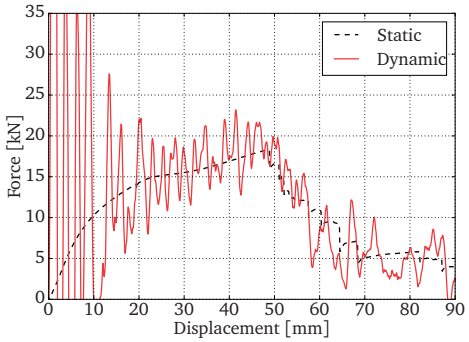

Fig. 10. Representative force vs. trolley displacement in dynamic test compared to a representative force-displacement curve from the quasi-static tests.

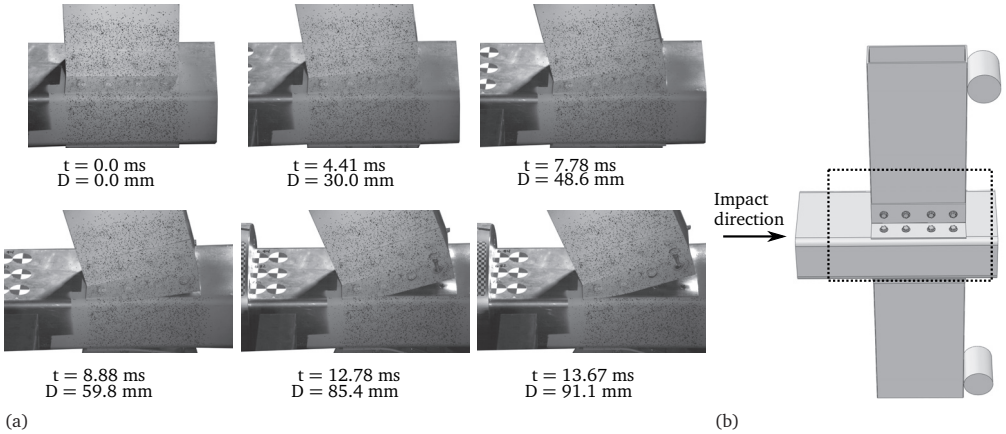

Fig. 11. Pictures of the specimen in dynamic test 1 at various times, as recorded by one of the high-speed cameras. (a) Different frames. (b) Overview showing where the pictures were taken.

the third connection failed. In the last frame the third connection had failed and the test came to an end. The collection of frames clearly shows the propagating failure of the screw connections. Two of the specimens had a symmetric deformation mode, while the remaining three deformed asymmetrically.

3 Finite element modelling

3.1 Numerical set-up

In this section the finite element models are explained in detail. All tests (including the single-connector tests) were simulated with the same approach, therefore a general description of the numerical set-up is given here.

3.1.1 Material model

The extrusion materials were modelled with a rate-independent hypoelastic-plastic material model. An isotropic yield surface was used, the associated flow rule was assumed, and isotropic work hardening was applied. It is known that the 6005-alloy is somewhat strain-rate sensitive [14]. However, in the component test the significant strains in the 6005-alloy were localised in the vicinity of the screw, which were included in the macroscopic model of the connections (see Section 3.1.2). Furthermore, the 6060-alloy exhibits only slight strain-rate sensitivity [15]. It was therefore not necessary to include rate-sensitivity to model the extrusion materials.

To predict yielding the non-quadratic Hershey yield criterion was used [19]. The yield function is given as

$$f = \phi - (\sigma_0 + R) \leq 0,$$

where

$$\phi = \left[\frac{1}{2} \left\{ |s_1 - s_2|^a + |s_2 - s_3|^a + |s_3 - s_1|^a \right\} \right]^{\frac{1}{a}}.$$

Here σ_0 is the initial yield stress, R is an isotropic hardening variable, s_1, s_2 and s_3 are the principal deviatoric stresses, and a is a parameter defining the curvature of the yield surface. The value of a was set to 8, as this value has been shown to describe the behaviour of FCC materials [20]. To represent work hardening the Voce hardening law was used. With the

Table 1
Material model parameters for the extrusion materials.

	ρ [kg/m^3]	E [MPa]	ν [-]	a [-]	σ_0 [MPa]	Q_{R1} [MPa]	θ_{R1} [MPa]	Q_{R2} [MPa]	θ_{R2} [MPa]	Q_{R3} [MPa]	θ_{R3} [MPa]
AA 6060 T6	2700	70000	0.33	8.0	183.2	2.5	5746.3	52.1	985.7	-	-
AA 6005 T6	2700	70000	0.33	8.0	275.7	8.6	7095.1	48.5	702.3	12.2	166.2

Voce law, the hardening variable is defined as

$$R = \sum_{i=1}^{N_R} Q_{Ri}\left(1 - \exp\left(-\frac{\theta_{Ri}}{Q_{Ri}}p\right)\right),$$

where p is the equivalent plastic strain, N_R is the number of terms, and Q_{Ri} and θ_{Ri} are the saturation value and initial hardening moduli for term i, respectively.

The material parameters σ_0, Q_{Ri} and θ_{Ri} were found according to the procedure described by Sønstabø et al. [5]. Uniaxial tensile tests were carried out in the extrusion directions, from which the parameters were found by inverse modelling using an optimisation algorithm. Typical aluminium values were used for the Young's modulus E, the Poisson ratio ν and the density ρ. The parameters are summarised in Table 1.

3.1.2 Macroscopic connection model

Due to time step limitations in large-scale simulations, the automotive industry cannot model the FDS connection in detail. Therefore a macroscopic model is required for the connections. Sønstabø et al. [5] evaluated different state-of-the-art models for FDS connections, and concluded that the self-piercing rivet model presented by Hanssen et al. [21] was the most accurate and the easiest to calibrate. This model was therefore chosen in this work. Cf. Hanssen et al. [21] and Sønstabø et al. [5] for detailed descriptions of the model. A general explanation of the model is given in the following.

A node placed between two shell sections' mid-surface defines the location of the connection.

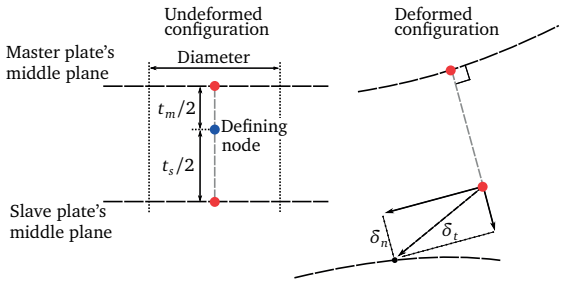

Fig. 12. Illustration of macroscopic connection model in plane of maximum opening.

Nodes on each shell surface within a user-specified diameter are included in the model. Local normal and tangential forces and a moment are transferred between the sheets, to the nodes within the specified diameter, calculated based on the relative motion between the master and slave surfaces. The model is defined in the plane of maximum opening. Figure 12 illustrates the kinematics, where t_m and t_s are the thickness of the master and slave sheet, respectively. The connection follows the master sheet, and the normal and tangential displacements δ_n and δ_t are calculated from the relative displacement to the slave sheet (see Fig. 12). The transferred normal and tangential forces f_n and f_t are calculated as

$$f_n = f_n^{\max} \frac{\delta_n}{\delta_n^{\text{fail}} \eta_{\max}} \hat{f}_n(\eta_{\max})$$
$$f_t = f_t^{\max} \frac{\delta_t}{\delta_t^{\text{fail}} \eta_{\max}} \hat{f}_t(\eta_{\max}),$$

where $f_n^{\max}$ and $f_t^{\max}$ are the maximum forces under pure tension and pure shear loading, respectively, and δ_n^{fail} and δ_t^{fail} are the corresponding local displacements at failure. The empirical functions $\hat{f}_n(\eta_{\max})$ and $\hat{f}_t(\eta_{\max})$ characterise the shape of the force-displacement response. They are defined and illustrated in Fig. 13a. The parameters ξ_n and ξ_t in Fig. 13a are the normalised displacements at which softening starts. Further, $\eta_{\max}$ is a damage parameter defined as the highest value of the effective displacement measure η, i.e. $\eta_{\max} = \max(\eta, \eta_{\max})$. Fig. 13b defines and illustrates the effective displacement measure η, which depends on the mode mixity defined by the angle $\theta = \arctan(\delta_n/\delta_t)$. The variable α makes the mode-mixity dependence damage-dependent, where α_1, α_2 and α_3 are user-parameters.

After the forces $f_n^{\max}$ and $f_t^{\max}$ have been determined, the moments transferred to the nodes on the master and slave sheets, M_m and M_s, respectively, are calculated using the relations

$$M_m = \begin{cases} \dfrac{t_m + t_s}{4} f_t & \eta_{\max} < \xi_t \\ \dfrac{t_m + t_s}{4} \left(1 + \dfrac{\eta_{\max} - \xi_t}{1 - \xi_t}\right) f_t & \eta_{\max} \geq \xi_t \end{cases}$$
$$M_s = \begin{cases} \dfrac{t_m + t_s}{4} f_t & \eta_{\max} < \xi_t \\ \dfrac{t_m + t_s}{4} \left(1 - \dfrac{\eta_{\max} - \xi_t}{1 - \xi_t}\right) f_t & \eta_{\max} \geq \xi_t \end{cases}.$$

Moment balance is thus satisfied.

The following parameters must be calibrated to tests by the user of the model: $f_n^{\max}$, δ_n^{fail}, ξ_n, $f_t^{\max}$, δ_t^{fail}, ξ_t, α_1, α_2, α_3, and the diameter of influence. They were identified through reverse engineering of the chosen single-connector tests, by comparing global force-

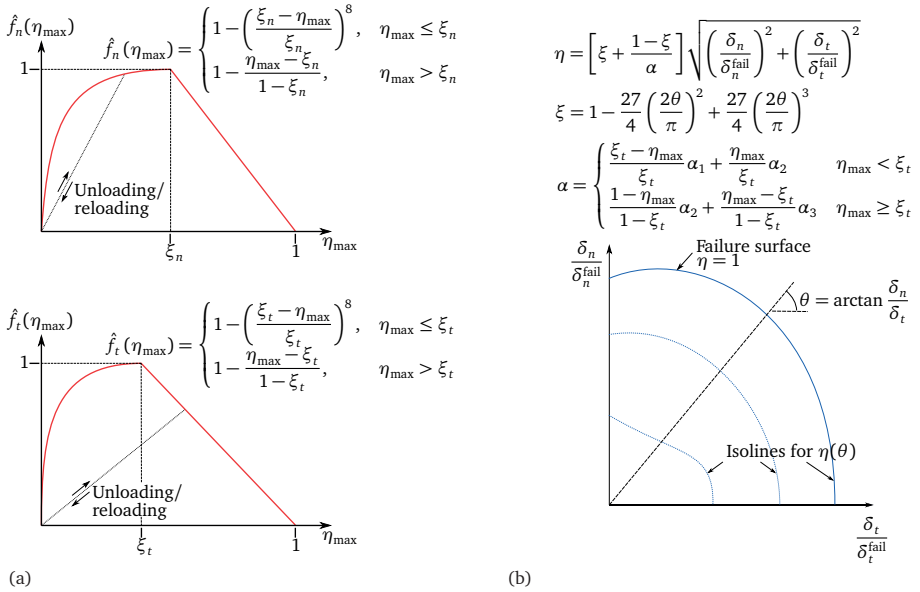

Fig. 13. Definition and illustration of (a) local forces and (b) effective displacement measure in connection model.

displacement curves from simulations to the corresponding curves from experimental tests. Some parameters were taken directly from the experiments ($f_n^{\max}$ and $f_t^{\max}$) or manually tuned to fit the results (δ_n^{fail} and δ_t^{fail}). The remaining parameters were optimised with the Levenberg-Marquardt algorithm, using the mean squared error between the simulation and experimental force-displacement curves as residual function. The optimisation software LS-OPT® (version 5.2) was used. The remaining tension and shear parameters (ξ_n and ξ_t) were optimised first, followed by the mode-mixity parameters (α_1, α_2 and α_3). The diameter of influence affects the stiffness and force response in tension. An increasing diameter increases the stiffness of the plates. The diameter of the screw head and shaft was 13 and 5 mm, respectively. The average diameter of 9 mm was therefore chosen as diameter of influence of the connection model.

No information regarding dynamic single-connector testing of FDS connections is available in the scientific literature. Such tests are difficult to perform. Thus, it is not known if FDS connections are rate sensitive. This model does not exhibit rate sensitivity.

3.1.3 Limitations of macroscopic modelling

There are certain inherent limitations associated with representing the connection with a macroscopic model. First of all it is important to understand that the model is merely

intended to represent the global force-displacement behaviour of the connection, and not the local deformation. This means that the deformation of the screw, and the surrounding plate material close to it, is embedded into the macroscopic model. The connection is not physically modelled, it is just represented by a mathematical constraint. This implies that one can not always expect to correctly predict deformation and failure modes occurring in physical tests. For instance, in an FDS connection one side has the screw head on top, while the other has the screw tail sticking out. These geometrical features are not manifested in the model. Sønstabø et al. [3] and Sønstabø et al. [5] reported deformation and failure modes occurring due to contact between the tail of the screw and other parts. Such modes can not be captured by this type of model.

An example of a limitation is shown in Figs. 14a and 14b which depict the deformation of a peeling test and corresponding simulation, respectively. As seen, the deformation pattern was not correctly predicted. In the test a clear bend was visible in the bottom plate close to the screw, while it did not appear in the simulation. The connection model is symmetric in the sense that the diameter is the same for both sides of the connection. Thus, since the top extrusion had a lower yield stress than the bottom, deformation localised there. In the test, however, the presence of the screw head stiffened the top plate, causing the bottom extrusion to bend as well. As a remedy to try and capture the correct deformation mode it was decided to include a simple model of the screw head, consisting of a circular patch with diameter 13 mm and height 4 mm (see Fig. 1c). The patch was modelled with 20 regular eight-node brick elements with reduced integration, and was attached to the top extrusion's shell mid-surface using a tie constraint. The elements were assigned a purely elastic material model with typical steel parameters ($E = 210000$ MPa, $\nu = 0.33$ and $\rho = 7800$ kg/m^3). Fig. 14c depicts the resulting deformation. As seen the deformation mode now correlated better with the experiments. The solid elements stiffened the top plate as intended, a bend was clearly visible in the bottom plate close to the screw. Therefore it was decided to include

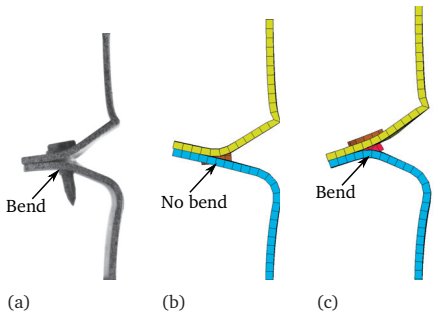

Fig. 14. Deformed peeling specimen (HS-connection) in (a) experiment, (b) simulation with no head and (c) simulation with head.

the head in all simulations in this study.

3.1.4 Finite element models

Fig. 15 depicts the finite element models used in the present investigation. The extrusions were discretised with fully integrated Belytschko-Lin-Tsay shell elements [22] with a mesh size of 3x3 mm and five integration points through the thickness. This mesh size was chosen because it is known to be used in the automotive industry. The shell thickness was set to 2.43 mm for the rectangular profile, and 2.57 and 1.747 mm for the outer and inner wall of the double-chamber profile, respectively. These values were the averages of thickness measurements at various locations. Contact between the different parts was modelled with a surface-to-surface penalty algorithm, where a static friction coefficient of 0.2 was chosen. The connection model described in Section 3.1.2 was applied at all connection locations.

Since the experimental set-up was the same for the quasi-static and dynamic component tests, the same numerical set-up was used for the simulations. The model is shown in Fig. 15a. The supports were modelled as rigid bodies, and a friction coefficient of 0.2 was chosen for the contact between the specimen and the supports. The impactor was modelled as a rigid wall. In the quasi-static simulation a prescribed velocity was assigned to the wall (as indicated with arrows in Fig. 15a), and the force was recorded from the reaction force on the wall. In the dynamic simulation the rigid wall was assigned a mass of 400 kg and an initial velocity of 7 m/s. The displacement and acceleration of the rigid wall was recorded, and the force acting on the rigid wall from the specimen was calculated by dividing the wall acceleration by its mass.

The finite element models of the single-connector tests that were used for calibration and validation of the macroscopic connection model are shown in Figs. 15b to 15e. The

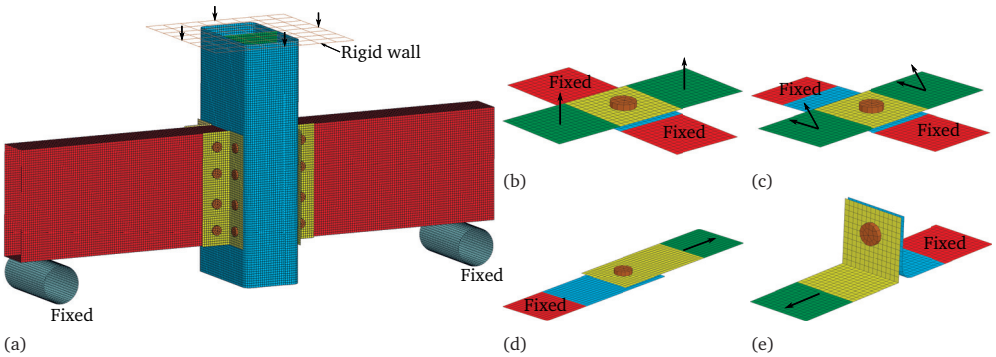

Fig. 15. FE models. (a) Component (b) Cross tension. (c) Cross mixed and shear. (d) Single lap-joint. (e) Peeling.

red and green parts in the figures correspond to the areas that were clamped in the experiments. These parts were modelled as rigid bodies. The red parts were constrained against displacement and rotation in any direction, while a prescribed velocity in the loading direction was assigned to the green parts, as shown with arrows. The global force and displacement was recorded from the boundary force and displacement of the green parts, respectively. Details of the single-connector tests are reported in Appendix A.

All simulations were carried out with the explicit solver LS-DYNA® version R9.1 with double precision. For the simulations of the quasi-static tests time scaling was applied to facilitate reasonable computational times. Inertia effects were ensured negligible by confirming that the kinetic energy was insignificant compared to the internal energy of the materials.

3.2 Calibration of connection model parameters

Sønstabø et al. [5] presented a calibration/validation procedure which was adopted here. The procedure involves calibrating the connection model using simple single-connector tests under controlled loading conditions. A different set of single-connector tests is subsequently used for a first validation of the model. The validation tests should challenge the model under different loadings than the calibration tests and have varying degrees of complexity. A second level of validation is achieved with component tests, which represent more complex loadings on the connections. Sønstabø et al. [5] calibrated to cross tests in tension, mixed mode and shear. The single lap-joint and peeling tests were used for the first validation step, while a T-component test was used for the second.

In this work the tension parameters $f_n^{\max}$, δ_n^{fail} and ξ_n were calibrated to the cross tension tests, and the mode-mixity parameters α_1, α_2 and α_3 to the cross mixed tests. The shear parameters $f_t^{\max}$, δ_t^{fail} and ξ_t were, however, calibrated to the single lap-joint tests, and not the cross shear tests. The reason for this choice is linked to Fig. 16, which shows the force-displacement response in the cross shear and single lap-joint tests plotted together. Both the cross shear and single lap-joint tests were shear dominated, and a similar response was expected, and, as seen in the figure, both tests gave the same response until maximum force. After maximum force, however, a significantly dissimilar behaviour developed. In the cross shear tests the force remained at a plateau before a near linear decrease. In the single lap-joint tests the force started to slowly decay immediately after maximum force, before a rapid failure where the force suddenly decreased to zero. This difference is possibly explained by the different boundary conditions in the two tests (readers are referred to Appendix A for details on the test set-ups). During the single lap-joint tests the plates were allowed to bend near the connection (see Fig. 17a). In the cross shear specimens this bending was prevented by more restrictive clamping. Thus, the loading conditions were different in the

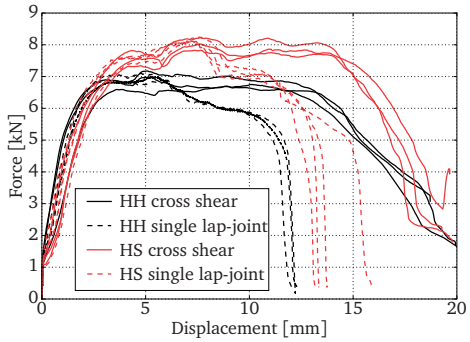

Fig. 16. Comparison of results from cross shear and single lap-joint tests for both connections.

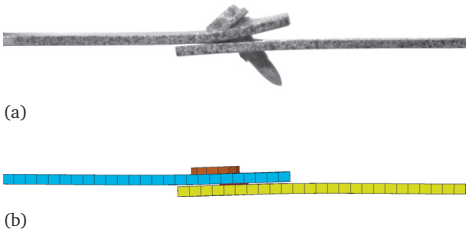

Fig. 17. Deformed single lap-joint specimen at 10 mm displacement (HS-connection). (a) Experiment. (b) Simulation.

two tests. The rotation of the screw shaft and the presence of the pre-hole in the top plate facilitated the bending. The macroscopic connection model does not include the screw, however, and hence this effect cannot be captured in the simulations. The simulations of the cross shear and single lap-joint tests gave instead almost identical force-displacement result. Fig. 17 compares a picture from the experiments with the deformation in the single lap-joint simulation. It is seen that the simulation did not properly capture the bend of the top plate, with the result that the connection was loaded in almost pure shear. It is believed that if the bending of the plates had been properly captured, a larger tensile component would emerge and effectively reduce the ductility. Therefore a choice had to be made: to try and predict the cross shear or the single lap-joint test. Both approaches were tried, but when the parameters were calibrated to the cross shear test the ductility and maximum force of the peeling test were severely over-predicted. With calibration to the single lap-joint test better predictions in peeling were achieved. For this reason the calibration to the single lap-joint test was chosen. The resulting model parameters are summarised in Table 2.

The force-displacement curves from the simulations of the single-connector tests with all parameters calibrated are compared to the experimental curves in Figs. 18 and 19 for the HH and HS-connections, respectively. As seen, acceptable fits were achieved for the calibration simulations (cross tension, cross mixed and single lap-joint), for both connections. In cross tension the simulation had a higher force response than in the test. This was because of the discretisation of the connection. The numerical diameter was set to 9 mm, while

Table 2
Connection model parameters for the FDS connections.

	Diameter [mm]	$f_n^{\max}$ [N]	δ_n^{fail} [mm]	ξ_n [-]	$f_t^{\max}$ [N]	δ_t^{fail} [mm]	ξ_t [-]	α_1 [-]	α_2 [-]	α_3 [-]
HH-connection	9.0	4200	4.2	0.89	7000	13.5	0.60	0.992	0.909	1.299
HS-connection	9.0	5400	6.2	0.82	7800	14.0	0.81	1.176	0.815	1.346

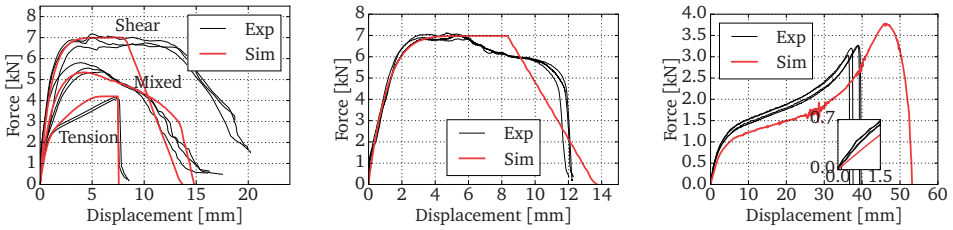

(a) (b) (c)

Fig. 18. Simulation results for the single-connector simulations of the HH-connections. (a) Cross simulations. (b) Single lap-joint simulations. (c) Peeling simulations.

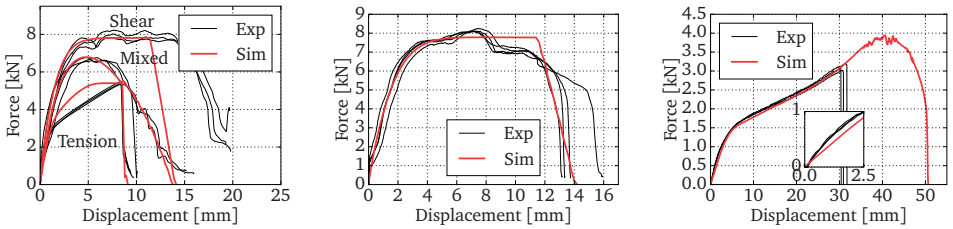

(a) (b) (c)

Fig. 19. Simulation results for the single-connector simulations of the HS-connections. (a) Cross simulations. (b) Single lap-joint simulations. (c) Peeling simulations.

the diameter of the screw shaft was 5 mm. Thus, the bottom plate behaved stiffer than in reality, causing a stiffer response in the simulation. The initial stiffness was correctly predicted, however. The two-step failure seen in the single lap-joint tests (slow softening followed by abrupt decrease of force) was not captured, since the connection model features linear softening. The ductility of the cross shear tests was under-estimated (as expected, see discussion above), while the force level was well predicted. In the peeling simulations the ductility and maximum force were over-predicted. Inserted zoomed-in details of the start of the simulations in Figs. 18c and 19c show that the initial stiffness was somewhat under-predicted. These discrepancies between tests and simulations under peeling loading is probably linked to the lack of physics in the connection model, caused by the poor discretisation of the connection, and highlights the challenges associated with macroscopic modelling of connections. Overall, considering the requirements for large-scale crash analyses, the simulations of the single-connector tests gave satisfying results.

4 Component simulations

In this section the component simulation results are presented and discussed. The quasi-static simulation is addressed first, followed by the dynamic. A parametric study from the

quasi-static simulation is presented in the end of the section.

4.1 Quasi-static component simulation

The global force-displacement curve from the quasi-static component simulation is presented in Fig. 20a. As seen, an acceptable prediction of the global behaviour was obtained in the simulation. As a first note, the maximum force level was correctly predicted. However, failure initiation occurred approximately 10 mm later than in the test. It is also noted that the value of the force plateau due to buckling of the inner wall was correctly captured, but also occurred approximately 10 mm later than in the test. It is believed that this shift in displacement of approximately 10 mm was caused by under-estimation of the initial stiffness. Fig. 20a includes an inserted box that details the start of the curves, where the under-prediction of the initial stiffness is obvious. A similar observation was made for the peeling test simulations, as shown in Figs. 18c and 19c and discussed in Section 3.2. It is believed that this is an inherent limitation of this type of macroscopic connection model. It seems that the model is incapable of describing the correct elastic deformation. The buckling of the inner wall and the failure initiation occurs when the force reaches a specific level. Thus it seems likely that had the initial stiffness been correctly predicted, the force plateau and maximum force would have occurred for the correct displacements.

Figs. 20b and 20c shows pictures of the deformation seen in the simulation, with numbers indicating the corresponding points on the force-displacement curve. In the pictures showing the inner wall in Fig. 20b one can clearly see how the buckle developed at the

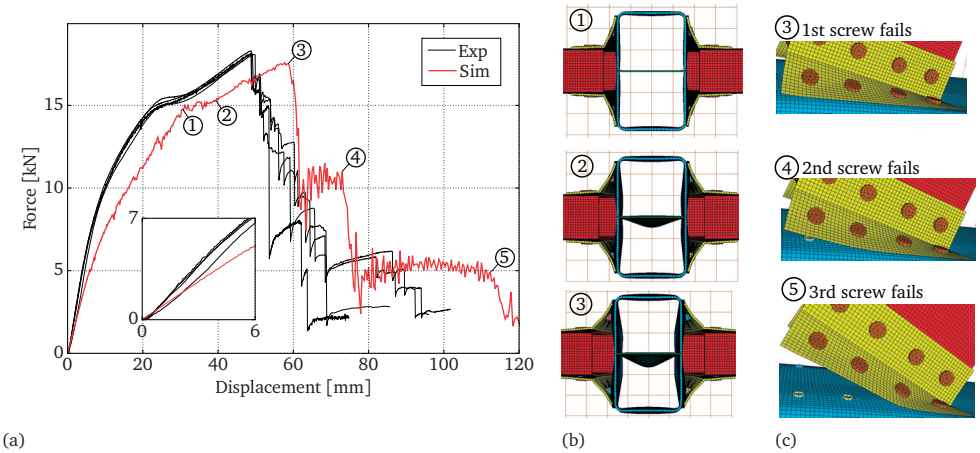

Fig. 20. Results from quasi-static component simulation. (a) Global force-displacement curve compared with tests. (b) Bottom view of specimen, showing development of the buckle of the inner wall. (c) Side view showing the propagation of connection failure. Numbers relate each picture to the corresponding point on the force-displacement curve.

force plateau. The pictures close up to the HS-connections in Fig. 20c show how failure propagated along the row of screws. In the experiments the four lowest HS-connections failed one after another, separated with a short time. In the simulation, however, all four failed at the same time. This was probably because the connection model parameters were identical for all connections, while in the experiments the connection failure properties were subjected to natural statistical variation. It is seen that failure in the third screw occurred much later in the simulation than in the experiment. This may indicate that the model is not able to redistribute forces accurately, and that prediction of failure propagation may be difficult with this modelling technique. No failure was observed in the HH-connections, as was the case in the experimental tests.

Fig. 21a shows the evolution of the local connection model forces, f_n and f_t, in the four HS-connections in one of the angles. The axial and shear force are plotted together, and the numbers 1-4 signify the connection number from the bottom and up (see Fig. 21b). As expected, in the start the forces were highest in the lowermost connection (number 1). When this connection failed the second connection took over, then the third. It is also seen that the axial force dominated in the three first connections. The shear force component was approximately 50 % lower. This is similar to what is typically observed in simulations of peeling tests, and suggests that the loading on the connections in the component test was somewhat similar to a peeling test.

In addition to the 3 mm mesh size, simulations were run with mesh sizes of 4 and 5 mm. The results are summarised in Fig. 22a. A small mesh-size effect is seen on the force-displacement curve, as failure occurred somewhat later in the simulation with 4 mm mesh size. Embedded in the figure are three pictures of a connection, showing how the mesh

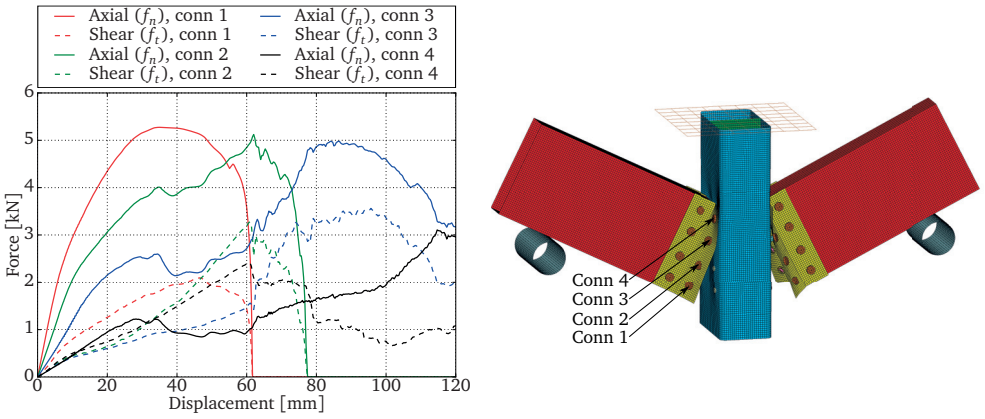

(a) (b)

Fig. 21. Local forces in connection model along one row of HS-connections. (a) Forces. (b) Illustration of connections 1 to 4.

size can affect the number of nodes lying within the diameter of influence of the connection model. It is apparent that the mesh size can have an effect on the macroscopic response of the connection.

Fig. 22b shows the effect of varying the friction coefficient between the specimen and supports from 0.0 to 0.5. As is typical for three-point bending tests, an effect is seen on the force level as well as the initial stiffness. Fig. 22c shows that the effect of varying the friction coefficient between the different parts in the component is insignificant. For friction coefficients 0.0 and 0.1 the force plateau at 15 kN disappeared, which was due to a change in deformation mode. Instead of buckling of the inner wall, the corner of the rectangular profiles collapsed. Considering that this did not occur in the tests, this mode was judged to be non-physical.

Fig. 23 shows the effect of excluding the elastic solid elements resembling the screw head. The simulation without the head was run with connection model parameters that were specifically calibrated without the head (i.e. not the ones reported in Table 2). As seen,

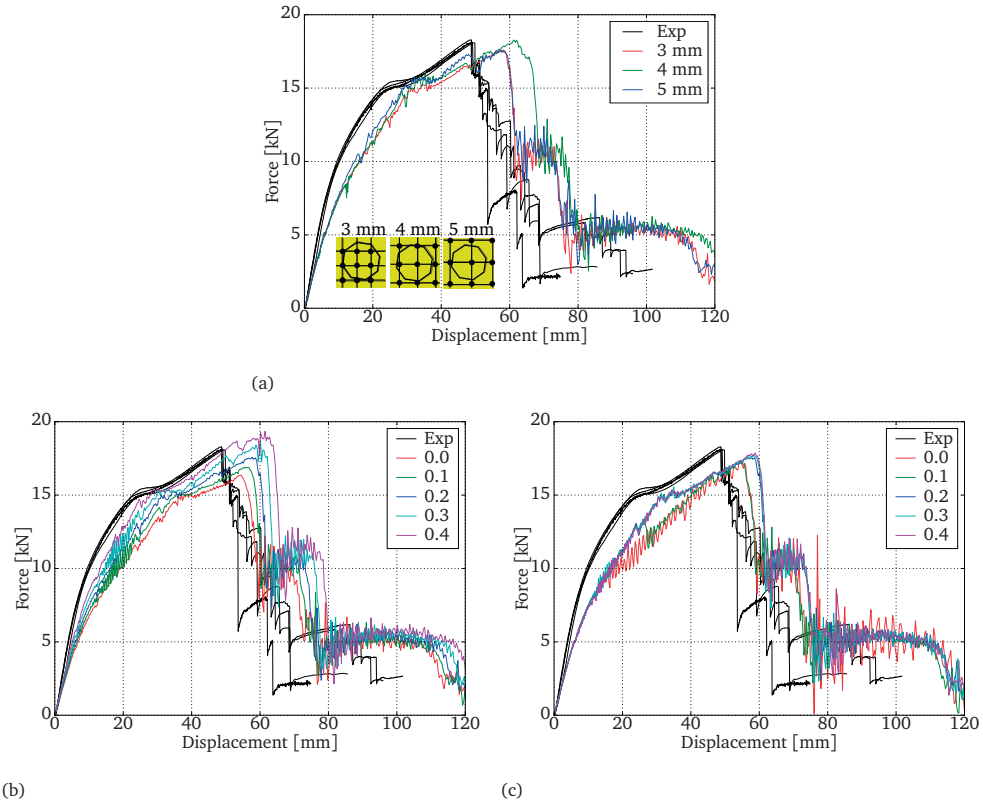

Fig. 22. Effect of varying the (a) mesh size, (b) friction coefficient between the supports and the specimen, and (c) the friction coefficient in the specimen.

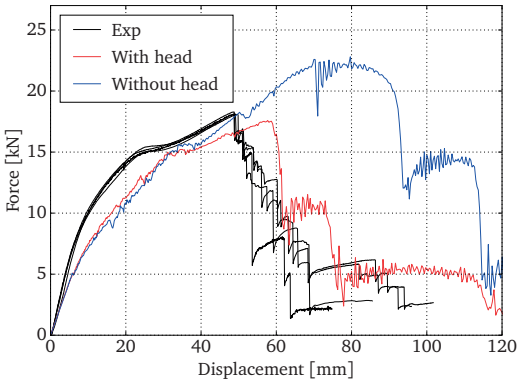

Fig. 23. Quasi-static component simulation with and without screw head.

without the head the results were dramatically deteriorated. The maximum force and failure displacements became significantly over-predicted. This supports the choice of including the simple model of the screw head when modelling FDS connections with this model.

4.2 Dynamic component simulation

Fig. 24 presents the force-displacement curve from the dynamic component simulation compared with experiments. Only one experimental curve is included for clarity. The quasi-static simulation result is also plotted. The dynamic simulation curve starts with several large peaks, separated by gaps with zero force. This was due to multiple impacts between the rigid wall and the specimen, each peak corresponding to one hit. The force was zero

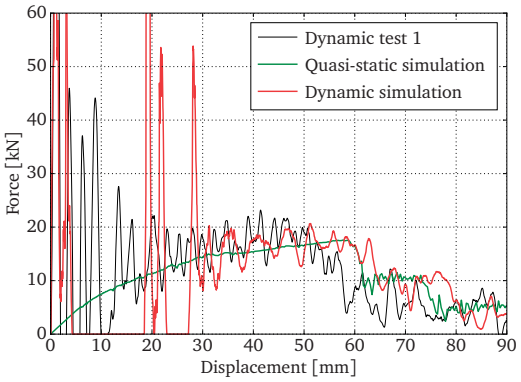

Fig. 24. Force-displacement curve from simulation of dynamic component test.

between the peaks because the rigid wall then had zero acceleration. The phenomenon with several hits was also seen in the experiments (see Fig. 7), but lasted for a significantly shorter period of time. The difference in "time without contact" between simulation and experiment was possibly a consequence of the under-estimated initial stiffness. Had the initial stiffness been correctly predicted, it is believed that the time with no contact between the load cell and the specimen would have been better estimated. After 30 mm displacement, firm contact was achieved between the specimen and the rigid wall, and from here on the force level correlated adequately with the experiments.

The curves from the dynamic and quasi-static simulations more or less overlaid each other after 30 mm displacement, except that the dynamic curve oscillated. This supports the observation that inertia effects in the specimen did not alter the structural response of the component. Differences between simulations and tests were present both in the quasi-static and dynamic cases, and were thus not related to dynamic effects. Therefore it was sufficient to address the quasi-static case to evaluate differences between tests and simulation.

4.3 Parametric study in quasi-static component simulation

As discussed in Section 2.3, variations in the structural response of FDS connections can occur due to geometrical and process variations. To study how such variations can affect the test results, simulations were carried out with connection model parameters δ_n^{fail}, δ_t^{fail}, f_n^{max} and f_t^{max} randomly distributed using a regular Gauss distribution. The mean value μ was set to the initial parameter value, and the standard deviation σ was chosen based on the scatter seen in the single-connector tests (Fig. A.2). The chosen values are given in Table 3. Each of the HS-connections were assigned a parameter value picked randomly from the Gauss distribution. Only one parameter (δ_n^{fail}, δ_t^{fail}, f_n^{max} or f_t^{max}) was changed per simulation, thus in total four simulations were carried out. The resulting force-displacement curves are plotted in Fig. 25a, with zoomed-in details in Fig. 25b. As seen, an effect was seen only for the parameter δ_n^{fail}, where the deformation mode changed from symmetrical to unsymmetrical (see Figs. 25c and 25d). This makes sense, since the loading on the connections was tensile dominated (recall Fig. 21), and since the test was displacement controlled. When one side had lower ductility, an unsymmetrical deformation mode was expected. This supports the discussion in Section 2.3.

Table 3
Parameters used in statistical distributions of connection model parameters.

Parameter	μ	σ
δ_n^{fail} [mm]	6.2	0.087
δ_t^{fail} [mm]	14.0	0.94
f_n^{max} [N]	5400	53.0
f_t^{max} [N]	7800	60.7

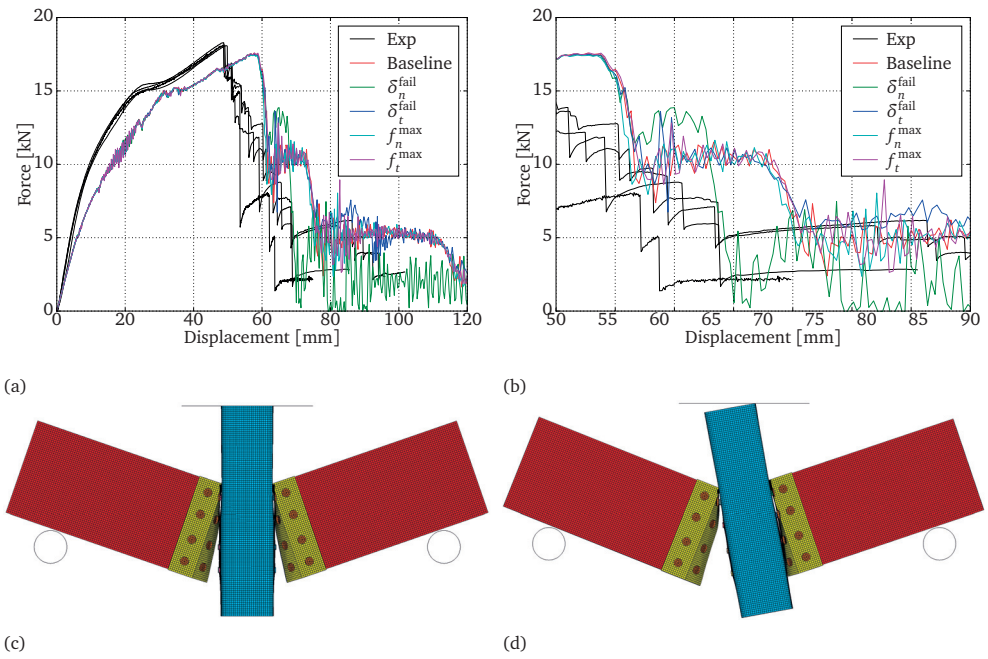

Fig. 25. Effect of statistical variation of connection model parameters. (a) Force curves. (b) Zoomed-in force curves. (c) Symmetrical component deformation. (d) Unsymmetrical deformation when varying δ_n^{fail}.

5 Summary and conclusions

In this work a novel component test suited for quasi-static and dynamic testing of flow-drill screw connections was presented. The component consisted of two rectangular extrusions of aluminium alloy AA 6060 in T6 temper joined to a double-chamber profile of aluminium alloy AA 6005 in T6 temper. The quasi-static tests were conducted in a regular tensile testing machine, while the dynamic were performed in a pendulum accelerator rig designed for impact testing. The tests were simulated with large-scale finite element models, where a macroscopic model for large-scale simulations was used for the connections. An improvement of the connection modelling technique was presented.

The following main conclusions were drawn from the experimental part of the study:

- High test repeatability was obtained, which makes the test suitable for validation of numerical models.
- The force-displacement curves from the dynamic and quasi-static tests were similar, indicating that no global inertia and strain-rate effects in the specimen influenced the structural response, for the investigated velocity range.
- In both the quasi-static and dynamic component tests a propagating connection failure was achieved. The test is thus suited to evaluate failure propagation in numerical simulations.

The following main conclusions were drawn from the numerical part of the study:

- By including a simple elastic model of the screw head, the component simulation results were significantly improved. It is advised to include a model of the head when modelling flow-drill screw connections.
- Good agreement with experiments was obtained for the quasi-static component simulation. The initial stiffness was too low, causing buckling of the inner wall, maximum force and failure initiation to occur somewhat later than in the test. The low initial stiffness indicates that the macroscopic model is incapable of representing the correct elastic deformations.
- Since each connection had identical connection model parameters, failure initiated simultaneously in the lowest connection on all sides of the component. In the experiment they did not fail at the same time, because of natural variation of the mechanical properties of the connections. Nevertheless, good correlation was seen for the failure of the two first connections, which occurred somewhat later than in the experiments. The third connection failed much later than in the experiments. This indicates that prediction of failure propagation may be difficult with this modelling

technique.

– The force-displacement curve from the dynamic simulation correlated adequately with the experiments. The time without contact between the trolley and the specimen was significantly large, and failure initiation occurred somewhat later than the experiments. However, the force-displacement curves from the quasi-static and dynamic simulations agreed well, indicating that the above observations were caused by the low initial stiffness. This further indicated that the physics of the dynamic test were well captured in the simulation.

Appendix A Characterization of connections

The FDS connections in the joint were characterised by means of single-connector tests. Specimens with plates of varying geometry joined by a single screw were pulled apart in different directions, producing various loadings on the connections. The main reason for performing such tests was that they were necessary to calibrate and validate the macroscopic connection model for the large-scale finite element simulation of the component test. In addition, they provided useful knowledge of the structural performance of the connections under different loadings, for instance maximum force, stiffness and ductility, as well as information about failure mechanisms.

The single-connector tests carried out in this work were cross tests in tension, mixed mode and shear, and single lap-joint and peeling tests. The test set-ups and results are presented in the following sections.

A.1 Cross tests

Fig. A.1a illustrates the principle of the cross tests. The coloured areas in the figure were clamped in the tests. To allow for relative sliding of the plates, only half of the area on one side of the bottom plate was clamped in the cross mixed and shear tests. This is indicated with a lighter red colour where the clamping was omitted. The bottom plate was fixed, while the top plate was pulled in the direction of the arrows in the figure.

A schematic drawing of the cross test specimen is shown in Fig. A.1b, where the clamped areas are indicated with grey colour. The darker grey indicates the area where a smaller clamping was used in the cross mixed and shear tests.

Fig. A.1c shows a principle drawing of the cross tension test set-up. The specimen was mounted on two steel fixtures, using screws and clamping blocks. A picture of the set-up

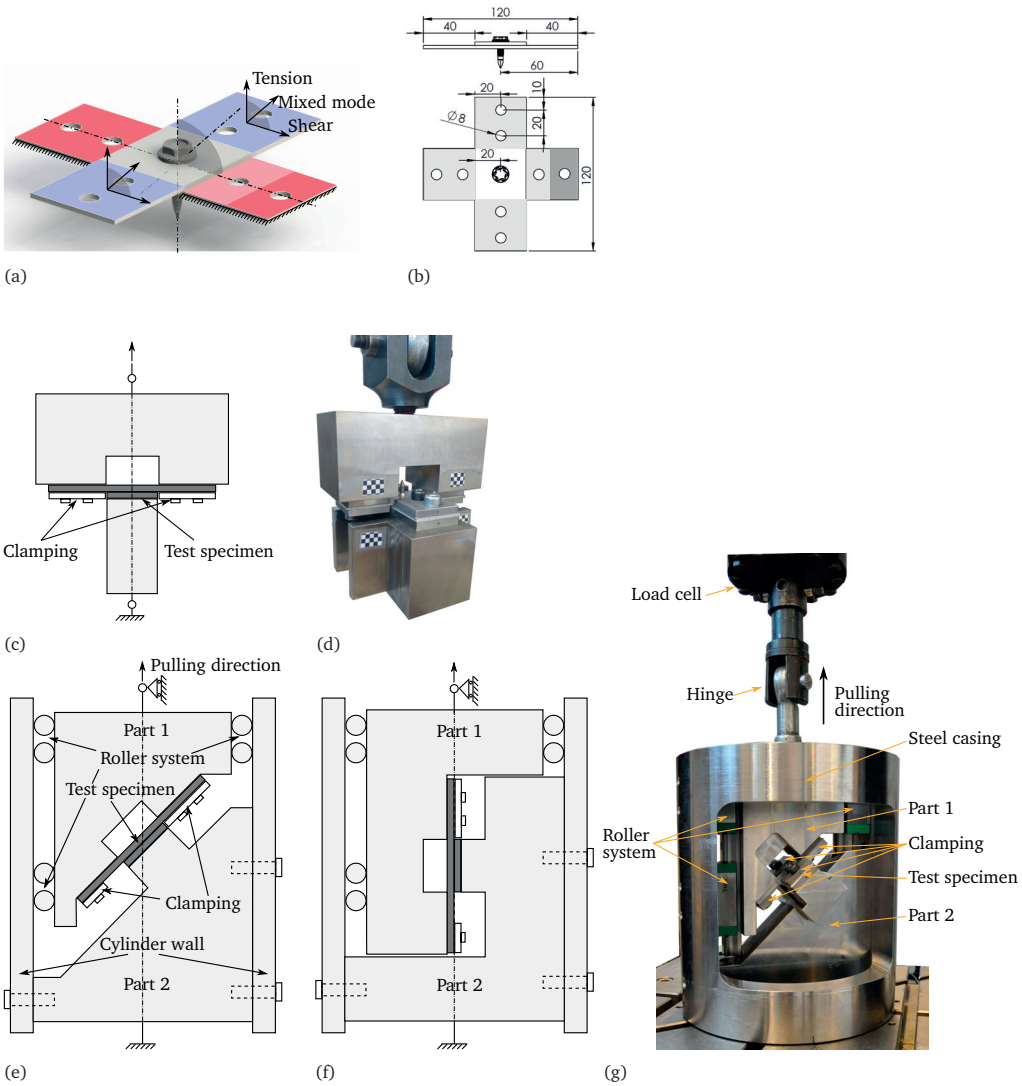

Fig. A.1. Illustrations of the set-ups in the cross tests. (a) Principle of the cross tests. (b) Drawing of the cross test specimen. (c) Principle drawing of the tension set-up. (d) Picture of the tension set-up. (e) Principle drawing of the mixed-mode set-up. (f) Principle drawing of the shear set-up. (g) Picture of the mixed mode set-up.

is shown in Fig. A.1d. The steel fixtures were placed in a regular Instron tensile testing machine, where they were pulled apart in the vertical direction. Pure tensile loading was ensured by hinging the fixture in each end. The pulling force was measured with a load cell mounted in series between the top fixture and the cross beam of the testing machine. A camera was used to take photographs during the tests, which were later used to measure the relative displacement of the steel fixtures with a DIC method.

The shear and mixed mode cross tests were carried out using a rig designed for testing of connections under controlled boundary conditions. Principle drawings of the set-up are shown in Figs. A.1e and A.1f, and Fig. A.1g shows a picture of the mixed-mode set-up. The cross specimen was clamped to two main steel parts (denoted part 1 and part 2 in Fig. A.1) with screws and clamping blocks. The main steel parts were placed inside a cylindrical steel casing, to prevent rotation and translation of part 1 in other directions than in the pulling direction, thus ensuring controlled boundary conditions in the test. Part 1 was attached to the cylinder with a roller system, allowing for smooth motion in the loading direction, whereas part 2 was bolted to the casing. The rig was designed such that the load application line passed exactly through the centre of the specimen (as indicated with stippled-dotted lines in Figs. A.1a, A.1c, A.1e and A.1f).

The rig was placed in a regular Instron tensile testing machine. The rig was hinged in the top, and attached to the testing machine with a single bolt between the centre of the bottom of part 2 and the testing machine. A load cell was mounted between the top hinge and the cross-beam of the testing machine. It was confirmed by in-house testing that the friction force in the rollers was negligible compared to the pulling force, and thus that the force measured was equal to the force transmitted through the specimen. The clamping of the specimen was carefully monitored to verify that no slipping occurred. A camera was used to take photographs during the tests, to later measure the rigid-body motion of parts 1 and 2 with DIC. It was verified that the rotation and translation in other directions than the pulling direction were negligible. The cross-head velocity in all cross tests was set to 5 mm/min, which was assumed to render quasi-static conditions.

Results from cross tests of both connections are presented as force-displacement curves in Fig. A.2, where the displacement was calculated as the relative displacement between the top and bottom steel parts using DIC. The two connections behaved similarly in terms of force-displacement curves and deformation modes. Both connections were strongest in shear and weakest in tension. Due to the significantly stronger bottom extrusion, the HS-connection sustained higher forces than the HH-connection. Mechanical tests on connections are expected to show some degree of scatter in the results, due to uncertainties in the joining process (e.g. rotational speed, tightening torque, cleanliness). The repeatability obtained here was considered acceptable.

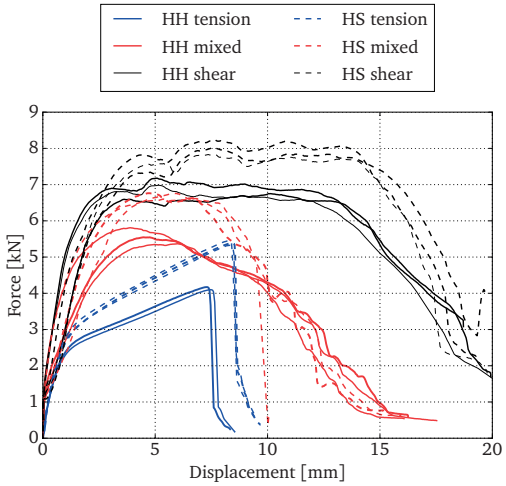

Fig. A.2. Force-displacement curves from cross tests.

In tension the majority of the measured displacement was caused by plastic bending of the plates. Little deformation occurred locally in the connection before the maximum force capacity was reached, where the threads in the bottom extrusion were abruptly stripped. The maximum force in tension was approximately 30 % higher for the HS-connection, and the displacement at failure was approximately 13 % higher.

In mixed mode the force increased gradually until maximum force was reached. For the HH-connection the force started to decrease instantly after maximum force was achieved, while for the HS-connection the force flattened out to a small plateau before decreasing. The screw rotated slightly during testing, such that threads were engaged on one side of the screw hole only. The specimens failed by thread stripping from the bottom plate. The maximum force was approximately 15-20 % higher for the HS-connection. The ductility was similar.

A significant force plateau was observed for both connections in shear, after which the force dropped nearly linearly. The maximum force was approximately 15 % higher for the HS-connection, and the ductility was similar. In these tests the screw rotated significantly, engaging threads on only one side of the screw hole, and the connections failed by a through-thickness shear failure.

A.2 Single lap-joint and peeling tests

Drawings of the single lap-joint and peeling specimens are shown in Figs. A.3a to A.3c. In the single lap-joint test the only difference for the two connections was the thickness of the

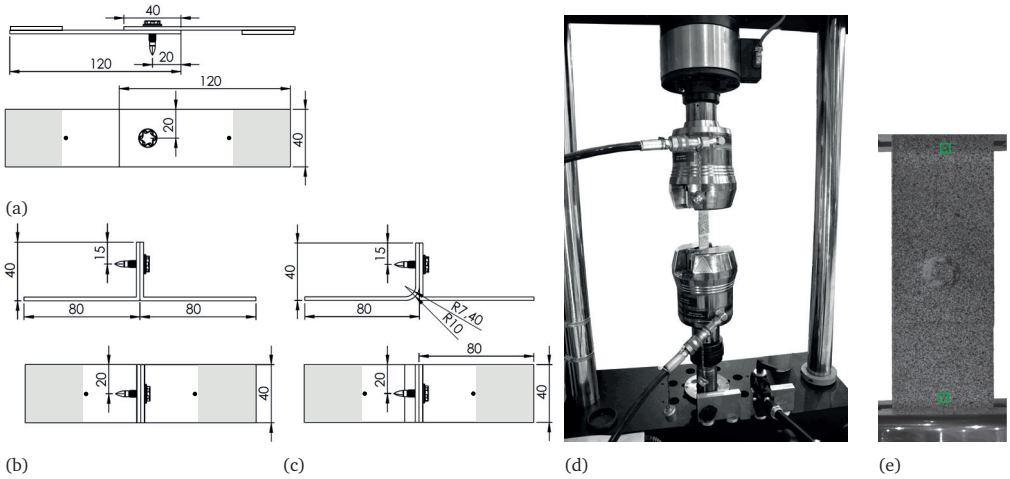

Fig. A.3. Illustrations of the single lap-joint and peeling test set-ups. (a) Schematic drawing of the single lap-joint specimen. (b-c) Schematic drawings of the peeling specimens. Grey areas indicate the gripping area of the clamps. Black dots indicate the locations from where local relative displacement was recorded. (d) Picture of test set-up. (e) Example of pictures used to measure local relative displacement (tracking points shown with green boxes).

bottom extrusion, otherwise the specimen geometry was unchanged. The geometry of the peeling specimen, on the other hand, was different for the two connections, hence is the drawing for each of them included.

The single lap-joint and peeling specimens were clamped with hydraulic grips in a regular Instron tensile test machine (clamping area is indicated with grey colour in Figs. A.3a to A.3c). Since the clamps were aligned in the testing machine, it was chosen to glue additional plates on the clamping area of the single lap-joint tests, to avoid deformation of the specimen upon clamping. The extra plates are indicated in Fig. A.3a. The specimens were pulled apart under displacement control at a cross-head velocity of 2.5 and 5 mm/min for the single lap-joint and peeling tests, respectively. The pulling force was recorded by a load cell mounted between the upper clamp and the cross-head beam of the testing machine. The local relative displacement was recorded by tracking two points on the specimen (indicated with black dots in Figs. A.3a to A.3c) with a camera taking one picture per second during testing. Fig. A.3d depicts the test set-up and Fig. A.3e shows an example of a picture during a single lap-joint test, where the tracking points for local relative displacement are indicated with green boxes.

Resulting force-displacement curves are shown in Fig. A.4. In the single lap-joint test the HS-connection gave approximately 17 % higher force and approximately 13 % higher ductility than the HH-connection. After maximum force was reached, the force decreased slowly until a rapid failure occurred where it dropped to zero. The screw and top plate rotated during deformation, and the connection failed by thread stripping from the bottom plate.

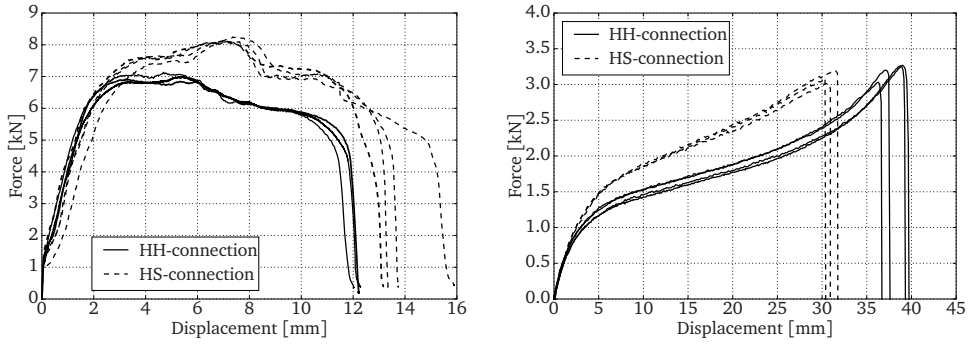

(a) (b)

Fig. A.4. Force-displacement curves from (a) single lap-joint and (b) peeling tests.

In the peeling test highest force was achieved for the HS-connection. The maximum force, however, was similar for the two connections. The specimen with the HH-connection was approximately 24 % more ductile than with the HS-connection. These observations are explained by the stronger bottom extrusion in the HS-connection.

References

[1] Szlosarek, R., Karall, T., Enzinger, N., Hahne, C. and Meyer, N. "Mechanical testing of flow drill screw joints between fibre-reinforced plastics and metals". *Materials Testing* 55.10 (2013), pp. 737–742. https://doi.org/10.3139/120.110495.

[2] Skovron, J., Mears, L., Ulutan, D., Detwiler, D., Paolini, D., Baeumler, B. and Claus, L. "Characterization of Flow Drill Screwdriving Process Parameters on Joint Quality". *SAE Int. J. Mater. Manf.* 8 (Sept. 2014), pp. 35–44. https://doi.org/10.4271/2014-01-2241.

[3] Sønstabø, J. K., Holmstrøm, P. H., Morin, D. and Langseth, M. "Macroscopic strength and failure properties of flow-drill screw connections". *Journal of Materials Processing Technology* 222 (2015), pp. 1–12. https://doi.org/10.1016/j.jmatprotec.2015.02.031.

[4] Skovron, J. D., Prasad, R. R., Ulutan, D., Mears, L., Detwiler, D., Paolini, D., Baeumler, B. and Claus, L. "Effect of Thermal Assistance on the Joint Quality of Al6063-T5A During Flow Drill Screwdriving". *Journal of Manufacturing Science and Engineering* 137.5 (2015), p. 051019. https://doi.org/10.1115/1.4031242.

[5] Sønstabø, J. K., Morin, D. and Langseth, M. "Macroscopic modelling of flow-drill screw connections in thin-walled aluminium structures". *Thin-Walled Structures* 105 (2016), pp. 185–206. https://doi.org/10.1016/j.tws.2016.04.013.

[6] Porcaro, R., Hanssen, A., Aalberg, A. and Langseth, M. “Joining of aluminium using self-piercing riveting: testing, modelling and analysis”. *International journal of crashworthiness* 9.2 (2004), pp. 141–154. https://doi.org/https://doi.org/10.1533/ijcr.2004.0279.

[7] Belingardi, G., Goglio, L. and Rossetto, M. “Impact behaviour of bonded built-up beams: experimental results”. *International Journal of Adhesion and Adhesives* 25.2 (2005), pp. 173–180. https://doi.org/10.1016/j.ijadhadh.2004.06.004.

[8] Xiang, Y., Wang, Q., Fan, Z. and Fang, H. “Optimal crashworthiness design of a spot-welded thin-walled hat section”. *Finite Elements in Analysis and Design* 42.10 (2006), pp. 846–855. https://doi.org/10.1016/j.finel.2006.01.001.

[9] Zhou, Y., Lan, F. and Chen, J. “Crashworthiness research on S-shaped front rails made of steelaluminum hybrid materials”. *Thin-Walled Structures* 49.2 (2011), pp. 291–297. https://doi.org/10.1016/j.tws.2010.10.007.

[10] Chen, W. “Experimental and numerical study on bending collapse of aluminum foam-filled hat profiles”. *International Journal of Solids and Structures* 38.44 (2001), pp. 7919–7944. https://doi.org/10.1016/S0020-7683(01)00094-4.

[11] Carlberger, T. and Stigh, U. “Dynamic testing and simulation of hybrid joined bi-material beam”. *Thin-Walled Structures* 48.8 (2010), pp. 609–619. https://doi.org/10.1016/j.tws.2010.03.003.

[12] Qi, C., Sun, Y., Hu, H.-T., Wang, D.-Z., Cao, G.-J. and Yang, S. “On design of hybrid material double-hat thin-walled beams under lateral impact”. *International Journal of Mechanical Sciences* 118.Supplement C (2016), pp. 21–35. https://doi.org/10.1016/j.ijmecsci.2016.09.009.

[13] Hoang, N.-H., Hanssen, A.-G., Langseth, M. and Porcaro, R. “Structural behaviour of aluminium self-piercing riveted joints: An experimental and numerical investigation”. *International Journal of Solids and Structures* 49.23 (2012), pp. 3211–3223. https://doi.org/10.1016/j.ijsolstr.2012.05.039.

[14] Børvik, T., Clausen, A. H., Eriksson, M., Berstad, T., Hopperstad, O. S. and Langseth, M. “Experimental and numerical study on the perforation of AA6005-T6 panels”. *International Journal of Impact Engineering* 32.1 (2005). Fifth International Symposium on Impact Engineering, pp. 35–64. https://doi.org/10.1016/j.ijimpeng.2005.05.001.

[15] Chen, Y., Clausen, A., Hopperstad, O. and Langseth, M. “Stress-strain behaviour of aluminium alloys at a wide range of strain rates”. *International Journal of Solids and Structures* 46.21 (2009), pp. 3825–3835. https://doi.org/10.1016/j.ijsolstr.2009.07.013.

[16] Grimsmo, E., Clausen, A., Langseth, M. and Aalberg, A. “An experimental study of static and dynamic behaviour of bolted end-plate joints of steel”. *International Journal*

of Impact Engineering 85 (2015), pp. 132–145. https://doi.org/10.1016/j.ijimpeng.2015.07.001.

[17] Hanssen, A. G., Auestad, T., Tryland, T. and Langseth, M. "The kicking machine: A device for impact testing of structural components". *International Journal of Crashworthiness* 8.4 (Jan. 2003), pp. 385–392. https://doi.org/10.1533/ijcr.2003.0246.

[18] Fagerholt, E. "Field measurements in mechanical testing using close-range photogrammetry and digital image analysis". PhD thesis. Norges teknisk-naturvitenskapelige universitet (NTNU), 2012.

[19] Hershey, A. "The plasticity of an isotropic aggregate of anisotropic face-centered cubic crystals". *Journal of Applied Mechanics-Transactions of the Asme* 21.3 (1954), pp. 241–249.

[20] Barlat, F., Aretz, H., Yoon, J., Karabin, M., Brem, J. and Dick, R. "Linear transfomation-based anisotropic yield functions". *International Journal of Plasticity* 21.5 (2005), pp. 1009–1039. https://doi.org/10.1016/j.ijplas.2004.06.004.

[21] Hanssen, A., Olovsson, L., Porcaro, R. and Langseth, M. "A large-scale finite element point-connector model for self-piercing rivet connections". *European Journal of Mechanics - A/Solids* 29.4 (2010), pp. 484–495. https://doi.org/10.1016/j.euromechsol.2010.02.010.

[22] Belytschko, T., Lin, J. I. and Chen-Shyh, T. "Explicit algorithms for the nonlinear dynamics of shells". *Computer Methods in Applied Mechanics and Engineering* 42.2 (1984), pp. 225–251. https://doi.org/10.1016/0045-7825(84)90026-4.

DEPARTMENT OF STRUCTURAL ENGINEERING
NORWEGIAN UNIVERSITY OF SCIENCE AND TECHNOLOGY

N–7491 TRONDHEIM, NORWAY
Telephone: +47 73 59 47 00 Telefax: +47 73 59 47 01

"Reliability Analysis of Structural Systems using Nonlinear Finite Element Methods",
C. A. Holm, 1990:23, ISBN 82-7119-178-0.

"Uniform Stratified Flow Interaction with a Submerged Horizontal Cylinder",
Ø. Arntsen, 1990:32, ISBN 82-7119-188-8.

"Large Displacement Analysis of Flexible and Rigid Systems Considering Displacement-Dependent Loads and Nonlinear Constraints",
K. M. Mathisen, 1990:33, ISBN 82-7119-189-6.

"Solid Mechanics and Material Models including Large Deformations",
E. Levold, 1990:56, ISBN 82-7119-214-0, ISSN 0802-3271.

"Inelastic Deformation Capacity of Flexurally-Loaded Aluminium Alloy Structures",
T. Welo, 1990:62, ISBN 82-7119-220-5, ISSN 0802-3271.

"Visualization of Results from Mechanical Engineering Analysis",
K. Aamnes, 1990:63, ISBN 82-7119-221-3, ISSN 0802-3271.

"Object-Oriented Product Modeling for Structural Design",
S. I. Dale, 1991:6, ISBN 82-7119-258-2, ISSN 0802-3271.

"Parallel Techniques for Solving Finite Element Problems on Transputer Networks",
T. H. Hansen, 1991:19, ISBN 82-7119-273-6, ISSN 0802-3271.

"Statistical Description and Estimation of Ocean Drift Ice Environments",
R. Korsnes, 1991:24, ISBN 82-7119-278-7, ISSN 0802-3271.

“Properties of concrete related to fatigue damage: with emphasis on high strength concrete”,
G. Petkovic, 1991:35, ISBN 82-7119-290-6, ISSN 0802-3271.

"Turbidity Current Modelling",
B. Brørs, 1991:38, ISBN 82-7119-293-0, ISSN 0802-3271.

"Zero-Slump Concrete: Rheology, Degree of Compaction and Strength. Effects of Fillers as Part Cement-Replacement",
C. Sørensen, 1992:8, ISBN 82-7119-357-0, ISSN 0802-3271.

"Nonlinear Analysis of Reinforced Concrete Structures Exposed to Transient Loading",
K. V. Høiseth, 1992:15, ISBN 82-7119-364-3, ISSN 0802-3271.

"Finite Element Formulations and Solution Algorithms for Buckling and Collapse Analysis of Thin Shells",
R. O. Bjærum, 1992:30, ISBN 82-7119-380-5, ISSN 0802-3271.

"Response Statistics of Nonlinear Dynamic Systems",
J. M. Johnsen, 1992:42, ISBN 82-7119-393-7, ISSN 0802-3271.

"Digital Models in Engineering. A Study on why and how engineers build and operate digital models for decisison support",
J. Høyte, 1992:75, ISBN 82-7119-429-1, ISSN 0802-3271.

"Sparse Solution of Finite Element Equations",
A. C. Damhaug, 1992:76, ISBN 82-7119-430-5, ISSN 0802-3271.

"Some Aspects of Floating Ice Related to Sea Surface Operations in the Barents Sea",
S. Løset, 1992:95, ISBN 82-7119-452-6, ISSN 0802-3271.

"Modelling of Cyclic Plasticity with Application to Steel and Aluminium Structures",
O. S. Hopperstad, 1993:7, ISBN 82-7119-461-5, ISSN 0802-3271.

"The Free Formulation: Linear Theory and Extensions with Applications to Tetrahedral Elements
with Rotational Freedoms",
G. Skeie, 1993:17, ISBN 82-7119-472-0, ISSN 0802-3271.

"Høyfast betongs motstand mot piggdekkslitasje. Analyse av resultater fra prøving i Veisliter'n",
T. Tveter, 1993:62, ISBN 82-7119-522-0, ISSN 0802-3271.

"A Nonlinear Finite Element Based on Free Formulation Theory for Analysis of Sandwich Structures",
O. Aamlid, 1993:72, ISBN 82-7119-534-4, ISSN 0802-3271.

"The Effect of Curing Temperature and Silica Fume on Chloride Migration and Pore Structure of High Strength Concrete",
C. J. Hauck, 1993:90, ISBN 82-7119-553-0, ISSN 0802-3271.

"Failure of Concrete under Compressive Strain Gradients",
G. Markeset, 1993:110, ISBN 82-7119-575-1, ISSN 0802-3271.

"An experimental study of internal tidal amphidromes in Vestfjorden",
J. H. Nilsen, 1994:39, ISBN 82-7119-640-5, ISSN 0802-3271.

"Structural analysis of oil wells with emphasis on conductor design",
H. Larsen, 1994:46, ISBN 82-7119-648-0, ISSN 0802-3271.

"Adaptive methods for non-linear finite element analysis of shell structures",
K. M. Okstad, 1994:66, ISBN 82-7119-670-7, ISSN 0802-3271.

"On constitutive modelling in nonlinear analysis of concrete structures",
O. Fyrileiv, 1994:115, ISBN 82-7119-725-8, ISSN 0802-3271.

"Fluctuating wind load and response of a line-like engineering structure with emphasis on motion-induced wind forces",
J. Bogunovic Jakobsen, 1995:62, ISBN 82-7119-809-2, ISSN 0802-3271.

"An experimental study of beam-columns subjected to combined torsion, bending and axial actions",
A. Aalberg, 1995:66, ISBN 82-7119-813-0, ISSN 0802-3271.

"Scaling and cracking in unsealed freeze/thaw testing of Portland cement and silica fume concretes",
S. Jacobsen, 1995:101, ISBN 82-7119-851-3, ISSN 0802-3271.

"Damping of water waves by submerged vegetation. A case study of laminaria hyperborea",
A. M. Dubi, 1995:108, ISBN 82-7119-859-9, ISSN 0802-3271.

"The dynamics of a slope current in the Barents Sea",
Sheng Li, 1995:109, ISBN 82-7119-860-2, ISSN 0802-3271.

"Modellering av delmaterialenes betydning for betongens konsistens",
Ernst Mørtsell, 1996:12, ISBN 82-7119-894-7, ISSN 0802-3271.

"Bending of thin-walled aluminium extrusions",
Birgit Søvik Opheim, 1996:60, ISBN 82-7119-947-1, ISSN 0802-3271.

"Material modelling of aluminium for crashworthiness analysis",
Torodd Berstad, 1996:89, ISBN 82-7119-980-3, ISSN 0802-3271.

"Estimation of structural parameters from response measurements on submerged floating tunnels",
Rolf Magne Larssen, 1996:119, ISBN 82-471-0014-2, ISSN 0802-3271.

“Numerical modelling of plain and reinforced concrete by damage mechanics”,
Mario A. Polanco-Loria, 1997:20, ISBN 82-471-0049-5, ISSN 0802-3271.

“Nonlinear random vibrations - numerical analysis by path integration methods”,
Vibeke Moe, 1997:26, ISBN 82-471-0056-8, ISSN 0802-3271.

“Numerical prediction of vortex-induced vibration by the finite element method”, Joar Martin Dalheim, 1997:63, ISBN 82-471-0096-7, ISSN 0802-3271.

“Time domain calculations of buffeting response for wind sensitive structures”,
Ketil Aas-Jakobsen, 1997:148, ISBN 82-471-0189-0, ISSN 0802-3271.

"A numerical study of flow about fixed and flexibly mounted circular cylinders",
Trond Stokka Meling, 1998:48, ISBN 82-471-0244-7, ISSN 0802-3271.

“Estimation of chloride penetration into concrete bridges in coastal areas”,
Per Egil Steen, 1998:89, ISBN 82-471-0290-0, ISSN 0802-3271.

“Stress-resultant material models for reinforced concrete plates and shells”,
Jan Arve Øverli, 1998:95, ISBN 82-471-0297-8, ISSN 0802-3271.

“Chloride binding in concrete. Effect of surrounding environment and concrete composition”, Claus Kenneth Larsen, 1998:101, ISBN 82-471-0337-0, ISSN 0802-3271.

“Rotational capacity of aluminium alloy beams”,
Lars A. Moen, 1999:1, ISBN 82-471-0365-6, ISSN 0802-3271.

“Stretch Bending of Aluminium Extrusions”,
Arild H. Clausen, 1999:29, ISBN 82-471-0396-6, ISSN 0802-3271.

“Aluminium and Steel Beams under Concentrated Loading”,
Tore Tryland, 1999:30, ISBN 82-471-0397-4, ISSN 0802-3271.

"Engineering Models of Elastoplasticity and Fracture for Aluminium Alloys",
Odd-Geir Lademo, 1999:39, ISBN 82-471-0406-7, ISSN 0802-3271.

"Kapasitet og duktilitet av dybelforbindelser i trekonstruksjoner",
Jan Siem, 1999:46, ISBN 82-471-0414-8, ISSN 0802-3271.

“Etablering av distribuert ingeniørarbeid; Teknologiske og organisatoriske erfaringer fra en norsk ingeniørbedrift”,
Lars Line, 1999:52, ISBN 82-471-0420-2, ISSN 0802-3271.

“Estimation of Earthquake-Induced Response”,
Símon Ólafsson, 1999:73, ISBN 82-471-0443-1, ISSN 0802-3271.

“Coastal Concrete Bridges: Moisture State, Chloride Permeability and Aging Effects”
Ragnhild Holen Relling, 1999:74, ISBN 82-471-0445-8, ISSN 0802-3271.

”Capacity Assessment of Titanium Pipes Subjected to Bending and External Pressure”,
Arve Bjørset, 1999:100, ISBN 82-471-0473-3, ISSN 0802-3271.

“Validation of Numerical Collapse Behaviour of Thin-Walled Corrugated Panels”,
Håvar Ilstad, 1999:101, ISBN 82-471-0474-1, ISSN 0802-3271.

“Strength and Ductility of Welded Structures in Aluminium Alloys”,
Miroslaw Matusiak, 1999:113, ISBN 82-471-0487-3, ISSN 0802-3271.

“Thermal Dilation and Autogenous Deformation as Driving Forces to Self-Induced Stresses in High Performance Concrete”,
Øyvind Bjøntegaard, 1999:121, ISBN 82-7984-002-8, ISSN 0802-3271.

“Some Aspects of Ski Base Sliding Friction and Ski Base Structure”,
Dag Anders Moldestad, 1999:137, ISBN 82-7984-019-2, ISSN 0802-3271.

"Electrode reactions and corrosion resistance for steel in mortar and concrete",
Roy Antonsen, 2000:10, ISBN 82-7984-030-3, ISSN 0802-3271.

"Hydro-Physical Conditions in Kelp Forests and the Effect on Wave Damping and Dune Erosion. A case study on Laminaria Hyperborea",
Stig Magnar Løvås, 2000:28, ISBN 82-7984-050-8, ISSN 0802-3271.

"Random Vibration and the Path Integral Method",
Christian Skaug, 2000:39, ISBN 82-7984-061-3, ISSN 0802-3271.

"Buckling and geometrical nonlinear beam-type analyses of timber structures",
Trond Even Eggen, 2000:56, ISBN 82-7984-081-8, ISSN 0802-3271.

”Structural Crashworthiness of Aluminium Foam-Based Components”,
Arve Grønsund Hanssen, 2000:76, ISBN 82-7984-102-4, ISSN 0809-103X.

“Measurements and simulations of the consolidation in first-year sea ice ridges, and some aspects of mechanical behaviour”,
Knut V. Høyland, 2000:94, ISBN 82-7984-121-0, ISSN 0809-103X.

”Kinematics in Regular and Irregular Waves based on a Lagrangian Formulation”,
Svein Helge Gjøsund, 2000-86, ISBN 82-7984-112-1, ISSN 0809-103X.

”Self-Induced Cracking Problems in Hardening Concrete Structures”,
Daniela Bosnjak, 2000-121, ISBN 82-7984-151-2, ISSN 0809-103X.

"Ballistic Penetration and Perforation of Steel Plates",
Tore Børvik, 2000:124, ISBN 82-7984-154-7, ISSN 0809-103X.

"Freeze-Thaw resistance of Concrete. Effect of: Curing Conditions, Moisture Exchange and Materials",
Terje Finnerup Rønning, 2001:14, ISBN 82-7984-165-2, ISSN 0809-103X

"Structural behaviour of post tensioned concrete structures. Flat slab. Slabs on ground",
Steinar Trygstad, 2001:52, ISBN 82-471-5314-9, ISSN 0809-103X.

"Slipforming of Vertical Concrete Structures. Friction between concrete and slipform panel",
Kjell Tore Fosså, 2001:61, ISBN 82-471-5325-4, ISSN 0809-103X.

"Some numerical methods for the simulation of laminar and turbulent incompressible flows",
Jens Holmen, 2002:6, ISBN 82-471-5396-3, ISSN 0809-103X.

“Improved Fatigue Performance of Threaded Drillstring Connections by Cold Rolling”,
Steinar Kristoffersen, 2002:11, ISBN: 82-421-5402-1, ISSN 0809-103X.

"Deformations in Concrete Cantilever Bridges: Observations and Theoretical Modelling",
Peter F. Takâcs, 2002:23, ISBN 82-471-5415-3, ISSN 0809-103X.

"Stiffened aluminium plates subjected to impact loading",
Hilde Giæver Hildrum, 2002:69, ISBN 82-471-5467-6, ISSN 0809-103X.

"Full- and model scale study of wind effects on a medium-rise building in a built up area",
Jónas Thór Snæbjørnsson, 2002:95, ISBN82-471-5495-1, ISSN 0809-103X.

“Evaluation of Concepts for Loading of Hydrocarbons in Ice-infested water”,
Arnor Jensen, 2002:114, ISBN 82-417-5506-0, ISSN 0809-103X.

”Numerical and Physical Modelling of Oil Spreading in Broken Ice”,
Janne K. Økland Gjøsteen, 2002:130, ISBN 82-471-5523-0, ISSN 0809-103X.

”Diagnosis and protection of corroding steel in concrete”,
Franz Pruckner, 20002:140, ISBN 82-471-5555-4, ISSN 0809-103X.

“Tensile and Compressive Creep of Young Concrete: Testing and Modelling”,
Dawood Atrushi, 2003:17, ISBN 82-471-5565-6, ISSN 0809-103X.

“Rheology of Particle Suspensions. Fresh Concrete, Mortar and Cement Paste with Various Types of Lignosulfonates”,
Jon Elvar Wallevik, 2003:18, ISBN 82-471-5566-4, ISSN 0809-103X.

“Oblique Loading of Aluminium Crash Components”,
Aase Reyes, 2003:15, ISBN 82-471-5562-1, ISSN 0809-103X.

“Utilization of Ethiopian Natural Pozzolans”,
Surafel Ketema Desta, 2003:26, ISSN 82-471-5574-5, ISSN:0809-103X.

“Behaviour and strength prediction of reinforced concrete structures with discontinuity regions”, Helge Brå, 2004:11, ISBN 82-471-6222-9, ISSN 1503-8181.

“High-strength steel plates subjected to projectile impact. An experimental and numerical study”, Sumita Dey, 2004:38, ISBN 82-471-6282-2 (printed version), ISBN 82-471-6281-4 (electronic version), ISSN 1503-8181.

“Alkali-reactive and inert fillers in concrete. Rheology of fresh mixtures and expansive reactions.”
Bård M. Pedersen, 2004:92, ISBN 82-471-6401-9 (printed version), ISBN 82-471-6400-0 (electronic version), ISSN 1503-8181.

“On the Shear Capacity of Steel Girders with Large Web Openings”.
Nils Christian Hagen, 2005:9 ISBN 82-471-6878-2 (printed version), ISBN 82-471-6877-4 (electronic version), ISSN 1503-8181.

”Behaviour of aluminium extrusions subjected to axial loading”.
Østen Jensen, 2005:7, ISBN 82-471-6873-1 (printed version), ISBN 82-471-6872-3 (electronic version), ISSN 1503-8181.

”Thermal Aspects of corrosion of Steel in Concrete”.
Jan-Magnus Østvik, 2005:5, ISBN 82-471-6869-3 (printed version), ISBN 82-471-6868 (electronic version), ISSN 1503-8181.

”Mechanical and adaptive behaviour of bone in relation to hip replacement.” A study of bone remodelling and bone grafting.
Sébastien Muller, 2005:34, ISBN 82-471-6933-9 (printed version), ISBN 82-471-6932-0 (electronic version), ISSN 1503-8181.

“Analysis of geometrical nonlinearities with applications to timber structures”.
Lars Wollebæk, 2005:74, ISBN 82-471-7050-5 (printed version), ISBN 82-471-7019-1 (electronic version), ISSN 1503-8181.

“Pedestrian induced lateral vibrations of slender footbridges”,
Anders Rönnquist, 2005:102, ISBN 82-471-7082-5 (printed version), ISBN 82-471-7081-7 (electronic version), ISSN 1503-8181.

“Initial Strength Development of Fly Ash and Limestone Blended Cements at Various Temperatures Predicted by Ultrasonic Pulse Velocity”,
Tom Ivar Fredvik, 2005:112, ISBN 82-471-7105-8 (printed version), ISBN 82-471-7103-1 (electronic version), ISSN 1503-8181.

“Behaviour and modelling of thin-walled cast components”,
Cato Dørum, 2005:128, ISBN 82-471-7140-6 (printed version), ISBN 82-471-7139-2 (electronic version), ISSN 1503-8181.

“Behaviour and modelling of selfpiercing riveted connections”,
Raffaele Porcaro, 2005:165, ISBN 82-471-7219-4 (printed version), ISBN 82-471-7218-6 (electronic version), ISSN 1503-8181.

”Behaviour and Modelling og Aluminium Plates subjected to Compressive Load”,
Lars Rønning, 2005:154, ISBN 82-471-7169-1 (printed version), ISBN 82-471-7195-3 (electronic version), ISSN 1503-8181.

”Bumper beam-longitudinal system subjected to offset impact loading”,
Satyanarayana Kokkula, 2005:193, ISBN 82-471-7280-1 (printed version), ISBN 82-471-7279-8 (electronic version), ISSN 1503-8181.

“Control of Chloride Penetration into Concrete Structures at Early Age”,
Guofei Liu, 2006:46, ISBN 82-471-7838-9 (printed version), ISBN 82-471-7837-0 (electronic version), ISSN 1503-8181.

“Modelling of Welded Thin-Walled Aluminium Structures”,
Ting Wang, 2006:78, ISBN 82-471-7907-5 (printed version), ISBN 82-471-7906-7 (electronic version), ISSN 1503-8181.

”Time-variant reliability of dynamic systems by importance sampling and probabilistic analysis of ice loads”,
Anna Ivanova Olsen, 2006:139, ISBN 82-471-8041-3 (printed version), ISBN 82-471-8040-5 (electronic version), ISSN 1503-8181.

“Fatigue life prediction of an aluminium alloy automotive component using finite element analysis of surface topography”.
Sigmund Kyrre Ås, 2006:25, ISBN 82-471-7791-9 (printed version), ISBN 82-471-7791-9 (electronic version), ISSN 1503-8181.

”Constitutive models of elastoplasticity and fracture for aluminium alloys under strain path change”,
Dasharatha Achani, 2006:76, ISBN 82-471-7903-2 (printed version), ISBN 82-471-7902-4 (electronic version), ISSN 1503-8181.

“Simulations of 2D dynamic brittle fracture by the Element-free Galerkin method and linear fracture mechanics”,
Tommy Karlsson, 2006:125, ISBN 82-471-8011-1 (printed version), ISBN 82-471-8010-3 (electronic version), ISSN 1503-8181.

“Penetration and Perforation of Granite Targets by Hard Projectiles”,
Chong Chiang Seah, 2006:188, ISBN 82-471-8150-9 (printed version), ISBN 82-471-8149-5 (electronic version), ISSN 1503-8181.

“Deformations, strain capacity and cracking of concrete in plastic and early hardening phases”,
Tor Arne Hammer, 2007:234, ISBN 978-82-471-5191-4 (printed version), ISBN 978-82-471-5207-2 (electronic version), ISSN 1503-8181.

“Crashworthiness of dual-phase high-strength steel: Material and Component behaviour”, Venkatapathi Tarigopula, 2007:230, ISBN 82-471-5076-4 (printed version), ISBN 82-471-5093-1 (electronic version), ISSN 1503-8181.

“Fibre reinforcement in load carrying concrete structures”,
Åse Lyslo Døssland, 2008:50, ISBN 978-82-471-6910-0 (printed version), ISBN 978-82-471-6924-7 (electronic version), ISSN 1503-8181.

“Low-velocity penetration of aluminium plates”,
Frode Grytten, 2008:46, ISBN 978-82-471-6826-4 (printed version), ISBN 978-82-471-6843-1 (electronic version), ISSN 1503-8181.

“Robustness studies of structures subjected to large deformations”,
Ørjan Fyllingen, 2008:24, ISBN 978-82-471-6339-9 (printed version), ISBN 978-82-471-6342-9 (electronic version), ISSN 1503-8181.

“Constitutive modelling of morsellised bone”,
Knut Birger Lunde, 2008:92, ISBN 978-82-471-7829-4 (printed version), ISBN 978-82-471-7832-4 (electronic version), ISSN 1503-8181.

“Experimental Investigations of Wind Loading on a Suspension Bridge Girder”,
Bjørn Isaksen, 2008:131, ISBN 978-82-471-8656-5 (printed version), ISBN 978-82-471-8673-2 (electronic version), ISSN 1503-8181.

“Cracking Risk of Concrete Structures in The Hardening Phase”,
Guomin Ji, 2008:198, ISBN 978-82-471-1079-9 (printed version), ISBN 978-82-471-1080-5 (electronic version), ISSN 1503-8181.

“Modelling and numerical analysis of the porcine and human mitral apparatus”,
Victorien Emile Prot, 2008:249, ISBN 978-82-471-1192-5 (printed version), ISBN 978-82-471-1193-2 (electronic version), ISSN 1503-8181.

“Strength analysis of net structures”,
Heidi Moe, 2009:48, ISBN 978-82-471-1468-1 (printed version), ISBN 978-82-471-1469-8 (electronic version), ISSN1503-8181.

“Numerical analysis of ductile fracture in surface cracked shells”,
Espen Berg, 2009:80, ISBN 978-82-471-1537-4 (printed version), ISBN 978-82-471-1538-1 (electronic version), ISSN 1503-8181.

“Subject specific finite element analysis of bone – for evaluation of the healing of a leg lengthening and evaluation of femoral stem design”,
Sune Hansborg Pettersen, 2009:99, ISBN 978-82-471-1579-4 (printed version), ISBN 978-82-471-1580-0 (electronic version), ISSN 1503-8181.

“Evaluation of fracture parameters for notched multi-layered structures”,
Lingyun Shang, 2009:137, ISBN 978-82-471-1662-3 (printed version), ISBN 978-82-471-1663-0 (electronic version), ISSN 1503-8181.

"Modelling of Dynamic Material Behaviour and Fracture of Aluminium Alloys for Structural Applications"
Yan Chen, 2009:69, ISBN 978-82-471-1515-2 (printed version), ISBN 978-82 471-1516-9 (electronic version), ISSN 1503-8181.

"Nanomechanics of polymer and composite particles"
Jianying He 2009:213, ISBN 978-82-471-1828-3 (printed version), ISBN 978-82-471-1829-0 (electronic version), ISSN 1503-8181.

"Mechanical properties of clear wood from Norway spruce"
Kristian Berbom Dahl 2009:250, ISBN 978-82-471-1911-2 (printed version) ISBN 978-82-471-1912-9 (electronic version), ISSN 1503-8181.

"Modeling of the degradation of TiB_2 mechanical properties by residual stresses and liquid Al penetration along grain boundaries"
Micol Pezzotta 2009:254, ISBN 978-82-471-1923-5 (printed version) ISBN 978-82-471-1924-2 (electronic version) ISSN 1503-8181.

"Effect of welding residual stress on fracture"
Xiabo Ren 2010:77, ISBN 978-82-471-2115-3 (printed version) ISBN 978-82-471-2116-0 (electronic version), ISSN 1503-8181.

"Pan-based carbon fiber as anode material in cathodic protection system for concrete structures"
Mahdi Chini 2010:122, ISBN 978-82-471-2210-5 (printed version) ISBN 978-82-471-2213-6 (electronic version), ISSN 1503-8181.

"Structural Behaviour of deteriorated and retrofitted concrete structures"
Irina Vasililjeva Sæther 2010:171, ISBN 978-82-471-2315-7 (printed version) ISBN 978-82-471-2316-4 (electronic version) ISSN 1503-8181.

"Prediction of local snow loads on roofs"
Vivian Meløysund 2010:247, ISBN 978-82-471-2490-1 (printed version) ISBN 978-82-471-2491-8 (electronic version) ISSN 1503-8181.

"Behaviour and modelling of polymers for crash applications"
Virgile Delhaye 2010:251, ISBN 978-82-471-2501-4 (printed version) ISBN 978-82-471-2502-1 (electronic version) ISSN 1503-8181.

"Blended cement with reducted CO_2 emission – Utilizing the Fly Ash-Limestone Synergy",
Klaartje De Weerdt 2011:32, ISBN 978-82-471-2584-7 (printed version) ISBN 978-82-471-2584-4 (electronic version) ISSN 1503-8181.

"Chloride induced reinforcement corrosion in concrete" Concept of critical chloride content – methods and mechanisms.
Ueli Angst 2011:113, ISBN 978-82-471-2769-9 (printed version) ISBN 978-82-471-2763-6 (electronic version) ISSN 1503-8181.

"A thermo-electric-Mechanical study of the carbon anode and contact interface for Energy savings in the production of aluminium".
Dag Herman Andersen 2011:157, ISBN 978-82-471-2859-6 (printed version) ISBN 978-82-471-2860-2 (electronic version) ISSN 1503-8181.

"Structural Capacity of Anchorage Ties in Masonry Veneer Walls Subjected to Earthquake". The implications of Eurocode 8 and Eurocode 6 on a typical Norwegain veneer wall.
Ahmed Mohamed Yousry Hamed 2011:181, ISBN 978-82-471-2911-1 (printed version) ISBN 978-82-471-2912-8 (electronic ver.) ISSN 1503-8181.

"Work-hardening behaviour in age-hardenable Al-Zn-Mg(-Cu) alloys".
Ida Westermann , 2011:247, ISBN 978-82-471-3056-8 (printed ver.) ISBN 978-82-471-3057-5 (electronic ver.) ISSN 1503-8181.

"Behaviour and modelling of selfpiercing riveted connections using aluminium rivets". Nguyen-Hieu Hoang, 2011:266, ISBN 978-82-471-3097-1 (printed ver.) ISBN 978-82-471-3099-5 (electronic ver.) ISSN 1503-8181.

"Fibre reinforced concrete".
Sindre Sandbakk, 2011:297, ISBN 978-82-471-3167-1 (printed ver.) ISBN 978-82-471-3168-8 (electronic ver) ISSN 1503:8181.

"Dynamic behaviour of cablesupported bridges subjected to strong natural wind".
Ole Andre Øiseth, 2011:315, ISBN 978-82-471-3209-8 (printed ver.) ISBN 978-82-471-3210-4 (electronic ver.) ISSN 1503-8181.

"Constitutive modeling of solargrade silicon materials"
Julien Cochard, 2011:307, ISBN 978-82-471-3189-3 (printed ver). ISBN 978-82-471-3190-9 (electronic ver.) ISSN 1503-8181.

“Constitutive behavior and fracture of shape memory alloys”
Jim Stian Olsen, 2012:57, ISBN 978-82-471-3382-8 (printed ver.) ISBN 978-82-471-3383-5 (electronic ver.) ISSN 1503-8181.

“Field measurements in mechanical testing using close-range photogrammetry and digital image analysis”
Egil Fagerholt, 2012:95, ISBN 978-82-471-3466-5 (printed ver.) ISBN 978-82-471-3467-2 (electronic ver.) ISSN 1503-8181.

“Towards a better under standing of the ultimate behaviour of lightweight aggregate concrete in compression and bending”,
Håvard Nedrelid, 2012:123, ISBN 978-82-471-3527-3 (printed ver.) ISBN 978-82-471-3528-0 (electronic ver.) ISSN 1503-8181.

“Numerical simulations of blood flow in the left side of the heart”
Sigrid Kaarstad Dahl, 2012:135, ISBN 978-82-471-3553-2 (printed ver.) ISBN 978-82-471-3555-6 (electronic ver.) ISSN 1503-8181.

“Moisture induced stresses in glulam”
Vanessa Angst-Nicollier, 2012:139, ISBN 978-82-471-3562-4 (printed ver.) ISBN 978-82-471-3563-1 (electronic ver.) ISSN 1503-8181.

“Biomechanical aspects of distraction osteogensis”
Valentina La Russa, 2012:250, ISBN 978-82-471-3807-6 (printed ver.) ISBN 978-82-471-3808-3 (electronic ver.) ISSN 1503-8181.

“Ductile fracture in dual-phase steel. Theoretical, experimental and numerical study”
Gaute Gruben, 2012:257, ISBN 978-82-471-3822-9 (printed ver.) ISBN 978-82-471-3823-6 (electronic ver.) ISSN 1503-8181.

“Damping in Timber Structures”
Nathalie Labonnote, 2012:263, ISBN 978-82-471-3836-6 (printed ver.) ISBN 978-82-471-3837-3 (electronic ver.) ISSN 1503-8181.

“Biomechanical modeling of fetal veins: The umbilical vein and ductus venosus bifurcation”
Paul Roger Leinan, 2012:299, ISBN 978-82-471-3915-8 (printed ver.) ISBN 978-82-471-3916-5 (electronic ver.) ISSN 1503-8181.

“Large-Deformation behaviour of thermoplastics at various stress states”
Anne Serine Ognedal, 2012:298, ISBN 978-82-471-3913-4 (printed ver.) ISBN 978-82-471-3914-1 (electronic ver.) ISSN 1503-8181.

“Hardening accelerator for fly ash blended cement”
Kien Dinh Hoang, 2012:366, ISBN 978-82-471-4063-5 (printed ver.) ISBN 978-82-471-4064-2 (electronic ver.) ISSN 1503-8181.

“From molecular structure to mechanical properties”
Jianyang Wu, 2013:186, ISBN 978-82-471-4485-5 (printed ver.) ISBN 978-82-471-4486-2 (electronic ver.) ISSN 1503-8181.

“Experimental and numerical study of hybrid concrete structures”
Linn Grepstad Nes, 2013:259, ISBN 978-82-471-4644-6 (printed ver.) ISBN 978-82-471-4645-3 (electronic ver.) ISSN 1503-8181.

“Mechanics of ultra-thin multi crystalline silicon wafers”
Saber Saffar, 2013:199, ISBN 978-82-471-4511-1 (printed ver.) ISBN 978-82-471-4513-5 (electronic ver). ISSN 1503-8181.

“Through process modelling of welded aluminium structures”
Anizahyati Alisibramulisi, 2013:325, ISBN 978-82-471-4788-7 (printed ver.) ISBN 978-82-471-4789-4 (electronic ver.) ISSN 1503-8181.

“Combined blast and fragment loading on steel plates”
Knut Gaarder Rakvåg, 2013:361, ISBN978-82-471-4872-3 (printed ver.) ISBN 978-82-4873-0 (electronic ver.). ISSN 1503-8181.

“Characterization and modelling of the anisotropic behaviour of high-strength aluminium alloy”
Marion Fourmeau, 2014:37, ISBN 978-82-326-0008-3 (printed ver.) ISBN 978-82-326-0009-0 (electronic ver.) ISSN 1503-8181.

“Behaviour of threated steel fasteners at elevated deformation rates”
Henning Fransplass, 2014:65, ISBN 978-82-326-0054-0 (printed ver.) ISBN 978-82-326-0055-7 (electronic ver.) ISSN 1503-8181.

“Sedimentation and Bleeding”
Ya Peng, 2014:89, ISBN 978-82-326-0102-8 (printed ver.) ISBN 978-82-326-0103-5 (electric ver.) ISSN 1503-8181.

“Impact against X65 offshore pipelines”
Martin Kristoffersen, 2014:362, ISBN 978-82-326-0636-8 (printed ver.) ISBN 978-82-326-0637-5 (electronic ver.) ISSN 1503-8181.

“Formability of aluminium alloy subjected to prestrain by rolling”
Dmitry Vysochinskiy, 2014:363,, ISBN 978-82-326-0638-2 (printed ver.) ISBN 978-82-326-0639-9 (electronic ver.) ISSN 1503-8181.

“Experimental and numerical study of Yielding, Work-Hardening and anisotropy in textured AA6xxx alloys using crystal plasticity models”
Mikhail Khadyko, 2015:28, ISBN 978-82-326-0724-2 (printed ver.) ISBN 978-82-326-0725-9 (electronic ver.) ISSN 1503-8181.

“Behaviour and Modelling of AA6xxx Aluminium Alloys Under a Wide Range of Temperatures and Strain Rates”
Vincent Vilamosa, 2015:63, ISBN 978-82-326-0786-0 (printed ver.) ISBN 978-82-326-0787-7 (electronic ver.) ISSN 1503-8181.

“A Probabilistic Approach in Failure Modelling of Aluminium High Pressure Die-Castings”
Octavian Knoll, 2015:137, ISBN 978-82-326-0930-7 (printed ver.) ISBN 978-82-326-0931-4 (electronic ver.) ISSN 1503-8181.

“Ice Abrasion on Marine Concrete Structures”
Egil Møen, 2015:189, ISBN 978-82-326-1034-1 (printed ver.) ISBN 978-82-326-1035-8 (electronic ver.) ISSN 1503-8181.

“Fibre Orientation in Steel-Fibre-Reinforced Concrete”
Giedrius Zirgulis, 2015:229, ISBN 978-82-326-1114-0 (printed ver.) ISBN 978-82-326-1115-7 (electronic ver.) ISSN 1503-8181.

“Effect of spatial variation and possible interference of localised corrosion on the residual capacity of a reinforced concrete beam”
Mohammad Mahdi Kioumarsi, 2015:282, ISBN 978-82-326-1220-8 (printed ver.) ISBN 978-82-1221-5 (electronic ver.) ISSN 1503-8181.

“The role of concrete resistivity in chloride-induced macro-cell corrosion”
Karla Horbostel, 2015:324, ISBN 978-82-326-1304-5 (printed ver.) ISBN 978-82-326-1305-2 (electonic ver.) ISSN 1503-8181.

“Flowable fibre-reinforced concrete for structural applications”
Elena Vidal Sarmiento, 2015-335, ISBN 978-82-326-1324-3 (printed ver.) ISBN 978-82-326-1325-0 (electronic ver.) ISSN 1503-8181.

“Development of chushed sand for concrete production with microproportioning” Rolands Cepuritis, 2016:19, ISBN 978-82-326-1382-3 (printed ver.) ISBN 978-82-326-1383-0 (electronic ver.) ISSN 1503-8181.

“Withdrawal properties of threaded rods embedded in glued-laminated timer elements”
Haris Stamatopoulos, 2016:48, ISBN 978-82-326-1436-3 (printed ver.) ISBN 978-82-326-1437-0 (electronic ver.) ISSN 1503-8181.

“An Experimental and numerical study of thermoplastics at large deformation”
Marius Andersen, 2016:191, ISBN 978-82-326-1720-3 (printed ver.) ISBN 978-82-326-1721-0 (electronic ver.) ISSN 1503-8181.

“Modeling and Simulation of Ballistic Impact”
Jens Kristian Holmen, 2016:240, ISBN 978-82-326-1818-7 (printed ver). ISBN 978-82-326-1819-4 (electronic ver.) ISSN 1503-8181.

“Early age crack assessment of concrete structures”
Anja B. Estensen Klausen, 2016:256, ISBN 978-82-326-1850-7 (printed ver). ISBN 978-82-326-1851-4 (electronic ver.) ISSN 1503-8181.

“Uncertainty quantification and sensitivity analysis for cardiovascular models”
Vinzenz Gregor Eck, 2016:234, ISBN 978-82-326-1806-4 (printed ver.) ISBN 978-82-326-1807-1 (electronic ver.) ISSN 1503-8181.

“Dynamic behaviour of existing and new railway catenary systems under Norwegain conditions”
Petter Røe Nåvik, 2016:298, ISBN 978-82-326-1935-1 (printed ver.) ISBN 978-82-326-1934-4 (electronic ver.) ISSN 1503-8181.

“Mechanical behaviour of particle-filled elastomers at various temperatures”
Arne Ilseng, 2016-295, ISBN978-82-326-1928-3 (printed ver.) ISBN 978-82-326-1929-0 (electronic ver.) ISSN 1503-8181.

“Nanotechnology for Anti-Icing Application”
Zhiwei He, 2016:348, ISBN 978-82-326-2038-8 (printed ver.) ISBN 978-82-326-2019-5 (electronic ver.) ISSN 1503-8181.

“Conduction Mechanisms in Conductive Adhesives with Metal-Coated Polyer Spheres”
Sigurd Rolland Pettersen, 2016:349, ISBN 978-326-2040-1 (printed ver,) ISBN 978-82-326-2041-8 (electronic ver.) ISSN 1503-8181.

“The interaction between calcium lignosulfonate and cement”
Alessia Colombo, 2017:20, ISBN 978-82-326-2122-4 (printed ver.) ISBN 978-82-326-2123-1 (electronic ver.) ISSN 1503-8181.

“Behaviour and Modelling of Flexible Structures Subjected to Blast Loading”
Vegard Aune, 2017:101, ISBN 978-82-326-2274-0 (printed ver.) ISBN 978-82-326-2275-7 (electronic ver.) ISSN 1503-8181.

“Behaviour of steel connections under quasi-static and impact loading”
Erik Løhre Grimsmo, 2017:159, ISBN 978-82-326-2390-7 (printed ver.) ISBN 978-82-326-2391-4 (electronic ver.) ISSN 1503-8181.

“An experimental and numerical study of cortical bone at he macro and Nano-scale”
Masoud Ramenzanzadehkoldeh,, 2017:208, ISBN 978-82-326-2488-1 (printed ver.) ISBN 978-82-326-2489-8 (electronic ver.) ISSN 1503-8181.

“Optoelectrical Properties of a Novel Organic Semiconductor: 6,13-Dichloropentacene” Mao Wang, 2017:130, ISBN 978-82-326-2332-7 (printed ver.) ISBN 978-82-326-2333-4) (electronic ver.) ISSN 1503-8181.

“Core-shell structured microgels and their behavior at oil and water interface”
Yi Gong, 2017:182, ISBN 978-82-326-2436-2 (printed. ver.) ISBN 978-82-326-2437-9 (electronic ver.) ISSN 1503-8181.

“Aspects of design of reinforced concrete structures using nonliear finite element analyses”
Morten Engen, 2017:149, ISBN 978-82-326-2370-9 (printed ver.) ISBN 978-82-326-2371-6 (electronic ver.) ISSN 1503-8181.

“Numerical studies on ductile failure of aluminium alloys”
Lars Edvard Dæhli, 2017:284, ISBN 978-82-326-2636-6 (printed ver.) ISBN 978-82-326-2637-3 (electronic ver.) ISSN 1503-8181.

“Modelling and Assessment of Hydrogen Embrittlement in Steels and Nickel Alloys”
Haiyang Yu, 2017:278, ISBN 978-82-326-2624-3 (printed. ver.) ISBN 978-82-326-2625-0 (electronic ver.) ISSN 1503-8181.

“Network arch timber bridges with light timber deck on transverse crossbeams”
Anna Weronika Ostrycharczyk, 2017:318, ISBN 978-82-326-2704-2 (printed ver.) ISBN 978-82-326-2705-9 (electronic ver.) ISSN 1503-8181.

“Splicing of Large Glued Laminated Timber Elements by Use of Long Threated Rods”
Martin Cepelka, 2017:320, ISBN 978-82-326-2708-0 (printed ver.) ISBN 978-82-326-2709-7 (electronic ver.) ISSN 1503-8181.

“Thermomechanical behaviour of semi-crystalline polymers: experiments, modelling and simulation”
Joakim Johnsen, 2017-317, ISBN 978-82-326-2702-8 (printed ver.) ISBN 978-82-326-2703-5 (electronic ver.) ISSN 1503-8181.

“Small-Scale Plasiticity under Hydrogen Environment”
Kai Zhao, 2017:356, ISBN 978-82-326-2782-0 (printed ver.) ISBN 978-82-326-2783-7 (electronic er.) ISSN 1503-8181.

“Risk and Reliability Based Calibration of Structural Design Codes”
Michele Baravalle, 2017:342, ISBN 978-82-326-2752-3 (printed ver,) ISBN 978-82-326-2753-0 (electronic ver.) ISSN 1503-8181.

“Dynamic behaviour of floating bridges exposed to wave excitation”
Knut Andreas Kvåle, 2017:365, ISBN 978-82-326-2800-1 (printed ver.) ISBN 978-82-326-2801-8 (electronic ver.) ISSN 1503-8181.

“Dolomite calcined clay composite cement – hydration and durability”
Alisa Lydia Machner, 2018:39, ISBN 978-82-326-2872-8 (printed ver.). ISBN 978-82-326-2873-5 (electronic ver.) ISSN 1503-8181.

“Modelling of the self-excited forces for bridge decks subjected to random motions: an experimental study”
Bartosz Siedziako, 2018:52, ISBN 978-82-326-2896-4 (printed ver.). ISBN 978-82-326-2897-1 (electronic ver.) ISSN 1503-8181.